

**Modification of Flow and Flow Driven Instabilities in the Auburn Linear EXperiment for
Instability Studies**

by

Ashley Christopher Eadon

A dissertation submitted to the Graduate Faculty of
Auburn University
in partial fulfillment of the
requirements for the Degree of
Doctor of Philosophy

Auburn, Alabama
May 9, 2011

Approved by

Edward E. Thomas, Jr., Chair, Professor of Physics
Gurudas Ganguli, Affiliate Professor of Physics
James Hanson, Professor of Physics
Stephen Knowlton, Professor of Physics
Yu Lin, Professor of Physics

Abstract

The primary focus of the experiments presented here is to study the impact of sheared flows on the stability of a magnetized plasma. Experiments will utilize sheared transverse flows to drive an instability in the ion cyclotron regime in a linear, magnetized Helium plasma. These flows will then be significantly modified by an imposed radial electric field to study the asymmetric response of the plasma. Specifically, the results presented here will show that, for the first time with a steady-state, filament-based linear magnetized column, the directionality of the radial electric field has been successfully changed over a large volume of the column, and the plasma response was significantly modified. Results will then be presented showing an instability in the ion cyclotron regime driven by shear in the field aligned plasma flow. This instability will be studied from initial generation, to maximum amplitude, to a transition away from resonance with the experimental device. To support both of these experiments, computational models were developed and will be discussed in the context of experimental observations.

Acknowledgements

First and foremost, I wish to thank my parents, Christopher and Carolyn Eadon, for their unfailing support and unwavering belief. Additionally, the love and encouragement of my brother, Jason, my sister, Lindsey, and their spouses, Autumn and Brent, have helped to buoy my spirits when the distance from home seemed too great. And nothing made the distance feel greater than the arrival of my amazing nephews and niece, Lucas, Pryce, and Grace...you can always call your Uncle Ash when the science fair rolls around.

This work could not have been started, much less completed, without the guidance and support of my advisor, Dr. Edward Thomas. From Denver to Tromsø, Dr. Thomas has shown by example the dedication it takes to be a world-class physicist, and never fails to inspire all of the students lucky enough to pass through his lab.

Speaking of students, my time at Auburn could not have been nearly as productive, or enjoyable, without my labmates and fellow graduate students Edwinn Wallace, John David Jackson, Jerimiah Williams, John McKee (Team PSL), Erik Tejero, Mark Cianciosa, Ross Fisher, and Ami DuBois. Thank you all for your help and inspiration with the countless projects that made this work possible. I only hope that I've been able to give back even a small fraction of all you've given me throughout the years.

Additionally, I would like to thank my committee members for their help and guidance not just with this dissertation, but throughout my time at Auburn. Nowhere is there a more

selfless, more dedicated, or more knowledgeable group of plasma physicists, and I consider myself very fortunate to have learned from you all.

Finally, I would like to thank my high school physics teacher, Tom Haff. Without him, I never would have started down this path. The term “contagious enthusiasm” is a complete understatement. Too few teachers really challenge their students to see the world differently, and this dissertation should serve to show that Mr. Haff didn’t just try, he succeeded.

In closing, I dedicate this dissertation to my parents, who have encouraged, supported, consoled, and loved me throughout my entire graduate school adventure. All that I am I owe to you both, so in my mind this is not just my dissertation, but ours.

Table of Contents

Abstract.....	ii
Acknowledgements.....	iii
List of Tables	ix
List of Figures.....	xi
1 Introduction.....	1
2 Theoretical derivations.....	8
2.1 E×B Drift	8
2.1.1 Slab geometry	9
2.1.2 Cylindrical derivation of E x B mechanism.....	13
2.1.3 Density and collisions	16
2.2 Instabilities.....	21
2.2.1 Drift Waves.....	21
2.2.2 Inhomogeneous Energy Density Driven Instability.....	23
2.2.3 Current Driven Ion Cyclotron Instability.....	30
3 Experimental Hardware	35
3.1 Introduction	35

3.2	Initial Filament Configuration	36
3.3	ALEXIS Hardware Upgrade to RF Configuration	42
3.3.1	Vacuum Vessel and Pumping Systems	43
3.3.2	Plasma Generation	47
3.3.3	Computer Integration	48
3.3.4	<i>In Situ</i> Diagnostics	52
4	Experimental Data	56
4.1	Introduction	56
4.2	Experiments in the ALEXIS-filament configuration.....	58
4.2.1	Modification of the plasma potential profile	60
4.2.2	Impact on electron density profiles.....	65
4.2.3	Measurements of plasma instabilities	68
4.2.4	Characterizing the suppression of plasma instabilities	72
4.2.5	Driven plasma oscillations.....	76
4.2.6	Characterizing the observed electrostatic instability	79
4.3	Multi-Species Experiments in ALEXIS – RF configuration.....	91
4.3.1	Introduction.....	91
4.3.2	Experimental Design.....	92
4.3.3	Multi-species measurements.....	93
a)	Group A measurements	95

b)	Group B measurements	98
4.3.4	Multi-species Summary	101
4.4	Experiments in Argon – RF configuration	103
4.4.1	Introduction.....	103
4.4.2	Modified Potential Structure.....	104
4.4.3	Calculated Flow Velocities	111
4.4.4	Plasma Response to the Potential Structure Modification	116
4.4.5	Characterizing the observed electrostatic instability	120
5	Discussion.....	129
5.1	Summary.....	129
5.2	Future Works	131
5.3	Concluding Remarks	131
	Bibliography	133
	Appendix I - Laser Induced Fluorescence	138
A.	LIF Theory.....	138
1.	Line Broadening Mechanisms	142
a)	Doppler Broadening	142
b)	Natural Linewidth.....	145
c)	Stark Broadening	146
d)	Zeeman Broadening	147

e) Instrumental Broadening	148
f) Comparison of Line Broadening Mechanisms	149
B. LIF Hardware	150
C. Measured Flow Velocities	156
D. Discussion.....	167
Appendix II – Computer Codes Used.....	175
LabVIEW codes used in Data Acquisition	175
Langmuir Probe	175
Double Probe	183
Emissive Probe.....	186
LabVIEW codes used in Data Analysis.....	190
Langmuir Probe	190
Double Probe	194
Emissive Probe.....	198

List of Tables

Table 2-1: The range of cyclotron frequencies possible for each gas species used in ALEXIS. .	10
Table 2-2: Parameters used to compare the calculated $E \times B$ velocities using a slab geometry and a cylindrical geometry.....	15
Table 2-3: Parameters used to compare the calculated $E \times B$ velocities using a cylindrical geometry with and without collisions.	18
Table 2-4: Comparison of the terms used in the equation for the cylindrical $E \times B$ drift.	20
Table 2-5: Parameters used in the computational model discussed in this section.	28
Table 2-6: Parameters used to generate Figure 2-5.	33
Table 3-1: Coil types and locations of the magnets on ALEXIS.....	38
Table 4-1: Operating conditions in ALEXIS – filament configuration	60
Table 4-2: Potentials applied to the rings for the different experimental cases. All voltages are given in units of volts (V).	61
Table 4-3: Currents measured at each ring for each case, measured in mA. Here, negative currents indicate the collection of a net electron current. Also noted in this table are the conditions under which spatially localized instabilities were present in the plasma – Case A and B (negative bias voltages) had instabilities present while Case C and D (positive bias voltages) did not observe instabilities.	65
Table 4-4: Parameters used in the computational model presented below.....	87
Table 4-5: Updated parameters used in the computational model presented below.....	88

Table 4-6: Conditions for the two cases presented in this section. Magnetic field strength is calculated from the current applied to the magnets. r_L/a is the ratio of the Larmor radius to the chamber radius.	94
Table 4-7: Summary of the plots in Section 4.3.3. For each case and each species the cyclotron frequency and the frequency of the observed instability are presented.	101
Table 4-8: Operating conditions in ALEXIS – RF configuration.....	103
Table 4-9: Parameters used in the computational model discussed in this section.	126
Table I-I-1: Comparison of the emission line broadening effects calculated for ALEXIS	149

List of Figures

Figure 2-1: A plot showing a comparison between the calculated $E \times B$ velocities using a slab geometry (green line) and a cylindrical geometry (red line). 16

Figure 2-2: Chart comparing the velocities calculated using all four models: $E \times B$ (green line), Cylindrical $E \times B$ (red line), Cylindrical $E \times B$ with the density gradient (light blue line), and Cylindrical $E \times B$ with the density gradient and collisions (dark blue line). 19

Figure 2-3: Chart comparing the velocities calculated using all four models, cast as a percentage of the unmodified $E \times B$ velocity: $E \times B$ (green line), Cylindrical $E \times B$ (red line), Cylindrical $E \times B$ with the density gradient (light blue line), and Cylindrical $E \times B$ with the density gradient and collisions (dark blue line). 20

Figure 2-4: Plot of Equation 2-27 using typical experimental parameters for ALEXIS. The plot shows the real component of ω (solid red line), the real component of ω_1 (dashed orange line), the imaginary component of ω (solid green line), and the imaginary component of ω_1 (dashed blue line). 29

Figure 2-5: The real (blue line) and imaginary (red line) parts of ω normalized to plotted versus k_z 34

Figure 3-1: Schematic of the initial chamber configuration of ALEXIS. 36

Figure 3-2: Magnet configuration for ALEXIS. Magnets 1 and 2 surround the plasma source, Magnet 9 is at the opposite end of the chamber near the biased rings. The coil type represents that different coil winding configurations that are given in Table 3-1. 39

Figure 3-3: The array of filaments used to generate He plasmas in ALEXIS. The three filament wires are coiled in order to minimize the mechanical stresses on the filament wires. The Macor block is the octagonal shape in the photograph..... 41

Figure 3-4: A photograph of the custom six-way vacuum box mounted on ALEXIS. Note the two magnets on either side of the box, the bellow that leads to the diffusion pump (near the bottom), and one of the “4-ring” electrode assemblies used to modify the electric field in the ALEXIS plasma. 44

Figure 3-5: Schematic of the matching network used in ALEXIS. The RF generator is a KJL R601, and the power meter is a Bird model 4391A. C1, C2, and C3 are the capacitors used to match the impedance of the circuit to the impedance of the R601. 48

Figure 3-6: Screenshot of the HMI used to control ALEXIS. In this screenshot are shown monitors for the current in the magnets (upper right, set at 100 A and 150 A in this image); for the mass flow controller (an applied voltage of 0.6 V for the Argon channel); for the RF source (showing a set point of 150W with 161 W measured as forward power and 0 W reflected); for the probe position; vacuum pressure in the chamber (as measured by the cold cathode and B/A ionization gauges), and the bias voltages on the ring electrodes. 51

Figure 3-7: Combination emissive probe (thin wire loop) and double Langmuir probe (straight wires). The ruler gives the scale in millimeters. 53

Figure 3-8: Photograph of the double probe used in ALEXIS. 54

Figure 3-9: Example of a double probe trace in ALEXIS from the VI used to acquire the data. A separate VI is used to fit an arctangent to the data. 54

Figure 3-10: Example k -probe data from ALEXIS. The probe angle is defined as 0° when the two probe tips are oriented parallel to the axial magnetic field as shown to the right. Shown is a measurement (blue dots) of the measured phase between two tips (separated by 2.5 mm) as the probe is rotated through 360° . The red curve is a sinusoidal fit to the phase data using $y = A \cos(\theta_{\text{probe}} + \phi)$ where ϕ is an arbitrary shift. 55

Figure 4-1: Rings used in initial experiments. These were four concentric copper gaskets. The outer diameter of each ring, starting at the center (Ring 1) and moving outward (Ring 4) are: 0.66 cm, 2.12 cm, 4.81 cm, and 8.23 cm, respectively. 59

Figure 4-2: Schematic of the initial chamber configuration of the ALEXIS device. The port numbers (listed 1 through 7 along the horizontal axis) will be used throughout this chapter to identify probe locations. 59

Figure 4-3: Measurements of the plasma potential as measured with the emissive probe. The probe is scanned radially across the plasma at the midplane. The four cases shown, A through D, are representative of the four cases shown in Table 2. Note that increase the overall plasma potential with increasing positive voltages on the inner three rings. Case A (solid circles) and Case B (solid square) are essentially overlapped. 62

Figure 4-4: Comparison of the normalized potential profiles (a) and (b) and the calculated electric fields (c) and (d) for the four bias voltage configurations applied to the ring electrodes. 64

Figure 4-5: Measurement of the electron density using a double probe at Port 2 ($z = 53$ cm) for the four bias voltage cases. This port location is 102 cm upstream from the location of the ring electrodes. 67

- Figure 4-6: Measurement of the electron density using a double probe at Port 6 ($z = 127$ cm) for the four bias voltage cases. This port location is 28 cm upstream from the location of the ring electrodes. 68
- Figure 4-7: Case A: A “waterfall” plot of the floating potential fluctuations in ALEXIS for a bias voltage of $V = -40V$ on the inner three rings. The plot shows the frequency from 0 to 40 KHz on the horizontal axis, position from $r = 0$ to $r = 5$ cm on the slanted axis and amplitude of the Fourier transform on the vertical axis. The measurements show the presence of a spatially localized instability (centered near $r = 3$ cm) at a frequency of $f \sim 16$ kHz (or $f/f_{ci} \approx 0.5$). 70
- Figure 4-8: Case B: A “waterfall” plot of the floating potential fluctuations in ALEXIS for a bias voltage of $V = -20V$ on the inner three rings. The measurements show the presence of a lower amplitude instability than for the -40 V case, but it remains spatially localized (centered near $r = 3$ cm) at a frequency of $f \sim 16$ kHz (or $f/f_{ci} \approx 0.5$). 70
- Figure 4-9: Case C: A “waterfall” plot of the floating potential fluctuations in ALEXIS for a bias voltage of $V = +40V$ on the inner three rings. The measurements show a broadband suppression of instabilities. Note that the scale on the vertical axis is 200 times smaller than for Figures 4-7 and 4-8. 70
- Figure 4-10: Case D: A “waterfall” plot of the floating potential fluctuations in ALEXIS for a bias voltage of $V = +80V$ on the inner three rings. The measurements show a broadband suppression of instabilities. Note that the scale on the vertical axis is 200 times smaller than for Figures 4-7 and 4-8. 71
- Figure 4-11: Plot of the radial profile of the amplitude of the Fourier transform at 15 kHz is plotted for the $V = -40$ V configuration (Case A, $V_1=V_2=V_3 = -40$ V, $V_4 = -50$ V).

Across the top of the figure are horizontal lines indicating the positions of the four rings.

..... 72

Figure 4-12: Semi-log plot of the power spectrum of the floating potential measured at $r = 3.25$ cm at Port 2 ($z = 53$ cm) in ALEXIS. The black curve represents Case A with the inner three rings biased at -80 V. The grey curve represents Case D with the inner three rings biased at $+40$ V. 73

Figure 4-13: Semi-log plot of the power spectrum of the floating potential measured at $r = 3.25$ cm at Port 6 ($z = 127$ cm) in ALEXIS. The black curve represents Case A with the inner three rings biased at -80 V. The grey curve represents Case D with the inner three rings biased at $+40$ V. 74

Figure 4-14: Comparison of the estimated azimuthal flow velocity for Case A (solid circles), Case D (open circles) and for the threshold conditions for wave growth in ALEXIS (solid line). 76

Figure 4-15: Radial profile of the amplitude of a launched wave in ALEXIS. The wave is launched from an antenna that is placed at the center of the ALEXIS plasma column at Port 1 ($z = 31$ cm) and is measured at Port 2 ($z = 53$ cm). 77

Figure 4-16: Radial profile of the amplitude of a launched wave in ALEXIS. The wave is launched from an antenna that is placed at the center of the ALEXIS plasma column at Port 1 ($z = 31$ cm) and is measured at Port 6 ($z = 127$ cm). 78

Figure 4-17: Three plots of the instabilities observed in ALEXIS for three different biases applied to Ring 3. From top to bottom the applied voltages are -107 V, -11 V, and $+21$ V. 81

Figure 4-18: The solid line is a fourth-order polynomial fit to the plasma potential measurements (black squares). The electric field is computed from the negative derivative of the potential curve fit. This measurement is taken when Ring 3 is biased very negative, i.e., drawing a low electron current. 83

Figure 4-19: Amplitudes of the instability plotted versus radial position for four different bias cases. This plot shows the radial localization of the instability, with the peak near Ring 3. 84

Figure 4-20: Density gradient near Ring 3 plotted versus the current collected by Ring 3, which has been shown to be proportional to the instability amplitude..... 85

Figure 4-21: Plot showing the output of the computational model based on experimental measurements for the region where the instability is observed. The plot shows the real component of ω (solid red line), the real component of ω_1 (dashed orange line), the imaginary component of ω (solid green line), and the imaginary component of ω_1 (dashed blue line). The dashed gray line shows the frequency measured in the lab frame. 88

Figure 4-22: Plot showing the output of the computational model utilizing the parameters given in Table 4-5 for the region where the instability is observed. The plot shows the real component of ω (solid red line), the real component of ω_1 (dashed orange line), the imaginary component of ω (solid green line), and the imaginary component of ω_1 (dashed blue line). The dashed gray line shows the frequency measured in the lab frame. 89

Figure 4-23: Case A, Argon: This experiment is performed with a magnetic field strength of $B = 330$ G. The dominant instability occurs at $f/f_{ci} \sim 0.5$ 96

Figure 4-24: Case A, Neon: This experiment is performed with a magnetic field strength of $B = 233$ G. The dominant instability occurs at $f/f_{ci} \sim 0.4$ 96

Figure 4-25: Case A, Nitrogen: This experiment is performed with a magnetic field strength of $B = 195$ G. The dominant instability occurs at $f/f_{ci} \sim 0.5$. Note that to calculate the ion cyclotron frequency, Nitrogen is assumed to be monoatomic, not N_2 97

Figure 4-26: Case A, Helium: This experiment is performed with a magnetic field strength of $B = 104$ G. The dominant instability occurs at $f/f_{ci} \sim 0.4$ 97

Figure 4-27: Case B, Argon: This experiment is performed with a magnetic field strength of $B = 240$ G. The dominant instability occurs at $f/f_{ci} \sim 1.6$ 99

Figure 4-28: Case B, Neon: This experiment is performed with a magnetic field strength of $B = 170$ G. The dominant instability occurs at $f/f_{ci} \sim 1.6$ 99

Figure 4-29: Case B, Nitrogen: This experiment is performed with a magnetic field strength of $B = 142$ G. The dominant instability occurs at $f/f_{ci} \sim 1.1$. Note that to calculate the ion cyclotron frequency, Nitrogen is assumed to be monoatomic, not N_2 100

Figure 4-30: Case B, Helium: This experiment is performed with a magnetic field strength of $B = 76$ G. The dominant instability occurs at $f/f_{ci} \sim 1.3$ 101

Figure 4-31: Schematic diagram of the rings used to modify the potential structure in ALEXIS. The inner ring is Ring 1, and the outer ring is Ring 2. Both rings are made of Aluminum and mounted on Macor. All dimensions are in cm. 105

Figure 4-32: Measured plasma potential profiles in ALEXIS. The horizontal axis is the radial location of the probe in cm, and the vertical axis is the plasma potential in Volts. The blue diamond markers are for the +30V bias, and the red circle markers are for the -50V bias. 106

Figure 4-33: Normalized measured plasma potential profiles in ALEXIS. The horizontal axis is the radial location of the probe in cm, and the vertical axis is the normalized plasma

potential in Volts. The blue diamond markers are for the +30V bias, and the red circle markers are for the -50V bias.....	107
Figure 4-34: Calculated radial electric fields in ALEXIS. The horizontal axis is the radial location of the probe in cm, and the vertical axis is the electric field strength in V/cm. The blue diamond markers are for the +30V bias, and the red circle markers are for the -50V bias.	108
Figure 4-35: Electric fields calculated from the current collected on Ring 2. The horizontal axis corresponds to the voltage applied to Ring 2, and the vertical axis is the calculated axial electric field.	110
Figure 4-36: Density profiles for Case A (red circles) and Case B (blue diamonds).	112
Figure 4-37: Velocities calculated using the measured plasma parameters for Case A (-50 V bias). The orange diamond markers are calculated using the slab $E \times B$ model, and the green circle markers are calculated using the cylindrically corrected $E \times B$ model.	113
Figure 4-38: Velocities calculated using the measured plasma parameters for Case B (+30 V bias). The orange diamond markers are calculated using the slab $E \times B$ model, and the green circle markers are calculated using the cylindrically corrected $E \times B$ model.	114
Figure 4-39: Azimuthal flow velocities calculated using the measured plasma parameters for Case A (-50 V bias) (red circles), and Case B (+30 V) (blue diamonds).	114
Figure 4-40: Calculated axial ion velocities as a function of bias voltage applied to Ring 2.....	115
Figure 4-41: Fourier spectrum of floating potential fluctuations for Case A (Ring 1 bias = -50 V, Ring 2 bias = - 50 V). The horizontal axis is the frequency, normalized to the ion cyclotron frequency. The vertical axis represents the radial position in cm. The color	

represents the intensity of the signal (in a.u.). The figure shows a broad, low frequency (~5 kHz) instability.....	117
Figure 4-42: Fourier spectrum of floating potential fluctuations for Case A (Ring 1 voltage is -50 V, Ring 2 Voltage is - 50 V). The vertical axis and the color represent the intensity of the signal (in a.u.). The left axis is frequency (normalized to the ion cyclotron frequency) and the right axis is radial position.....	118
Figure 4-43: Fourier spectrum of floating potential fluctuations for Case B (Ring 1 bias = -50 V, Ring 2 bias = +30 V). The horizontal axis is the frequency, normalized to the ion cyclotron frequency. The vertical axis represents the radial position in cm. The color represents the intensity of the signal (in a.u.). The figure shows a localized, narrow instability at approximately 10 kHz.....	119
Figure 4-44: Fourier spectrum of floating potential fluctuations for Case B (Ring 1 voltage is -50 V, Ring 2 voltage = +30 V). The vertical axis and the color represent the intensity of the signal (in a.u.). The left axis is frequency (normalized to the ion cyclotron frequency) and the right axis is radial position.....	120
Figure 4-45: Comparison between the normalized wave amplitude (orange diamonds) and the normalized current collected on Ring 2 (green squares) as a function of Ring 2 bias voltage.....	121
Figure 4-46: The ratio of the electron drift velocity and the ion thermal velocity as a function of the bias applied to Ring 2.....	122
Figure 4-47: Measured values of the parallel wave number as a function of the bias applied to Ring 2.....	124

Figure 4-48: The values of the ratio of the parallel wave number multiplied by the electron drift velocity to the wave frequency as a function of the bias applied to Ring 2. 124

Figure 4-49: Normalized ratio of the parallel wave number multiplied by the electron drift velocity to the wave frequency (blue triangles) and normalized wave amplitude (orange circles) plotted versus bias voltage applied to Ring 2..... 125

Figure 4-50: Output from the computational code using experimentally measured input parameters. The blue line is the frequency measured in the lab frame, and the red line is the imaginary component of the frequency. The vertical dashed line shows the parallel wavelength that corresponds to marginal stability. The horizontal dashed line shows the intersection of the vertical dashed line with the calculated frequency. 127

Figure I-1: Artistic example indicating the relationship between the laser linewidth (blue) and the Doppler broadened ion velocity distribution function (red) 140

Figure I-2: Pictorial representation of the transition scheme used in ALEXIS. 141

Figure I-3: Layout of the lasers and optics used for LIF. The ArII laser (black) is injected into the dye laser (green). All optical elements (mirror and beam-splitters) are in blue, and the optical choppers are represented by purple lines. The Iodine cell used for absolute reference is shown with its PMT (orange). 151

Figure I-4: Schematic showing the motion arm (gray), the injection optics (orange), laser light (red), collection optics (blue), and collected light (green). The enlarged section shows the interrogation region, where the laser light intersects the path of light collected by the collection optics. 154

Figure I-5: Example of LIF data from ALEXIS. The horizontal axis has been processed to be cast in velocity space. The vertical axis is the voltage output from the lock-in amplifier, and corresponds to the voltage from the PMT at the frequency of the optical chopper. 155

Figure I-6: Representative drawing of the relative locations of the diagnostics used on ALEXIS. The combination Langmuir probe and emissive probe (orange) is located at Port 6 ($z = 127$ cm, $\theta = 0$), the double probe (blue) is located at Port 5 ($z = 109$ cm, $\theta = \pi$), and the LIF system is located at $z = 150$ cm, $\theta = \pi/2$. The arrows indicate the direction of motion of the diagnostics to construct the radial profiles presented here. The green area shows the area scanned by the LIF system to measure the azimuthal (i.e. perpendicular) velocity. 157

Figure I-7: Schematic showing how the motion arm is moved (vertically) to make a radial scan of the perpendicular velocity. The relative placement of the injection and collection optics does not change, but the entire Motion Arm is moved vertically. 158

Figure I-8: Perpendicular flow velocities measured using LIF. The scans were done with two measurements at each point, and each point is separated by 4mm. Case A (-50V bias on Ring 2) is shown as the red line with circle markers, and Case B (+30V bias on Ring 2) is shown as the blue line with diamond markers. 159

Figure I-9: Flow velocities measured using LIF. The scans were done with one measurement at each point, and each point is separated by 1 cm. The red circles are Case A, and the blue diamonds are Case B. 160

Figure I-10: LIF measurements of the perpendicular component of the ion velocity measured at $r = 15$ mm as a function of bias applied to Ring 2. 161

Figure I-11: Measured velocity with laser injection at finite angle with respect to the magnetic field. The red circles are Case A, and the blue diamonds are Case B. 162

Figure I-12: Parallel velocities as a function of position measured using LIF. The red circles are Case A ($V_2 = -50$ V), and the blue diamonds are Case B ($V_2 = +30$ V)..... 163

Figure I-13: Perpendicular velocities calculated from the angled injection of the laser. The red circles are Case A ($V_2 = -50$ V), and the blue diamonds are Case B ($V_2 = +30$ V) 164

Figure I-14: Comparison between the directly measured (DM) perpendicular velocity, and the velocity resolved from the angled laser injection (RV). Case A: DM (dark green squares), RV (light green diamonds). Case B: DM (dark blue), RV (light blue triangles)..... 165

Figure I-15: Comparison of the measured (green squares) and calculated (orange diamonds) axial velocities at a fixed radial position ($r = 1.5$ cm) as a function of the bias applied to Ring 2..... 166

Figure I-16: Rendering of a possible means of better collocating the emissive probe (orange) and LIF measurements (green). The emissive probe would need a linear motion feed-through mounted to the clear polycarbonate window (light blue). 169

Figure I-17: Models of the perpendicular velocity profiles based upon the LIF measurements for Case A and Case B. The plots show velocity vectors (shown as the red arrows) along a central chord of ALEXIS. The length of the arrow corresponds to magnitude of the velocity with a maximum length of 250 m/s for Case A and a maximum length of 300 m/s for Case B. The locations of the rings are show as the gray circles in the background of each image. 171

Figure I-18: Models showing the different flow patterns for Case A ($V_2 = -50$ V) from the measured electric field (blue, left), and the measured ion flows from the LIF

measurement (red, right). The length of the arrow corresponds to magnitude of the velocity with a maximum length of 2000 m/s (blue) and 250 m/s (red). The locations of the rings are show as the gray circles in the background of each image. 172

Figure I-19: Models showing the different flow patterns for Case B ($V_2 = +30V$) from the measured electric field (blue, left), and the measured ion flows from the LIF measurement (red, right). The length of the arrow corresponds to magnitude of the velocity with a maximum length of 2000 m/s (blue) and 300 m/s (red). The locations of the rings are show as the gray circles in the background of each image. 173

1 Introduction

Plasma is the most common state of matter in our universe, by both volume and mass. First studied by Sir William Crooke in 1879,¹ the complex nature of what he termed “radiant matter” sparked a field of research that continues to this day, and has grown in size and importance beyond what any of the early pioneers in the field could have imagined. At the dawn of the 21st century, people are exposed to plasmas every day, although most are not aware of the important role plasmas play in their lives. Plasmas are used to manufacture most of the computer chips that power computers and cell phones. They are used in fluorescent and high efficiency light bulbs, street lamps, televisions and more. More importantly, plasma based fusion energy may be the solution to the global energy crisis within our lifetimes.

In 1928, Irving Langmuir was the first to use the word “plasma” in regards to the region of a gas discharge that contained a quasi-neutral balance of electrons and ions.^{2,3} This definition has been relaxed some to include a broad range of novel plasma systems including non-neutral plasmas,^{4,5} dusty plasmas^{6,7,8,9}, and microplasmas.¹⁰ In general, plasmas are characterized by three key parameters:¹¹ the number density of ions and electrons (n_i , n_e), the kinetic temperatures of the ions and electrons (T_i , T_e), and the electric potential of the plasma (ϕ_p). All of these quantities can vary in time and space and give rise to both the steady state and time evolved properties of plasmas.

A common theme that pervades almost all areas of plasma science research is the presence of plasma instabilities.^{2,12,13,14} Many laboratory and naturally-occurring plasmas consist of sources of free energy. One source of free energy can be pressure gradients (i.e., temperature or density gradients), which have been shown to drive a broad range of magnetohydrodynamic (MHD) instabilities.¹⁵ The ubiquity of these instabilities – across diverse ranges of plasma parameters and vastly different experimental configurations – points to the commonality of the underlying physics that can be used to describe the plasma.

In addition to pressure gradients, gradients in plasma flow are often a source of free energy for plasmas.^{14,16,17} In particular, for magnetized plasmas, it is important to consider flows that are parallel and perpendicular to the direction of the applied magnetic field. Satellite observations have shown that regions of large potential gradients can be formed naturally in the near-earth space environment.^{17,18} Combined with the Earth's magnetic fields, the potential gradients will cause particles in the region to experience a drift in the $\vec{E} \times \vec{B}$ direction.¹¹ Spatial variations in the magnitude of this drift can be a source of free energy to generate a broad range of instabilities.^{16,19,20} Theoretical models have shown that such flows in near-earth plasmas can lead to Kelvin-Helmholtz,^{21,22} ion acoustic,¹⁷ or ion cyclotron²³ instabilities. The following is a brief introduction to the history of the study of shear driven instabilities.

Sheared flows in fluids have been studied for over a century. Early studies of sound waves and shear driven instabilities were summarized and expanded upon by Raleigh in 1877.²⁴ Concepts such as sound speed, pitch, application of Laplace's function to acoustics, and more were presented and discussed. Years later, Chandrashekhar published a survey of hydrodynamic and hydromagnetic stability as a branch of experimental physics.²⁵ His work examined the stability of a layer of fluid as it is heated, Couette flows, and the Kelvin-Helmholtz instability.

These early works may have been primarily developed for fluids, but the ideas and discoveries of these pioneers paved the way for plasma physicists, who would apply and expand the concepts to laboratory and near-earth plasmas almost a century later.

By the middle part of the 20th century, a variety of studies had been performed on plasma instabilities present in flowing plasmas. For example, a review article by L. Kovasznay in *Reviews of Modern Physics* in 1960 summarized the state of understanding at that time particularly in the context of plasma turbulence in flowing fusion plasmas.²⁶ However, a key development in the study of flowing plasmas and plasma instabilities – in general – was the development of the Q-machine, first reported by Rynn and D’Angelo in 1960.²⁷ The “quiescent” nature of the Q-machine plasmas – a typically alkali metal plasma with approximately equal ion and electron temperatures – made them an ideal device for studying a broad range of phenomena. In particular, it will be noted that many of the experimental advances in the study of flow shear driven instabilities in plasma were performed using Q-machines.

In the following paragraphs, a brief summary of the investigations of flow shear driven instabilities in plasmas will be presented. This discussion will span almost fifty years, and serves to illustrate the important interplay between theoretical and experimental physics. First, low frequency waves will be briefly discussed, and then higher frequency waves, of the order of the ion cyclotron frequency, will be chronicled. These waves can be driven by parallel or perpendicular flows, and are modified by shear in the flows or the presence of electric fields.

Early work on parallel flows was performed by Motley and D’Angelo at Princeton in 1963 using the Q-machine.²⁸ These experimental studies confirmed the theoretical work done the preceding year by Drummond and Rosenbluth²⁹ that showed that currents parallel to a

background magnetic field could excite instabilities in a plasma. After its initial discovery, this Current Driven Ion Cyclotron Instability (CDICI) would be extensively studied in laboratory Q-machines for decades, and this cooperation between theorists and experimentalists is a central theme in the progression of the field.²⁷ For example, theoretical work by Bakshi, et al., in the early 1980's studied the effect of a finite current channel size.³⁰ They found that as the current channel decreased in width below a few ion Larmor radii the instability was no longer supported. This "filament quenching" was then verified and studied in the laboratory at the University of Iowa by Cartier, et al.,³¹ who found excellent agreement with the nonlocal theory of Bakshi, et al.

While the aforementioned studies focused on flows parallel to the magnetic field, it is noted that there was also a strong effort on the study of flows perpendicular to the magnetic field. Again using the Q-machine, it was observed that there was a peak in the amplitude of the low frequency oscillations was collocated with a strong, localized, radial electric field.^{32,33} Enriques used a split endplate composed of two concentric rings to drive coherent low frequency oscillations when the radial electric field was greater than an apparent threshold value (found to be approximately 0.1 V/cm).³³

At Tohoku University in Japan, Sato, et al.,³⁴ studied ion cyclotron instabilities driven by three dimensional double layers. Their research controlled the position and shape of the double layers by forming mirror configurations of the background magnetic field, which simulated the magnetic field structure above the Earth's auroral oval. They found that the oscillations were driven by the inhomogeneous radial electric field, and that the instabilities propagated azimuthally in their experiment, i.e., perpendicular to both the background magnetic field and the

radial electric field.³⁴ Their findings motivated theoretical works to understand the plasma response to perpendicular electric fields.

In the mid 1980's, Ganguli, et al., presented a new mechanism that showed a non-uniform electric field, perpendicular to the background magnetic field, can destabilize kinetic ion cyclotron waves.²³ This work was then extended to include both high and low temperature limits,³⁵ as well as associated ion heating.³⁶ Early experimental observation of this Inhomogeneous Energy Density Driven Instability (IEDDI) may have been seen as early as 1991 in the work of van Kiekerk, et al., which observed an azimuthally propagating ion cyclotron mode driven by a localized radial electric field.³⁷

In many physical systems, such as the near Earth space plasma environment, electric fields perpendicular to the magnetic field (and therefore perpendicular flows) are often associated with parallel plasma flows. This led Ganguli, et al., to generalize their model to include parallel flow. These early works^{36,38} neglected shear in the parallel flow, and found that the presence of a perpendicular electric field lowered the threshold value for the parallel current required to drive the plasma unstable. These theoretical works led to experimental works at West Virginia University that focused on experimental verification of the impact of a radial electric field on Current Driven Ion Cyclotron Instabilities.³⁹ The works of Amatucci, et al.,⁴⁰ and Koepke et al.,⁴¹ in 1994 provided the first experimental verifications of the impact of transverse velocity shear on ion cyclotron waves. Just a few years later, now at the Naval Research Laboratory, Amatucci, et al.,^{16,42} successfully isolated a purely perpendicular electric field, with no parallel current, to conclusively drive the Inhomogeneous Energy Density Driven Instability. Once the IEDDI could be reproducibly driven in a laboratory setting, the NRL group proceeded to study ion heating due to wave-particle interaction.^{43,44} Also at NRL, the previously used “slab”

geometry model was cast into cylindrical coordinates to facilitate a better understanding of laboratory experiments.⁴⁵ As will be shown later in this work, geometric effects can be significant for experimental devices, especially at radial locations approaching the origin.

As mentioned previously, the theoretical framework established by Ganguli, et al., incorporating parallel plasma flow neglected shear in the parallel flows. Between 1998 and 2002 this model was generalized by Gavrishchaka, et al.,^{17,46} and Ganguli, et al.,⁴⁷ to include inhomogeneous parallel flows. They found that sheared ion flow parallel to the magnetic field, in conjunction with a transverse electric field, can generate a broadband multimode wave spectrum and multi-scale spatially coherent structures, consistent with satellite observations.^{48,49,50} An additional contribution of these works is that it was the first kinetic treatment of parallel flow shear in a plasma. D'Angelo's fluid approach showed a zero frequency, long wavelength mode, driven by parallel flow shear, that he classified as a Kelvin-Helmholtz instability.⁵¹ The kinetic approach revealed that, in addition to the mode studied by D'Angelo, ion acoustic, ion cyclotron, and lower hybrid (LH) waves can all be excited by parallel flow shear. Consequently, the authors chose to call the branch studied by D'Angelo⁵¹ the "D'Angelo mode". This is an attempt to distinguish this mechanism from the wide array of other parallel flow shear driven modes.¹⁷

In the early 2000's, the theoretical works of Gavrishchaka, et al., and Ganguli, et al., led to a series of experiments at the University of Iowa and at West Virginia University to experimentally verify the existence of the predicted parallel shear driven modes. Agrimson, et al., found both ion acoustic-like⁵² and ion cyclotron-like⁵³ waves, and the works of Koepke, et al.,¹⁹ and Teodorescu, et al.,⁵⁴ studied the modification of parallel flow shear driven instabilities and compared the results to observations from the auroral ionosphere.

For the last decade, a laboratory experiment at Auburn University has been investigating the role of sheared flows on the stability of magnetized plasmas.^{55,56,57} The Auburn Linear EXperiment for Instability Studies (ALEXIS) device is a 170 cm long, 10 cm diameter vacuum chamber that produces a magnetized, cylindrical plasma column. The goal of the ALEXIS project is to study the plasma response to flow. Specifically, how sheared flows, both parallel and perpendicular to the background magnetic field, affect the instabilities in a plasma.

The works presented in this dissertation focus on instabilities in the ion cyclotron regime, and extend the understanding of the influence of electric field directionality on transverse flows in a cylindrical laboratory device, as well as the evolution of a parallel flow shear driven mode in the upgraded ALEXIS device. Specifically, the results presented here will show that, for the first time with a steady-state, filament-based linear magnetized column, the directionality of the radial electric field has been successfully changed over a large volume of the column, and the plasma response was significantly modified.

This dissertation is organized into five chapters. Following the introduction, Chapter 2 presents some of the theoretical work explaining the dynamics and processes of relevance to this work. In Chapter 3, the ALEXIS device and the data acquisition and diagnostic capabilities are described. Chapter 4 discusses the experimental results of the project, and is broken into three parts: initial results with a filament generated plasma using Helium, a multi-species study using four different gases, and finally results using Argon in a radio frequency generated plasma. Chapter 5 is concluding remarks and discusses future possible work.

2 Theoretical derivations

This chapter will serve to introduce the theoretical framework that will be used in this work. Section 2.1 discusses the plasma response to magnetic and electric fields. This section will show the importance of geometric effects, especially in a device the size of ALEXIS. Also, the relative contributions of density gradients and ion-neutral collisions will be discussed. Then, in Section 2.2 the classes of instabilities commonly observed in ALEXIS will be described, as well as the mechanisms that drive each class of instability.

2.1 $E \times B$ Drift

One of the fundamental plasma responses, that is seen across all scale lengths of plasmas from astrophysical plasmas to fusion plasmas, is the plasma response to perpendicular, or crossed, magnetic and electric fields.¹¹ This is called the “E cross B” drift. It is crucial for a laboratory experiment, such as ALEXIS, to use the appropriate geometrical coordinates.⁴⁵ The next section will introduce some basic plasma concepts in Cartesian, or “slab,” geometry. Then, the same phenomena will be examined in cylindrical coordinates, which is the appropriate coordinate system for a linear plasma device.

2.1.1 Slab geometry

The equation of motion for a charged particle is:¹¹

$$m \frac{d\vec{v}}{dt} = q \vec{v} \times \vec{B} \tag{2-1}$$

In the presence of a uniform magnetic field, a charged particle will gyrate in a plane perpendicular to the field line with a cyclotron frequency given by:¹¹

$$\omega_c \equiv \frac{|q|B}{m} \tag{2-2}$$

Using the cyclotron frequency as a normalizing factor, instabilities can be compared between lab plasmas, space plasmas, and fusion plasmas.¹¹ It also separates and defines classes of instabilities.^{58,59} Much work in ALEXIS is focused on ion cyclotron instabilities, that have a frequency at approximately equation (2-2), with $m = m_i$.

With the magnetic field being only along the z-axis, equation (2-1) gives $\dot{v}_z = 0$, which means that the particle is not accelerated along the field line by the electric field, so $v_z = v_{z_0}$ and

$$v_{x,y} = v_{\perp} \exp[\pm i\omega_c t] \tag{2-3}$$

This equation gives circular motion in a plane perpendicular to \vec{B} with radius

$$\frac{m v_{\perp}}{|q|B} = \frac{v_{\perp}}{\omega_c} \equiv r_L$$

(2-4)

Where r_L is defined as the Larmor orbit.¹¹ Much like the cyclotron frequency, this value can be used to normalize plasma phenomena, so that comparisons can be made between what would seem to be vastly different plasma environments.

For the range of possible parameters in the ALEXIS device, the electron and ion cyclotron frequencies are given below:

Table 2-1: The range of cyclotron frequencies possible for each gas species used in ALEXIS.

<u>Species</u>	<u>Minimum Cyclotron Freq.</u>	<u>Maximum Cyclotron Freq.</u>
Helium	11.4 kHz	343.1 kHz
Nitrogen	3.3 kHz	98 kHz
Neon	2.3 kHz	68.6 kHz
Argon	1.1 kHz	34.3 kHz
Electron	83.8 MHz	2.5 GHz

In the presence of both electric and magnetic fields, the motion of the charged particles deviates from planar cyclotron motion. The particles acquire an additional drift due to the Lorentz force as is shown below.

So now the physical picture is $E_y = 0, E_{x,z} \neq 0$ and $B_{x,y} = 0, B_z \neq 0$

Using these new conditions, equation (2-1) becomes:

$$m \frac{d\vec{v}}{dt} = q (\vec{E} + \vec{v} \times \vec{B})$$

(2-5)

Now the directional components are:

$$\frac{dv_x}{dt} = \frac{q}{m} E_x \pm \omega_c v_y$$

$$\frac{dv_y}{dt} = \frac{q}{m} E_y \pm \omega_c v_x$$

$$\frac{dv_z}{dt} = \frac{q}{m} E_z$$

Solving the above three equations gives (respectively):

$$v_x = v_{\perp} \exp[i\omega_c t]$$

$$v_y = v_{\perp} \exp[i\omega_c t] - \frac{E_x}{B}$$

$$v_z = \frac{qE_z}{m} t + v_{z_0}$$

The result of adding the electric field is the inclusion of a guiding center drift in the $-y$ -direction. The Larmor (or “cyclotron”) motion in the plane perpendicular to the magnetic field remains unchanged. Comparing this derivation with the one in the preceding section it can be seen that the cyclotron motion stems from the “ $m \frac{d\vec{v}_{\perp}}{dt}$ ” part of the equation.¹¹ If this side of the equation is omitted, i.e., set to equal zero, then this gives:

$$\vec{E} + \vec{v} \times \vec{B} = 0$$

So,

$$\vec{E} = -(\vec{v} \times \vec{B})$$

Now take the cross-product of this equation with \vec{B} :

$$\vec{E} \times \vec{B} = \vec{B} \times (\vec{v} \times \vec{B})$$

Then using the property of a double cross product becomes:

$$\vec{E} \times \vec{B} = \vec{v}B^2 - \vec{B}(\vec{v} \cdot \vec{B})$$

Then the transverse components of the above equation give $\vec{v}_\perp = \frac{\vec{E} \times \vec{B}}{B^2} = \vec{v}_E$, that is, the “E cross B” velocity. In slab geometry, $|\vec{v}_E| = \frac{E}{B}$.¹¹ This is the motion of the guiding center of the particle trajectory. That is, in the presence of crossed electric and magnetic fields, a particle will follow a trajectory that is the summation of the gyromotion and the guiding center motion. In the slab coordinates discussed here, that motion is a helix.

It can be shown that this approach can be generalized to a generic force \vec{F} which gives¹¹

$$\vec{v}_F = \frac{1}{q} \frac{\vec{F} \times \vec{B}}{B^2}$$

Where \vec{F} can be any generic force, such as gravity, centrifugal, etc.

2.1.2 Cylindrical derivation of E x B mechanism

This section will show how the derivation of 2.2.1 is modified when cylindrical coordinates $(\hat{\rho}, \hat{\phi}, \hat{z})$ are used. As previously mentioned, cylindrical coordinates are the natural coordinate system to use with a linear, magnetized plasma column like ALEXIS.

While the vector approach used above could be applied again, here instead a different approach will be employed.⁶⁰ Start by constructing the Lagrangian for the system, using the magnetic and electric potentials

$$\vec{A} = \frac{1}{2}\rho B_0 \hat{\phi} \tag{2-6}$$

And

$$\Phi = -\rho E_0 \tag{2-7}$$

Now the kinetic energy term needed for the Lagrangian is:

$$T = \frac{1}{2}m\dot{\rho}^2 + \frac{1}{2}m\rho^2\dot{\phi}^2 + \frac{1}{2}m\dot{z}^2 \tag{2-8}$$

So the full Lagrangian becomes:

$$L = \frac{1}{2}m\dot{\rho}^2 + \frac{1}{2}m\rho^2\dot{\phi}^2 + \frac{1}{2}m\dot{z}^2 - q\Phi(\rho) + \frac{q\rho^2}{2}B_0\dot{\phi}$$

(2-9)

Then proceed using:

$$\frac{\partial}{\partial t} \left(\frac{\partial L}{\partial \dot{q}_i} \right) - \frac{\partial L}{\partial q_i} = 0$$

(2-10)

Where q_i is the generalized coordinate representing, here, $\hat{\rho}$, $\hat{\phi}$, \hat{z} . Evaluating (2-10) for all three coordinates gives

$$\ddot{\rho} = \rho\dot{\phi}^2 + \frac{q}{m}E + \frac{q\rho}{m}B_0\dot{\phi}$$

(2-11)

$$\ddot{\phi} = -2\dot{\rho}\dot{\phi} - \frac{q}{m}B_0\dot{\rho}$$

(2-12)

$$\ddot{z} = 0$$

(2-13)

Using equation (2-11), $\dot{\phi}$ can be solved for directly. The equation is quadratic in $\dot{\phi}$, so:

$$\dot{\phi} = \frac{-\Omega_c \pm \sqrt{\Omega_c^2 - \frac{4}{\rho} \left(\frac{q}{m} E_0 - \ddot{\rho} \right)}}{2}$$

(2-14)

Where

$$\Omega_c = \frac{qB_0}{m_i}$$

This can then be written as

$$\dot{\phi} = \frac{-\Omega_c}{2} \left(1 \pm \sqrt{1 - \frac{4}{\rho B_0 \Omega_c} \left(E_0 - \frac{m}{q} \ddot{\rho} \right)} \right)$$

(2-15)

For now, assume no radial acceleration, and set $\ddot{\rho} = 0$. It is now possible to compare this velocity to the slab “E cross B” velocity derived in the earlier section using typical operating parameters for the ALEXIS device. The parameters used are given in Table 2-2, and the results of the comparison are plotted in Figure 2-1.

Table 2-2: Parameters used to compare the calculated $E \times B$ velocities using a slab geometry and a cylindrical geometry.

<u>Term</u>	<u>Value</u>
E	100 V/m
B	0.06 T
m	$6.64 \cdot 10^{-26}$ kg
q	1

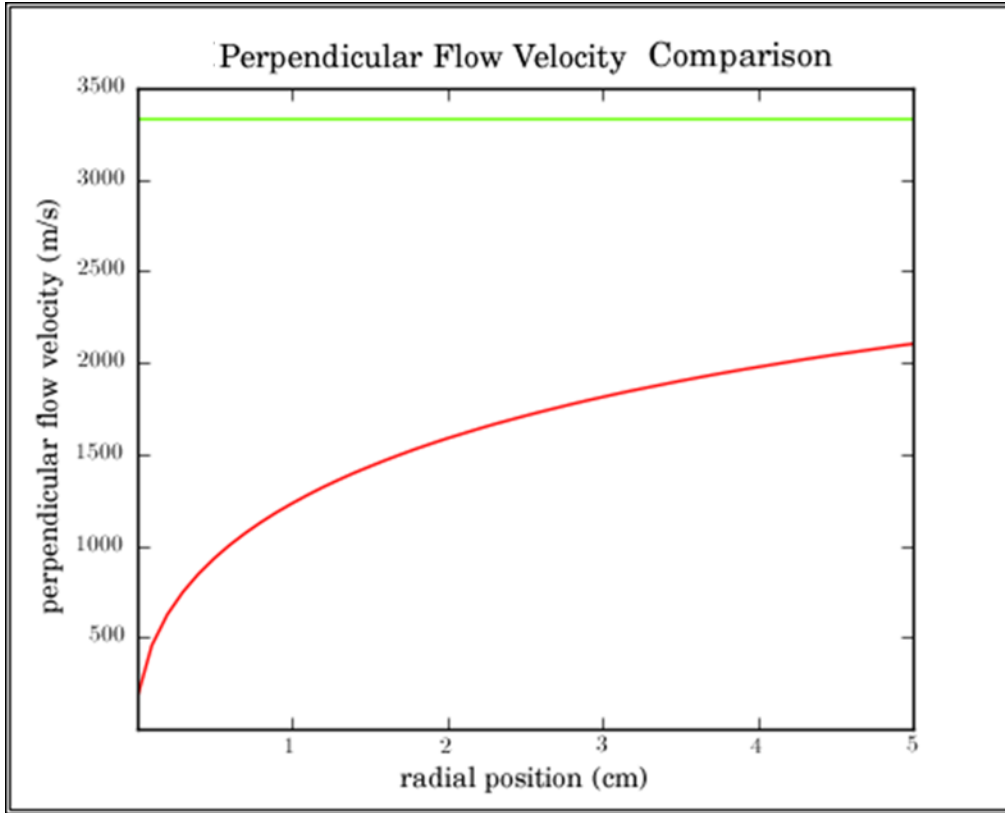


Figure 2-1: A plot showing a comparison between the calculated $E \times B$ velocities using a slab geometry (green line) and a cylindrical geometry (red line).

The figure above shows that, especially for small radial values, i.e., close to the center of the plasma column, the difference between the two equations can be quite significant. In fact, because of the physical size of the ALEXIS device, the best match between the two models is still off by more than 25%.

2.1.3 Density and collisions

Additional physical parameters to consider are the roles of the plasma density and collisions. Specifically, a gradient in the density can lead to an imbalance in the potential energy of the system, which in turn can be a source of energy to drive flows in a plasma column. The density gradient manifests itself as a pressure gradient, which appears in the fluid equation as:¹¹

$$m_i n_0 \left[\frac{\partial}{\partial t} + (\vec{v} \cdot \nabla) \right] \vec{v} = n_0 e (\vec{E} + \vec{v}_i \times \vec{B}_0) - \nabla p_i - m_i n_0 v_{in} \vec{v}_i$$

(2-16)

Which then, for zero-order, in slab geometry gives:

$$\hat{x}: \quad 0 = en_0 E_0 + en_0 B_0 v_{0y} - k_B T_i \frac{dn_0}{dx} - \frac{m_i n_0 v_{in} v_{0x}}{e}$$

$$\hat{y}: \quad 0 = -en_0 B_0 v_{0x} - mn_0 v_{in} v_{0y}$$

$$\hat{z}: \quad 0 = mn_0 v_{in} v_{0z}$$

$$0 = -en_0 B_0 v_{0y} - \frac{k_B T_i}{en_0} \frac{dn_0}{dx} + \frac{m_i v_{in}^2 v_{0y}}{e \omega_{ci}}$$

As discussed in the previous section, cylindrical effects are significant in ALEXIS. With

this in mind, equation $m_i n_0 \left[\frac{\partial}{\partial t} + (\vec{v} \cdot \nabla) \right] \vec{v} = n_0 e (\vec{E} + \vec{v}_i \times \vec{B}_0) - \nabla p_i - m_i n_0 v_{in} \vec{v}_i$

(2-16) can be written into its cylindrical components as

$$\hat{\theta}: \quad 0 = \frac{m}{r} v_\theta^2 + E_0 + B_0 v_\theta - \frac{k_B T_i}{en_0} \frac{dn_0}{dx} - \frac{m_i v_{in} v_r}{e}$$

(2-17)

$$\hat{r}: \quad 0 = m \frac{v_r v_\theta}{r} + e v_r B_0 + mn v v_\theta$$

(2-18)

Solving equation (2-18) for the radial velocity component gives

$$v_r = -\frac{rvv_\theta}{r\Omega_{ci} + v_\theta}$$

(2-19)

And then the azimuthal component becomes

$$v_\theta = -\frac{r\Omega_{ci}}{2} + \sqrt{r^2\Omega_{ci}^2 - 4r\left(\frac{eE_0}{m} - \frac{k_B T_i}{mn_0} \frac{dn_0}{dr} - v_{in}v_r\right)}$$

(2-20)

To assess the impact the addition of the density gradient and collision terms, an approach similar to the previous section will be employed. Using typical operating parameters for ALEXIS listed in Table 2-3

Table 2-3: Parameters used to compare the calculated $E \times B$ velocities using a cylindrical geometry with and without collisions.

Term	Value
Electric field (E)	100 V/m
Magnetic field (B)	0.06 T
Ion mass (m, Argon)	6.64×10^{-26} kg
Charge (q)	1.6×10^{-19} C
Ion temperature (T_i)	0.05 eV
Density gradient (dn_0/dx)	4×10^{17} m ⁻⁴
Ion-neutral collision frequency (v_{in})	8 kHz
Radial drift velocity (v_r)	100 m/s

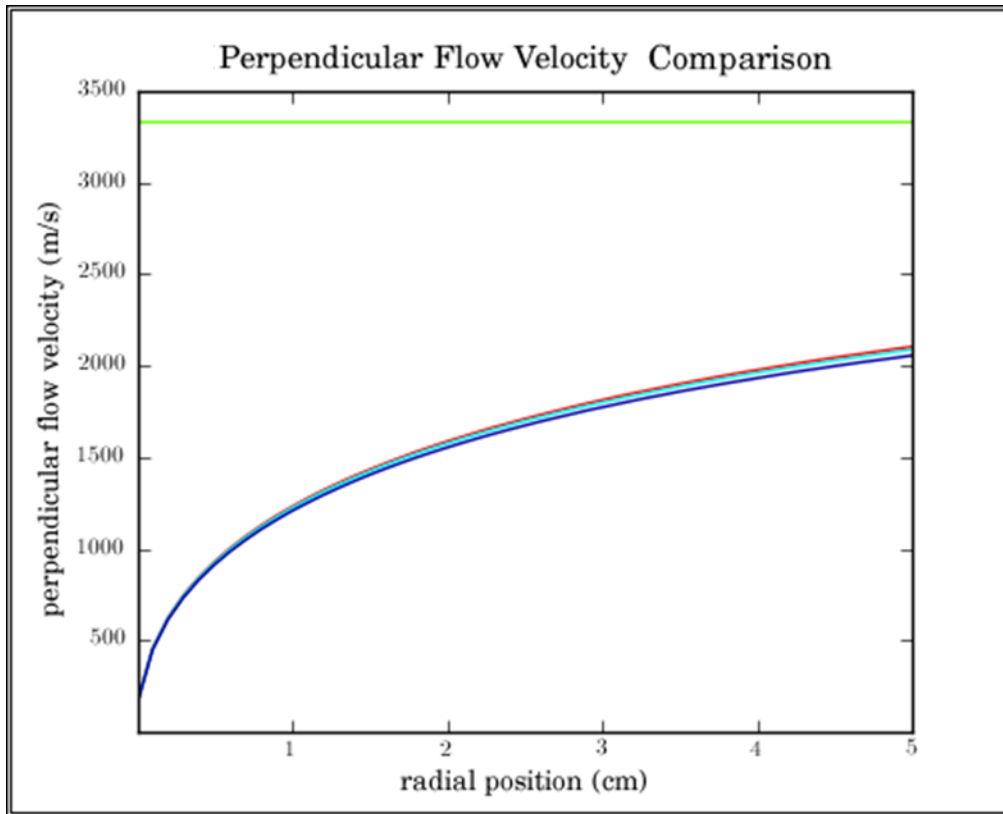


Figure 2-2: Chart comparing the velocities calculated using all four models: E×B (green line), Cylindrical E×B (red line), Cylindrical E×B with the density gradient (light blue line), and Cylindrical E×B with the density gradient and collisions (dark blue line).

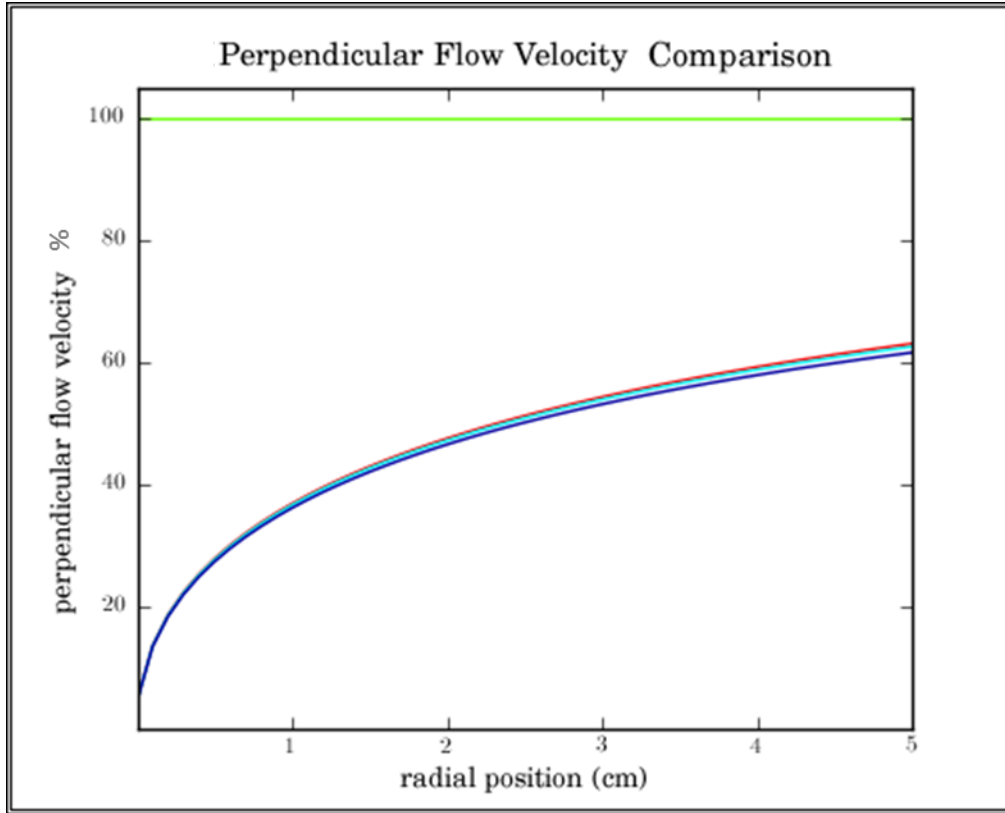


Figure 2-3: Chart comparing the velocities calculated using all four models, cast as a percentage of the unmodified $E \times B$ velocity: $E \times B$ (green line), Cylindrical $E \times B$ (red line), Cylindrical $E \times B$ with the density gradient (light blue line), and Cylindrical $E \times B$ with the density gradient and collisions (dark blue line).

To better determine the impact of the density gradient and the collision terms in the equation for the azimuthal drift, Table 2-4 shows the relative size of all three terms. It also gives the relative size of each term. The values used to calculate each term are given in Table 2-3.

Table 2-4: Comparison of the terms used in the equation for the cylindrical $E \times B$ drift.

<u>Term</u>	<u>Value</u>	<u>Percentage</u>
Electric Field Term	3333	100%
Pressure Term	33.3	1.0%
Collision Term	69.9	2.1%

As can be seen from Table 2-4, the pressure and collision terms do not contribute significantly to modify the azimuthal $E \times B$ velocity. The percentages will change based on the plasma parameters (density, magnetic field, collisionality, etc.). Also, any deviation from cylindrical symmetry would render the above derivation unapplicable.

2.2 Instabilities

As mentioned in the previous chapter, ALEXIS was designed with the goal of studying the impact flow have on the classes of instabilities that can be supported, as well as the impact flow modification has on any instabilities that are present. This section will briefly introduce the three classes of instabilities that are commonly observed in ALEXIS. Here, the goal is not to present a full derivation of each instability, but rather to discuss the key features of each one as they relate to the observations in the ALEXIS device. Additionally, the discussion will be limited to electrostatic instabilities. Research efforts have only recently commenced on ALEXIS to find electromagnetic instabilities and will not be discussed in this work.

2.2.1 Drift Waves

Resistive drift waves (or simply drift waves) are nearly ubiquitous in plasmas.^{15,61} In fact, almost any plasma with a finite density gradient and a uniform magnetic field can drive drift waves.¹¹ The driving force behind drift waves is the pressure gradient in a plasma, $k_B T \nabla n_0$.

Drift waves have a small component of the wave vector, k , parallel to the background magnetic field, B_0 , and a large component of k perpendicular to B_0 .¹¹ In a cylindrical plasma this means that the wave will travel around the plasma column as it slowly propagates along the axis.

In slab geometry, the dispersion relation for drift waves is given by:¹¹

$$\omega^2 + i \frac{k_z^2}{k_y^2} \Omega_{ci} \Omega_{ce} \tau_{ei} (\omega - k_y v_{De}) = 0$$

(2-21)

Where ω is the wave frequency, Ω_{ci} is the ion cyclotron frequency, Ω_{ce} is the electron cyclotron frequency, τ_{ei} is the electron-ion collision period, v_{De} is the electron diamagnetic drift speed (given by $\frac{k_B T_e}{eB} (n'/n)$), k_y is the y-component of the wave vector, and k_z is the z-component of the wave vector.

Some of the behaviors associated with drift waves are:

- The maximum amplitude of the density fluctuations corresponds to the maximum in the radial density gradient
- The amplitude of the density fluctuations normalized to n_0 is approximately equal to the electrostatic fluctuations divided by the electron temperature
- The phase velocity scales like the electron diamagnetic drift velocity

In ALEXIS, drift waves are typically observed in the 5 kHz range, although frequencies as low as 1 kHz have been observed. The drift waves observed in ALEXIS are not the main focus of this dissertation, and the discussion presented here is done so more in the interest of the completeness of this document than as a complete description of the behavior of drift waves.

2.2.2 Inhomogeneous Energy Density Driven Instability

In laboratory devices that utilize a cylindrical symmetry, the effect of a radial electric field with a background axial magnetic field is to induce an azimuthal flow. An important difference to consider between a slab geometry and a cylindrical geometry is that the azimuthal drift is mass dependent.⁴⁵ This dependence on mass can lead to a difference in the azimuthal flow velocities of ions and electrons, which can result in a transverse current that can drive instabilities.⁴⁵

The IEDDI is driven by shear in the transverse electric field, which results in shear in the velocity profile.^{23,35} Localized electric fields, of the order of the ion gyroradius, can lead to an instability being sustained by the shear. If the shear layer is larger than the ion gyroradius, the magnetized ions will stay inside the shear layer for their entire gyro-orbit.

To describe the behavior of instabilities driven by transverse shear flow in ALEXIS, the formalism of Peñano et al. will be used.⁴⁵ The purpose is to describe the linear instabilities in a magnetized plasma when a non-uniform radial dc electric field is imposed on the system and a sheared azimuthal flow is induced. The derivation begins with assuming cold, fluid ions such that:

$$\frac{\partial n_i}{\partial t} + \nabla \cdot (n_i \vec{v}_i) = 0$$

(2-22)

$$\left(\frac{\partial}{\partial t} + \vec{v}_i \cdot \nabla \right) \vec{v}_i = \frac{e}{m_i} (\vec{E} + \vec{v}_i \times \vec{B})$$

(2-23)

Where m_i is the mass of the ions, e is the unit of charge, v_i is the ion fluid velocity, and n_i is the ion density. For ALEXIS, the background magnetic field, B_0 , is assumed uniform and directed along the z direction such that $\vec{B}_0 = B_0 \hat{z}$. Proceed by linearizing equations (2-22) and (2-23) with:

$$\vec{E} = \vec{E}_0 + \vec{E}_1$$

$$\vec{v}_i = \vec{V}_0 + \vec{v}_1 = V_{0i} \hat{\theta} + \vec{v}_1$$

$$n_i = n_{i0} + \tilde{n}_{i1}$$

This then yields, for the ions,

$$V_{0i} = \frac{r\Omega_i}{2} \left(-1 \pm \sqrt{1 + 4 \frac{V_E}{r\Omega_i}} \right)$$

(2-24)

Where Ω_i is the ion cyclotron frequency, and V_E is the $\vec{E} \times \vec{B}$ velocity. Previous experimental works¹⁶ have shown the “-” branch, which corresponds to gyromotion about $r = 0$

in the limit of $V_E \rightarrow 0$, is not dominant in cylindrical devices like ALEXIS. The “+” branch is relevant, and represents a modification of the $\vec{E} \times \vec{B}$ flow by a centrifugal force.

Limiting the derivation to electrostatic fluctuations, such that $\vec{E}_1 = -\nabla\phi_1$, and having all fluctuations be of the form $\tilde{\phi}_1 = \phi_1(r) e^{i(k_z z + m\theta - \omega t)}$ gives the ion velocity and density fluctuations as:

$$v_{1r} = -i \frac{e}{m_i D} \left[\omega_{1i} \partial_r \phi_1 - \left(\frac{m}{r} \right) \bar{\Omega}_i \phi_1 \right]$$

$$v_{1\theta} = -\frac{e}{m_i D} \left[\eta \bar{\Omega}_i \phi_1 - \left(\frac{m}{r} \right) \omega_{1i} \phi_1 \right]$$

$$v_{1z} = \frac{e k_z}{m_i \omega_{1i}} \phi_1$$

$$n_{i1} = \frac{n_0}{i \omega_{1i}} \left[\frac{1}{r} \partial_r (r v_{1r}) + \frac{i m}{r} v_{1\theta} + i k_z v_{1z} \right]$$

Where

$$\omega_{1i} = \omega - \left(\frac{m}{r} \right) V_{0i}$$

$$\bar{\Omega}_i = \Omega_i + 2V_{0i}/r$$

$$D = \omega_{1i}^2 - \eta \bar{\Omega}_i^2$$

$$\eta = 1 + (\partial_r V_{0i} - \frac{V_{0i}}{r}) / \bar{\Omega}_i$$

The derivation is again limited to flow layers with widths much greater than the electron Larmor radius, fluctuations far below the electron cyclotron frequency, and shear frequencies such that $\partial_r V_E / \Omega_e \ll 1$. In ALEXIS, the electron Larmor radius is of order 0.1 mm, the observed fluctuations are of order the ion cyclotron frequency, and the shear frequencies are typically well

below the electron cyclotron frequency, so the assumptions used in this derivation are still relevant to the typical operating conditions in ALEXIS.⁵⁶

In the regime described above, and assuming the absence of collisions, it is appropriate to describe the distribution of electron guiding drift centers, $f_e(\vec{r}, v_z)$, with a drift-kinetic equation:⁵⁹

$$\frac{\partial}{\partial t} f_e + v_z \frac{\partial}{\partial z} f_e + \nabla_{\perp} \cdot (\vec{v}_{\perp} f_e) - \frac{e}{m_e} E_z \frac{\partial}{\partial v_z} f_e = 0 \quad (2-25)$$

Additionally, the dc $\vec{E} \times \vec{B}$ flow velocity is limited to the range of $V_E \ll r_0 \Omega_e$. This means that the electrons do not experience a centrifugal force, and the electron polarization drift can be neglected. This means that the perpendicular component of the flow velocity, \vec{v}_{\perp} , can be written as $\vec{v}_{\perp} = \vec{E} \times \vec{B} / B^2$. Proceed by linearizing Equation (2-25) utilizing:

$$\vec{v}_{\perp} = \vec{V}_{0e} + \vec{v}_{1e} = V_E \hat{\theta} + \vec{E}_1 \times \hat{z} / B_0$$

$$f_e = f_{0e}(v_z) + f_{1e}(\vec{r}, v_z)$$

Where it is assumed that f_{0e} is Maxwellian with a uniform density, n_{0e} , and uniform thermal velocity, $\bar{v}_e = \sqrt{T_e/m_e}$ so that

$$f_{0e}(v_z) = \frac{n_{0e}}{\sqrt{2\pi\bar{v}_e^2}} e^{-\frac{v_z^2}{2\bar{v}_e^2}}$$

With these assumptions, proceed by solving for the fluctuating part of the distribution function and then integrate over v_z to find the density fluctuation in terms of the plasma dispersion function:⁶²

$$\frac{n_{1e}}{n_{0e}} = -\frac{e\phi_1}{2T_e} Z'(\zeta_e)$$

Where $Z'(\zeta_e)$ is the derivative of the plasma dispersion function with respect to its argument, $\zeta_e = \omega_{1e}/\sqrt{2}k_z\bar{v}_e$, and $\omega_{1e} = \omega - \left(\frac{m}{r}\right)V_E$, where m is the mode number of the wave.

Assuming that $(\partial_r V_E/\Omega_i)(\Omega_i/\omega_{pi})^2 \ll 1$ and $\omega_{pi}^2/\omega_{1i}^2 \gg 1$ means that the equilibrium charge separation can be neglected, and that the plasma is quasi-neutral to first order ($n_{0i} \approx n_{0e} \equiv n_0$ and $n_{1i} \approx n_{1e}$). This then yields the eigenvalue equation that describes the linear instabilities in a magnetized plasma arising from sheared flows driven by radial electric fields:⁴⁵

$$\frac{D}{r} \partial_r \left(\frac{r}{D} \partial_r \phi_1 \right) + \left[K^2(\omega, r) - \frac{m^2}{r^2} \right] \phi_1 = 0$$

(2-26)

Where

$$K^2(\omega, r) = -\frac{k_z^2 D}{\omega_{1i}^2} \left[1 + \frac{m_i}{m_e} \left(\frac{\omega_{1i}}{\sqrt{2}k_z\bar{v}_e} \right)^2 Z'(\zeta_e) \right] - \frac{m}{r} \frac{\bar{\Omega}_i}{\omega_{1i}} \left[\frac{1}{\bar{\Omega}_i} \partial_r \bar{\Omega}_i - \frac{1}{D} \partial_r D \right]$$

For determination of the wave character the eigenvalue condition Equation (2-26) must be solved for typical experimental parameters. Alternatively, albeit somewhat crudely, instead of solving Equation (2-26) we may check whether the experimental parameters are consistent with Equation (2-26). Selecting the later procedure, a Fourier transform is performed on Equation (2-26) and a substitution is made such that $\partial_r \phi_1 \rightarrow -ik_r \phi_1$,⁶³ to obtain;

$$-ik_r \left(\frac{1}{r} - ik_r - \frac{1}{D} \frac{\partial D}{\partial r} \right) + K^2(\omega, r) - \frac{m^2}{r^2} = 0$$

(2-27)

In which the radial wavelength is approximately the width of the localized wave packet observed in the experiment. Other than the parallel wave vector, k_z , the parameters are all determined from experimental constraints. To study the IEDDI in ALEXIS, the consistency of the observations is checked with Equation (2-27) for the given experimental. Initial parameters used for this model are listed in Table 2-5, and are based on measurements and observations where possible. For example, the value for k_θ was determined from $k_\theta = m/r$, where the mode number, m , has been measured to be approximately 2.⁵⁶ Also, k_r is calculated based on the radial wave packet thickness (L_r) as determined from observations of the instability. The frequency and k_z values observed in the experiment are checked for consistency with Equation (2-27) within experimental error. The results of this calculation are shown in Figure 2-4.

Table 2-5: Parameters used in the computational model discussed in this section.

Parameter	Value
Species	Helium
Magnetic Field Strength	90 Gauss
T_e	8 eV
T_i	0.05 eV
Radial position	3 cm
k_r	$2 \pi / L_r = 2 \pi / 0.008 \text{ m}^{-1}$

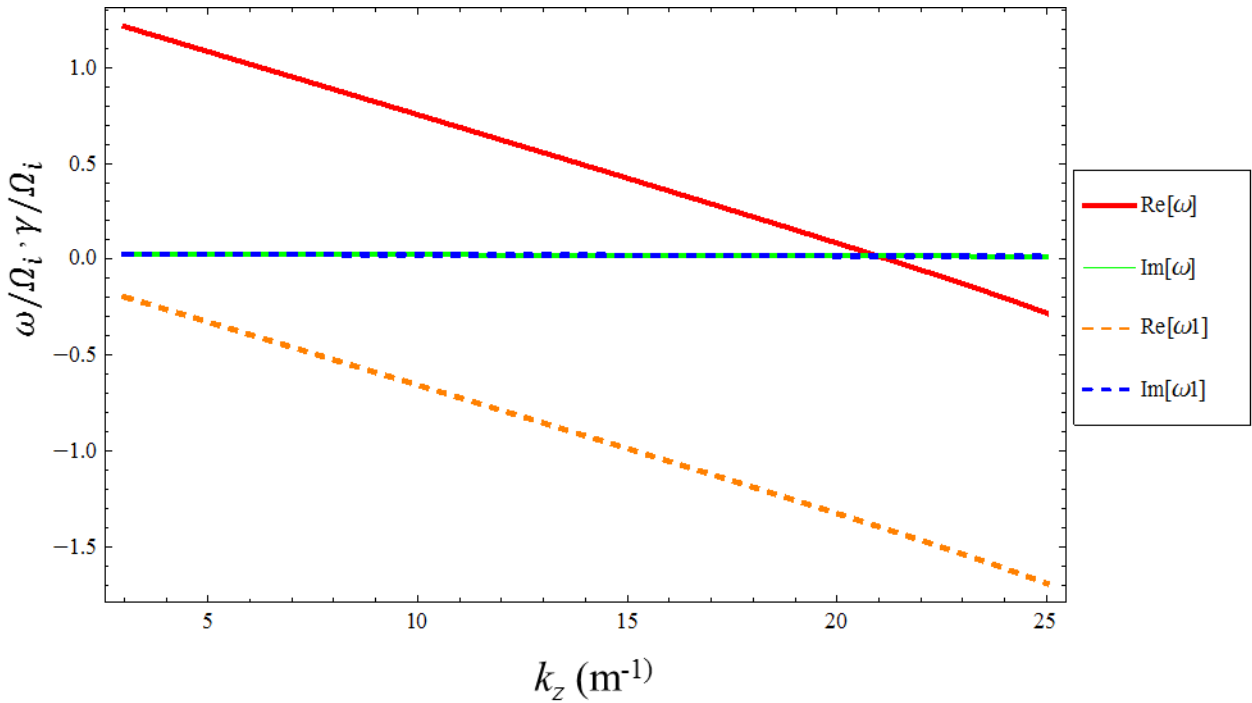


Figure 2-4: Plot of Equation 2-27 using typical experimental parameters for ALEXIS. The plot shows the real component of ω (solid red line), the real component of ω_1 (dashed orange line), the imaginary component of ω (solid green line), and the imaginary component of ω_1 (dashed blue line).

The IEDDI, which is a negative energy density wave, has the necessary condition that $Re(\omega) \times Re(\omega_1) < 0$.^{23,45} Figure 2-4 shows that for parallel wave numbers less than approximately 21 m^{-1} , this condition can be satisfied. Also, the growth rate for that range of parallel wave numbers, although small, is positive. These two conditions would seem to indicate that the IEDDI can be supported in ALEXIS for the given parameters. It should also be noted, however, that the Doppler shifted frequency is typically expected to be near an harmonic of the ion cyclotron frequency, so that $Re(\omega_1) \approx n\Omega_i$. Figure 2-4 shows that this condition is satisfied for a parallel wave number of approximately 15 m^{-1} for $n = 1$.

Physical signatures of this class of instability are that the wave propagates predominantly in the direction of the $E \times B$ flow, and that wave is broad and “spikey” in frequency space. The early experimental works in ALEXIS focused on modifying the azimuthal flow in a Helium plasma column to drive the IEDDI.⁵⁶ This work is presented in Chapter 4.

2.2.3 Current Driven Ion Cyclotron Instability

The Current Driven Ion Cyclotron Instability (CDICI) has been extensively studied in laboratory plasmas for several decades.^{28,29,64} It is an electrostatic instability that is excited in a plasma when electrons drift along magnetic field lines. Many laboratory experiments were performed in Q-machines, with a circular connector at one end biased to draw an electron current.⁶⁴

To describe the behavior of instabilities driven by parallel shear flow in ALEXIS, the formalism of Ganguli et al. will be used.⁴⁷ The physical picture used in their work⁴⁷ is very similar to the radio frequency configuration used in this dissertation. A uniform background magnetic field is assumed in the z direction, and a non-uniform electric field is present in the x direction. This leads to a non-uniform $E \times B$ flow in the y direction, such that $V_E(x) = -E(x)/B$. Additionally, a non-uniform flow parallel to the magnetic field (i.e., in the z direction) is present. This flow is labeled $V_d(x)$.

In the results presented in Chapter 4, the parallel flow shear is spatially very localized compared to the shear induced by the radial electric field, such that, for this derivation, $L_E \gg L_d$.

Proceeding then, the electric field is treated as effectively uniform compared to the parallel flow structure.

A further simplification is that the flow is locally linear, which means $V_d(x)$ can be expanded to give:

$$V_{di}(x) = V_{di} + \frac{dV_{di}}{dx}x \quad (2-28)$$

$$V_{de}(x) = V_{de} + \frac{dV_{de}}{dx}x \quad (2-29)$$

Now assume that the flows of the ions and the electrons have the same shear, so that:

$$\frac{dV_{di}}{dx} = \frac{dV_{de}}{dx} \equiv \frac{dV_d}{dx}$$

A transformation to the ion frame is performed (i.e., $V_{di} = 0$ and V_{de} is the relative drift between ions and electrons), and then the general dispersion relation (for magnetized ions and electrons), given as:⁶⁵

$$\left(\rho_i^2 \frac{d}{dx} - \frac{1 + \sum_n \Gamma_n(b)F_{ni} + \tau(1 + F_{0e})}{\sum_n \Gamma'_{ni}(b)F_{ni}} \right) \phi = 0 \quad (2-30)$$

is then simplified, in the local limit, to:⁴⁷

$$1 + \sum_n \Gamma_n(b) F_{ni} + \tau(1 + F_{0e}) = 0$$

(2-31)

Where

$$F_{ni} = \left(\frac{\omega}{\sqrt{2}|k_z|v_{ti}} \right) Z \left(\frac{\omega - n\Omega_i}{\sqrt{2}|k_z|v_{ti}} \right) - \frac{k_y}{k_z} \frac{1}{\Omega_i} \frac{dV_d}{dx} \left[1 + \left(\frac{\omega - n\Omega_i}{\sqrt{2}|k_z|v_{ti}} \right) Z \left(\frac{\omega - n\Omega_i}{\sqrt{2}|k_z|v_{ti}} \right) \right]$$

$$F_{0e} = \left(\frac{\omega - k_z V_{de}}{\sqrt{2}|k_z|v_{te}} \right) Z \left(\frac{\omega - k_z V_{de}}{\sqrt{2}|k_z|v_{te}} \right) + \frac{k_y}{k_z} \frac{1}{\mu\Omega_i} \frac{dV_d}{dx} \left[1 + \left(\frac{\omega - k_z V_{de}}{\sqrt{2}|k_z|v_{te}} \right) Z \left(\frac{\omega - k_z V_{de}}{\sqrt{2}|k_z|v_{te}} \right) \right]$$

And

$$\Gamma_n(b) = I_n(b)e^{-b}$$

Where $b = (k_y \rho_i)^2$ and $I_n(b)$ is the modified Bessel function.⁶² Also, v_{te} is the electron thermal velocity, v_{ti} is the ion thermal velocity, and the temperature and mass ratios are given as (respectively):

$$\tau = \frac{T_i}{T_e}$$

$$\mu = \frac{M_i}{m_e}$$

It should be noted that if there is no shear ($dV_d/dx \rightarrow 0$), then the dispersion relation given here reduces to the homogeneous flow dispersion relation originally given in the works of Drummond and Rosenbluth²⁹ and Kindel and Kennel⁶⁶.

To evaluate the dispersion relation for the instabilities seen in ALEXIS, Equation (2-31) is used. Utilizing a typical value for k_y the dispersion relation can be solved at the typical

location of the peak wave amplitude ($r = 1$ cm). The parameters used in Equation (2-31) to generate Figure 2-5 are listed in Table 2-6.

Table 2-6: Parameters used to generate Figure 2-5.

Input Parameter	Value
Species	Argon
Magnetic field strength	300 Gauss
Electron temperature	5 eV
Ion temperature	0.025 eV
Electron drift velocity	25 km/s
k_y	50 m^{-1}

Figure 2-5 shows the real part of the calculated frequency (normalized to the ion cyclotron frequency) versus the parallel wave number for a typical electron drift velocity.

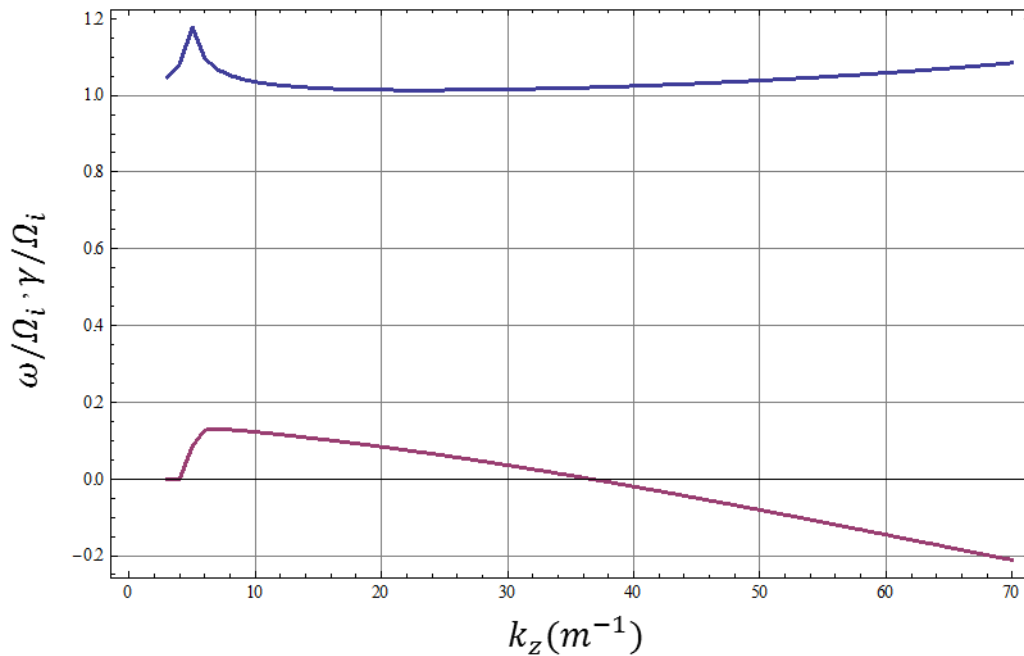


Figure 2-5: The real (blue line) and imaginary (red line) parts of ω normalized to plotted versus k_z .

Experimental considerations limit the range of possible parameters, and will be discussed more in Chapter 4. For example, the finite width of the ALEXIS device limits the range of shear sizes available. Additionally, shear sizes of less than 1 cm are not considered here because shear sizes of less than approximately 1 ion gyroradius have been shown to not typically drive the CDICI, an effect referred to as “filament quenching.”⁶⁴

The above studies have shown that for ALEXIS-like conditions, the CDICI does appear to be supported. Various experimental effects⁶⁴, such as finite chamber diameter (i.e., grounded chamber walls), the ratio of the current channel diameter to the chamber diameter, and collisional effect have not been emphasized in the above discussion. Also, the experimental task of how to accelerate the electrons to the necessary drift velocity has not been addressed here, and will be the considered in Chapter 4.

3 Experimental Hardware

3.1 Introduction

The experiments presented in this work were performed on the Auburn Linear Experiment for Instability Studies (ALEXIS). ALEXIS is a laboratory plasma physics experiment that was designed to investigate the role of spatially non-uniform $\vec{E} \times \vec{B}$ drifts in a magnetized, cylindrical plasma column.

The research presented here spans two different hardware configurations.

The initial configuration of ALEXIS was built using components from an earlier experiment named PHLUX (Plasma Hybrid Linear University Experiment). Parts of the PHLUX vacuum chamber and vacuum pumps were incorporated into the ALEXIS design. This initial configuration of ALEXIS was in use between 2001 and 2007.⁵⁵ The next major upgrade to the ALEXIS device was made over an approximately 4-month period in early 2007. The most important difference between the two configurations is the plasma source: the initial ALEXIS configuration used heated filaments to generate the plasma while the current ALEXIS configuration makes use of a radio frequency (rf) plasma source.

The experiments presented in Section 4.2 were made using the configuration presented in Section 3.2. The experiments presented in Sections 4.3 and 4.4 were performed using the configuration presented in Section 3.3. Finally, Section 3.3 will also discuss the experimental considerations that motivated this change in the ALEXIS configuration.

3.2 Initial Filament Configuration

The ALEXIS chamber is a 170 cm long stainless steel vacuum vessel, generally based upon the ISO-100 (i.e., 100 mm diameter) flange configuration. A schematic of the ALEXIS device is shown in Figure 3-1. The chamber is comprised of four primary components: the water-cooled section that houses the filament source (A), a standard ISO-100 six-way cross (B), a custom designed main chamber (C), and a final ISO-100 six-way cross (D). Each of these components is described in further detail below. This configuration was summarized in a 2004 article in *Review of Scientific Instruments* by Wallace, et al.⁵⁵

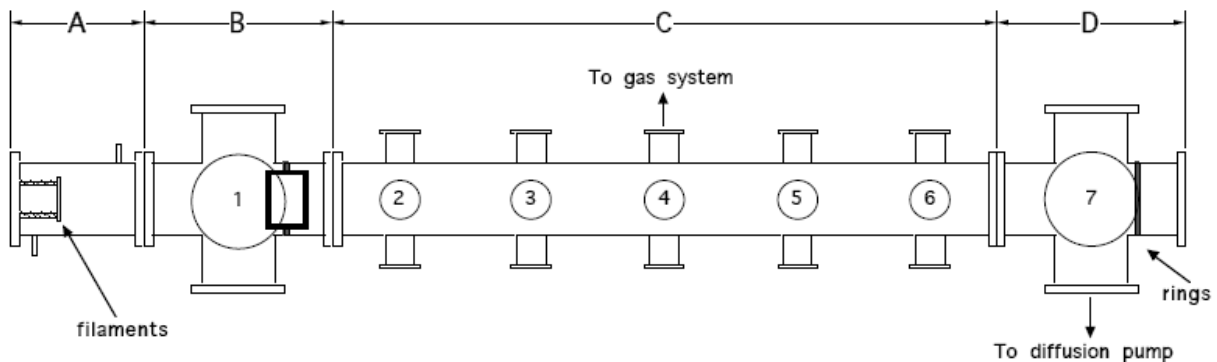


Figure 3-1: Schematic of the initial chamber configuration of ALEXIS

The first section (labeled “A” in Figure 3-1) houses the filaments that are used as the plasma source. It has a double-wall construction that allows for ¼” diameter cooling lines to run

between the walls. The water-cooling is necessary to protect against the large amount of heat generated by the filament source.

The water-cooled section is connected to an ISO-100 six-way cross (labeled “B” in Figure 3-1). This is a “standard” six-way cross, with a 10 cm inner diameter, and length in each direction of 26 cm. The side ports of the cross are fitted with ISO-100 windows, which have a 6.3 cm diameter viewing area, to observe and monitor the plasma, as well as provide access for spectroscopic measurements. This section serves as the transitional region between the plasma source and the main experimental region of the ALEXIS device.

Following the six-way cross is the main experimental section of ALEXIS (labeled “C” in Figure 3-1). It is 91 cm long (36 inches), with a 10 cm inner diameter. The ends of the chamber are fitted with ISO-100 flanges, and the cylindrical body is surrounded by twenty QF-40 (40 mm diameter, “quick flange”) ports. The ports are separated horizontally by 18.3 cm, with five port locations along the axis of the main chamber. The ports are distributed azimuthally around the chamber, with ports at 0°, 90°, 180°, and 270°, effectively creating five “groups” of ports. This allows multiple diagnostic systems physical or optical access to the same region of plasma. This is particularly valuable when using different types of *in-situ* probes to measure complementary properties of the plasma (e.g., using emissive probes for plasma potential measurements and double probes for plasma density and electron temperature measurements of the same plasma volume), or for verifying the azimuthal symmetry of various plasma properties. In addition to diagnostic access, the ports are also used to attach the gas inlets, roughing vacuum line, and antenna for wave launching experiments. Also, by utilizing the QF-40 as the standard port size, probe locations can be easily changed allowing greater flexibility in plasma characterization.

The final section (labeled “D” in Figure 3-1) is a second, ISO-100 six-way cross. This section houses the rings that are used to modify the potential structure of the plasma. Additionally, an Edwards 100/300C Diffstak diffusion pump is mounted to the bottom flange of the six-way cross.

The Diffstak diffusion pump has a pumping rate of up to 300 L per second. This pump is backed by an Alcatel Model SD-2010 rotary vane roughing pump with a pumping speed of 2.8 L per second. The combination of pumps gets ALEXIS to a base pressure of 4 to 6×10^{-7} Torr. Helium gas flows into the chamber by means of a Varian sapphire-sealed leak valve. Typical operating pressures in ALEXIS are in the 10^{-4} to 10^{-3} Torr range.

An axial magnetic field in ALEXIS of up to 1,000 Gauss on axis is produced by a set of nine electromagnets. The magnets were originally designed and manufactured by the Everson Electric Company (now Everson Tesla, Incorporated, Nazareth, PA). The magnets on ALEXIS are comprised of three different coil configurations (A, B, and C) as indicated in Table 3-1. This variation of design is used to compensate for the uneven spacing of some of the magnets.

Table 3-1: Coil types and locations of the magnets on ALEXIS

Coil type	Turns								
A	48								
B	50								
C	59								
Coil Layout									
Number	1	2	3	4	5	6	7	8	9
z (cm)	0	26	44	63	81	99	118	136	162
Type	A	A	C	A	B	B	A	C	A

Each magnet, regardless of configuration, is wound from 0.71 cm outer diameter, 0.36 cm inner diameter hollow copper tubing. The inner diameter allows for water-cooling. Fiberglass tape is used to insulate the copper. After being wound, the magnets were potted with an epoxy

resin such that all the magnets, independent of the specific coil configuration, has the same dimensions of 20 cm, an outer diameter of 33 cm, and an axial length of 6.4 cm.

The electromagnets use two independent power supplies. The two magnets (#1 and #2) that surround the plasma source and the magnet at the opposite end of the column are connected to a Power Ten model P63C-10330 6.6 kW power supply. The remaining six magnets (#3 to #8) are connected to a Power Ten model P66C-40330, 13 kW power supply. Each power supply can provide a dc current of up to 330 A. The magnets are arranged such that ALEXIS can be operated in a magnetic mirror-like configuration; i.e., with a higher magnetic field strengths at the ends of the machine than in the main experimental region.

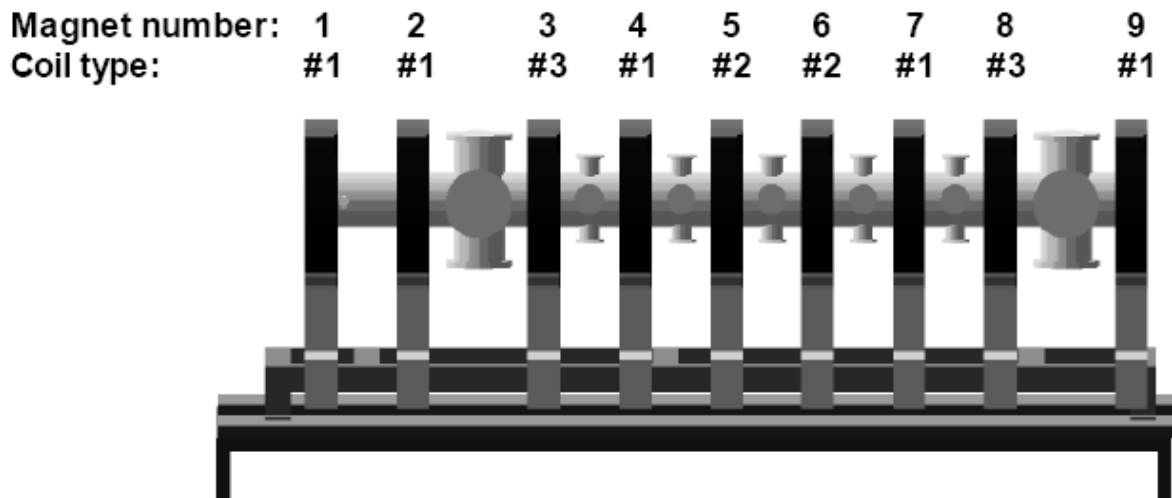


Figure 3-2: Magnet configuration for ALEXIS. Magnets 1 and 2 surround the plasma source, Magnet 9 is at the opposite end of the chamber near the biased rings. The coil type represents that different coil winding configurations that are given in Table 3-1.

The hot filament discharge is one of the oldest plasma generation techniques with its origins extending to the work of Irving Langmuir.³ The hot filament discharge is based upon the thermionic emission of electrons from a heated, biased wire. As the wire is heated to a temperature of between 1000 and 1500 K, there is an emission of electrons as described by Richardson's equation:⁶⁷

$$J = AT^2 e^{-e\phi/k_B T} \quad (3-1)$$

where J is the current density, T is the surface temperature of the metal, ϕ is the work function of the metal, and A is the emission constant, which is a property of the material. To prevent the recapture of the emitted electrons, the wire is generally biased negatively with respect to a grid or the vacuum chamber walls to accelerate the electrons away from the filament.

In this configuration of ALEXIS, plasmas were generated by an array of heated Tungsten filaments, shown in Figure 3-3. The filaments are 0.25 mm diameter Tungsten wire, wound into 3 cm long coils. The coils are mounted onto a 7.5 cm diameter Macor insulating block. The filaments are heated with up to 7 A of heating current, to get the filaments into thermionic emission. To accelerate the electrons away from the filaments, a negative bias voltage is applied to the filaments using a Xantrex XHR600-1.7 (600 V / 1.7 A) power supply. For most experiments, the power supply is operated in constant current mode, with an emission current in the range 80 to 200 mA in order to maintain a constant flux of electrons into the plasma. However, when operated in constant current mode, the bias voltage of the power supply varies between 100 and 300 V, allowing the primary electrons to gain a significant parallel velocity.

To reduce the population of these energetic primary electrons, an electrically grounded tungsten wire mesh grid is set approximately 7.6 cm from the filament source. The mesh is used to decelerate the electrons, and to help reduce the number of high energy primary electrons that enter the main chamber. Nonetheless, some fraction of the primary electrons was always present in the plasma and contributed to an axial current in the device.

The filament plasma source produces a 160 cm long plasma column. The plasma is quasineutral, with ion and electron densities of up to $1 \times 10^{16} \text{ m}^{-3}$. The ions remain at approximately room temperature, with $T_i \leq 0.1 \text{ eV}$. The electron temperatures are in the range of 3 – 8 eV. Typically, the ionization fraction in ALEXIS is approximately 0.1%.

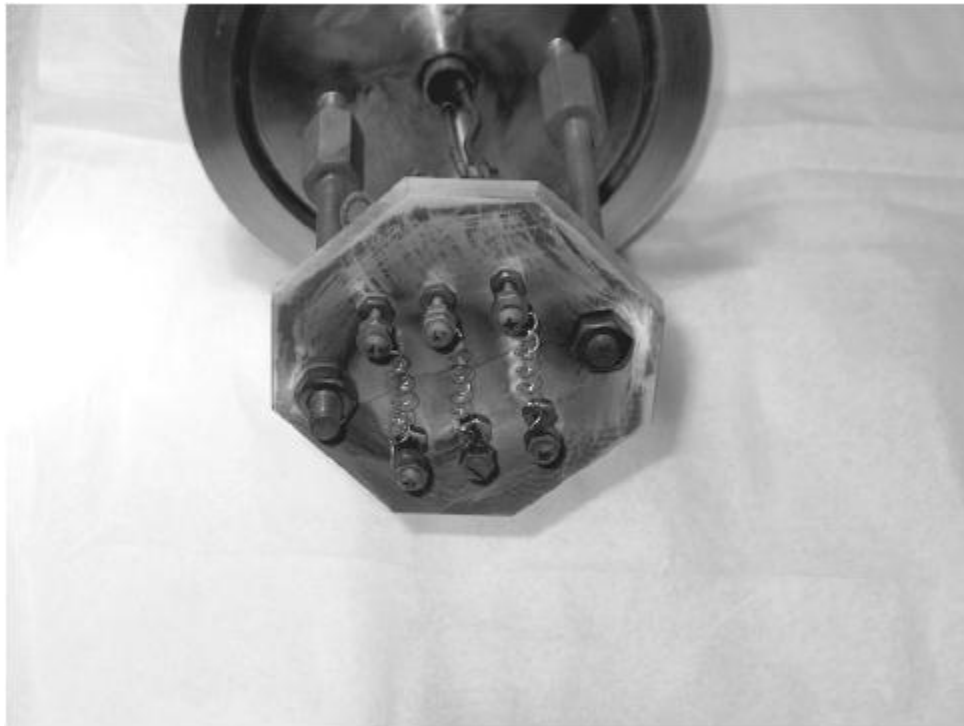


Figure 3-3: The array of filaments used to generate He plasmas in ALEXIS. The three filament wires are coiled in order to minimize the mechanical stresses on the filament wires. The Macor block is the octagonal shape in the photograph.

The plasmas in ALEXIS are modified by a series of four concentric rings, located at the end of the chamber, opposite the plasma source. The rings are made from copper gaskets,

mounted on a Macor plate, and placed in the ISO-100 six-way cross. The outer diameters of the rings, from the center out, are 0.66, 2.12, 4.81, and 8.23 cm. Previous experiments in ALEXIS have shown that changing the biases to the rings successfully modifies the potential structure in ALEXIS.⁵⁷

The diagnostics on ALEXIS consist of floating Langmuir probes to measure the electrostatic fluctuations, biased Langmuir probes to measure the density, and heated emissive probes to measure the plasma potential. Signals from the various probes are measured and sent to the computer using an IoTech WaveBook model 516 with 16 channels and a total data rate of 1 MHz. That is, the maximum data acquisition rate was determined by 1 MHz divided by the number of active channels.

3.3 ALEXIS Hardware Upgrade to RF Configuration

As noted in Section 3.2, an important aspect of the initial ALEXIS configuration was the use of heated filaments for plasma generation. While filament-based plasma sources are a well-documented and long-used experimental configuration, for the studies performed using ALEXIS the presence of the primary electron population was a concern. In particular, because of the ALEXIS project's interest is studying low frequency plasma instabilities in the ion cyclotron regime, it is noted that transverse sheared flows, parallel sheared flows, and parallel currents are all mechanisms that can excite this class of instabilities.^{23,52,58,59,29}

While the early studies on ALEXIS have focused on transverse shear, the presence of the parallel current could play a role in modifying the instabilities.^{57,47} Therefore, after significant

deliberation, it was decided to reconfigure the ALEXIS device to minimize the parallel current. In February, 2007, the ALEXIS device was shut down and a major series of upgrades to the device were initiated. Primary among them was the replacement of the filaments with a fixed frequency ($f = 13.56$ MHz), 600 W radio frequency (rf) plasma source. Other simultaneous upgrades included: the addition of computer-controlled probe systems, and computer integration of the safety and machine-state controls. In 2010, some additional changes were made to the vacuum vessel design in order to better accommodate a newly refurbished Laser Induced Fluorescence system, discussed in Appendix I.

This section focuses on the results of those upgrades, with an emphasis on the new capabilities of this improved device. The following sections will discuss changes made to each of the ALEXIS components: vacuum vessel and pumping systems, plasma generation, computer integration, and diagnostics.

3.3.1 Vacuum Vessel and Pumping Systems

The main chamber is the same as described above, with one exception. In 2010, the final six-way cross (identified as section “D” in Fig. 3.1) was replaced with a custom designed vacuum box. This box replaces a six-way cross that was previously located after the main experimental chamber. In order to minimize the perturbation of the magnetic geometry of the experiment, it was essential for the new vacuum box to have the same overall dimensions as the six-way cross. Nonetheless, the objective of the vacuum box was to maximize optical access for

the laser induced fluorescence (LIF) diagnostic system that is discussed in Appendix 1. Figure 3-4 shows a photograph of this section.



Figure 3-4: A photograph of the custom six-way vacuum box mounted on ALEXIS. Note the two magnets on either side of the box, the bellow that leads to the diffusion pump (near the bottom), and one of the “4-ring” electrode assemblies used to modify the electric field in the ALEXIS plasma.

This vacuum box section is comprised of six sides – 3 sides have ISO100 ports and three sides have large polycarbonate windows. The ISO100 ports are used to connect hardware that was previously used in the six-way cross. This includes a diffusion pump at the bottom, the ring electrodes used for plasma flow control at one end, and the connection to the remainder of the ALEXIS vacuum chamber. The three large windows have a viewing area of 30 cm by 50 cm or 150 cm². The windows are composed of approximately 2 cm thick polycarbonate, sealed with Viton O-rings. As indicated in the photograph in Figure 3-4, these windows provide substantial optical access to the plasma.

The pumps on ALEXIS were all replaced. There are now an Axiden (Alcatel) model 2010SD, 2.8 liter/sec roughing pump, an Edwards 100/300C Diffstak 300 liter/sec diffusion pump, and a Varian VPS-630 adsorption (or sorption) pump. The roughing pump and the diffusion pump are the two main components of the vacuum system and are in essentially the same configuration as described in Sec. 3.1. As an auxiliary to the roughing/diffusion pump combination, ALEXIS also makes use of an adsorption pump. Adsorption pumps are very simple vacuum pump devices that have no mechanical parts. Once the main vacuum chamber is at a roughing vacuum ($p \leq 100$ mTorr), a valve between the chamber and the adsorption pump is opened. A high surface area material, e.g., Zeolite, which is cooled to liquid nitrogen temperatures, provides the “pumping” action in an adsorption pump. Gas molecules are then “frozen” onto the surface of the material causing a decrease in pressure. When equilibrium is reached at approximately $p = 0.1$ Torr the valve is shut. As the adsorption pump warms up, a pressure release valve keeps the pump from over-pressurizing.

Once the valve to the adsorption pump is closed, the gate valve separating the diffusion pump from the experimental chamber is opened. Use of the adsorption pump is not necessary, but greatly expedites the return to lowest base pressures, which is below 10^{-6} Torr. Without the adsorption pump, it takes between 24 and 48 hours to achieve good vacuum conditions. However, by using the adsorption pump, the same conditions can be obtained in as little as six hours. This greatly improves the operational efficiency of ALEXIS by reducing the time needed for maintenance.

The second component of the gas and vacuum subsystem is gas regulation. This system has been recently redesigned to improve both its consistency and its flexibility. The previous design of the gas system on ALEXIS utilized a Varian sapphire sealed manual leak valve. While

this valve allowed for fine control of the inlet gas, stabilizing the pressure consistently from day to day required significant time before experiments could be conducted. This valve has been replaced by two, MKS Instruments Model 1179A mass flow controllers that regulate flows up to 10 sccm. These valves are connected to a MKS Instruments Type 247 controller, which is integrated into the Data Acquisition System discussed in section 3.3.3. These new valves allow for better pressure regulation via automation, and better day-to-day reproducibility. Furthermore, the availability of two separate gas lines allows for the use of multiple species with a controllable mixing ratio.

Pressure measurement in ALEXIS is performed using a combination of thermocouple gauges (for pressures down to 10^{-3} Torr) and Bayerd-Alpert ionization gauges (for pressures down to 10^{-7} Torr). Both styles of pressure gauges are measured using a Kurt J. Lesker KJL 4500 Ion Gauge controller that has ports for two thermocouple gauges and one B-A gauge. The B-A ionization gauge is mounted on a 60.96 cm (24 inch) long, QF40 extended nipple. This extension is used to ensure that the gauge remains outside of the main magnetic field, which can negatively impact the performance of the B-A gauge.

Two thermocouple gauges are used on ALEXIS. The first is mounted on the main experimental section of the vacuum chamber and is used to monitor the chamber pressure during the pump down process. The second is attached to the roughing pump line between the diffusion pump and roughing pump and is used to monitor the pressure between the two pumps. The gauge controller is integrated into the data acquisition system so that the pressure can be continuously monitored.

3.3.2 Plasma Generation

The conversion of the ALEXIS plasma source from filaments to an RF source was a substantial undertaking. The decision to upgrade was strongly motivated by the physics mission of the ALEXIS project. In particular, the early experiments on ALEXIS focused on the generation and suppression of low frequency electrostatic waves in the ion cyclotron frequency regime by driven flows parallel and perpendicular to the magnetic field. However, with the use of filaments, there was always a small population of beam electrons that produced a finite axial current in the device. Additionally, plasmas generated using the filament source were generally limited to peak densities in the 10^{15} m^{-3} range.

After the upgrade, plasmas are now produced in ALEXIS by a radio frequency (rf) power supply. Here, the rf power is provided by a Kurt J. Lesker model R601, 600W power supply at a fixed frequency of 13.56 MHz. The rf power is coupled into the plasma using a matching network and an antenna. The design of the matching network is based on a modified L network,⁶⁸ and consists of two load capacitors (connected in parallel), and a tune capacitor, Figure 3-5. The load capacitors are a Comet CV1C-500UIHN (15-500 pF, 15kV 79A, labeled C1) and a Jennings Radio Capacitor (25-2500 MMFD, 6000 Volts, labeled C2). The tuning capacitor is a Comet CV05C-1500 LON/5 (10-1500 pF, 5kV/3kV, labeled C3). A Byrd model 4391A power meter is placed in-line between the rf generator and the load capacitors. This is the primary tool used to tune the matching network so that the reflected power is minimized. The rf generator is integrated into the data acquisition system, which allows control of the power generated, and also monitors the supply's internal power meter.

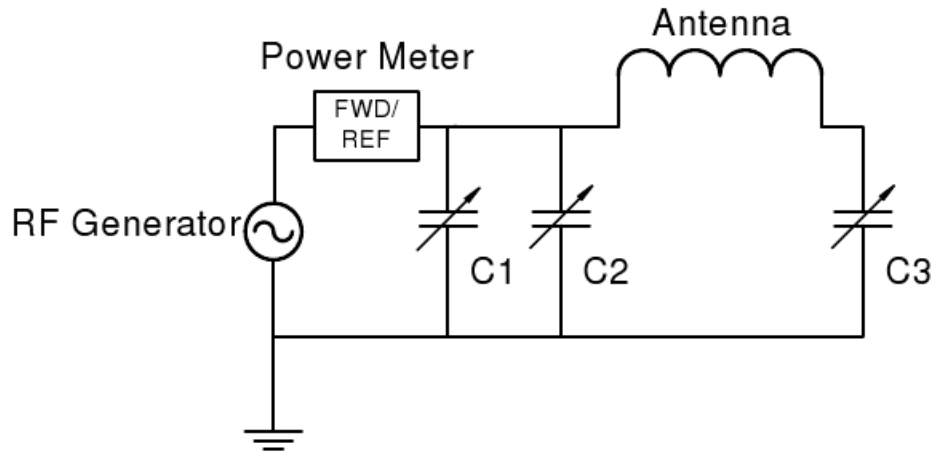


Figure 3-5: Schematic of the matching network used in ALEXIS. The RF generator is a KJL R601, and the power meter is a Bird model 4391A. C1, C2, and C3 are the capacitors used to match the impedance of the circuit to the impedance of the R601.

3.3.3 Computer Integration

The computer control system for ALEXIS consists of both system monitoring and data acquisition activities. By system monitoring, this means that the “state” of the ALEXIS experiment is recorded. This monitoring includes activities such as regulating the flow of gas into the experiment, controlling the rf power supply (e.g., forward and reflected power levels), recording the pressure in the experiment, and controlling the bias voltage on the ring electrodes. This contrasts with the data acquisition activities, which include recording current and voltage levels from *in-situ* probes and collecting voltage signals from photomultiplier tubes attached to various optical diagnostic systems.

The core of this system is a Dell Vostro 420 desktop PC which runs the LabVIEW software package from National Instruments. The LabVIEW programming suite includes many

independent software programs. For ALEXIS, the LabVIEW core development package, as well as the Measurement and Automation Explorer (which provides software access to the connected hardware devices), and DataSocket Server (which allows remote computers to access the hardware connected to the local PC). National Instruments PCI-6723 and PCI-6010 cards provide a combined 16 analog inputs, 32 analog outputs, and 10 digital input/output (i/o) channels.

The analog input channels operate at a combined (or single channel) rate of up to 2×10^5 samples per second (i.e., 200 kS/s). They are used to monitor voltage outputs from the pressure gauges, the magnet power supplies, and the rf system. The analog output channels are used for sending set point values to the magnet power supplies, the rf generator, the mass flow controller, and the programmable power supplies. The analog out channels have a rate of 45 kS/s and are capable of outputting waveforms of up to 10 kHz. The digital input/output (i/o) channels are used for digital interlocks on the mass flow controller, magnet power supplies and the rf generator. These channels work in parallel with a physical relay based safety system that protects the ALEXIS hardware in the event of a vital sub-system failure, such as insufficient water flow to cool the magnets and diffusion pump, a loss of vacuum, or excessive reflected power from the rf generator.

Additionally, this PC houses a National Instruments PCI-7344 motion controller that is used to provide up to four axes of motion control. Currently, two of the axes are used on linear (radial) probe drives located at ports X and Y on ALEXIS. These two drives are operated independently of each other. The remaining axes are operated as a combined pair to drive a “XY” Bi-Slide configuration from Velmex, Inc. This two-axis motion system is used for the injection and collection optics for laser induced fluorescence system, enabling a plane

perpendicular to the magnetic field to be scanned. Additionally, the injection optics can be mounted “off-plane” and the laser light can be injected such that the k -vector of the beam has components along both the parallel and perpendicular flow velocities.

All of these subsystems are controlled with a NI LabVIEW interface that can be accessed by remote computers over the internet. The LabVIEW virtual instruments (VI's) running on the remote PC's can read and write to all of the analog and digital channels enumerated above by using National Instruments proprietary data socket transport protocol. This protocol allows the channels to be addressed (either read from or written to) as if they were local, and removes the burden of manually associating programming variables to physical hardware addresses. This flexibility means that VI's developed on one PC can be run on any other PC without a need to update the code. Figure 3-6 is an example of a VI written and deployed on multiple PC's.

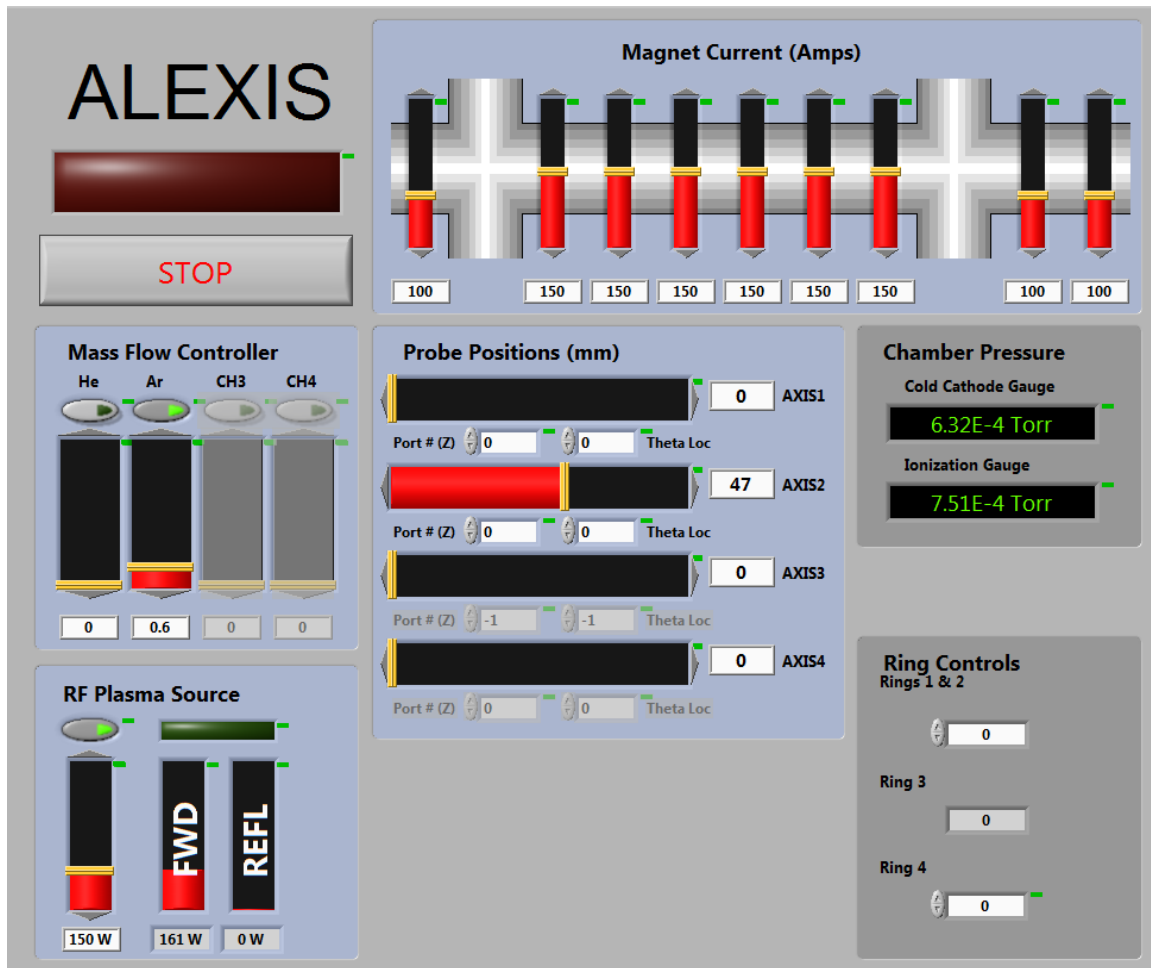


Figure 3-6: Screenshot of the HMI used to control ALEXIS. In this screenshot are shown monitors for the current in the magnets (upper right, set at 100 A and 150 A in this image); for the mass flow controller (an applied voltage of 0.6 V for the Argon channel); for the RF source (showing a set point of 150W with 161 W measured as forward power and 0 W reflected); for the probe position; vacuum pressure in the chamber (as measured by the cold cathode and B/A ionization gauges), and the bias voltages on the ring electrodes.

This VI allows the user to monitor and update the values of the current to the magnets, the pressure, the rf power, bias voltages of the rings, probe positions, and gas flow rates. Other VIs are used to acquire and record data from various GPIB (general-purpose instrument bus) devices including: several digital oscilloscopes, a Keithley 2400 sourcemeter, three Agilent 34401A digital multimeters and a National Instruments NI-9215 multichannel input device. The NI 9215 is a four channel, 16-bit, 100 kS/s per channel voltage input device that serves as the primary acquisition device for the various *in-situ* probes on ALEXIS.

3.3.4 *In Situ* Diagnostics

The chamber size and number of ports on ALEXIS allow simultaneous diagnostic access for multiple probes. Current probe mounts include manual rotary probes, manual linear feed-through mounted probes, and two motor driven linear probe mounts. The motor driven probes are controlled by the computer interface described in section 3.3.3.

All of the aforementioned probe mounts can accept a wide range of probe designs. Currently on the ALEXIS device there are a broad range of electrostatic and electromagnetic probes. The electrostatic probes include: single-tipped Langmuir probes, double probes, emissive probes, and a double-tipped “*k*-probe” that is used to determine the wavelength of electrostatic plasma instabilities. To measure magnetic fluctuations, a so-called “B-dot” probe is used.^{69,70} This broad assortment of probes allows investigators on ALEXIS to characterize the plasma conditions. These various probe configurations are each briefly described below.

The single tipped Langmuir probe is one of the oldest plasma diagnostics.⁷¹ On ALEXIS, these probes are used to measure both electrostatic potential fluctuations (when the probe is electrically floating) or monitor density fluctuations (when the probe is biased negatively into ion saturation; i.e., to repel electrons and collect ions). A Langmuir probe is considered a “cold” probe in that it can only serve as a sink of ions or electrons from the plasma. By contrast, an emissive probe is a “heated” version of a Langmuir probe that can act as both a source and sink of current.⁷² As a result, a “floating” emissive probe heated to the point of thermionic emission can record the both the dc level and the fluctuations in the plasma potential.



Figure 3-7: Combination emissive probe (thin wire loop) and double Langmuir probe (straight wires). The ruler gives the scale in millimeters.

On ALEXIS, the linear motion drives use a combination probe that combines two, 2mm long single tipped Langmuir probes and an emissive probe (Figure 3-7). The emissive probe is made of 0.1mm diameter tungsten wire set in a 3mm diameter loop. To reduce the heat and power requirements, the Tungsten is only at the tip of the probe, with copper running the length of the ceramic and back to the flange with four electrical feed-throughs.

To measure the electron density and electron temperature of the plasma, another variant of the Langmuir probe, the “double probe” is used.^{71,73} A double probe is a two-tip Langmuir probe in which a bias voltage is applied between the two tips and the current flowing from one probe to the other is recorded. The double probe in ALEXIS, shown in Figure 3-8, is made of two pieces of 4 mm diameter stainless steel inside of 5 mm diameter ceramic insulator. The voltage between the double probe tips and the current flowing between them is controlled and measured using a computer-controlled Keithley 2400 source meter. An example double probe trace is shown in Figure 3-9.

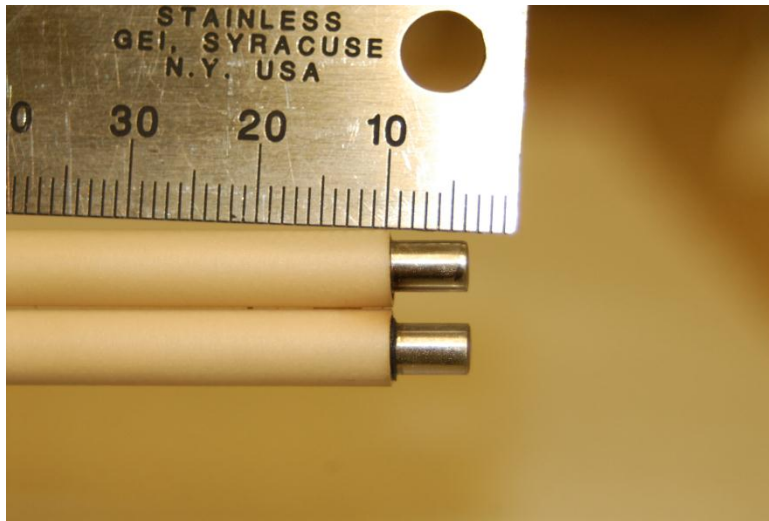


Figure 3-8: Photograph of the double probe used in ALEXIS.

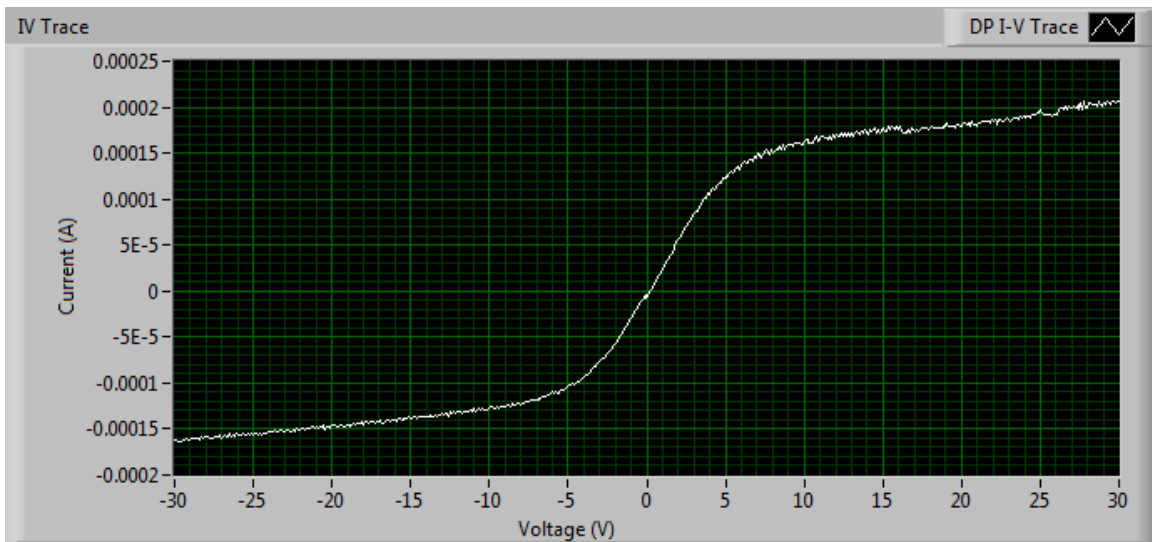


Figure 3-9: Example of a double probe trace in ALEXIS from the VI used to acquire the data. A separate VI is used to fit an arctangent to the data.

The ALEXIS “*k*-probe” is a double probe that is mounted on a rotatable linear feed-through, and is used to measure the wavelength of the electrostatic instabilities in ALEXIS.⁷³ Both probe tips are electrically floating to measure the voltage fluctuations on each tip. The signals from each tip are recorded simultaneously. As the probe is rotated at a fixed radial position, a sequence of phase differences is recorded. The largest phase difference is usually observed at close to $\pm 90^\circ$, which indicates that many of the instabilities detected in ALEXIS

propagate perpendicular to the axial magnetic field. Figure 3-10 shows typical data from the k -probe.

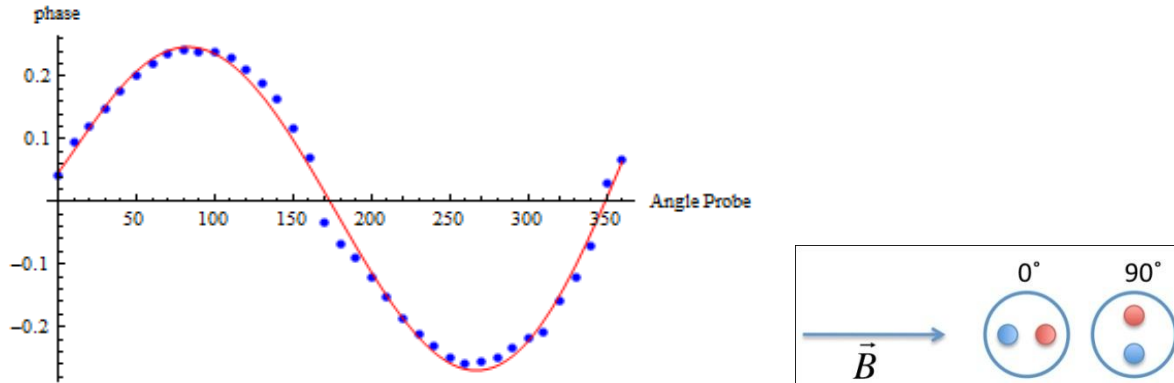


Figure 3-10: Example k -probe data from ALEXIS. The probe angle is defined as 0° when the two probe tips are oriented parallel to the axial magnetic field as shown to the right. Shown is a measurement (blue dots) of the measured phase between two tips (separated by 2.5 mm) as the probe is rotated through 360° . The red curve is a sinusoidal fit to the phase data using $y = A \cos(\theta_{\text{probe}} + \varphi)$ where φ is an arbitrary shift.

4 Experimental Data

4.1 Introduction

This chapter is separated into three sections, corresponding to three different experiments. These experiments show the evolution of the ALEXIS project over the past six years, as the experimental capabilities have been upgraded and the project focus has been refined. The original motivation for the ALEXIS project derived from the PI's experience with plasma flow modification on a fusion experiment, the Compact Auburn Toristron (CAT). Early works were focused on successfully modifying the radial electric field in ALEXIS, with the goal of significantly altering the plasma flows and instabilities.^{56,57} The first section of this chapter presents the evidence that this mission was successful, and documents the modification of the plasma using all diagnostics that were available at that time.

The second section of this chapter begins with upgrade of the ALEXIS plasma source. Historically, at this time the physics mission of ALEXIS was evolving to include the study of electromagnetic instabilities. To generate plasmas that could support the propagation of electromagnetic waves, higher density plasmas were deemed necessary. In an effort to better leverage the previous successes in ALEXIS, a series of experiments was performed to determine if the physical processes observed in the original configuration could be reproduced in the new

device. To this end, a series of gases of different mass were used to determine an appropriate scaling that could be applied to early experimental conditions, to bring that knowledge and experience forward to the new device configuration. As shown in this section, a distinct transition between two wave modes was observed in each gas, at approximately the same value of a parameter that is defined in that section.

Finally, the last section of this chapter presents the results of a plasma potential modification experiment performed in an Argon plasma. While the filament based plasma source produced transverse flow shear driven instabilities, the new configuration excited parallel flow shear driven instabilities. The instability mechanism and experimental results will be discussed in the context of the theory presented in Chapter 2.

4.2 Experiments in the ALEXIS-filament configuration

Initial investigations on ALEXIS focused primarily on the influence the direction of the electric field had on plasma stability. Specifically, motivated by the work of Ganguli et al.,^{23,35,45} much effort was spent trying to determine the optimal means of changing the directionality of the electric field from its normally radially inward direction to a radially outward, or positive, direction.

Once this change in directionality was accomplished, research efforts focused on characterizing the plasma response to the change in the direction of the electric field. The main feature of this response was a dramatic change in the amplitude and spatial distribution of plasma instabilities. Plasma configurations with radially inward electric fields allowed the self-generation of coherent plasma instabilities at or below the ion cyclotron frequency. However, plasma configurations in which a radially outward electric field was formed in a region of the plasma showed a broad suppression of plasma instabilities. It is noted that experiments using instabilities launched from an antenna were performed and both cases showed a similar response to the direction of the electric field.

For these experiments, ALEXIS was in its initial configuration (i.e., hot filament plasma source) configuration as described in Chapter 3. All of the experiments reported in Section 4.2 were performed in helium plasmas. The electric field in ALEXIS was modified using the four-ring electrode configuration as shown in Figure 4-1. The rings are located in the final six-way cross section (labeled Port 7) as shown in Figure 4-2 at $z = 155$ cm. Measurements during these experiments were made using only *in-situ* probes – Langmuir probes and emissive probes. All of

these studies were made prior to the development of the ALEXIS optical diagnostic suite. The probes are located at ports 2 and 6. Operating conditions used during this round of experiments are described in Table 4-1.

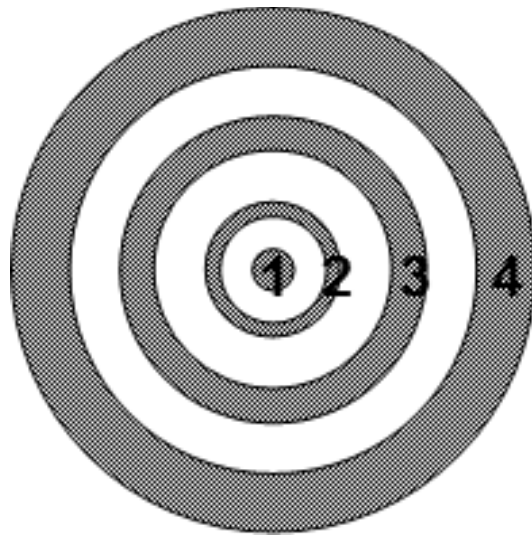


Figure 4-1: Rings used in initial experiments. These were four concentric copper gaskets. The outer diameter of each ring, starting at the center (Ring 1) and moving outward (Ring 4) are: 0.66 cm, 2.12 cm, 4.81 cm, and 8.23 cm, respectively.

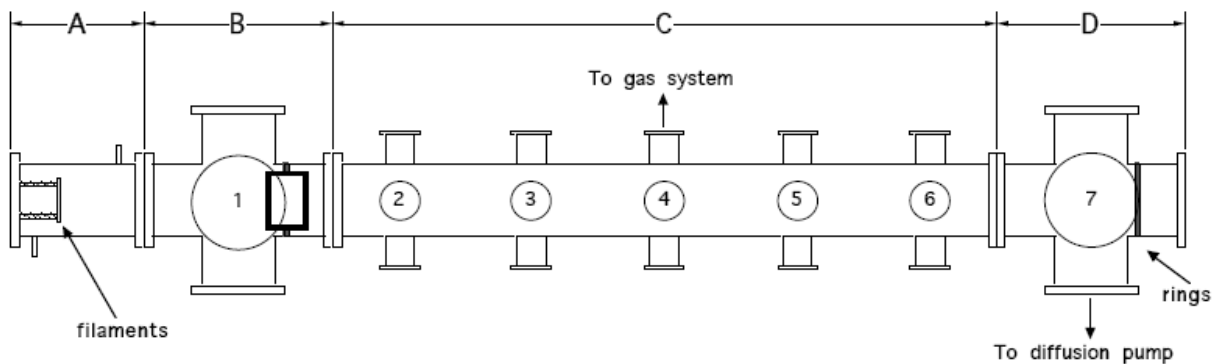


Figure 4-2: Schematic of the initial chamber configuration of the ALEXIS device. The port numbers (listed 1 through 7 along the horizontal axis) will be used throughout this chapter to identify probe locations.

Table 4-1: Operating conditions in ALEXIS – filament configuration

Plasma species	Helium ($A = 4$)
Peak magnetic field (B_{max})	1000 Gauss
Operating magnetic field (B_{typ})	90 – 120 Gauss
Plasma density (n_e)	$0.8 - 1.3 \times 10^{16} \text{ m}^{-3}$
Electron temperature (T_e)	5 – 10 eV
Ion temperature (T_i)	< 0.05 eV
Operating pressure	0.65 – 0.8 mTorr
Filament emission current (I_{emit})	85 mA
Ion cyclotron frequency (f_{ci})	~34 to 46 kHz
Ion plasma frequency (f_{pi})	~9.4 MHz
Ion-neutral collision mean free path	9 cm
Ion gyroradius/Chamber radius (ρ_i/a)	0.11 – 0.14

4.2.1 Modification of the plasma potential profile

The first experimental goal was to verify that the structure of the plasma potential profile could be modified by changing the potentials applied to the rings. To change the bias voltages, the rings were connected to independent power supplies. Rings 1 and 2 were electrically connected. Ring 3 is biased separately from Rings 1 and 2, but is biased at the same potential as

the inner two rings (i.e., $V_1 = V_2 = V_3$). For all of these studies, Ring 4 (the outermost ring) is maintained at a potential of $V_4 = -50$ V.

The experiment is divided into four distinct cases: Case A, B, C, and D. The difference between the cases is the voltages applied to each ring. The voltages applied to each ring are given in Table 4-2.

Table 4-2: Potentials applied to the rings for the different experimental cases. All voltages are given in units of volts (V).

	Ring 1	Ring 2	Ring 3	Ring 4
Case A	-40	-40	-40	-50
Case B	-20	-20	-20	-50
Case C	40	40	40	-50
Case D	80	80	80	-50

To measure the effect of biasing the rings on the plasma potential, an emissive probe was mounted at Port 6, approximately 28 cm upstream from the rings. Plasma potential profiles were generated by scanning the emissive probe radially across the plasma column, from the outermost edge ($r = 5$ cm) to the center of the column ($r = 0$ cm) along the plasma mid-plane. Results of these scans are presented in Figure 4-3.

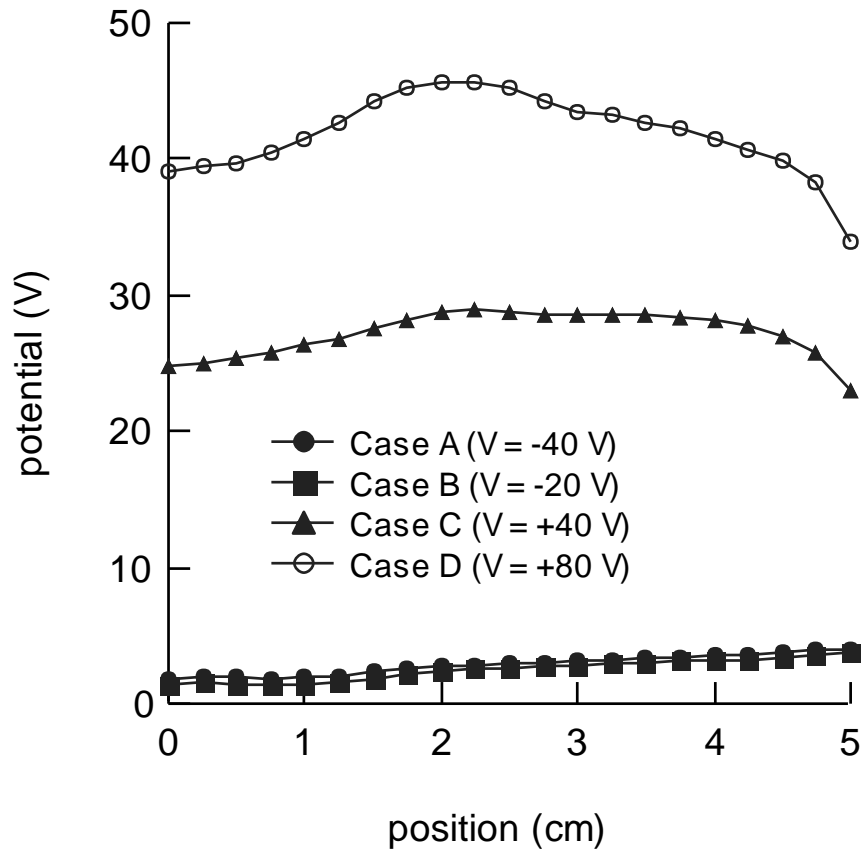


Figure 4-3: Measurements of the plasma potential as measured with the emissive probe. The probe is scanned radially across the plasma at the midplane. The four cases shown, A through D, are representative of the four cases shown in Table 2. Note that increase the overall plasma potential with increasing positive voltages on the inner three rings. Case A (solid circles) and Case B (solid square) are essentially overlapped.

The data presented in Figure 4-3 shows two main features of this experiment. The first feature, as the bias voltage on the inner rings (Rings 1, 2, and 3) is increased from negative voltages to positive voltages, there is a general rise in the plasma potential. Further, negative voltages appeared to have little impact on the potential profiles. It is noted that an additional experiment was performed for a bias voltage of -80 V on the inner rings with no significant change in the potential profiles shown for Cases A and B.

The second feature is that with increasingly positive voltages, the spatial structure of the potential is also becoming modified. To better facilitate comparisons, the above potentials are re-plotted by normalizing the potentials so that the potential at $r = 0$ cm for each case is 0 volts. The offset potentials are then broken into two groups, the first group is the negatively biased cases (Case A and Case B) and the second group is the positively biased cases (Case C and Case D). The offsets are:

Case A	1.1 V
Case B	0.6 V
Case C	22.3 V
Case D	43.5 V

Plotted in Figure 4-4 are the normalized potential profiles for the four cases along with the calculated electric fields. At the top of each figure, there are four horizontal lines which indicate the locations of the four ring electrodes. In Figure 4-4, the four graphs are: (a) the offset potential profiles for Case A and Case B, (b) the calculated radial electric fields for Case A and Case B, (c) the offset potential profiles for Case C and Case D, and (d) the calculated electric fields for Case C and Case D.

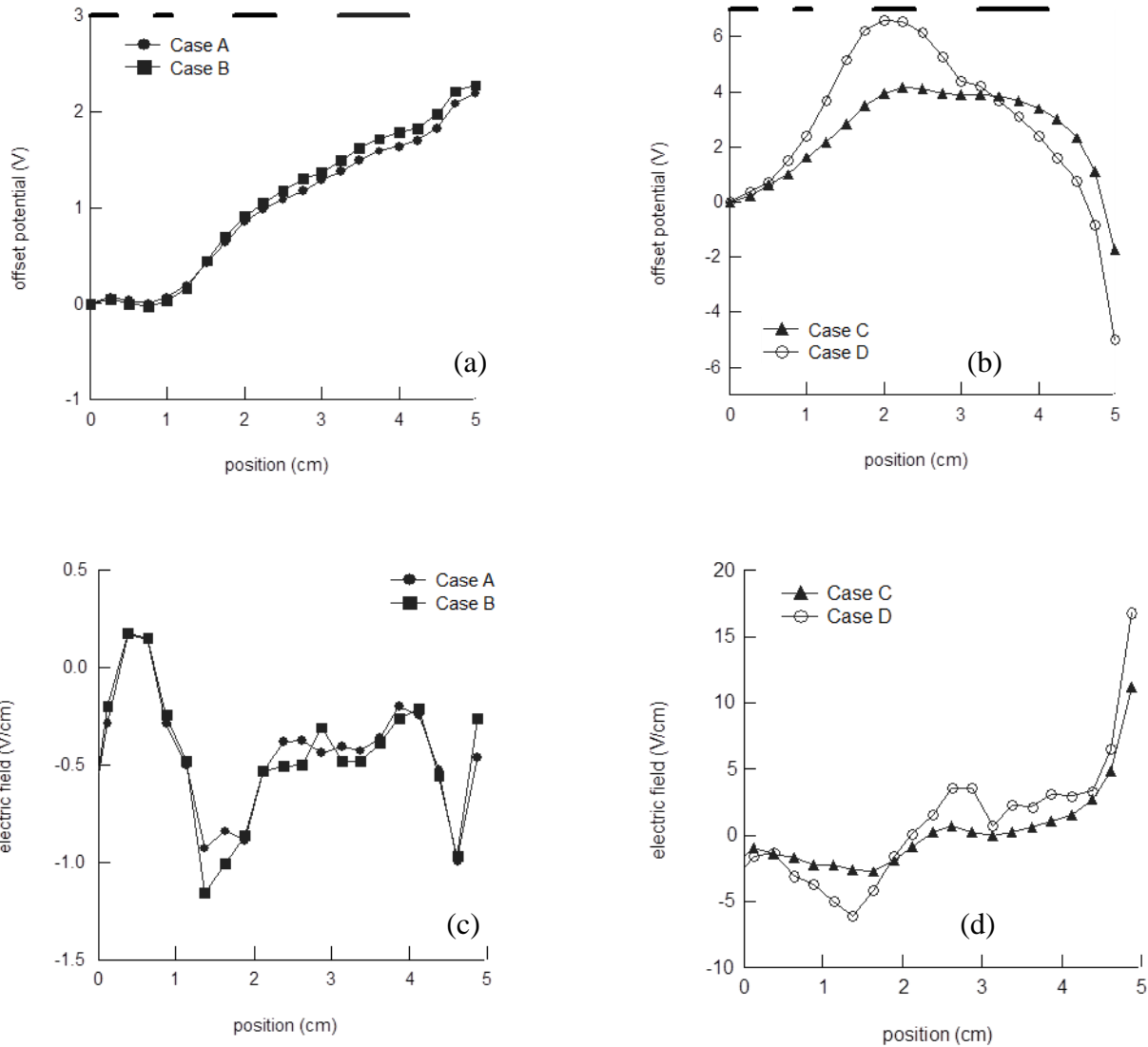


Figure 4-4: Comparison of the normalized potential profiles (a) and (b) and the calculated electric fields (c) and (d) for the four bias voltage configurations applied to the ring electrodes.

Notice in the above figure that for Case A and Case B, the radial electric fields were negative for a majority of the column. Conversely, in Case C and Case D, the electric fields are larger in magnitude, and mostly positive. This change in the measured electric field is suggestive that there should be a corresponding change in the plasma flow perpendicular to the magnetic field based upon the $\vec{E} \times \vec{B}$ drift velocity.

In addition to a transverse plasma flow, currents collected by the rings for the four cases suggest that parallel plasma flows may also contribute to the plasma response. To assess the possible role of flows parallel to the magnetic field, albeit qualitatively, the current collected by the rings when biased was measured. The measured currents are reported in Table 4-3. It can be seen that there is a significant increase (up to a factor of 15) in the current collected for the cases with positively biased rings (Case C and Case D) as compared to the negatively biased rings (Case A and Case B). Here, negative current represents a net collection of electrons. It is noted that even for negative bias voltages, there remains a net collection of electrons. This suggested that there was a population of primary electrons that were able to enter the main plasma column. Although this current is not thought to have made a significant modification to the experimental results presented in the following section, it was measurements of this type that motivated the decision to modify the plasma source in ALEXIS.

Table 4-3: Currents measured at each ring for each case, measured in mA. Here, negative currents indicate the collection of a net electron current. Also noted in this table are the conditions under which spatially localized instabilities were present in the plasma – Case A and B (negative bias voltages) had instabilities present while Case C and D (positive bias voltages) did not observe instabilities.

	Ring 1	Ring 2	Ring 3	Ring 4	Instability
Case A	-2	-2	-4	-0.9	Yes
Case B	-4	-4	-7	-0.9	Yes
Case C	-27	-27	-54	-1.3	No
Case D	-30	-30	-51	-1.3	No

4.2.2 Impact on electron density profiles

Because the experimental measurements clearly showed that the rings modified the plasma potential profiles, it was also necessary to characterize the effect on other plasma

parameters. Of particular importance was the effect on the electron density profile. To measure the impact that changing the ring bias voltages had on the density profiles, two double probes were mounted onto ALEXIS. One probe was mounted at Port 2 ($z = 53$ cm, approximately 102 cm upstream from the rings), and the second was mounted at Port 6 ($z = 127$ cm, approximately 28 cm upstream from the rings).

The double probes were swept radially across the plasma column for each of the four cases. Figure 4-5 and Figure 4-6 present the data for each of the four cases. In all four cases, the outer part of the plasma column (for $r > 1$ cm) there is minimal modification to the plasma density or to the plasma density profile. The center of the plasma column ($r < 1$ cm) is modified by roughly 10 – 15% with a decreasing electron density from $\sim 8 \times 10^{15} \text{ m}^{-3}$ for negative bias voltages to $\sim 6 \times 10^{15} \text{ m}^{-3}$ for the most positive bias voltages. More importantly, the density gradient is only slightly modified.

As shown in Chapter 2, section 2.2.3, there is a density gradient term that enters into the equation for the azimuthal flow velocity in cylindrical coordinates, Equation (4-1). With little modification to the density gradient, it can be concluded that the contribution of the density gradient term is approximately equal for all four cases.

$$v_{\theta} = -\frac{r\Omega_{ci}}{2} + \sqrt{r^2\Omega_{ci}^2 - 4r\left(\frac{eE_0}{m} - \frac{k_B T_i}{mn_0} \frac{dn_0}{dr} - v_{in}v_r\right)}$$

(4-1)

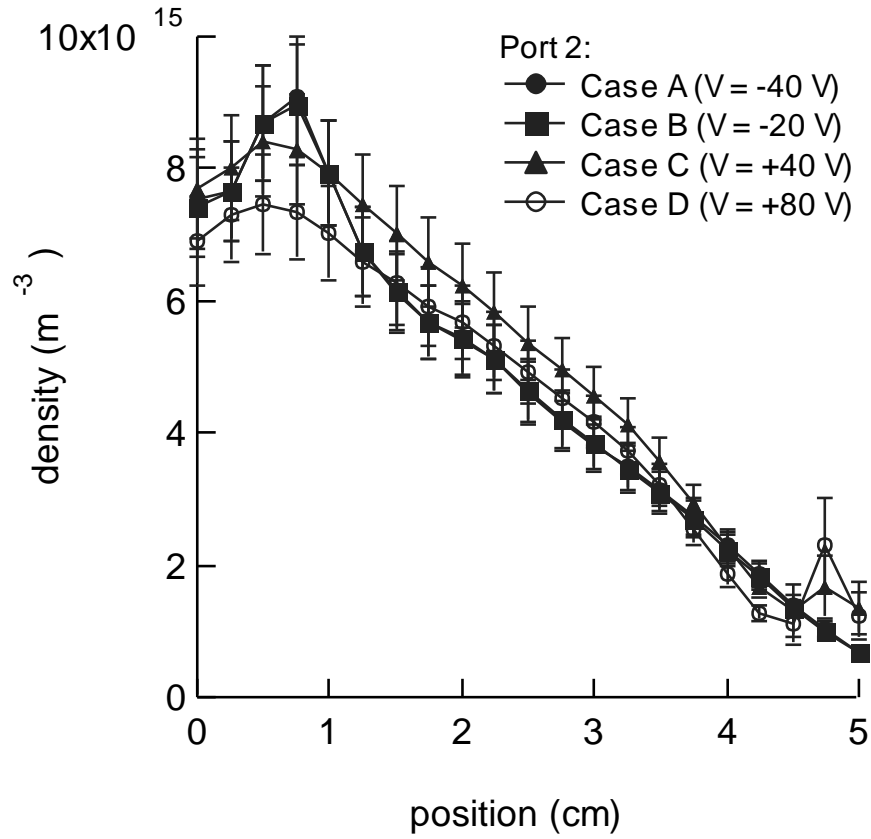


Figure 4-5: Measurement of the electron density using a double probe at Port 2 ($z = 53$ cm) for the four bias voltage cases. This port location is 102 cm upstream from the location of the ring electrodes.

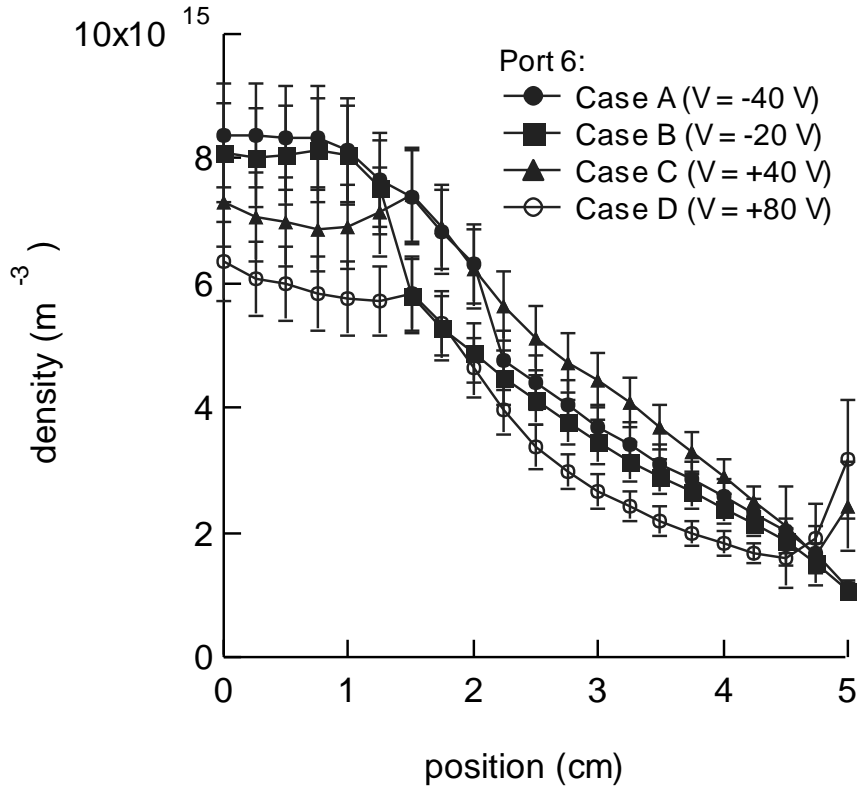


Figure 4-6: Measurement of the electron density using a double probe at Port 6 ($z = 127$ cm) for the four bias voltage cases. This port location is 28 cm upstream from the location of the ring electrodes.

4.2.3 Measurements of plasma instabilities

With the completed measurements of the steady-state plasma response to the modification of the plasma potential profile, experiments then focused on the response of the plasma fluctuations to the modifications. For these measurements, a single tipped Langmuir probe was used to measure spatial profiles of fluctuations of the floating potential. As with the density and plasma potential measurements, the Langmuir probe is inserted from a side port and radial measurements are made across the mid-plane of the plasma column. The probe was moved radially in 2 mm steps. At each location a time series of the fluctuations of the floating potential

were digitized and recorded. Then a Fourier transform (FT) of the potential fluctuations were calculated. These FT's were plotted in a “waterfall” plot with the axes being frequency, radial position, and signal amplitude. A plot was generated for each of the four ring biases. The results are plotted in Figures 4-7, 4-8, 4-9, and 4-10 for -40 V, -20 V, +40 V, and +80 V, respectively.

In considering the measurements presented in the following figures, it is important to also recall the data presented in Table 4-3. It was reported that for Case A and B, localized instabilities are present in the plasma. This can be seen in Figure 4-7 and Figure 4-8. By contrast, for Case C and D, not only is there no evidence of a localized instability, there is a broadband suppression of all low frequency plasma instabilities. This suppression will be discussed in further detail in the next section.

However, one important point that must be noted here is that the presence of the spatially localized plasma instability was *anti*-correlated with the current collected by the rings. This was an important feature of these experimental results and it indicated that the observed instabilities may be driven by sheared azimuthal flows in the plasma.

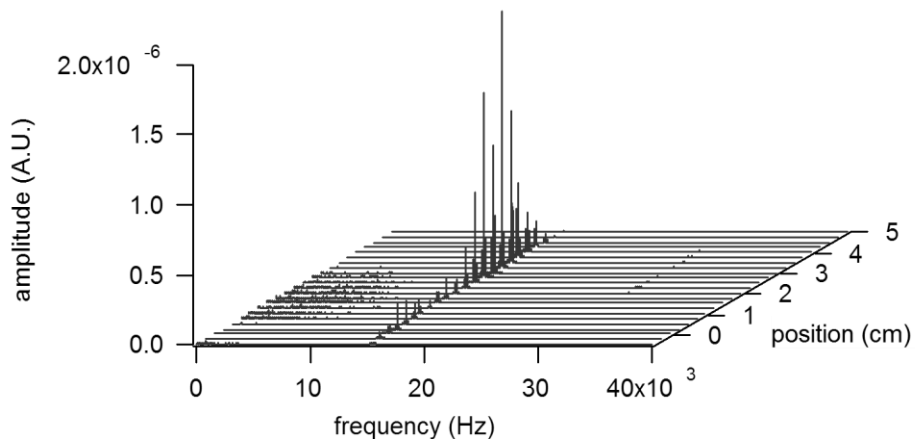


Figure 4-7: Case A: A “waterfall” plot of the floating potential fluctuations in ALEXIS for a bias voltage of $V = -40V$ on the inner three rings. The plot shows the frequency from 0 to 40 KHz on the horizontal axis, position from $r = 0$ to $r = 5$ cm on the slanted axis and amplitude of the Fourier transform on the vertical axis. The measurements show the presence of a spatially localized instability (centered near $r = 3$ cm) at a frequency of $f \sim 16$ kHz (or $f/f_{ci} \approx 0.5$).

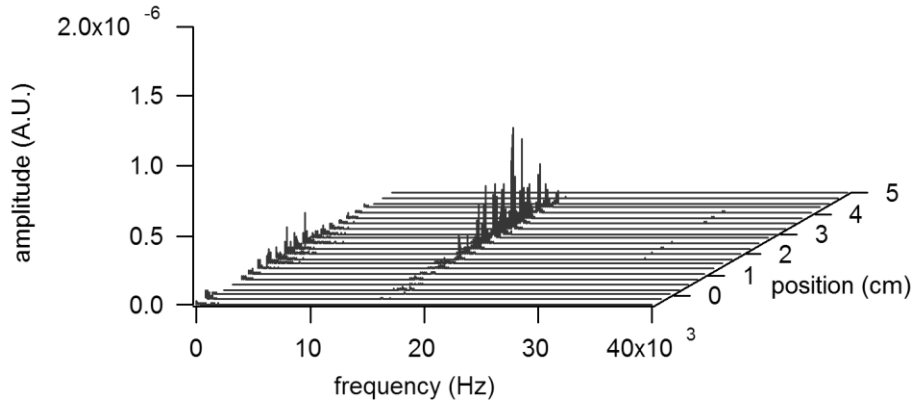


Figure 4-8: Case B: A “waterfall” plot of the floating potential fluctuations in ALEXIS for a bias voltage of $V = -20V$ on the inner three rings. The measurements show the presence of a lower amplitude instability than for the -40 V case, but it remains spatially localized (centered near $r = 3$ cm) at a frequency of $f \sim 16$ kHz (or $f/f_{ci} \approx 0.5$).

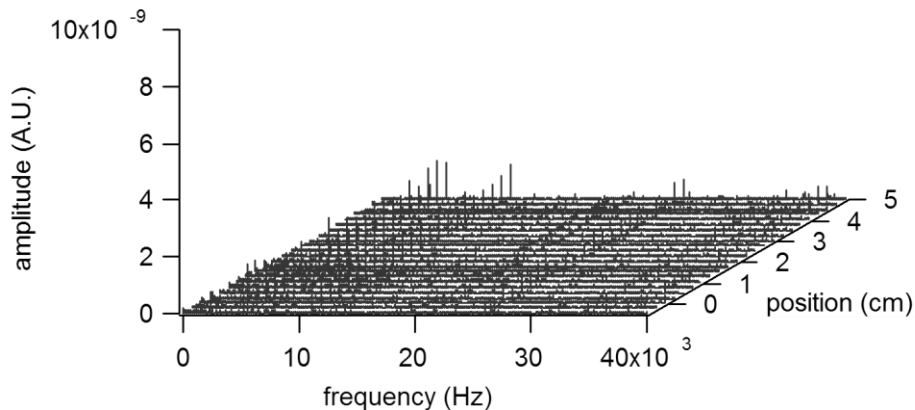


Figure 4-9: Case C: A “waterfall” plot of the floating potential fluctuations in ALEXIS for a bias voltage of $V = +40V$ on the inner three rings. The measurements show a broadband suppression of instabilities. Note that the scale on the vertical axis is 200 times smaller than for Figures 4-7 and 4-8.

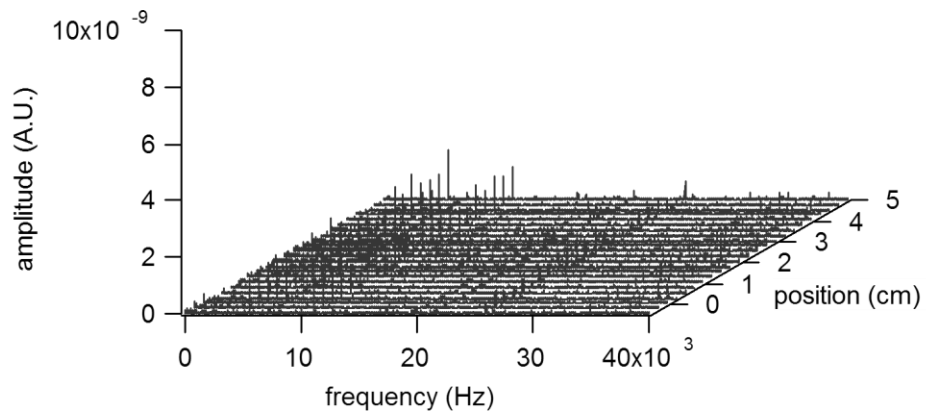


Figure 4-10: Case D: A “waterfall” plot of the floating potential fluctuations in ALEXIS for a bias voltage of $V = +80V$ on the inner three rings. The measurements show a broadband suppression of instabilities. Note that the scale on the vertical axis is 200 times smaller than for Figures 4-7 and 4-8.

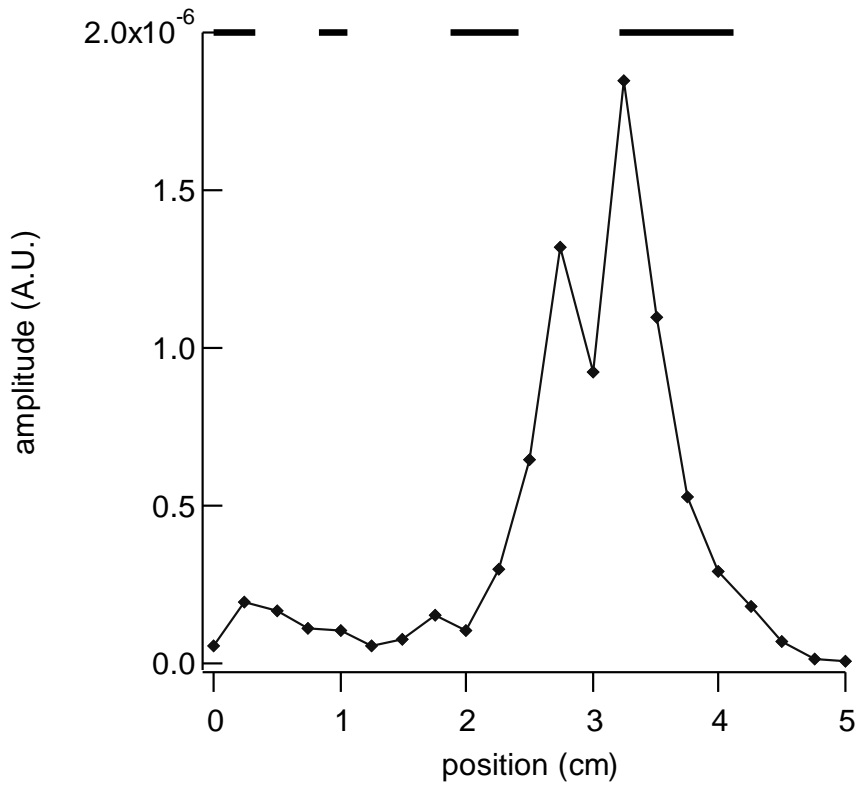


Figure 4-11: Plot of the radial profile of the amplitude of the Fourier transform at 15 kHz is plotted for the $V = -40$ V configuration (Case A, $V_1=V_2=V_3 = -40$ V, $V_4 = -50$ V). Across the top of the figure are horizontal lines indicating the positions of the four rings.

4.2.4 Characterizing the suppression of plasma instabilities

One unexpected feature of these experiments was the suppression of the plasma instabilities during the positive biasing experiments (as shown in Figure 4-9 and Figure 4-10). It was anticipated that as the plasma conditions were varied, there would be a change in the conditions that give rise to the shear-driven ion cyclotron wave, but the observed “quieting” was unexpected.

First, consider just the spectral properties of the plasma instabilities between Case A (with the instability) and Case D (without the instability). This is shown in Figure 4-12 and Figure 4-13 in which measurements of the plasma floating potential fluctuations were recorded at two different port locations - Port 2 ($z = 53$ cm) and Port 6 ($z = 127$ cm) on ALEXIS but at the same radial position of $r = 3.25$ cm. These two figures are semi-log plots of the Fourier transform of the floating potential fluctuations. In both figures, the black plot is Case A, and the grey plot is Case D.

In both Figure 4-12 and Figure 4-13, the Case A measurement shows the presence of a narrow band instability at 15 kHz with a second at 30 kHz. Case A also shows the presence of a third peak at 35 kHz. It is noted that due to limitations in the original ALEXIS data acquisition system, data could only be sampled up to 80 kHz, allowing reconstructed frequencies up to 40

kHz. Due to aliasing, the “35 kHz” signal is believed to be a third harmonic of the strong 15 kHz instability (this was confirmed when using an oscilloscope with a 60 MHz bandwidth). The Case A data for Figure 4-13 does not show this third instability feature.

This observation is generally consistent with the picture that sheared flows established by the rings are the source for this observed instability. If the waves are generated near the rings and propagating in the upstream direction, then they would first arrive at Port 6 and then Port 2. At Port 6 (Figure 4-13), the instability is more narrowly peaked with a second harmonic component that is ~90 to 100 times lower in amplitude. By contrast, at Port 2 (Figure 4-12), the primary instability is somewhat broader with lower amplitude and the second harmonic is ~10 to 20 times lower in amplitude. This may suggest that the instability is undergoing damping and dispersion as it travels along the length of the plasma column.

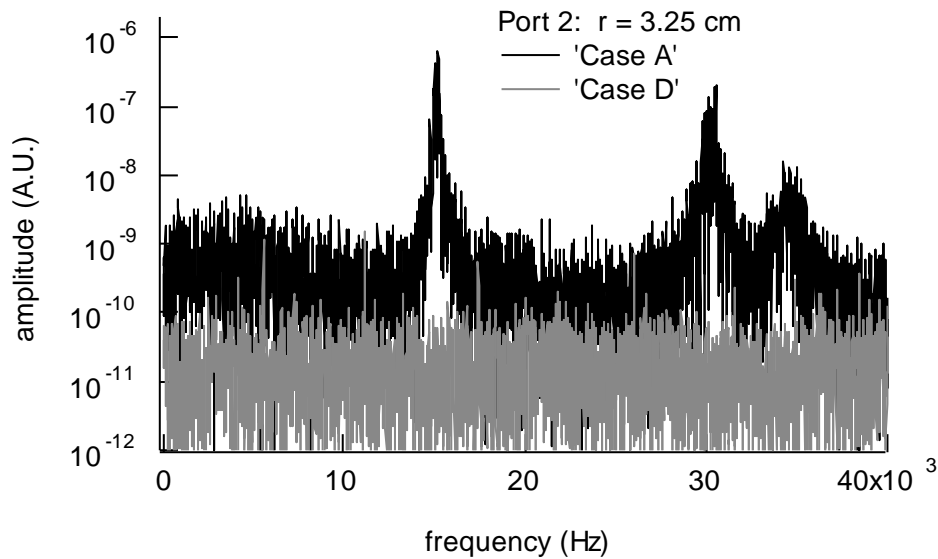


Figure 4-12: Semi-log plot of the power spectrum of the floating potential measured at $r = 3.25$ cm at Port 2 ($z = 53$ cm) in ALEXIS. The black curve represents Case A with the inner three rings biased at -80 V. The grey curve represents Case D with the inner three rings biased at +40 V.

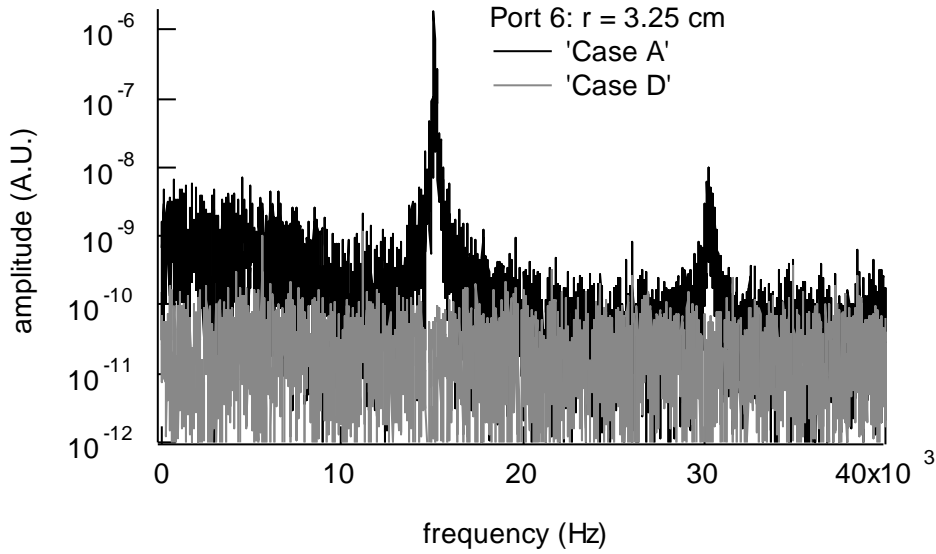


Figure 4-13: Semi-log plot of the power spectrum of the floating potential measured at $r = 3.25$ cm at Port 6 ($z = 127$ cm) in ALEXIS. The black curve represents Case A with the inner three rings biased at -80 V. The grey curve represents Case D with the inner three rings biased at $+40$ V.

For the Case D configuration, the measurements show that there is a general suppression of all instabilities. The two figures show that this suppression is more than an order of magnitude. In order to gain some insights into this observation, a re-examination of the properties of the velocity shear driven ion cyclotron instability discussed in Chapter 2 is considered.

In particular, consider the role of the azimuthal flow velocity as a function of radius shown in Equation 4-2).

$$v_{\theta} = -\frac{r\Omega_{ci}}{2} + \sqrt{r^2\Omega_{ci}^2 - 4r\left(\frac{eE_0}{m} - \frac{k_B T_i}{mn_0} \frac{dn_0}{dr}\right)} \quad (4-2)$$

The requirement of real values for the azimuthal velocities leads to a threshold condition on the value of the radial electric field that is needed to support the ion cyclotron instability.

For the conditions in these ALEXIS experiments, the density gradient term, is ~10-20 times smaller than the electric field term; making it reasonable to neglect this term for the estimate of the threshold condition. Using $B = 90$ Gauss, a critical value of the electric field can be calculated, above which the radical becomes imaginary (and consequently there is no equilibrium flow). For the conditions in this experiment, that critical electric field value is approximately $E_r = -0.1\text{V/cm}$. Then, using this value for the electric field, a threshold azimuthal velocity can be calculated. This threshold velocity is plotted as a function of radius along with the calculated azimuthal velocities of Case A and Case D in Figure 4-14. For Case A, where the instability is seen at $r = 3$ cm, ± 1 cm, the calculated flow velocity is above the threshold condition, meaning that the sheared azimuthal flow is sufficient to driven the ion cyclotron instability. Case D, however, fails this test for radial positions greater than 2 cm. While the calculated values of the azimuthal flow velocity are above the threshold for the center of the column, Equation (4-2) is only a necessary, not a sufficient condition for instability growth.

While the suppression of the ion cyclotron instability may be described by the analysis above, this does not explain the broadband suppression of instabilities throughout the plasma column. First, it is noted that with the data acquisition system available at the time, it was only possible to perform a detailed study of a small range of frequencies (up to 40 kHz). However, measurements with oscilloscopes did suggest that this suppression did extend up to a few hundred kHz. What is clear is that the changing bias voltage on the rings did alter the boundary conditions of the ALEXIS device in such a manner as to substantially suppress the generation of low frequency plasma instabilities. Additionally, this suppression is not only localized to the region near the rings, but extends throughout the entire plasma column as indicated by the

measurements at Ports 2 and 6. Ultimately, additional studies would need to be performed in order to fully understand the mechanism for this suppression.

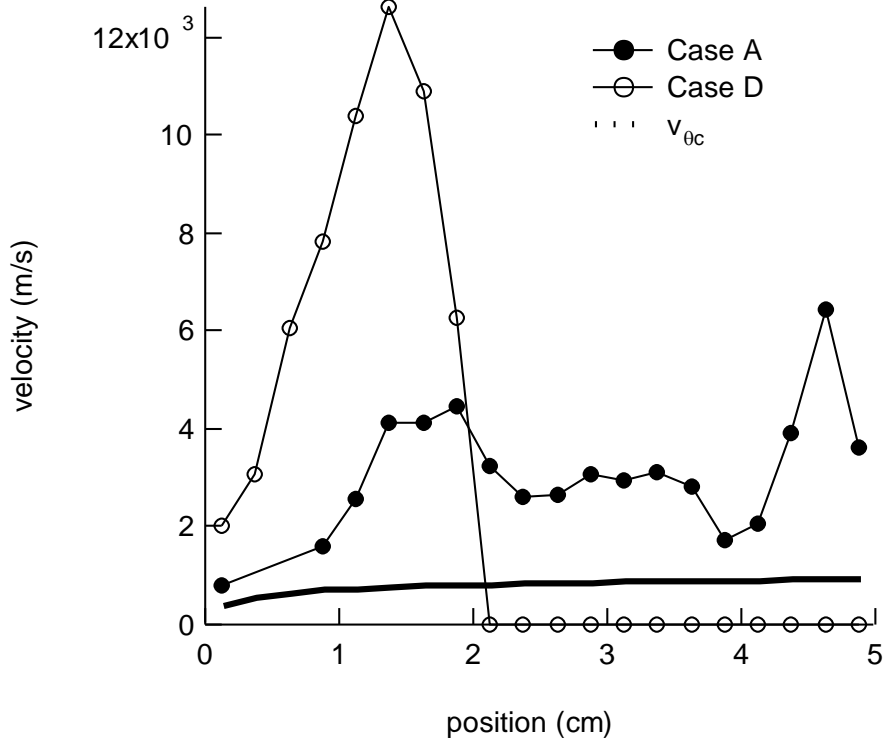


Figure 4-14: Comparison of the estimated azimuthal flow velocity for Case A (solid circles), Case D (open circles) and for the threshold conditions for wave growth in ALEXIS (solid line).

4.2.5 Driven plasma oscillations

To determine the level of active suppression corresponding to a positive bias on the rings, a 1.3 cm wire mesh antenna was placed into the plasma column to launch electrostatic waves. The antenna was placed at Port 1 ($z = 31$ cm) and at the center of the column ($r = 0$ cm), with its surface oriented perpendicular to the background magnetic field supplied by the electromagnets. A sinusoidal voltage was applied to the antenna, with frequencies ranging from 5 to 100 kHz and voltages of up to 10 V peak-to-peak. The launched wave was then detected downstream using

the Langmuir probes at Port 2 and Port 6. After the signal is detected, a Fourier transform is calculated and a narrow band ($\Delta f = 300$ Hz) around the launched wave frequency is analyzed.

The sum of the FT amplitudes in this narrow band is then used as a measure of the strength of the launched wave as a function of radial position. Figure 4-15 and Figure 4-16 show the results of this process for the four different ring biases previously discussed. Figure 4-15 shows a measurement at Port 1, approximately 22 cm from the location of the antenna. Figure 4-16 shows a measurement at Port 6, approximately 98 cm from the antenna. For these figures, the launched wave was a sine wave with $f = 20$ kHz, a dc offset of +9 V, and a peak-to-peak amplitude of 7.5 V.

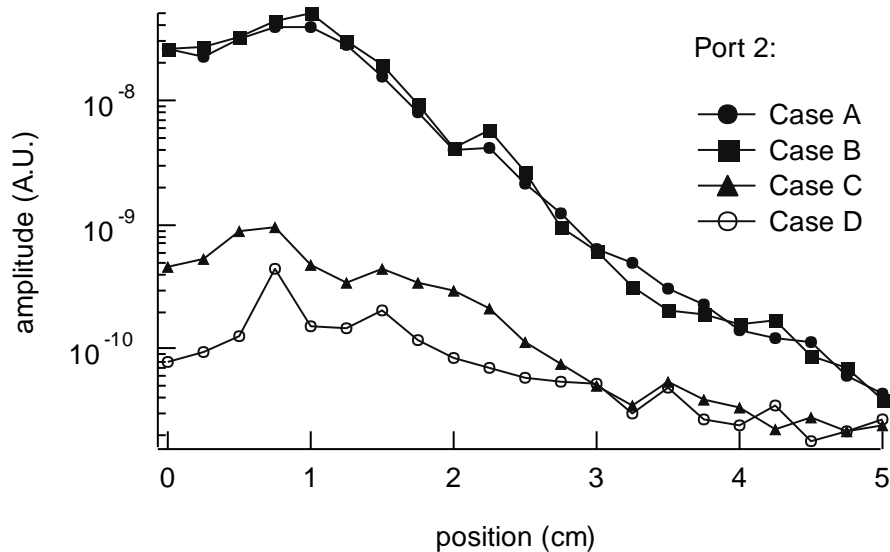


Figure 4-15: Radial profile of the amplitude of a launched wave in ALEXIS. The wave is launched from an antenna that is placed at the center of the ALEXIS plasma column at Port 1 ($z = 31$ cm) and is measured at Port 2 ($z = 53$ cm).

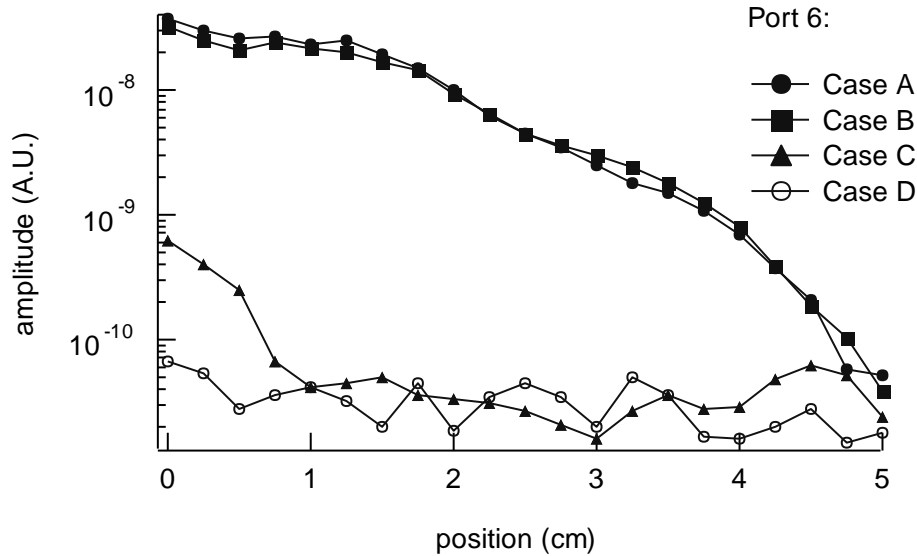


Figure 4-16: Radial profile of the amplitude of a launched wave in ALEXIS. The wave is launched from an antenna that is placed at the center of the ALEXIS plasma column at Port 1 ($z = 31$ cm) and is measured at Port 6 ($z = 127$ cm).

Figure 4-15, which is located closest to the antenna, shows that for Case A and Case B the launched wave is peaked near the center of the plasma with a radial decay of the wave. For Figure 4-16 Case A and Case B show more radial propagation, as indicated by the broad structure of the amplitude. In both Figure 4-15 and Figure 4-16, Case C and Case D indicate a substantially reduced wave amplitude at the center of the plasma column (by factors of 20 to 50). The data also shows significantly less radial broadening than Case A and Case B. In particular, Figure 4-16, Case C and Case D, show very little propagation downstream, and indicate that the small amount of wave energy that did remain in the column downstream was confined to the center of the plasma column, inside of the shear layer generated by the radial electric field.

The results of the launched wave experiment are generally consistent with the results of the self-excited studies described previously. Case A and Case B have conditions that allow the propagation of the IEDDI and the launched waves. As the plasma conditions are modified for Case C and Case D, the self-excited wave is no longer generated. Moreover, as shown by the

broadband suppression of instabilities in Figure 4-12 and 4-13, these latter two cases also have a significant dissipation mechanism, or mechanisms, that inhibit the propagation of self-excited instabilities across a broad range of frequencies. For the case of the launched waves, these dissipation mechanics remain in place and the propagation of the launched wave appears to be restricted to a narrow region along the center of the ALEXIS plasma column.

The disappearance of the naturally occurring ion cyclotron-like instability is explained using the fluid theory presented above, because the imposed radial electric field is sufficiently positive that there is no equilibrium solution for the azimuthal flow velocity. The launched wave experiments presented above are consistent with the self-excited wave experiments. That is, the mechanism for wave growth is only present in Case A and Case B, and is not present in Case C and Case D.

4.2.6 Characterizing the observed electrostatic instability

The instability presented above was similar to the instability observed and reported on by Thomas, et al. in a letter published in *Physics of Plasmas*.⁵⁶ The configuration used in the following section is slightly different than the configuration presented above, but the driven instability, and the mechanism driving it, is the same. In both configurations the instabilities were radially localized, they were near the ion cyclotron frequency, and they were anti-correlated with parallel current.

The configuration of the rings used in the following discussion is as follows: Ring 1 was fixed at -120V, Ring 2 was fixed at -120V, Ring 3 was varied throughout the experiment, and

Ring 4 was fixed at 0V. The following section will proceed similar to Thomas, et al.⁵⁶ and show that the observed instability is not a parallel current driven instability, a drift wave, or a Kelvin-Helmholtz mode, but is most likely the Inhomogeneous Energy Density Driven Instability (IEDDI).

To show that the instabilities are anti-correlated with the current collected by Ring 3, three ring biases and collected currents are presented with the measured instability activity corresponding to each bias in Figure 4-17. The biases applied to Ring 3 and the respective currents collected are: -107 V and -2 mA, -11 V and -24 mA, and +21 V and -91 mA. As Figure 4-17 shows, the increase in current collected correlates to a decrease in the observed level of the coherent electrostatic fluctuation.

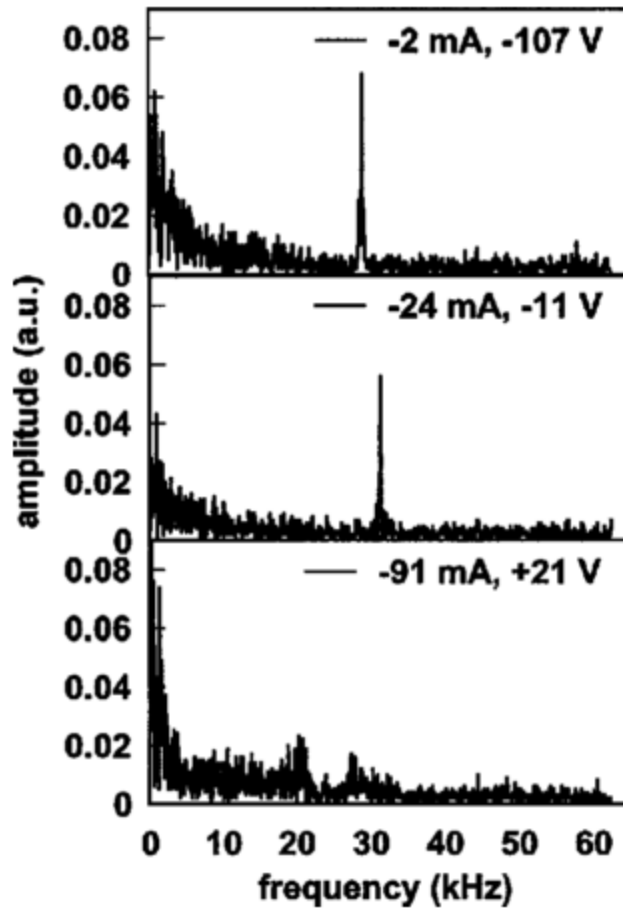


Figure 4-17: Three plots of the instabilities observed in ALEXIS for three different biases applied to Ring 3. From top to bottom the applied voltages are -107V, -11V, and +21V.

While the previous argument presents a good qualitative argument for the observed instability being anti-correlated to the parallel current, a more detailed investigation also collaborates this conclusion. To be a parallel current-driven instability, the phase velocity of the wave should be comparable to, or larger than, the electron drift velocity. Because there is a non-zero radial electric field, a non-local treatment of the observed wave frequency must be employed.⁴⁷ This is physically akin to accounting for the Doppler shift due to the azimuthal flow that results from the $E \times B$ flow.

$$v_{phase} = \frac{\omega_1}{k_{\parallel}} = \frac{\omega - k_{\perp} v_E}{k_{\parallel}}$$

$$v_{\parallel} = v_{De} = \frac{j}{en_0}$$

Experimentally measured values used in the above calculations are $j = 2.8 \text{ A m}^{-2}$, $k_y \approx 70 \text{ m}^{-1}$, $k_z \approx 8 \text{ m}^{-1}$. This then gives a ratio of the parallel drift velocity to the wave phase velocity of:

$$\left| v_{\parallel} / v_{phase} \right| \approx 0.02 \ll 1$$

This indicates that the electron drift velocity is not moving fast enough to drive a parallel current driven instability.

The next physical characteristic of the observed instability to study is the radial localization of the instability. Additionally, the peak amplitude of the wave was observed to be collocated with the shear in the radial electric field.

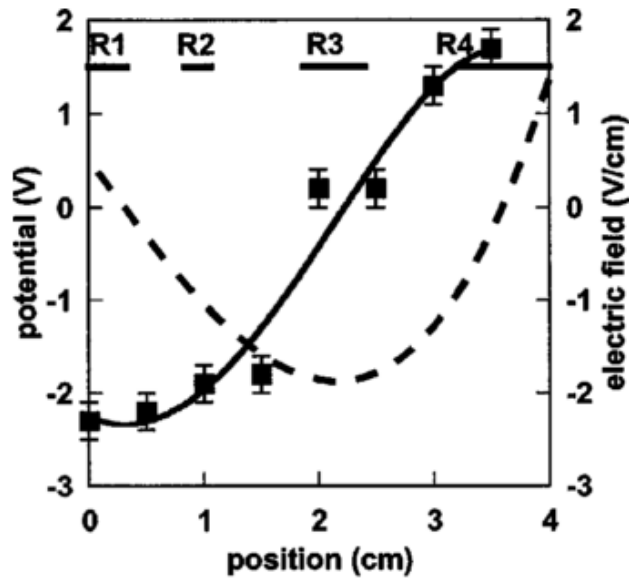


Figure 4-18: The solid line is a fourth-order polynomial fit to the plasma potential measurements (black squares). The electric field is computed from the negative derivative of the potential curve fit. This measurement is taken when Ring 3 is biased very negative, i.e., drawing a low electron current.

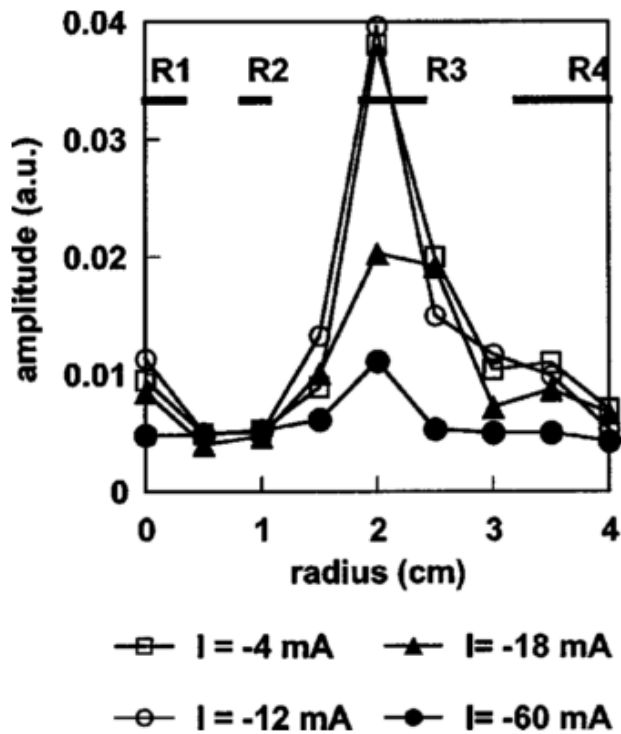


Figure 4-19: Amplitudes of the instability plotted versus radial position for four different bias cases. This plot shows the radial localization of the instability, with the peak near Ring 3.

Figure 4-18 shows the plasma potential as measured by an emissive probe. The Ring 3 bias used for this measurement is the low electron current case, which is Ring 3 biased very negatively and collecting approximately -4 mA of current. A fourth order polynomial is then fit to the plasma potential measurements. The derivative of this polynomial is then used to calculate the radial electric field, which is plotted as the dashed line in Figure 4-18. Notice that the maximum shear in the electric field is located near Ring 3 (as indicated by the black line labeled “R3”).

Figure 4-19 shows the amplitudes of the instability as a function of radial position for four different Ring 3 biases. This plot shows that when the instability is large the wave activity is localized to the region of plasma around Ring 3. Additionally, when the bias to Ring 3 is increased (and the parallel current collected by Ring 3 is increased) the instability amplitude decreases significantly. Comparing Figure 4-19 to Figure 4-18 shows that the wave amplitude is collocated with maximum shear in the radial electric field.

To study the impact of the density profile on the instability amplitude, a Langmuir probe was used to determine the density near Ring 3. This information was used to calculate the density gradient near Ring 3. Drift waves are driven by large density gradients,¹¹ so it was important to determine the approximate relationship between density gradient and wave amplitude. Figure 4-20 shows the density gradient as a function of the current collected on Ring 3. It has previously been shown that increased collected current corresponds to a decrease in wave amplitude (see Figure 4-17). Figure 4-20 shows that the density gradient is a minimum

when the current collected is at a minimum, i.e., when the observed instability amplitude is a maximum.

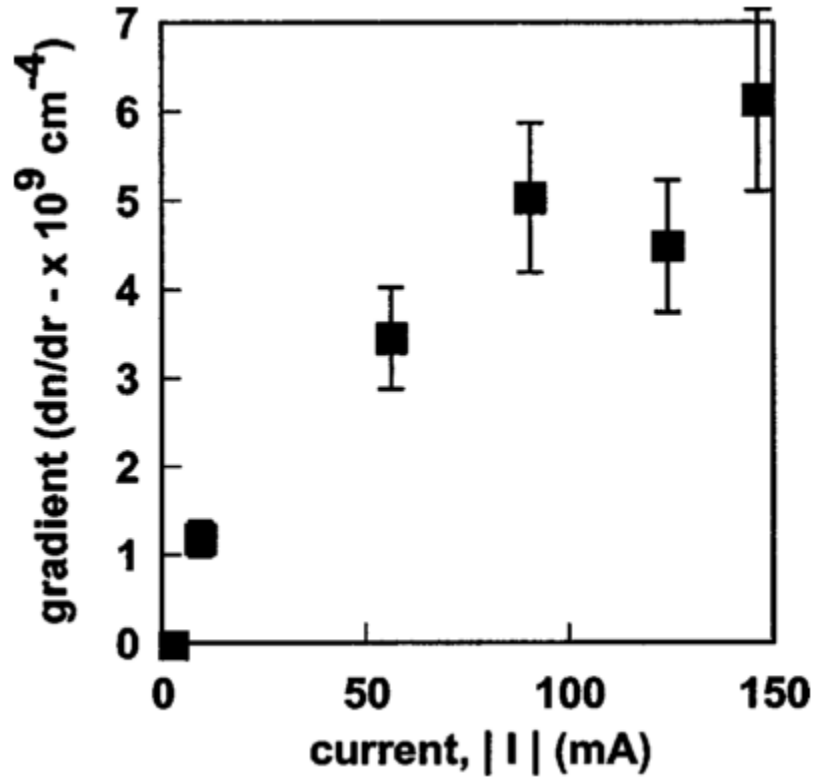


Figure 4-20: Density gradient near Ring 3 plotted versus the current collected by Ring 3, which has been shown to be proportional to the instability amplitude.

To better assess the impact of the density gradient, an estimate for the drift wave growth rate can be calculated. Assuming the presence of sheared transverse flows, the growth rate is given by:

$$\gamma = -\frac{\sqrt{\frac{\pi}{2}} \left(\frac{\omega_{1R}^2}{|k_z| v_{te}} \right) (\omega_{1R} - \omega_{*e})}{(2(1 + b_s) \omega_{1R} - \omega_{*e})}$$

(4-3)

Where b_s , the Doppler shifted wave frequency, and the diamagnetic drift frequency are:

$$b_s = \left(\frac{k_{\perp} C_s}{\Omega_i} \right)^2$$

$$\omega_{1R} = \text{Re}[\omega - k_{\perp} v_E] \sim 1.1 \times 10^6 \text{ rad/sec}$$

$$\omega_{*e} = k_{\perp} v_{De} = k_{\perp} \frac{k_B T_e}{eB} \left(\frac{1}{n} \right) \left(\frac{dn}{dr} \right) \sim 800 \text{ rad/sec}$$

Which gives $|\omega_{1R}| \gg |\omega_{*e}|$. This means that all the terms in Equation (4-3) are positive definite, which gives a negative growth rate for resistive drift waves. This suggests then that the observed instability is not a drift wave.

To determine if the observed instability is a Kelvin-Helmholtz (KH) mode, begin by parameterizing the plasma response to both parallel and transverse flows. This parameter is “R” where:

$$R = \frac{k_{\perp} v_E}{k_{\parallel} v_{\parallel}}$$

It has been shown that ion cyclotron waves can be driven unstable (even in the absence of field aligned current) for values of $R \gg 1$.³⁵ For the results presented here $R \approx 70$. Additionally, shear driven ion cyclotron modes prefer long azimuthal wavelengths, i.e., low m numbers. Measuring at $r = 2$ cm, $m = r k_{\perp}$ suggests an m value between 1 and 2. This also suggests that the observed instability is not a KH mode, because KH modes prefer high m numbers, and have no growth for $m = 1$.

To further bolster the claim that the observed mode is not KH, it is noted that KH modes are strongly Landau damped unless $k_{\parallel}/k_{\perp} \sim 0$.⁵⁹ An alternate interpretation of the parallel wave number going to zero for KH modes is that the parallel wavelength approaches infinity. Using

the parameters in this experiment, $k_{\parallel}/k_{\perp} \sim 0.11$. For these reasons, it appears unlikely that the observed wave mode is a Kelvin-Helmholtz instability.

At this point, the model developed in Chapter 2 will be employed to check the consistency of the observed wave behavior with the predictions of Equation (2-27). To accomplish this, the data presented in Sections 4.2.1 to 4.2.3 will be used to determine the input parameters for the model. Also, the parameters will be chosen based on the plasma parameters at the peak of the instability, i.e. $r \approx 3$ cm. Those parameters are summarized in Table 4-4.

Table 4-4: Parameters used in the computational model presented below.

Parameter	Value
Species	Helium
Magnetic Field Strength	90 Gauss
Electric Field Strength	-50 V/m
T_e	4 eV
T_i	0.025 eV
k_z	15 m^{-1}
k_r	785 m^{-1}

Using the above parameters, the code is executed and the following plot is produced:

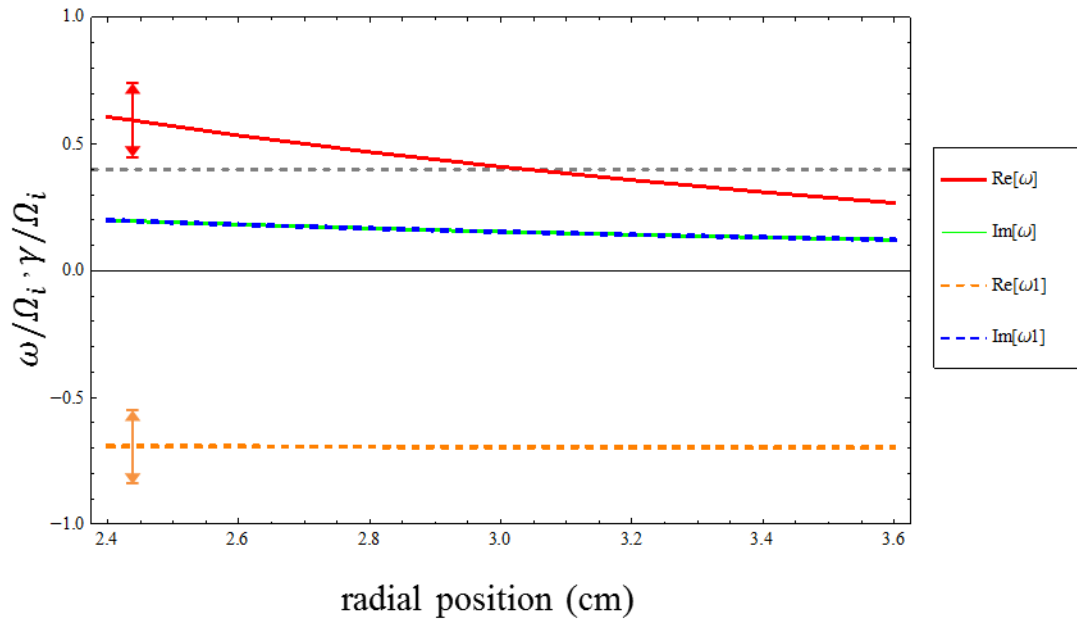


Figure 4-21: Plot showing the output of the computational model based on experimental measurements for the region where the instability is observed. The plot shows the real component of ω (solid red line), the real component of ω_1 (dashed orange line), the imaginary component of ω (solid green line), and the imaginary component of ω_1 (dashed blue line). The dashed gray line shows the frequency measured in the lab frame.

The above plot, Figure 4-21, shows agreement between the observed and the calculated instability frequencies, at approximately $0.4 * \Omega_i$. Unfortunately, the condition that the real component of the Doppler shifted frequency, $Re(\omega_1)$, should be near an harmonic of the ion cyclotron frequency is not met. This could be due to small errors in the measurements and estimations of the physical parameters used in the model, as well as due to simplifications in the model itself. Allowing for experimental error, the input parameters are varied slightly, and better agreement can be found. These new parameters are listed in Table 4-5, and the corresponding plot is show in Figure 4-22.

Table 4-5: Updated parameters used in the computational model presented below.

Parameter	Value
Species	Helium

Magnetic Field Strength	90 Gauss
Electric Field Strength	-75 V/m
T_e	8 eV
T_i	0.025 eV
k_z	15 m^{-1}
k_r	785 m^{-1}

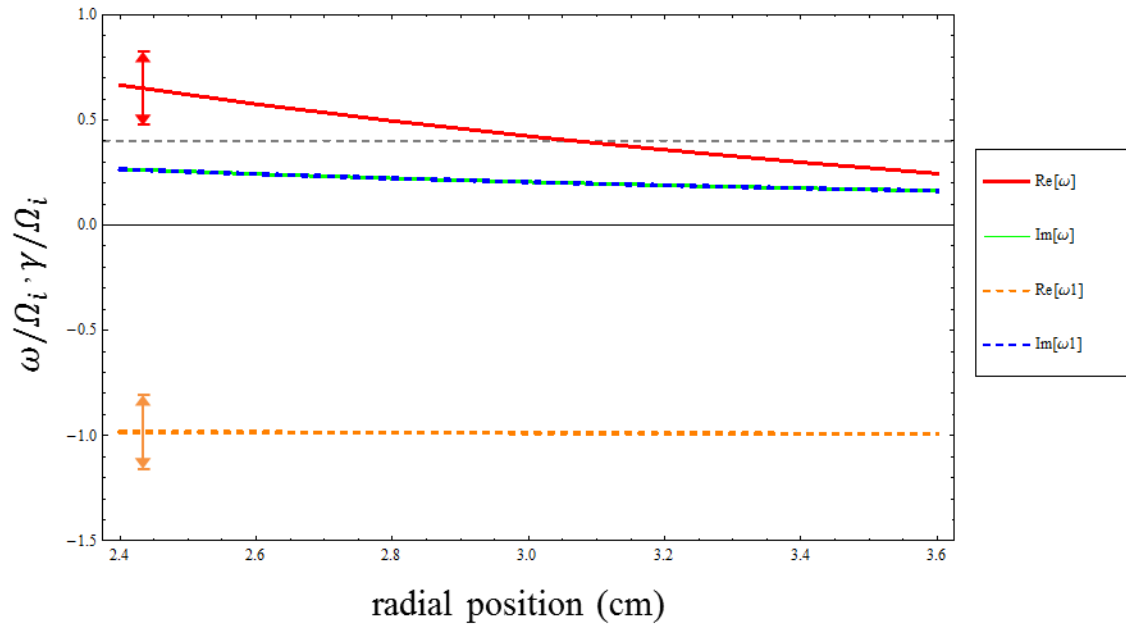


Figure 4-22: Plot showing the output of the computational model utilizing the parameters given in Table 4-5 for the region where the instability is observed. The plot shows the real component of ω (solid red line), the real component of ω_1 (dashed orange line), the imaginary component of ω (solid green line), and the imaginary component of ω_1 (dashed blue line). The dashed gray line shows the frequency measured in the lab frame.

Using these new parameters, Figure 4-22 shows good agreement again with the frequency measured in the lab frame. Additionally, the new parameters produce the predicted result that the condition that the real component of the Doppler shifted frequency, $Re(\omega_1)$,

should be near an harmonic of the ion cyclotron frequency. While the difference between the two input electric fields seems significant, it is within the experimental error of the measurement. The temperature of 8 eV is above the estimated temperature for ALEXIS, there is a population of beam electrons that likely exceed this temperature. An accurate measurement of the electron temperature was difficult with the diagnostics that were available at the time, so the value of 8 eV is not entirely unreasonable. Regardless, the model further confirms that the observed instability is likely the IEDDI.

4.3 Multi-Species Experiments in ALEXIS – RF configuration

4.3.1 Introduction

In Table 4-3 in Section 4.1.1., it was shown that primary electrons from the heated, biased filaments were likely contributing to an axial current in ALEXIS. Additionally, from the plasma parameter measurements it was shown that electron plasma densities were generally limited to below $1 \times 10^{16} \text{ m}^{-3}$. Part of the ongoing mission of the ALEXIS experiment is to study the properties of both electrostatic and electromagnetic waves in laboratory plasmas while making connections to both the fusion and space plasma communities. So, as discussed in Chapter 3, an upgrade was made to the ALEXIS device that substantially changed the operational parameters of the experiment. The most significant change was the switch from a hot-filament plasma source to a RF plasma source. The experiments described in this section are all performed in the ALEXIS-RF configuration.

One of the goals of this upgrade was to improve the diagnostic capabilities of ALEXIS – in particular, to move to non-invasive diagnostic tools for measuring ion flow velocities. For all of the experiments described in Section 4.1, the ion velocities are inferred from measurements of the plasma potential (electric field). For the next experiments, it is desirable to make direct measurements that can be compared to the inferred velocities. One diagnostic used in laboratory plasmas for ion velocity measurements is Laser Induced Fluorescence (LIF). This diagnostic is traditionally used on Argon plasmas, using a well-established transition scheme.⁷⁴

Of course, one challenge of transitioning to a new experimental configuration was to ensure that the experimental observations made in the previous ALEXIS configuration could be made in the new configuration. In particular, with the desire to perform LIF measurements using argon plasmas, the magnetic configuration of ALEXIS would need to be modified. This is because the argon mass is ten times larger than the helium mass and, for the same velocity, the argon gyroradius would be ~ 3 times larger. So, ALEXIS would need to be operated at larger magnetic field strengths in order to confine the argon.

In order to understand how the properties of ALEXIS plasmas scale with different ion species, a series of experiments was designed to test the scaling of plasma instabilities as the mass of the plasma ion was increased. The gases chosen for this test were Helium ($M = 4 M_p$), Nitrogen ($M = 14 M_p$), Neon ($M = 20 M_p$), and Argon ($M = 40 M_p$). The goal was to find a way to transition the plasma behaviors previously observed up to the new operating species. The key physical constraint that could not be changed, however, was the diameter of the chamber.

4.3.2 Experimental Design

To perform this scaling experiment, it was first necessary to determine an appropriate scaling condition. Because the experiment involves a comparison over a wide range of gases, it is important to ensure that they are all subject to the same conditions in ALEXIS. Because of the fixed size of the ALEXIS chamber, this means that it will be necessary to scale the magnetic field in order to maintain the same degree of confinement for each of the species. Alternatively,

the experiment should be operated in manner to keep the ratio of the ion gyroradius to chamber size constant.

Consider that the gyroradius is given by: $r_{Li} = (v_{ti}/\omega_{ci}) = (2k_B T_i)^{1/2} (m_i^{1/2}/qB)$; where v_{ti} is the ion thermal velocity. Under the assumption that all of the ion species are singly ionized, i.e., $q = e$ (elementary charge), then a generalized expression for the ratio of the gyroradius normalized to the chamber size (a) will be given by:

$$\frac{r_{Li}}{a} = \sqrt{\frac{2k_B T_i \sqrt{m_i}}{e^2 B}} \quad (4-4)$$

Therefore, under the assumption that all of the gas species will be at the same ion temperature, which is a reasonable assumption for the ALEXIS plasma conditions, then it is expected that the normalized gyroradius will scale as $m_i^{1/2}/B$.

So, a new constant, ζ (zeta), is defined as a constant such that for each species, “s”:

$$\zeta = \frac{m_{He}}{(B_{He})^2} = \frac{m_N}{(B_N)^2} = \frac{m_{Ne}}{(B_{Ne})^2} = \frac{m_{Ar}}{(B_{Ar})^2} \quad (4-5)$$

Therefore, using this scaling factor, it should be possible to operate ALEXIS with different gas species and then observe qualitatively similar phenomena.

4.3.3 Multi-species measurements

The results from the multi-species experiments are presented below in two groups. Group A are the results with $\zeta > 5 \times 10^{-4}$ and Group B are the results with $\zeta < 5 \times 10^{-4}$. Across all the species the plasma response (as measured by the floating potential fluctuations) is distinctly different between the two groups. For the Group A measurements, there is an observed instability in the plasma that generally has a wave frequency below the ion cyclotron frequency, i.e., $\omega \ll \omega_{ci}$. For the Group B measurements, there is an instability in the plasma that generally has the feature, $\omega \geq \omega_{ci}$.

For these experiments the rings are disconnected and allowed to electrically float. All instabilities observed are naturally occurring, that is, nothing is done to artificially launch or drive the instabilities. The naturally occurring potential structure (from the density gradient) leads to a small negative electric field, meaning pointing radially inward. The chamber is filled to the same neutral pressure for each gas (1 mTorr), and the same rf power is used to generate each plasma (150 W). To calculate Zeta, it is assumed that the ions have a temperature of 0.05 eV.

Table 4-6: Conditions for the two cases presented in this section. Magnetic field strength is calculated from the current applied to the magnets. r_L/a is the ratio of the Larmor radius to the chamber radius.

	Case A: $\zeta=3.7 \times 10^{-4}$ $r_L = 6.2 \text{ mm}$ $r_L/a = 0.12$ $0.4 < f/f_{ci} \leq 0.6$	Case B: $\zeta=6.9 \times 10^{-4}$ $r_L = 8.5 \text{ mm}$ $r_L/a = 0.18$ $1.1 < f/f_{ci} \leq 1.6$
<u>Species</u>	Magnetic Field (Gauss)	
Helium (A = 4)	104	76
Nitrogen (A=14)	195	142
Neon (A=20)	233	170

Argon (A=40)	330	240
--------------	-----	-----

a) Group A measurements

The measurements presented below are for Group A, with $\zeta = 3.7 \times 10^{-4}$. This gives a Larmor radius of 6.2 mm, and a ratio of the Larmor radius to the chamber radius of 0.12. Notice that the naturally occurring instabilities are all located at a normalized frequency (f/f_{ci}) of approximately 0.5. Additionally, the waves seem to be present across the entire column, that is, they do not appear to be peaked at a particular radius.

Each plot shows the amplitude of the Fourier Transform of the floating potential fluctuations plotted versus frequency and radial position. For the radial position axis, “0 cm” is the center of the column and “5 cm” is the outer edge. Color is used to indicate the amplitude of the Fourier Transform, with red indicating high amplitude (1×10^{-4}), and blue indicating low amplitude (1×10^{-8}), plotted on a logarithmic scale. For the frequency axis, the frequencies are normalized to the ion cyclotron frequency, and the range plotted is up to $1 * f_{ci}$.

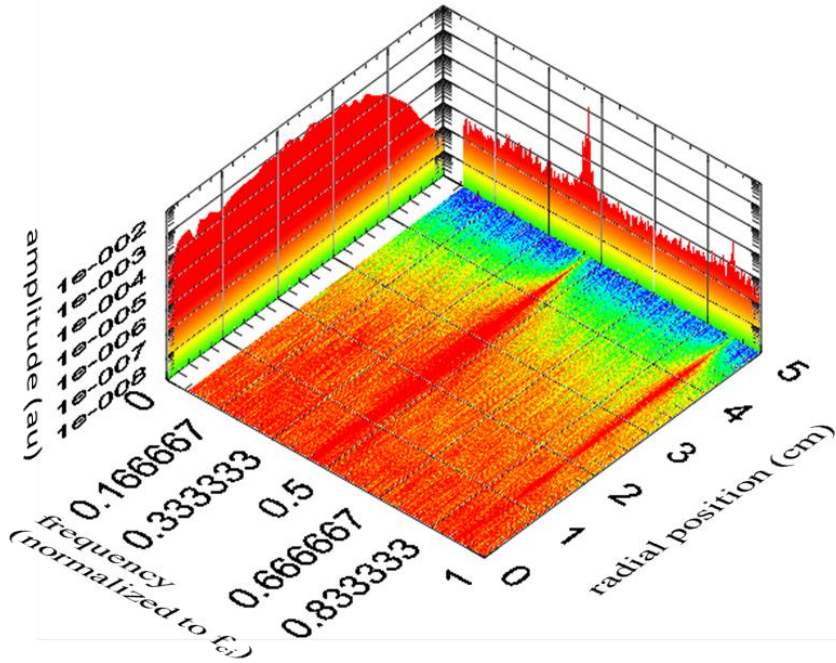


Figure 4-23: Case A, Argon: This experiment is performed with a magnetic field strength of $B = 330$ G. The dominant instability occurs at $f/f_{ci} \sim 0.5$.

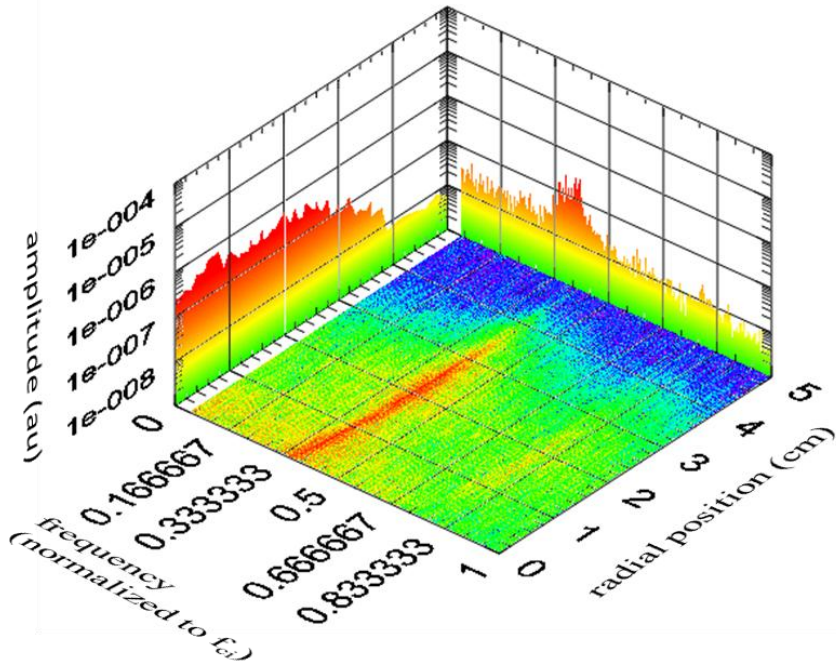


Figure 4-24: Case A, Neon: This experiment is performed with a magnetic field strength of $B = 233$ G. The dominant instability occurs at $f/f_{ci} \sim 0.4$.

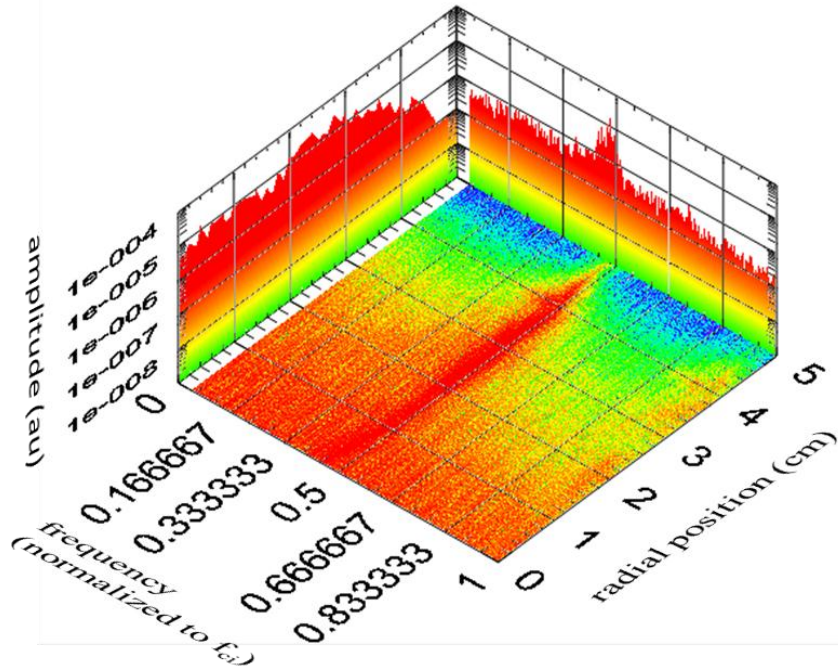


Figure 4-25: Case A, Nitrogen: This experiment is performed with a magnetic field strength of $B = 195$ G. The dominant instability occurs at $f/f_{ci} \sim 0.5$. Note that to calculate the ion cyclotron frequency, Nitrogen is assumed to be monoatomic, not N_2 .

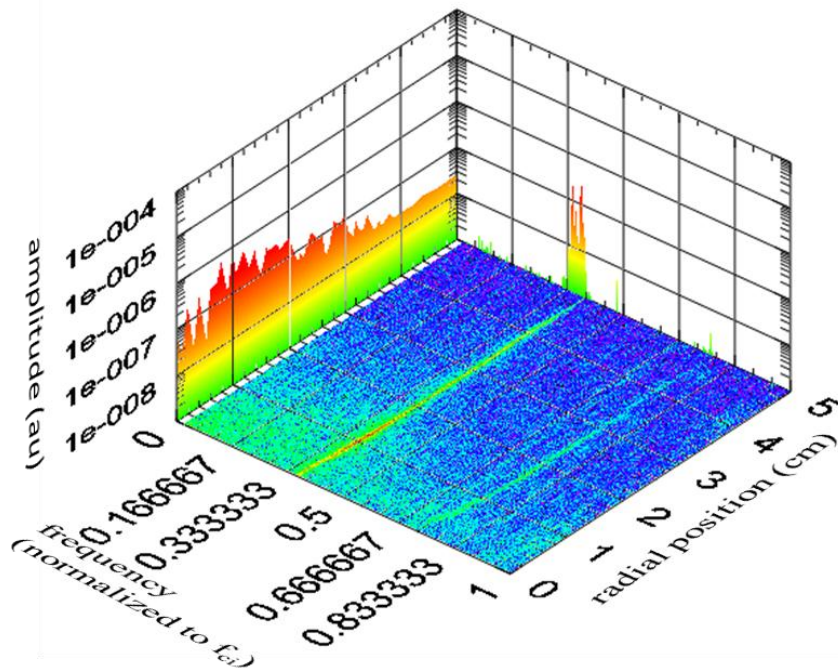


Figure 4-26: Case A, Helium: This experiment is performed with a magnetic field strength of $B = 104$ G. The dominant instability occurs at $f/f_{ci} \sim 0.4$.

b) Group B measurements

The measurements presented below are for Group A, with $\zeta = 6.9 \times 10^{-4}$. This gives a Larmor radius of 8.5 mm, and a ratio of the Larmor radius to the chamber radius of 0.18. Notice that the naturally occurring instabilities are all located at a normalized frequency (f/f_{ci}) of approximately 1.1 to 1.6. Additionally, the waves seem to be radially localized, that is, the amplitude is not uniform across the plasma column.

Each plot shows the amplitude of the Fourier Transform of the floating potential fluctuations plotted versus frequency and radial position. For the radial position axis, “0 cm” is the center of the column and “5 cm” is the outer edge. Color is used to indicate the amplitude of the Fourier Transform, with red indicating high amplitude (1×10^{-2}), and blue indicating low (1×10^{-8}), plotted on a logarithmic scale amplitude. For the frequency axis, the frequencies are normalized to the ion cyclotron frequency, and the range plotted is up to $2 * f_{ci}$.

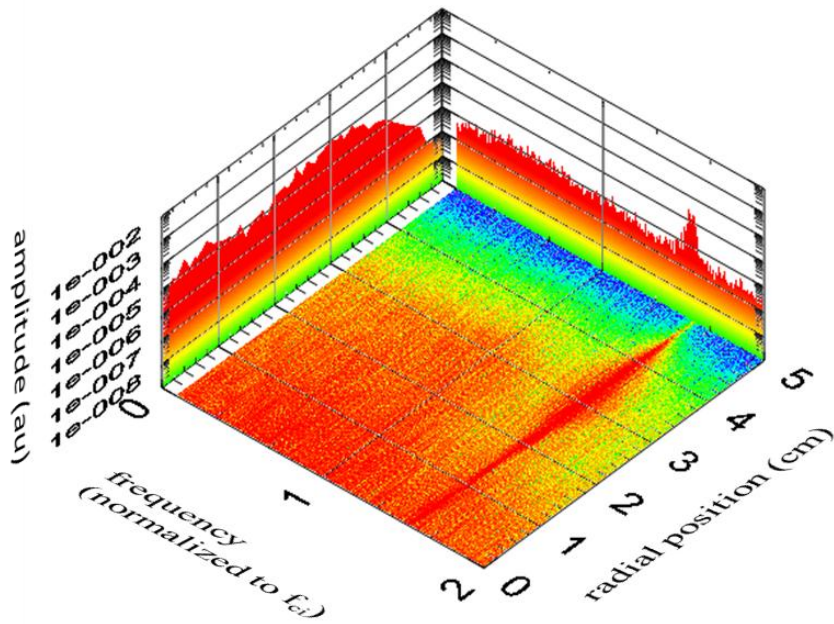


Figure 4-27: Case B, Argon: This experiment is performed with a magnetic field strength of $B = 240$ G. The dominant instability occurs at $f/f_{ci} \sim 1.6$.

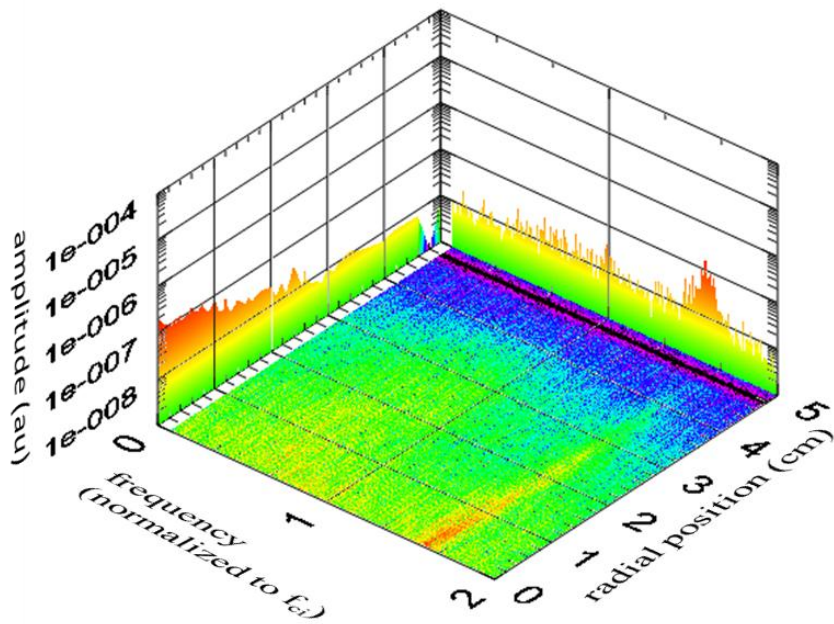


Figure 4-28: Case B, Neon: This experiment is performed with a magnetic field strength of $B = 170$ G. The dominant instability occurs at $f/f_{ci} \sim 1.6$.

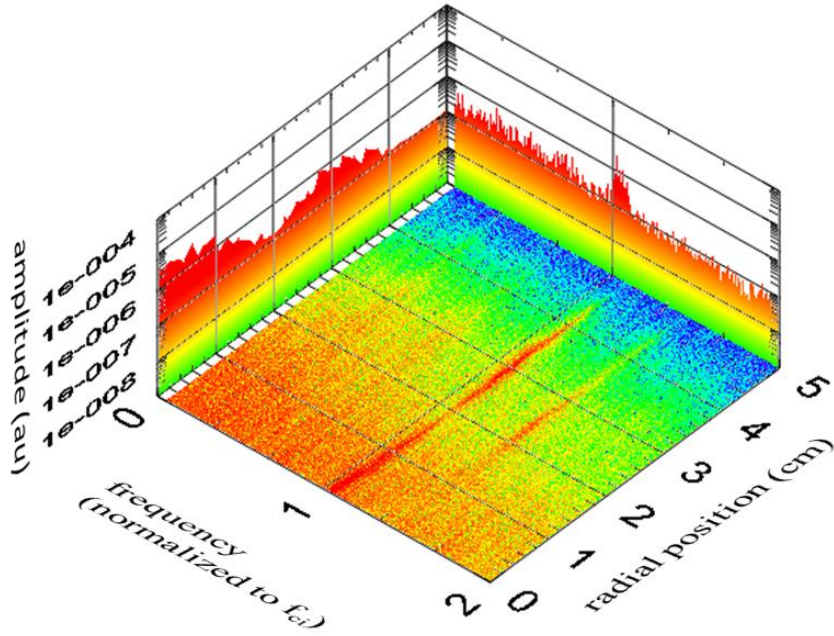


Figure 4-29: Case B, Nitrogen: This experiment is performed with a magnetic field strength of $B = 142$ G. The dominant instability occurs at $f/f_{ci} \sim 1.1$. Note that to calculate the ion cyclotron frequency, Nitrogen is assumed to be monoatomic, not N_2 .

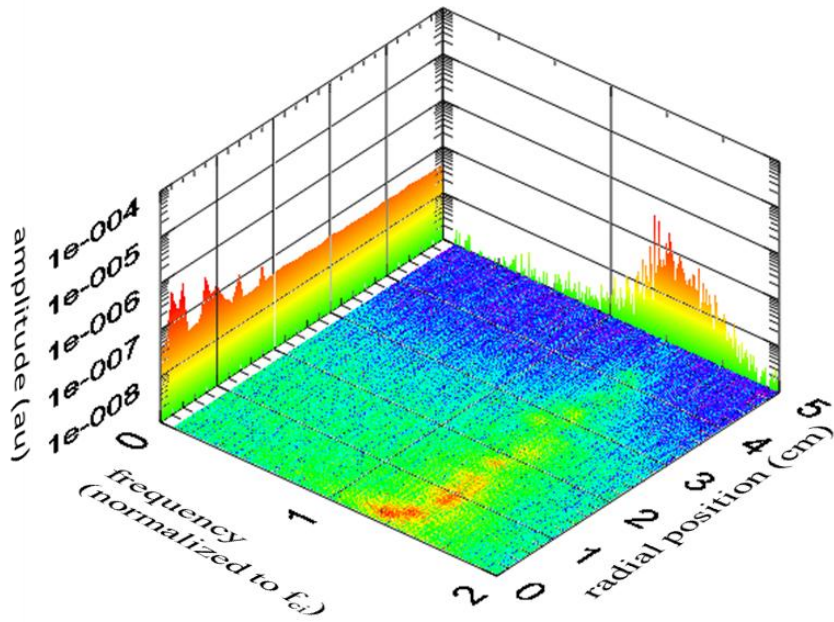


Figure 4-30: Case B, Helium: This experiment is performed with a magnetic field strength of $B = 76$ G. The dominant instability occurs at $f/f_{ci} \sim 1.3$.

4.3.4 Multi-species Summary

As a brief summary of the plots above, Table 4-6 presents information about the ion cyclotron frequency and the frequency of the observed instability for each of the species tested.

Table 4-7: Summary of the plots in Section 4.3.3. For each case and each species the cyclotron frequency and the frequency of the observed instability are presented.

Gas Species	Case A f_{ci}	Case A wave frequency	Case B f_{ci}	Case B wave frequency
He	33.2 kHz	.35 f_{ci}	22.8 kHz	1.3 f_{ci}
N	17.3 kHz	.48 f_{ci}	10.8 kHz	1.1 f_{ci}
Ne	14.6 kHz	.41 f_{ci}	9.1 kHz	1.6 f_{ci}
Ar	10.3 kHz	.46 f_{ci}	6.4 kHz	1.6 f_{ci}

The summary data in Table 4-6 shows two main results. First, range of ion cyclotron frequencies is vast, with the lowest ion cyclotron frequency being a factor of 5 smaller than the highest frequency. Most importantly, the frequencies of the dominant instabilities in Case A and Case B clearly fall into two distinct categories, with the Case A instabilities ranging from .35 to .48 f_{ci} , and the instabilities for Case B ranging from 1.1 to 1.6 f_{ci} . As noted previously, these wave modes are distinct, with an abrupt transition between the two modes.

The goal of the multi-species studies was to determine if the physical processes observed in the early, Helium based experiments, and the knowledge gained in performing them, could be leveraged to gain insight into the capabilities of ALEXIS after the transition to the new ALEXIS configuration. The graphs show that the instability results observed in the hot filament plasma source, helium plasma configuration of ALEXIS can be qualitatively scaled to the RF plasma source, argon plasma configuration of ALEXIS. It is acknowledged that differences in the electron density, electron temperatures, and plasma potential profiles will alter the results among the species, however, the experimental results are suggestive of common mechanisms at work in all four cases.

It should be noted that the inclusion of Nitrogen owes more to its availability in the ALEXIS lab than to an ideal physics argument. The challenge of Nitrogen is, obviously, that it is difficult to assess what the exact species is ionized. Nitrogen is diatomic, and as a gas is always N_2 . This makes it difficult to completely justify the treatment of a Nitrogen plasma as only being monoatomic.

4.4 Experiments in Argon – RF configuration

4.4.1 Introduction

For this final section of experiments, the focus will be on the experimental measurements of flows in the ALEXIS device, and the plasma response to these flows. All of these studies are performed using the upgraded ALEXIS-RF configuration.

First, the new experimental configuration of ALEXIS has led to a new operational regime for the device. These new parameters are summarized below, in Table 4-8. Electron densities are about a factor of 3 to 5 higher than in the previous configuration with electron temperatures about a factor of 2 lower. The plasma is operated at a higher magnetic field strength (300 Gauss as compared to 90 Gauss previously) in order to keep the gyroradius of Argon comparable to that of Helium for the older experiments. It is noted that RF plasma operations have also required operation at a slightly higher fill pressure, $p \sim 1$ mTorr, than in the previous experiments.

For the RF-generated plasmas, the plasma density profile remains hollow. The peak in the density profile is collocated with the radial location of the antenna (at approximately $r = 2$). It is believed that the ionization rate is a maximum at the location of the antenna, and falls off rapidly with distance.

Table 4-8: Operating conditions in ALEXIS – RF configuration

Plasma species	Argon ($A = 40$)
Peak magnetic field (B_{max})	1000 Gauss
Operating magnetic field (B_{typ})	300 – 400 Gauss
Plasma density (n_e)	$0.5 - 5.0 \times 10^{16} \text{ m}^{-3}$
Electron temperature (T_e)	3 - 5 eV
Ion temperature (T_i)	< 0.1 eV

Operating pressure	0.5 – 1.0 mTorr
RF power (P_{rf})	30 – 150 W
Ion cyclotron frequency (f_{ci})	~11 to 15 kHz
Ion plasma frequency (f_{pi})	~5 MHz
Ion-neutral collision mean free path	6 cm
Ion gyroradius/Chamber radius (ρ_i/a)	~0.1

In addition to the new ALEXIS plasma source configuration, the final experiments were also performed using a new two-ring configuration that is described below in Section 4.4.2. The following section of this chapter will present results on using the new ring configuration to modify the potential structure of the plasma. Then, the impact of the rings on the density, flow structure, and the instabilities present in the plasma will be presented.

4.4.2 Modified Potential Structure

The rings used in this configuration are two concentric aluminum rings mounted on a Macor block that rests in the custom six-way box at the end of ALEXIS. The inner ring is Ring 1, and the outer ring is Ring 2. . Ring 1 extends radially from $r = 0.42$ cm to $r = 1.11$ cm. Ring 2 extends radially from $r = 1.27$ to $r = 1.91$ cm.

Figure 4-30 shows the design of the Macor block and the placement of the ring electrodes. The two rings are electrically isolated so they can be biased independently of each other. The rings are located at the same location behind Port 7 (at $z = 155$ cm) as the previous ring electrode designs.

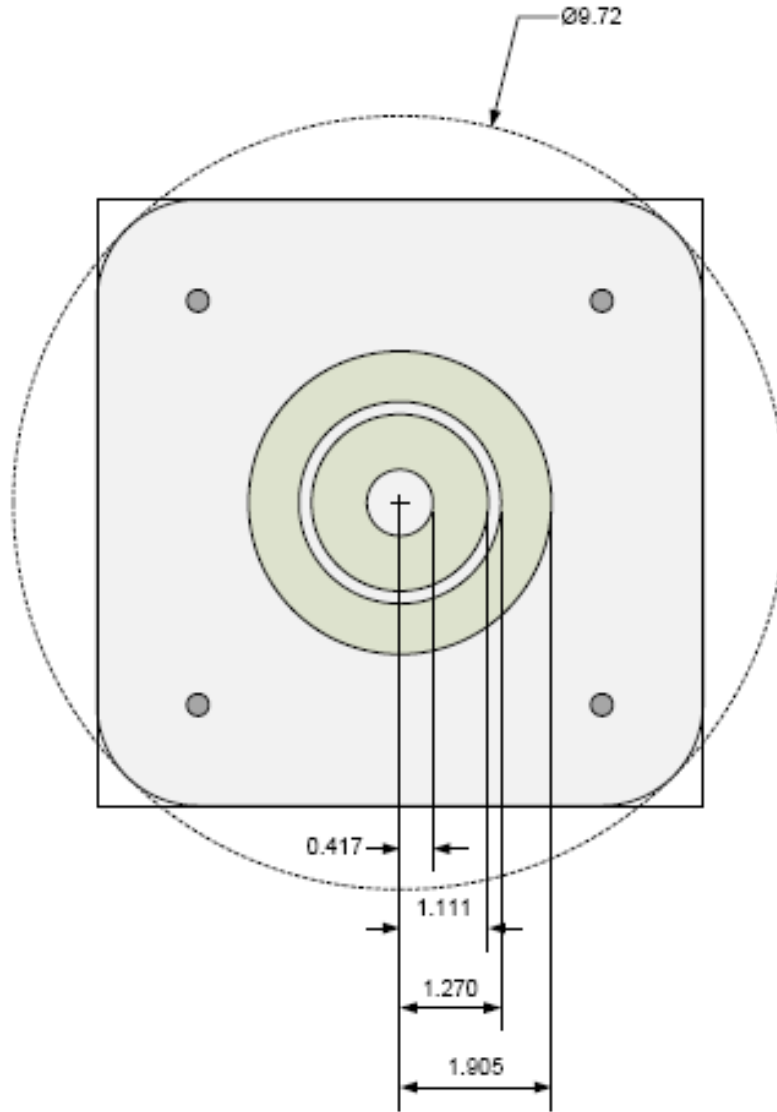


Figure 4-31: Schematic diagram of the rings used to modify the potential structure in ALEXIS. The inner ring is Ring 1, and the outer ring is Ring 2. Both rings are made of Aluminum and mounted on Macor. All dimensions are in cm.

For the experimental results presented in the next several sections, a comparison will be made between the two different rings configurations described in the previous section. For all the data that will be presented, Case A will represent a bias voltage of -50 V on Ring 1 and -50 V on Ring 2. Case B will represent a bias voltage of -50 V on Ring 1 and +30 V on Ring 2.

To measure the effect of the ring bias voltage on the plasma potential profile, an emissive probe is scanned radially across the plasma along the plasma mid-plane at Port 6 ($z = 127$ cm), upstream from the ring electrodes. An electric field is then computed from the plasma potential profile. Figure 4-32 shows the measured plasma potentials for two different Ring 2 biases discussed here. The calculated electric fields for the two cases are shown in Figure 4-33. For all three plots, the line with red circles has Ring 2 biased at -50 V (Case A), and the line with the blue diamonds has Ring 2 biased at $+30$ V (Case B).

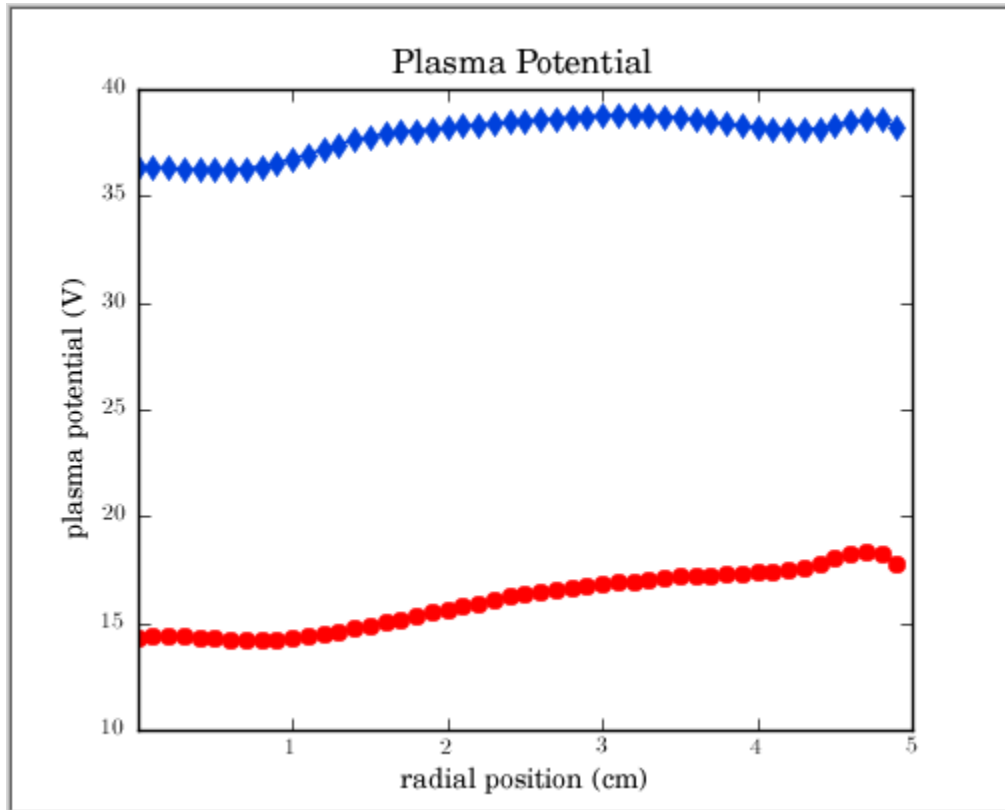


Figure 4-32: Measured plasma potential profiles in ALEXIS. The horizontal axis is the radial location of the probe in cm, and the vertical axis is the plasma potential in Volts. The blue diamond markers are for the $+30$ V bias, and the red circle markers are for the -50 V bias.

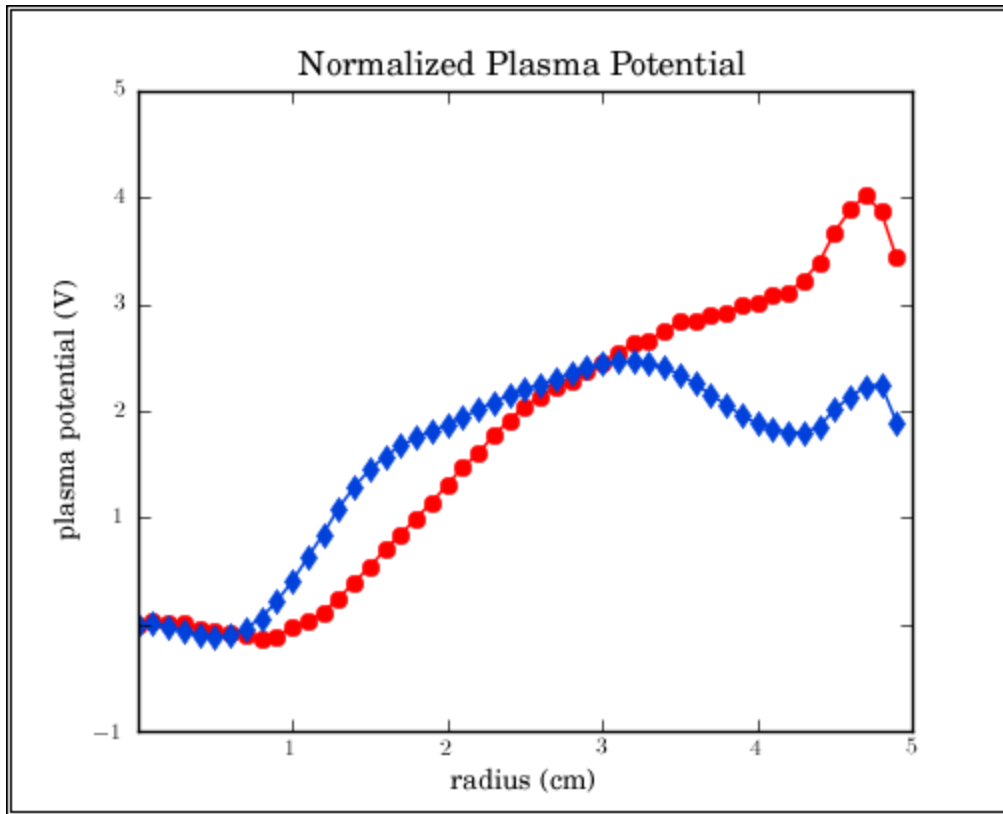


Figure 4-33: Normalized measured plasma potential profiles in ALEXIS. The horizontal axis is the radial location of the probe in cm, and the vertical axis is the normalized plasma potential in Volts. The blue diamond markers are for the +30V bias, and the red circle markers are for the -50V bias.

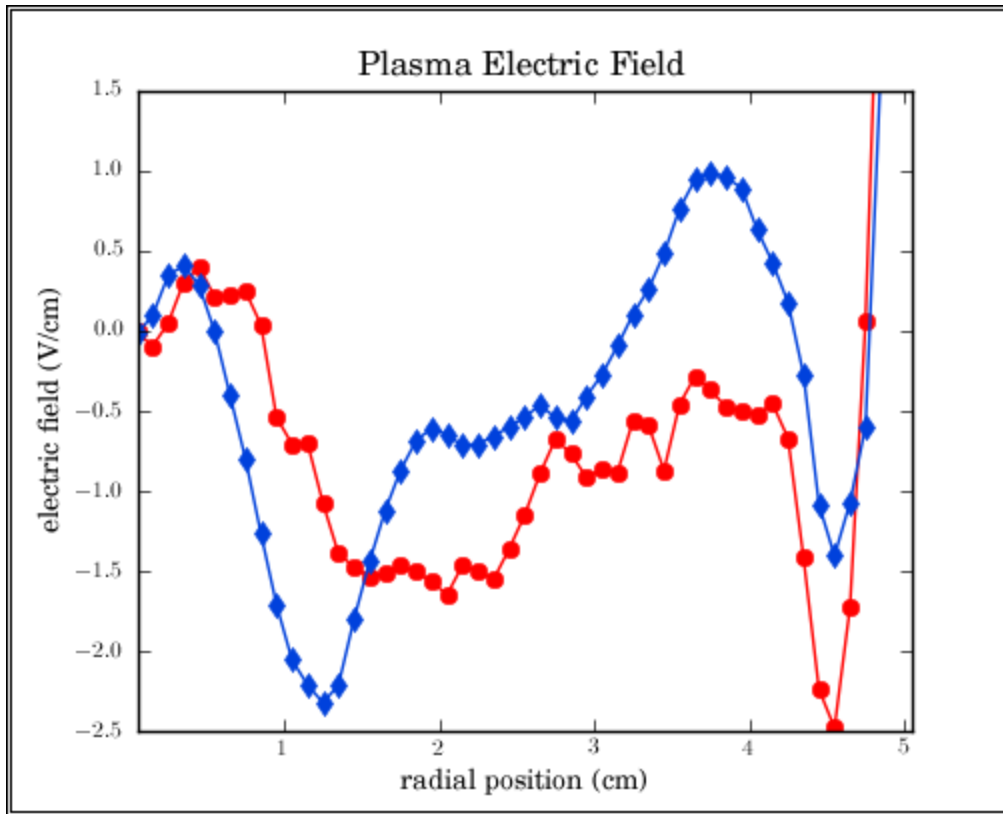


Figure 4-34: Calculated radial electric fields in ALEXIS. The horizontal axis is the radial location of the probe in cm, and the vertical axis is the electric field strength in V/cm. The blue diamond markers are for the +30V bias, and the red circle markers are for the -50V bias.

Figure 4-32 shows that biasing Ring 2 clearly has an effect on the dc offset level of the plasma in a manner similar to what was observed in the ALEXIS-filament configuration shown in Figure 4-3 and Figure 4-4. Figure 4-34 shows that changing the bias applied to Ring 2 also modifies the spatial structure of the radial electric field. It is noted that with this two ring configuration, changing the bias voltage on Ring 2 causes a large potential difference at the boundary between the two rings (near $r = 1.2$ cm) which causes an enhancement in the strength of the radially inward electric field by about 60%. However, for larger radii ($r > 3$ cm), this also leads to a change in the direction of the electric field from radially inward (negative) to radially outward (positive).

This is quite similar to the observations reported in Figure 4-3 which shows a localized enhancement of the radially inward electric field on the inner part of the plasma column and the formation of a radially outward electric field at the outer part of the plasma column. Additionally, similar to what is shown in Figure 4-4, this change appears to be correlated to the boundary between the two sets of biased electrodes.

To determine the axial electric field, the current collected by the rings is recorded for the different ring biases. For the two cases shown here, the current collected by Ring 2 is 55.8 mA for the +30 V bias case and the collected current is -7.7 mA for the -50V bias case. Here, a positive current corresponds to a net collection of electrons and a negative current corresponds to a net collection of ions. Using the collected current and the area of the ring, the current density along the column can be calculated. This is then entered into the equation

$$E = \frac{j}{\mu_e n_e e}$$

Where j is the current density and μ_e is given by

$$\mu_e = \frac{e D_e}{k_B T_e}$$

With D_e being the electron diffusivity, which, for a weakly ionized plasma, is

$$D_e = \frac{k_B T_e}{m_e \nu}$$

For the two cases presented above, the axial electric fields are calculated to be -0.1 V/m for the -50 V bias case, and +0.4 V/m for the +30 V bias case. The axial electric fields, calculated for a range of -50V to +50 V on Ring 2 are plotted in Figure 4-35.

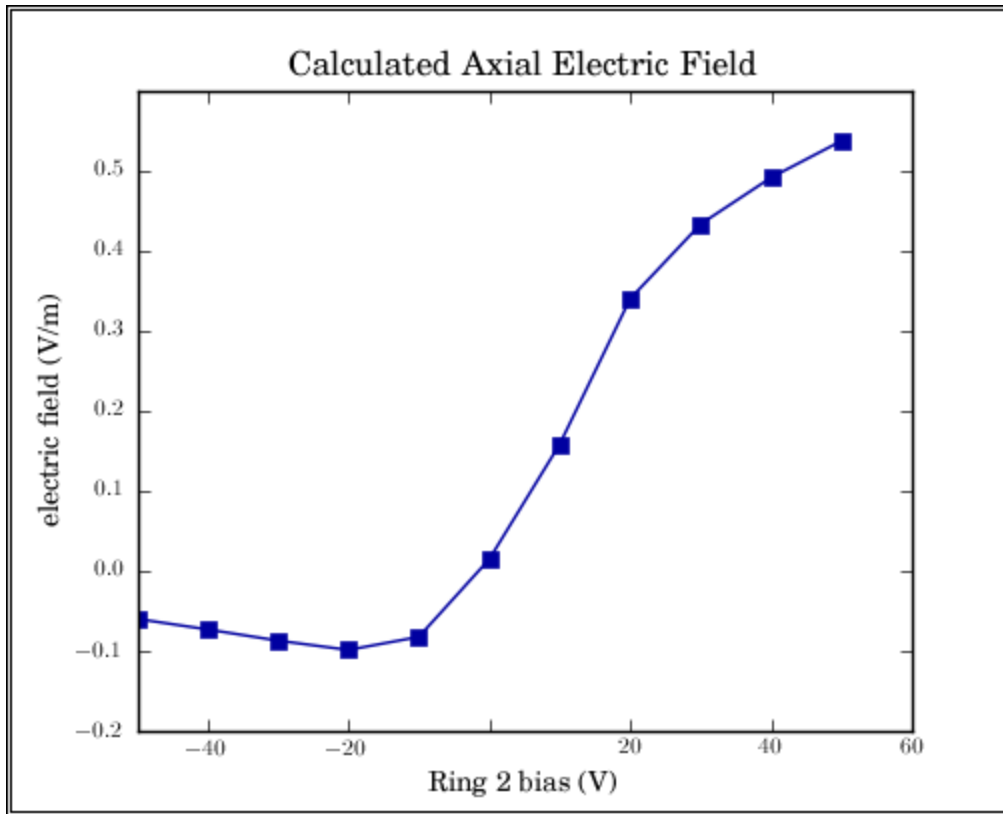


Figure 4-35: Electric fields calculated from the current collected on Ring 2. The horizontal axis corresponds to the voltage applied to Ring 2, and the vertical axis is the calculated axial electric field.

In comparing these cases to the Helium experiments in section 4.2, it can be seen that the electric fields presented here match, in structure, the electric fields in Cases A and B. While it is difficult to make a direct comparison because the source, species, and rings are all different, it is clear in both the Helium/filament experiments and in the Argon/rf data just presented that the structure of the electric field can be successfully modified. In the next section, the response of the plasma to the two plasma potential structures will be presented.

4.4.3 Calculated Flow Velocities

This section will discuss the calculated ion flow velocities perpendicular and parallel to the background magnetic field. The perpendicular flows will be calculated using the potential measurements presented in the previous section, and the parallel flows will be calculated from the current collected on Ring 2.

Using the measured values for plasma potential and electron density, the azimuthal flow velocity profiles can be calculated using the previously derived equation:

$$v_{\perp}(r) = \frac{r\Omega_{ci}}{2} \left(-1 + \sqrt{1 - \frac{4m_i}{r e B_0^2} \left(E_r - \frac{k_B T_i}{e n_i} \frac{\partial n_i}{\partial r} \right)} \right) \quad (4-6)$$

To calculate the perpendicular flow velocity, the density had to be measured. The results of that measurement are presented in Figure 4-36. The calculated flow profiles for Case A and Case B are shown in Figure 4-37 and Figure 4-38, respectively. Plotted in each figure is the radial profile of the azimuthal velocity calculated using the standard $E \times B$ drift velocity ($v_E = -E \times B / B^2$) compared against the cylindrically corrected azimuthal velocity, as given in Equation (4-6). The calculations clearly show that the geometric effects are important for the ALEXIS experimental configuration and need to be taken into account when determining the azimuthal velocity.

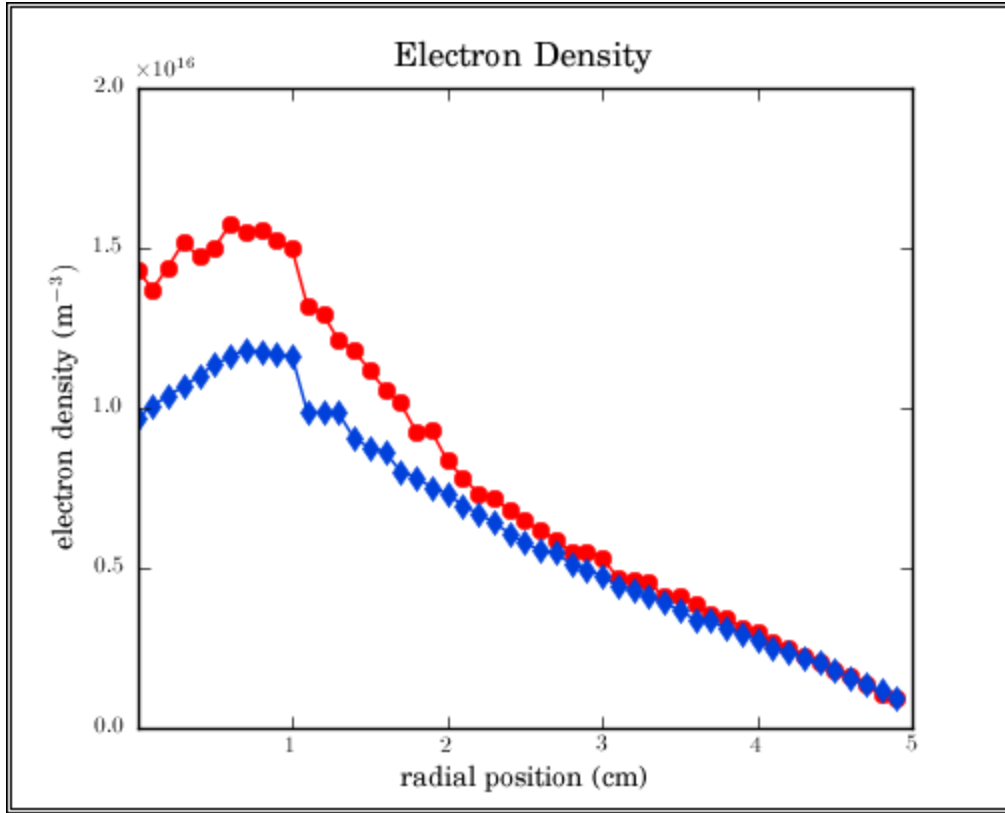


Figure 4-36: Density profiles for Case A (red circles) and Case B (blue diamonds).

Additionally, as discussed in Section 4.4.2, when Ring 2 is positively biased, there is a significant parallel current and, consequently, parallel electric field, that arises in ALEXIS. To determine the flow that might arise from the axial electric field, the bias voltage on ring 2 was increased in 10 V increments from -50 V to +50 V. For each bias the current collected was recorded, and the formalism introduced in Section 4.4.2 is followed. The calculated axial electric fields are shown in Figure 4-40.

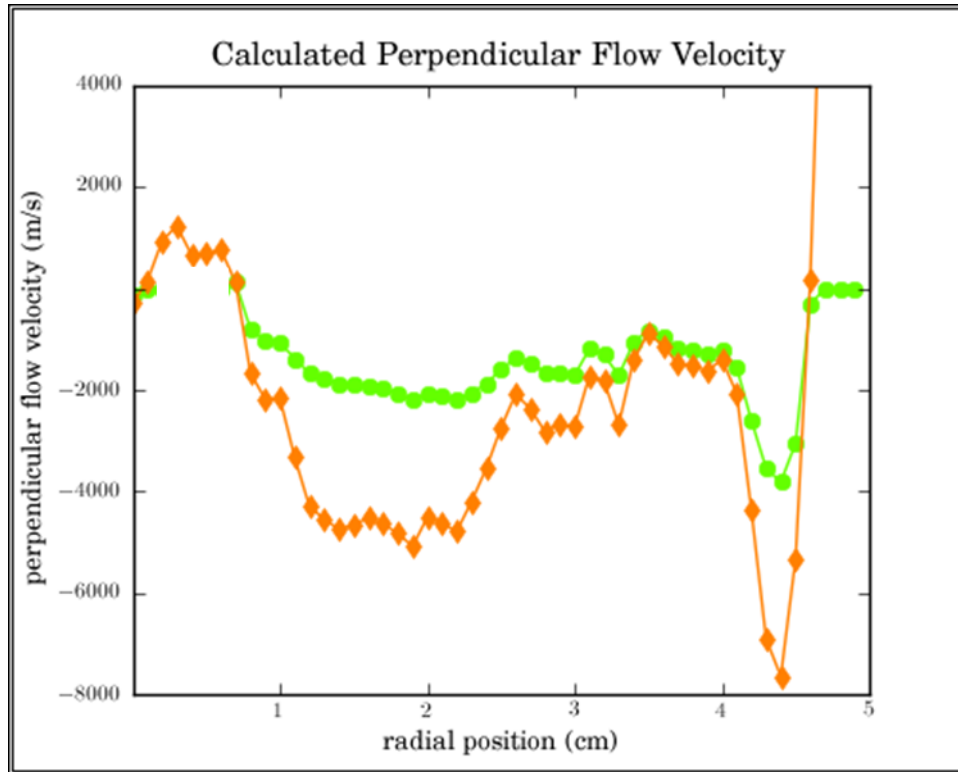


Figure 4-37: Velocities calculated using the measured plasma parameters for Case A (-50 V bias). The orange diamond markers are calculated using the slab $E \times B$ model, and the green circle markers are calculated using the cylindrically corrected $E \times B$ model.

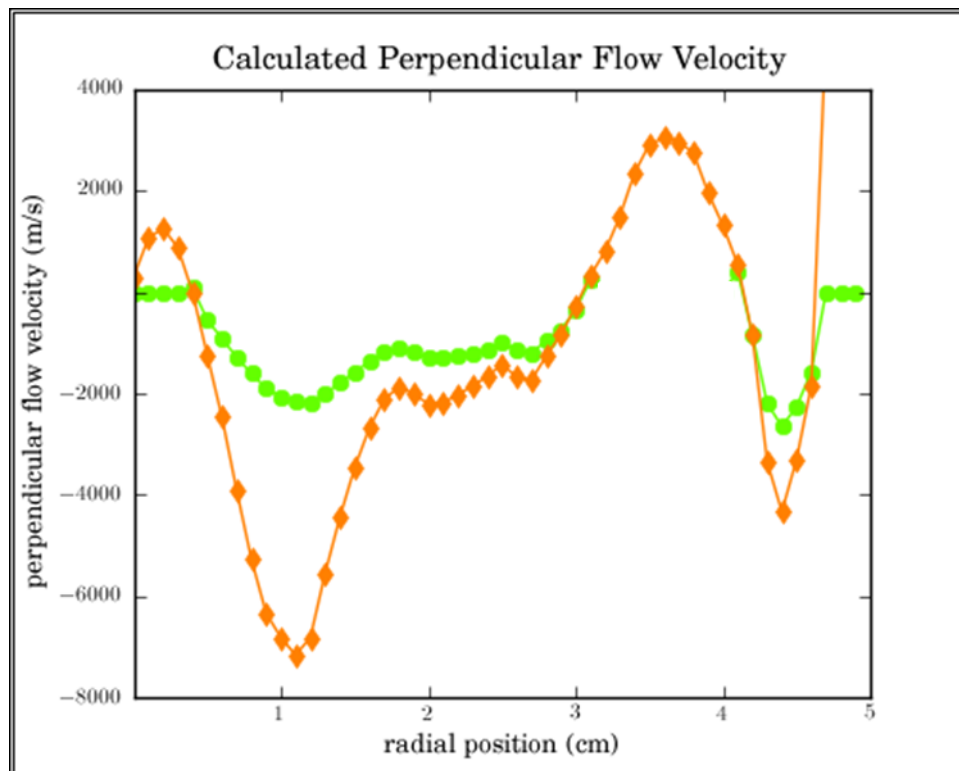


Figure 4-38: Velocities calculated using the measured plasma parameters for Case B (+30 V bias). The orange diamond markers are calculated using the slab $E \times B$ model, and the green circle markers are calculated using the cylindrically corrected $E \times B$ model.

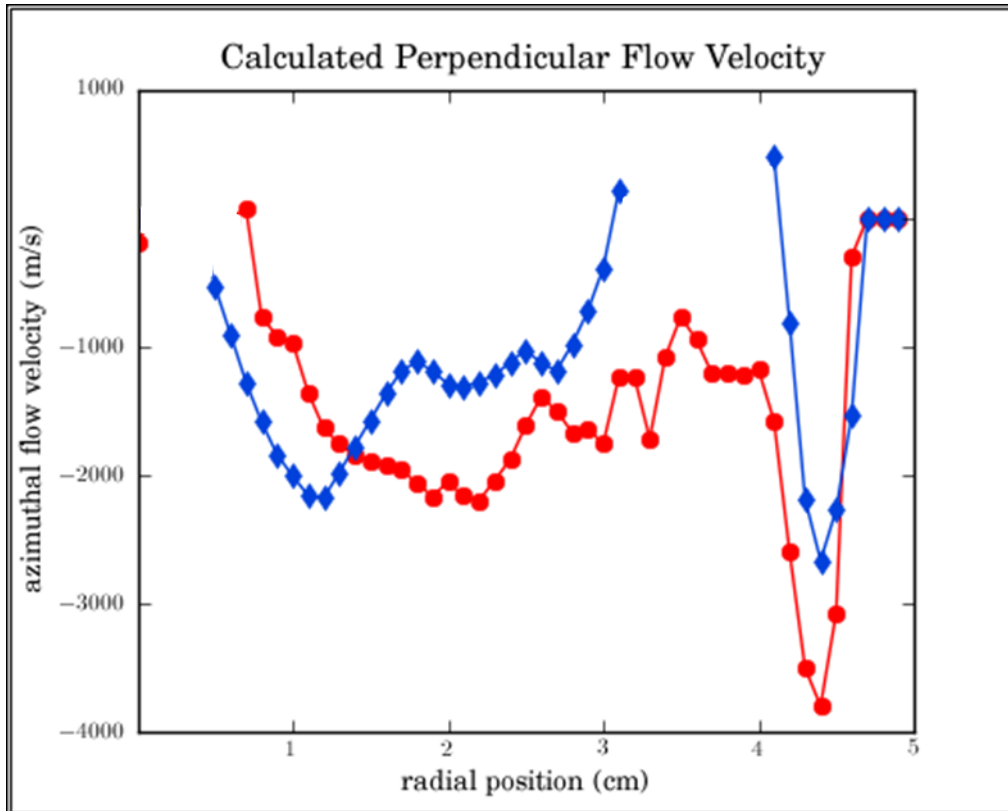


Figure 4-39: Azimuthal flow velocities calculated using the measured plasma parameters for Case A (-50 V bias) (red circles), and Case B (+30 V) (blue diamonds).

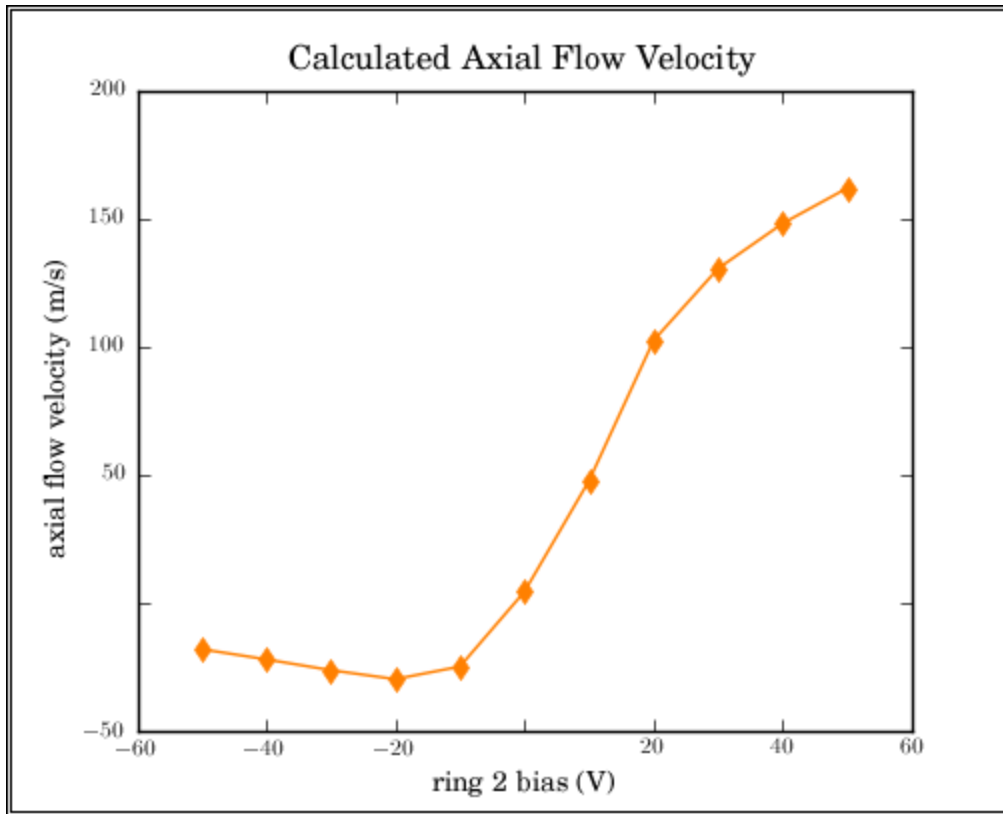


Figure 4-40: Calculated axial ion velocities as a function of bias voltage applied to Ring 2.

Comparing Figure 4-39 and Figure 4-40, it can be seen that the most significant change is in the axial flow velocities. Figure 4-39 shows some change to the azimuthal flow structure, but the magnitude, especially in the center of the column, is similar in magnitude between the two cases. Conversely, for the axial flow velocity, the calculated velocities for Case A (-50 V) and Case B (+30 V) are significantly different. It should be noted again that the axial velocities are only valid for the location of Ring 2.

4.4.4 Plasma Response to the Potential Structure Modification

This section will compare the electrostatic fluctuations as measured by an electrically floating Langmuir probe. Specifically, the different instability activity in Case A and Case B will be presented.

To measure the electrostatic fluctuations a single tipped Langmuir probe located at Port 6 is scanned radially across the plasma column in 2 mm increments. At each position, the floating potential of the plasma is recorded. A Fourier Transform of the floating potential measurements is taken in order to determine the frequency spectrum of the instabilities. For these measurements, the data acquisition system was operated at a data rate of 100 kHz, allowing frequencies up to 50 kHz to be identified in the resulting Fourier spectrum.

Experimental measurements presented in Figure 4-41 and Figure 4-43 show that there is a significant change in the frequency and radial structure of the plasma between Case A and Case B. In Case A ($V_2 = -50$ V), a low frequency instability is observed in the plasma with a peak at approximately 0.5 times the ion cyclotron frequency. This instability has a wide frequency bandwidth with $\Delta f \sim 2$ kHz. Spatially, this feature extends over a broad region of the plasma extending from near the center of the plasma column ($r = 0$ cm) out to the edge of the plasma column at ($r = 5$ cm).

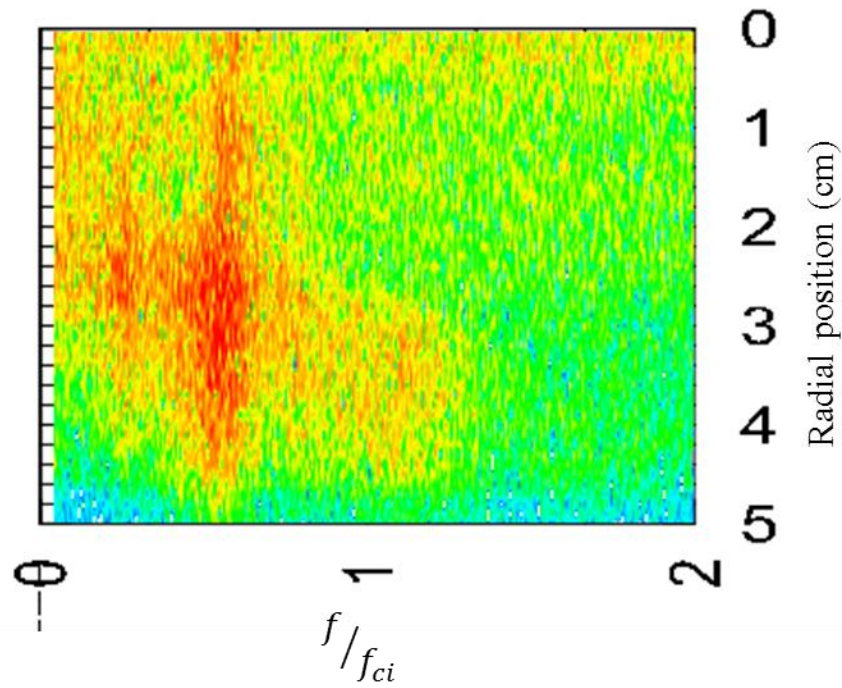


Figure 4-41: Fourier spectrum of floating potential fluctuations for Case A (Ring 1 bias = - 50 V, Ring 2 bias = - 50 V). The horizontal axis is the frequency, normalized to the ion cyclotron frequency. The vertical axis represents the radial position in cm. The color represents the intensity of the signal (in a.u.). The figure shows a broad, low frequency (~5 kHz) instability.

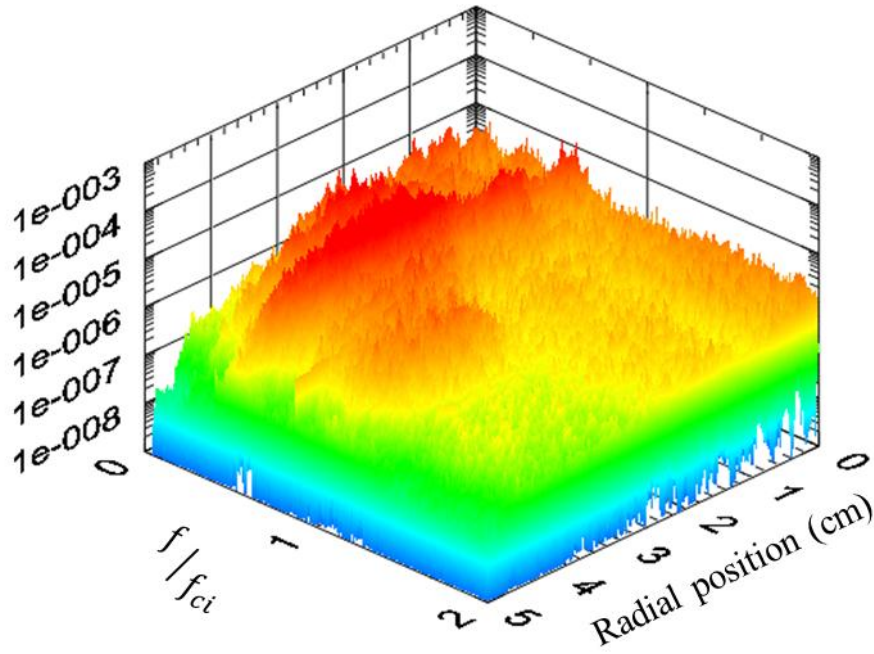


Figure 4-42: Fourier spectrum of floating potential fluctuations for Case A (Ring 1 voltage is -50 V, Ring 2 Voltage is - 50 V). The vertical axis and the color represent the intensity of the signal (in a.u.). The left axis is frequency (normalized to the ion cyclotron frequency) and the right axis is radial position.

This instability is very different from the feature that appears in the plasma column for Case B ($V_2 = +30$ V). This structure is shown in Figure 4-43 and Figure 4-44, which is at approximately the ion cyclotron frequency, is peaked in the center of the column, and is much narrower in frequency space.

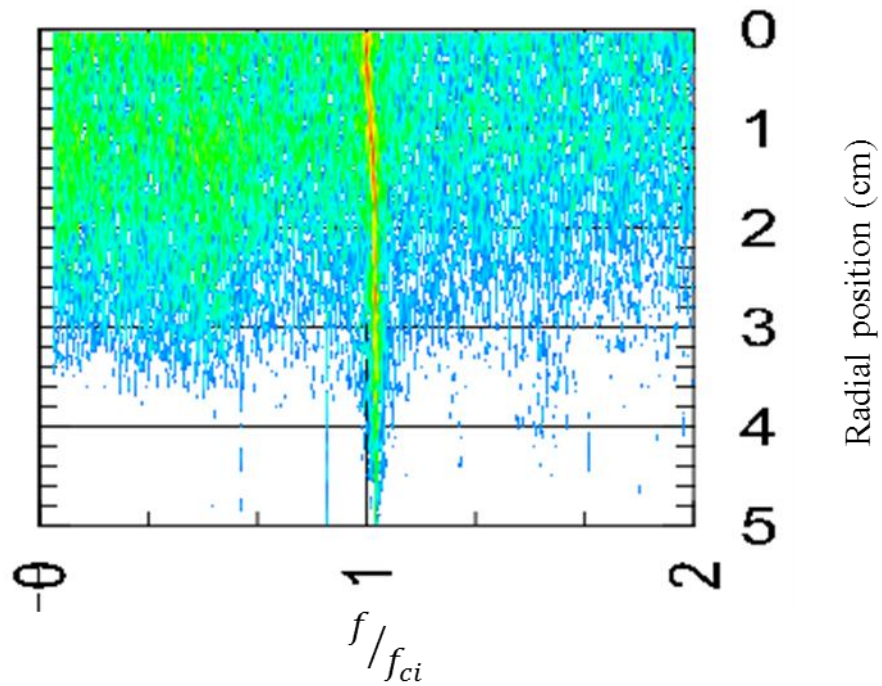


Figure 4-43: Fourier spectrum of floating potential fluctuations for Case B (Ring 1 bias = -50 V, Ring 2 bias = +30 V). The horizontal axis is the frequency, normalized to the ion cyclotron frequency. The vertical axis represents the radial position in cm. The color represents the intensity of the signal (in a.u.). The figure shows a localized, narrow instability at approximately 10 kHz.

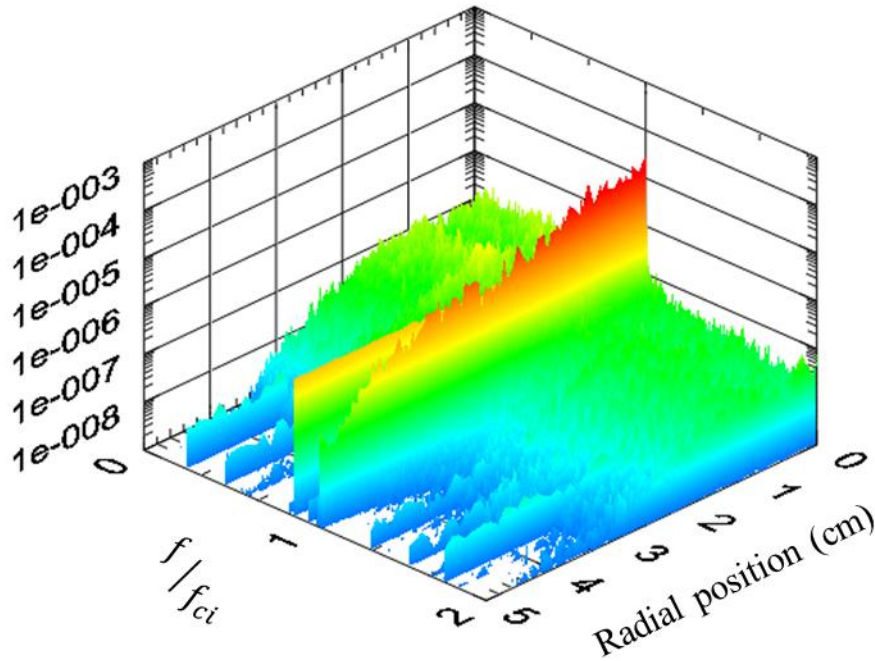


Figure 4-44: Fourier spectrum of floating potential fluctuations for Case B (Ring 1 voltage is -50 V, Ring 2 voltage = +30 V). The vertical axis and the color represent the intensity of the signal (in a.u.). The left axis is frequency (normalized to the ion cyclotron frequency) and the right axis is radial position.

This section has shown that the instability activity is significantly modified by changing the bias on Ring 2. The next section will identify the instabilities.

4.4.5 Characterizing the observed electrostatic instability

To classify the instability observed with the rings positively biased (Case B), the current collected by the biased ring (Ring 2) was measured as a function of the bias applied to the ring. Additionally, the amplitude of the electrostatic fluctuations measured at $r = 1$ cm and within a

frequency range of $\pm 10\%$ of the ion cyclotron frequency ($12 \text{ kHz} \pm 1.2 \text{ kHz}$) was recorded for each ring bias. The results of these measurements are plotted in Figure 4-45. The current collected by Ring 2 is normalized using the maximum value of the measured current, 69.2 mA.

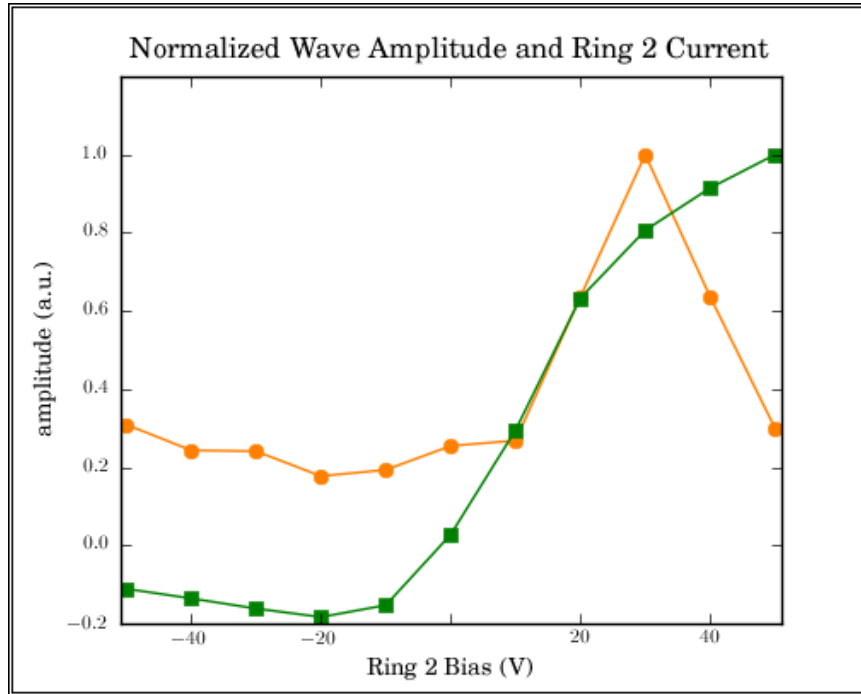


Figure 4-45: Comparison between the normalized wave amplitude (orange diamonds) and the normalized current collected on Ring 2 (green squares) as a function of Ring 2 bias voltage.

The observance of the wave correlates to the increase in parallel electron current. However, the measured amplitude decreases for the +40V and +50V cases, while the collected current continues to increase. The onset of the instability indicates a parallel current driven instability, such as the Current Driven Ion Cyclotron Instability (CDICI), first described theoretically by Drummond and Rosenbluth²⁹, and first observed in the lab by Motley and D'Angelo²⁸.

The physical mechanism behind the instability is that an electron current flows parallel to the background magnetic field. When the electron drift velocity is large enough, with respect to

the ion thermal velocity, the CDICI can be excited.⁶⁴ The thermal velocity is calculated assuming 0.05 eV ions, and the electron drift velocity is calculated using the area of Ring 2 to determine the current density. The results of these calculations are plotted in Figure 4-46.

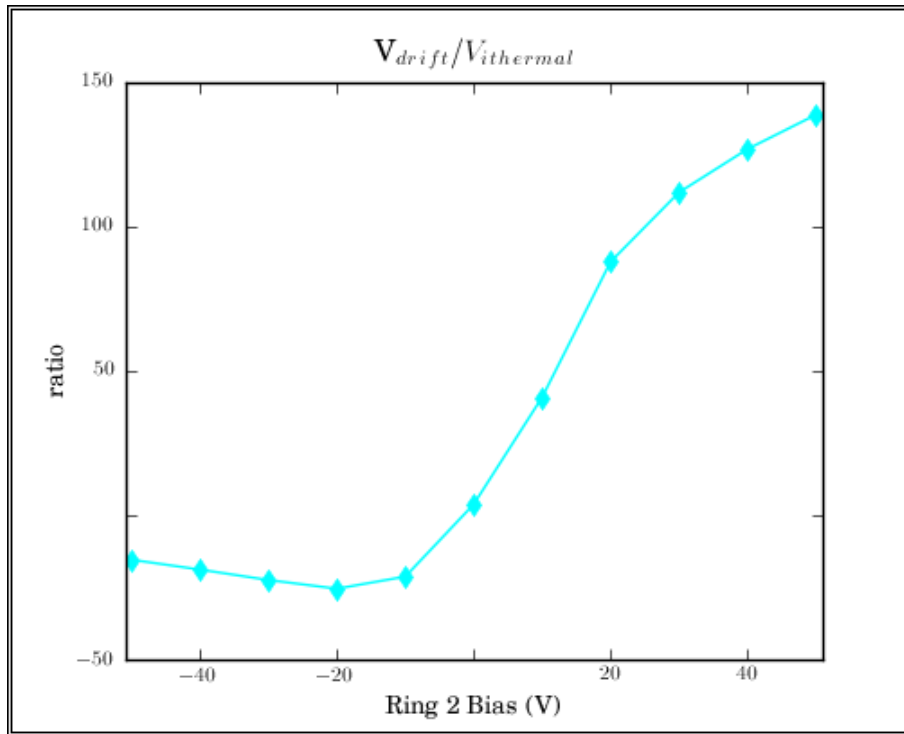


Figure 4-46: The ratio of the electron drift velocity and the ion thermal velocity as a function of the bias applied to Ring 2.

It has been observed that the critical value of the ratio of the electron drift velocity and the ion thermal speed is ~ 10 .²⁸ That is, the electron drift velocity must be ten times the ion thermal velocity to drive the instability. Most work to study the CDICI has been performed in Q-machines⁶⁴, where $T_i \approx T_e$. Kindel and Kennel⁶⁶ showed that even for high $T_e > T_i$, the critical electron drift velocity increased only weakly with T_e/T_i . Later, works by Ganguli, et al.,⁴⁷ showed that a localized transverse electric field (as measured in ALEXIS) actually reduces the critical electron drift velocity necessary for the instability to become unstable. Measurements in

ALEXIS show that the instability is observed when the ratio of the electron drift velocity to the ion thermal velocity reaches a value of almost 90.

While this threshold value is a necessary condition to the instability to be driven by the parallel current, it is not a sufficient condition. Drummond and Rosenbluth²⁹ use a kinetic theory to describe the interaction of the electrons with the CDICI. Their derivation shows that for the electrons to have sufficient energy to drive the instability, the peak of the electron distribution function (in velocity space) must exceed the velocity of the CDICI. That is, the phase velocity of the electrostatic ion cyclotron wave must lie on the positive slope of the electron distribution function to ensure instability due to electron Landau growth. The phase velocity of the wave is given by $v_{phase} = \omega/k_{\parallel}$. This gives the condition that

$$v_{De} \geq \omega/k_{\parallel} \tag{4-7}$$

Where v_{De} is the electron drift velocity, ω is the frequency of the instability, and k_{\parallel} is the parallel wave number of the instability. Equation (4-7) can be re-written to give a measurable, testable condition,

$$k_{\parallel}v_{De}/\omega \geq 1 \tag{4-8}$$

The parallel wave number and frequency were measured, and the electron drift velocity was calculated as before. The measured values for the parallel wave number are shown as a function of the bias applied to Ring 2 in Figure 4-47. The results of this analysis are presented below in Figure 4-48.

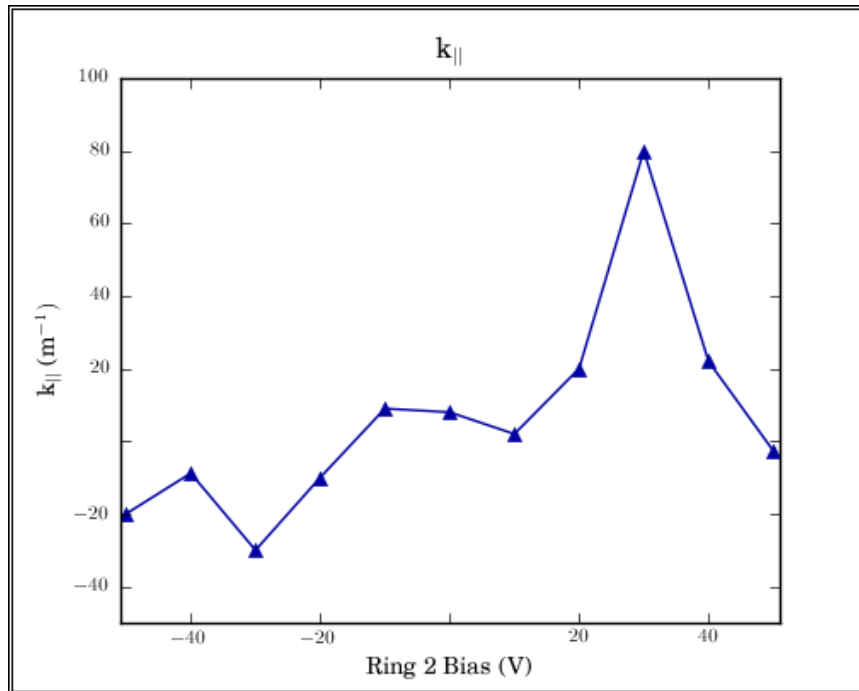


Figure 4-47: Measured values of the parallel wave number as a function of the bias applied to Ring 2.

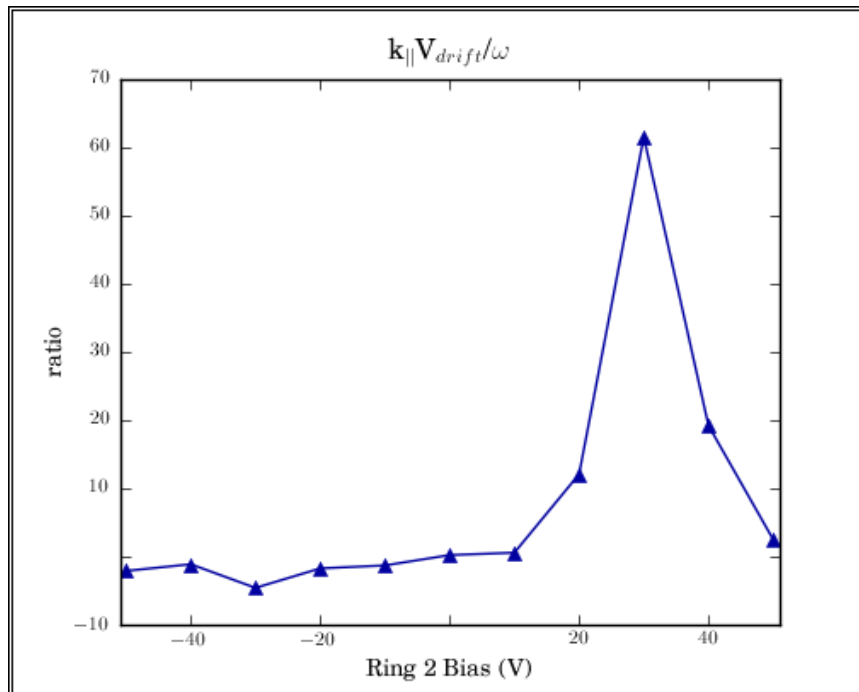


Figure 4-48: The values of the ratio of the parallel wave number multiplied by the electron drift velocity to the wave frequency as a function of the bias applied to Ring 2.

While the calculated electron drift velocity continues to increase for increasing bias voltages, the parallel wave numbers decrease for the two cases of largest bias. This ratio is normalized and plotted with the normalized wave amplitude in Figure 4-49.

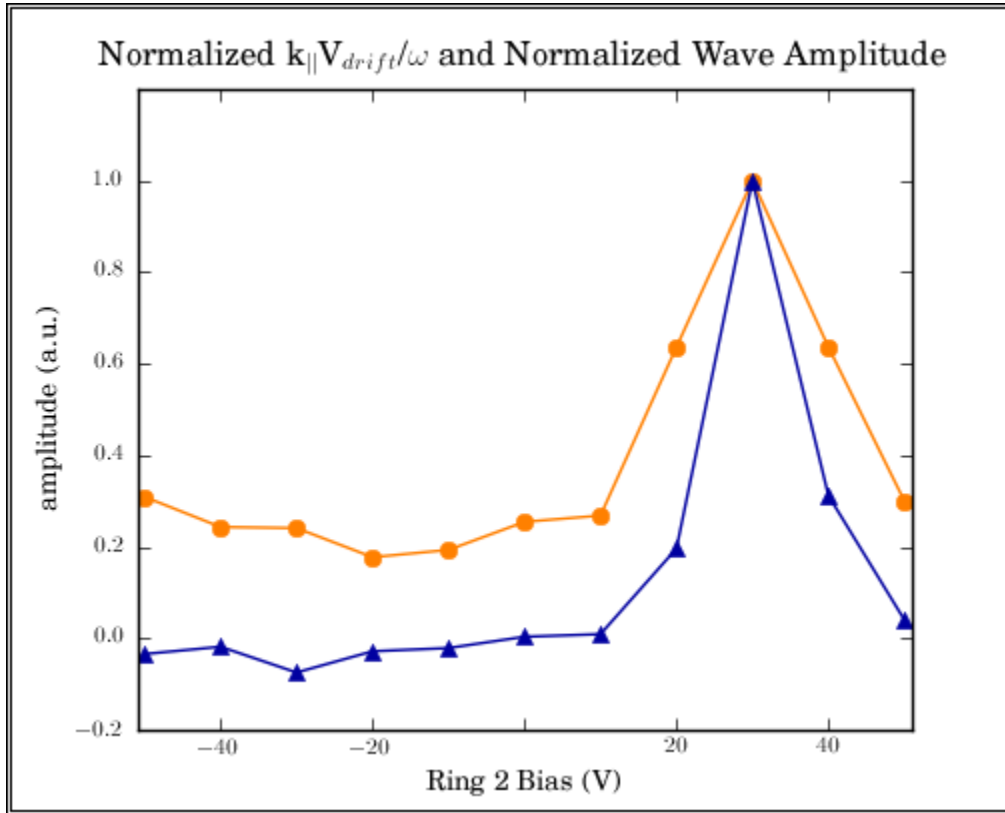


Figure 4-49: Normalized ratio of the parallel wave number multiplied by the electron drift velocity to the wave frequency (blue triangles) and normalized wave amplitude (orange circles) plotted versus bias voltage applied to Ring 2.

Figure 4-49 indicates that the observed instability behaves as predicted by existing theory for the CDICI. Not only does the onset of the instability correspond with the velocity threshold observed by Motley and D'Angelo²⁸, but the decrease in the observed instability also corresponds with the kinetic derivation of Drummond and Rosenbluth²⁹. Previous works that have studied CDICI's have done so primarily in Q-machines.⁶⁴ Also, most previous works limited their studies to the onset of the instability or its propagation.⁶⁴ The work presented here is unique in that it shows both the onset and the decrease in the driven instability amplitude in a

radio frequency based laboratory plasma. Earlier studies in ALEXIS with the filament based plasma source did not study CDICI's, and instead focused on instabilities driven by transverse flow shear.^{56,57}

At this point, the model developed in Chapter 2 will be employed to compare the observed wave behavior with the predictions of the computational model. As noted in Chapter 2, the current model assumes a uniform electric field. To accommodate this, the data presented earlier in this section will be used to determine the input parameters for the model. Also, the parameters will be chosen based on the plasma parameters at the peak of the instability, i.e. Ring 2 biased at +30 V. Those parameters are summarized in Table 4-9.

Table 4-9: Parameters used in the computational model discussed in this section.

Parameter	Value
Species	Argon
Magnetic Field Strength	300 Gauss
Electron Temperature	3 eV
Ion Temperature	0.035 eV
Electron Drift Velocity	55,000 m/s

The output of the computational model is plotted in Figure 4-50.

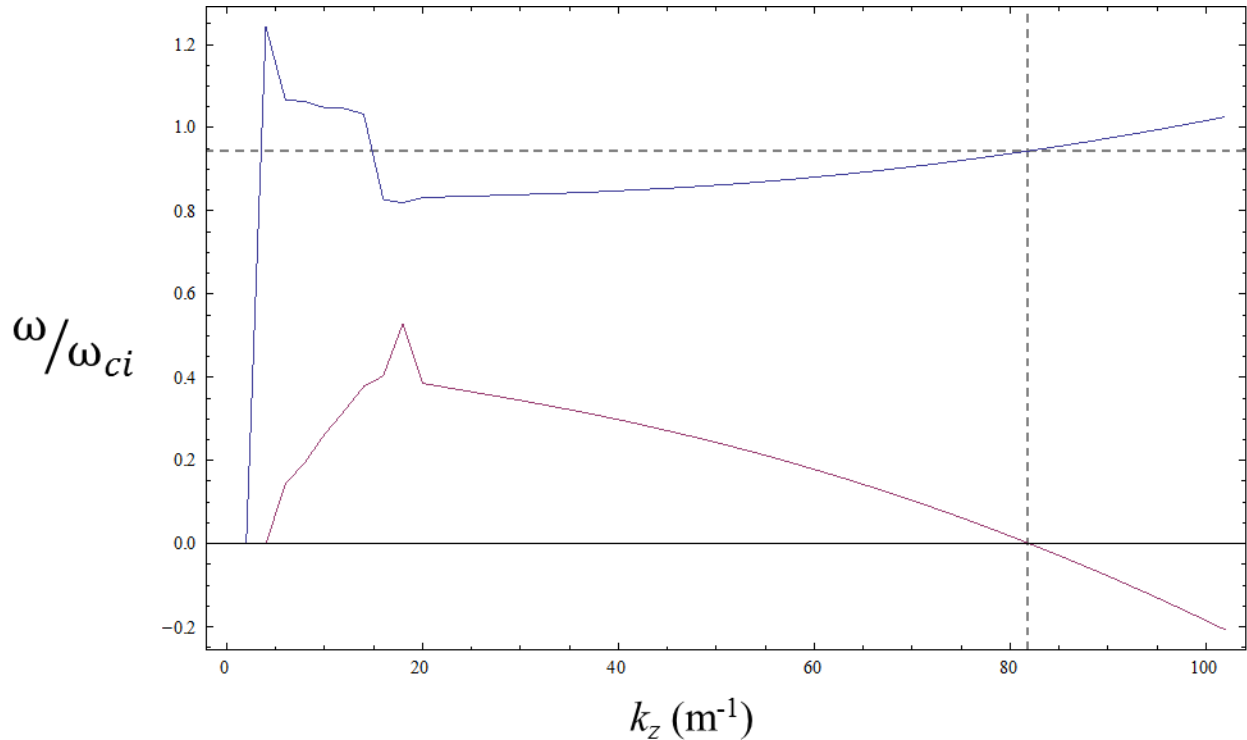


Figure 4-50: Output from the computational code using experimentally measured input parameters. The blue line is the frequency measured in the lab frame, and the red line is the imaginary component of the frequency. The vertical dashed line shows the parallel wavelength that corresponds to marginal stability. The horizontal dashed line shows the intersection of the vertical dashed line with the calculated frequency.

Figure 4-50 shows the output from the computational code using experimentally measured input parameters. The blue line is the frequency measured in the lab frame, and the red line is the imaginary component of the frequency. The vertical dashed line shows the parallel wavelength that corresponds to marginal stability. The horizontal dashed line shows the intersection of the vertical dashed line with the calculated frequency. The model shows the parallel wavelength that corresponds to the marginal stability (i.e., the imaginary component of ω) is approximately 82 m^{-1} . Experimentally, the parallel wave number at the peak instability amplitude is measured to be 80 m^{-1} . These two values are in very good agreement. The computational model predicts that with a parallel wave number of 82 m^{-1} the observed frequency should be at approximately $0.95 * \omega_{ci}$. At $r = 1$, where the peak of the instability is

experimentally observed, the observed frequency is at approximately the ion cyclotron frequency. This again is very good agreement between the computational model and the experimental data. Perhaps most importantly, the computational model justifies the observation in ALEXIS of the CDICI at a frequency lower than typical values reported in previous experiments.

5 Discussion

5.1 Summary

The work of this dissertation involved experimental studies of plasma potential structure and flow modification in a weakly-ionized laboratory plasma. The motivation was to study the plasma response to imposed radial electric fields. The experimental work was performed in the Auburn Linear Experiment for Instability Studies (ALEXIS) at Auburn University.

This section presents a summary of the experiments performed for this dissertation. There were three distinct experiments performed for this work. Each experiment will be briefly reviewed and the important results enumerated in the following paragraphs.

The first experimental studies were performed in Helium with a filament based plasma source. This experiment showed that by using a set of four concentric rings at the end of the plasma column opposite the plasma source, the potential structure of the plasma could be significantly modified. Measurements of the electrostatic fluctuations in the plasma showed that the naturally present wave-mode was suppressed in the presence of a positive radial electric field. This wave mode was determined to be the Inhomogeneous Energy Density Driven Instability, and was consistent with the theory presented in Chapter 2. This result was unique

because it was the first such result from a steady-state filament based plasma experiment where the direction of the electric field was reversed for a significant portion of the plasma column.

The second experimental study was performed using four different gas species, Helium, Nitrogen, Neon, and Argon. The mission of this experiment was to determine if the physics observed in the early Helium-based experiments could be scaled to the new, Argon-based experiments. The results of these experiments showed that by keeping constant the ratio of the ion mass to the square of the magnetic field strength, similar behaviors were observed in all four gas species.

The final experiments presented in this dissertation showed that the potential structure of an Argon plasma could also be successfully modified in ALEXIS. The behavior was, however, slightly different than the earlier Helium-based experiments, in that the case with the positive ring bias drove a wave-mode not previously seen in ALEXIS. Initial measurements indicate this is a Current Driven Ion Cyclotron wave. The results of this experiment are significant because previous studies of the CDICI were mostly performed in Q-machines, not steady-state rf-based plasma devices. Also, most previous works focused on the generation of the instability, while the results presented here show both the generation and the transition away from the instability resonance. The experimental parameters were put into a computational model, and very good agreement was found between the model predictions and the measured values of the instability.

5.2 Future Works

This section will present some suggestions for future research projects and experimental upgrades for ALEXIS. These suggestions are intended to help the next generation of researchers on ALEXIS identify future projects that could contribute immediately to the field of plasma physics and perhaps serve as a starting point for their dissertations.

The ALEXIS project would benefit from independent flow measurements. This would include a traditional Mach probe, and a multi-sided Mach probe. The Laser Induced Fluorescence system discussed in Appendix I will also contribute greatly to the experimental capabilities of the ALEXIS project.

Also, the ability to measure axial electric fields would greatly enhance the ability to completely diagnose the plasma conditions in ALEXIS. Ideally, an emissive probe that could be scanned axially could be designed, but given the limited diameter of the vacuum vessel this would be extremely challenging. Perhaps studies involving emissive probes at multiple port locations (varied in z) could reveal any modifications to the axial potential structure.

5.3 Concluding Remarks

It has been shown that the ALEXIS device has proven to be a robust platform for laboratory plasma experiments for almost a decade, and, with continued improvements, will continue to contribute to the field of basic plasma physics for years to come.

In conclusion, it should be noted that one of the most important, although previously not specifically mentioned aspects of the ALEXIS device is the large number of active collaborations. The flow modification work has been performed in conjunction with research on the Compact Toroidal Hybrid (CTH) device and the Space Physics Group at the Naval Research Labs. The LIF system used in this dissertation was developed with the help and guidance of the Plasma Physics Group at West Virginia University. Also, a new, passive optical diagnostic system using a monochromator is being developed in conjunction with the Atomic Physics group at Auburn. This high level of collaboration is one of the greatest strengths of the ALEXIS project, and one of the greatest benefits to the student researchers who work on it.

Bibliography

- ¹ W. Crookes, *Radiant Matter* (James W. Queen & Co., Philadelphia, PA, 1878).
- ² I. Langmuir, Proceedings Of the National Academy Of Sciences **14**, 627 (1928).
- ³ I. Langmuir, C. G. Found, and A. F. Dittmer, ScienceNew Series **60**, 392 (1924).
- ⁴ L. R. Brewer, J. D. Prestage, J. J. Bollinger, W. M. Itano, D. J. Larson, and D. J. Wineland, Phys. Rev. A **38**, 859 (1988).
- ⁵ D. Dubin, Physical Review Letters **6**, 2076 (1991).
- ⁶ P. K. Shukla, Physics Of Plasmas **8**, 1791 (2001).
- ⁷ P. K. Shukla and A. A. Mamun, *Introduction To Dusty Plasma Physics* (Institute of Physics Publishing, 2002), p. 270.
- ⁸ D. A. Mendis, Astrophysics and Space Science **65**, 5 (1979).
- ⁹ A. Barkan, N. D'Angelo, and R. L. Merlino, Physical Review Letters **73**, 3093 (1994).
- ¹⁰ K. H. Becker, K. H. Schoenbach, and J. G. Eden, Journal Of Physics D: Applied Physics **39**, R55 (2006).
- ¹¹ F. F. Chen, *Introduction To Plasma Physics and Controlled Fusion: Plasma Physics* (Springer, 1984), p. 421.
- ¹² S. Sazhin, Planetary and Space Science **40**, 681 (1992).
- ¹³ D. A. Brain, F. Bagenal, M. H. Acun, J. E. Connerney, and D. H. Crider, **107**, (2002).
- ¹⁴ M. E. Koepke, Physica Scripta **T107**, 182 (2004).
- ¹⁵ G. R. Tynan, A. Fujisawa, and G. McKee, Plasma Physics and Controlled Fusion **51**, 113001 (2009).

- ¹⁶ W. E. Amatuucci, D. N. Walker, G. I. Ganguli, J. A. Antoniadis, D. Duncan, J. H. Bowles, V. Gavrishchaka, and M. E. Koepke, *Physical Review Letters* **77**, 1978 (1996).
- ¹⁷ V. Gavrishchaka, S. Ganguli, and G. I. Ganguli, *Physical Review Letters* **80**, 728 (1998).
- ¹⁸ G. Marklund, L. Blomberg, and C. G. Fälthammar, *Geophysical Research* **21**, 1859 (1994).
- ¹⁹ M. E. Koepke, C. Teodorescu, and E. W. Reynolds, *Plasma Physics and Controlled Fusion* **45**, 869 (2003).
- ²⁰ G R Tynan, C. Holland, J H Yu, a James, D Nishijima, M Shimada, and N Taheri, *Plasma Physics and Controlled Fusion* **48**, S51-S73 (2006).
- ²¹ I. Voronkov, R. Rankin, P. Frycz, V. T. Tikhonchuk, and J. C. Samson, *Journal Of Geophysical Research* **102**, 9639 (1997).
- ²² G. S. Lakhina, *Journal Of Geophysical Research* **92**, 12,161-12,170 (1987).
- ²³ G. I. Ganguli, Y. C. Lee, and P. J. Palmadesso, *Physics Of Fluids* **28**, 761 (1985).
- ²⁴ Baron J. W. S. Rayleigh, J. W. S. Rayleigh, and R. B. Lindsay, *The theory Of Sound, Volume 2*, 2nd ed. (Courier Dover Publications, New York, 1945), p. 504.
- ²⁵ S. Chandrasekhar, *Hydrodynamic and Hydromagnetic Stability*, 3rd ed. (Courier Dover Publications, New York, 1981), p. 652.
- ²⁶ L. S. Kovasznay, *Review Of Modern Physics* **32**, 815 (1960).
- ²⁷ N. Rynn and N. D'Angelo, *Review Of Scientific Instruments* **31**, 1326 (1960).
- ²⁸ R. W. Motley and N. D'Angelo, *Physics Of Fluids* **6**, 296 (1963).
- ²⁹ W. E. Drummond and M. N. Rosenbluth, *Physics Of Fluids* **5**, 1507 (1962).
- ³⁰ P. Bakshi, G. I. Ganguli, and P. J. Palmadesso, *Physics Of Fluids* **26**, 1808 (1983).
- ³¹ S. L. Cartier, N. D'Angelo, P. H. Krumm, and R. L. Merlino, *Physics Of Fluids* **28**, 432 (1985).
- ³² L. Enriques, *Plasma Physics* **10**, 641 (1968).
- ³³ L. Enriques, A. M. Levine, and G. B. Righetti, in *Plasma Physics and Controlled Nuclear Fusion Research. Vol. I. Vienna, International Atomic Energy Agency, 1969.* (EURATOM-CNEN, Novosibirsk, USSR, 1969), p. 641.
- ³⁴ N. Sato, M. Nakamura, and R. Hatakeyama, *Physical Review Letters* **57**, 1227 (1986).

- ³⁵ G. I. Ganguli, Y. C. Lee, and P. J. Palmadesso, *Physics Of Fluids* **31**, 823 (1988).
- ³⁶ G. I. Ganguli, P. J. Palmadesso, and Y. C. Lee, *Geophysical Research Letters* **12**, 643 (1985).
- ³⁷ E. G. van Niekerk, P. H. Krumm, and M. J. Alport, *Plasma Physics and Controlled Fusion* **33**, 375 (1991).
- ³⁸ G. I. Ganguli, *Advances In Space Research* **8**, 161 (1988).
- ³⁹ W. E. Amatucci, *Experimental Observation Of Ion-Cyclotron Turbulence In the Presence Of Transverse-Velocity Shear*, 1994.
- ⁴⁰ W. E. Amatucci, M. E. Koepke, J. J. Carroll III, and T. E. Sheridan, *Geophysical Research Letters* **21**, 1595 (1994).
- ⁴¹ M. E. Koepke, W. E. Amatucci, J. J. Carroll III, and T. E. Sheridan, *Physical Review Letters* **72**, 3355 (1994).
- ⁴² W. E. Amatucci, D. N. Walker, G. I. Ganguli, D. Duncan, J. A. Antoniadis, J. H. Bowles, V. Gavrishchaka, and M. E. Koepke, *Journal Of Geophysical Research* **103**, 11711 (1998).
- ⁴³ W. E. Amatucci, G. I. Ganguli, D. N. Walker, and D. Duncan, *Phys. Plasmas* **6**, 619 (1999).
- ⁴⁴ D. N. Walker, W. E. Amatucci, G. I. Ganguli, J. A. Antoniadis, J. H. Bowles, D. Duncan, V. Gavrishchaka, and M. E. Koepke, *Geophysical Research Letters* **24**, 1187 (1997).
- ⁴⁵ J. R. Peñano, G. I. Ganguli, W. E. Amatucci, D. N. Walker, and V. Gavrishchaka, *Phys. Plasmas* **5**, 4377 (1998).
- ⁴⁶ V. V. Gavrishchaka, G. I. Ganguli, W. A. Scales, S. P. Slinker, C. C. Chaston, J. P. Mcfadden, R. E. Ergun, and C. W. Carlson, *Physical Review Letters* **85**, 4285 (2000).
- ⁴⁷ G. I. Ganguli, S. Slinker, V. Gavrishchaka, and W. A. Scales, *Phys. Plasmas* **9**, 2321 (2002).
- ⁴⁸ K. A. Lynch and R. L. Arnoldy, *Geophysical Research Letters* **23**, 3293 (1996).
- ⁴⁹ M. Andre, P. Norqvist, L. Andersson, L. Eliasson, A. I. Eriksson, L. Blomberg, R. E. Erlandson, and J. Waldemark, *Journal Of Geophysical Research* **103**, 4199 (1998).
- ⁵⁰ D. J. Knudsen and J. E. Wahlund, *Journal Of Geophysical Research* **103**, 4157 (1998).
- ⁵¹ N. D'Angelo, *Physics Of Fluids (U.S.)* **8**, 1748 (1965).
- ⁵² E. Agrimson, N. D'Angelo, and R. L. Merlino, *Physical Review Letters* **86**, 5282 (2001).
- ⁵³ E. Agrimson, S. Kim, N. D'Angelo, and R. L. Merlino, *Phys. Plasmas* **10**, 3850 (2003).

- ⁵⁴ C. Teodorescu, E. W. Reynolds, and M. E. Koepke, *Physical Review Letters* **88**, 185003 (2002).
- ⁵⁵ E. A. Wallace, E. E. Thomas, A. C. Eadon, and J. D. Jackson, *Review Of Scientific Instruments* **75**, 5160 (2004).
- ⁵⁶ E. E. Thomas, J. D. Jackson, E. A. Wallace, and G. I. Ganguli, *Phys. Plasmas* **10**, 1191 (2003).
- ⁵⁷ E. E. Thomas, A. C. Eadon, and E. A. Wallace, *Phys. Plasmas* **12**, 042109 (2005).
- ⁵⁸ D. G. Swanson, *Plasma Waves* (Institute of Physics Pub., 2003), p. 456.
- ⁵⁹ T. H. Stix, *Waves In Plasmas* (Springer, 1992), p. 566.
- ⁶⁰ E. Tejero, Private Communication 1-2 (2009).
- ⁶¹ D. A. Gurnett and A. Bhattacharjee, *Introduction To Plasma Physics: With Space and Laboratory Applications* (Cambridge University Press, 2005), p. 452.
- ⁶² J. D. Huba, *IEEE Electrical Insulation Magazine* **19**, 71 (2004).
- ⁶³ E. Tejero, Private Communication 1-1 (2010).
- ⁶⁴ J. J. Rasmussen and R. W. Schrittwieser, *IEEE Transactions On Plasma Science* **19**, 457 (1991).
- ⁶⁵ G. I. Ganguli, M. J. Keskinen, H. Romero, R. Heelis, T. Moore, and C. Pollock, *Journal Of Geophysical Research* **99**, 8873 (1994).
- ⁶⁶ J. M. Kindel and C. F. Kennel, *Journal Of Geophysical Research* **76**, 3055 (1971).
- ⁶⁷ O. W. Richardson and A. F. Young, *Proceedings Of the Royal Society A: Mathematical, Physical and Engineering Sciences* **107**, 377-410 (1925).
- ⁶⁸ P. A. Keiter, *Experimental Investigation Of Ion Temperature Anisotropy Driven Instabilities In a High Beta Plasma*, 1999.
- ⁶⁹ J. Hopwood, *Journal Of Vacuum Science & Technology A: Vacuum, Surfaces, and Films* **11**, 147 (1993).
- ⁷⁰ R. Piejak, V. Godyak, and B. Alexandrovich, *Review Of Scientific Instruments* **72**, 4002 (2001).
- ⁷¹ I. B. Bernstein and I. N. Rabinowitz, *Physics Of Fluids* **2**, 112 (1959).
- ⁷² R. F. Kemp, *Review Of Scientific Instruments* **37**, 455 (1966).

- ⁷³ I. H. Hutchinson, *Principles Of Plasma Diagnostics* (Cambridge University Press, 2002), p. 440.
- ⁷⁴ R. A. Stern and J. A. Johnson III, *Physical Review Letters* **34**, 1548 (1975).
- ⁷⁵ R. F. Boivin and E. E. Scime, *Review Of Scientific Instruments* **74**, 4352 (2003).
- ⁷⁶ A. M. Keesee, E. E. Scime, and R. F. Boivin, *Review Of Scientific Instruments* **75**, 4091 (2004).
- ⁷⁷ S. J. Sanders, P. M. Bellan, and R. a. Stern, *Phys. Plasmas* **5**, 716 (1998).
- ⁷⁸ E. E. Scime, C. Biloiu, C. Compton, F. Doss, D. Venture, J. Heard, E. Choueiri, and R. Spektor, *Review Of Scientific Instruments* **76**, 026107 (2005).
- ⁷⁹ J. L. Kline, C. Franck, and R. S. Spangler, *First Order Perturbed Velocity Distribution theory and Measurement* (2000), p. 42.
- ⁸⁰ R. F. Boivin, *Study Of the Different Line Broadening Mechanisms For the Laser Induced Fluorescence Diagnostic Of the HELIX and LEIA Plasmas* p. 33.
- ⁸¹ A. Corney, *Atomic and Laser Spectroscopy* (Clarendon Press, 1977), p. 763.
- ⁸² M. D. Levenson and S. Kano, *Introduction To Nonlinear Laser Spectroscopy* (Academic Press, 1988), p. 299.
- ⁸³ X. Sun, C. Biloiu, R. A. Hardin, and E. E. Scime, *Plasma Sources Science and Technology* **13**, 359 (2004).
- ⁸⁴ W. L. Wiese, B. M. Glennon, and M. W. Smith, *Sodium Through Calcium* (U.S. Dept. of Commerce, National Bureau of Standards, 1969), p. 268.
- ⁸⁵ H. R. Griem, *Spectral Line Broadening By Plasmas* (Academic Press, 1974), p. 408.

Appendix I - Laser Induced Fluorescence

Laser Induced Fluorescence (LIF) has been used in the study of plasma flows for several decades.^{74, 75, 76, 54, 77} LIF is a two-photon process in which an electron that is in an excited state is further excited into a higher energy level by the incoming photons from a laser at wavelength, λ_1 . The electron then emits a photon at a shorter wavelength, λ_2 to transition to a lower energy state. As laser technology has advanced over the last few decades, lasers capable of precise wavelength selection became available to plasma researchers. Laser linewidths that are much smaller than the linewidths of ion absorption can be used to measure the ion velocity distribution and temperature with high accuracy.⁶⁸

A. LIF Theory

One of the basic assumptions regarding the composition of a plasma is that the temperature is Maxwellian. For simplicity, start with a one dimensional, drifting Maxwellian distribution for the ions:

$$f(v) = A \exp\left[-\frac{\frac{1}{2}m_i(v - v_0)^2}{k_B T_i}\right] \quad (0-1)$$

Where m_i is the ion mass, v is the flow velocity, or drift, and v_0 is the rest velocity, T_i is the ion temperature, and k_B is the Boltzmann's constant, defined as:

$$k_B = 1.38 \times 10^{-23} \text{ J/K}$$

Equation (0-1), when normalized, gives:

$$A = n\sqrt{m/2\pi k_B T}$$

The average energy for a species in the plasma (ion or electron), can be found from the second moment of the distribution function, which is given in equation (0-2):

$$E_{avg.} = \frac{\int_{-\infty}^{\infty} \frac{1}{2} m u^2 f(u) du}{\int_{-\infty}^{\infty} f(u) du} = \frac{1}{2} k_B T = \frac{1}{4} m v_{th}^2 \quad (0-2)$$

Where the thermal velocity is defined as

$$v_{th} = \sqrt{\frac{2 k_B T}{m}} \quad (0-3)$$

To measure the velocity distribution of the ions in a plasma with LIF, the laser is used to optically pump an absorption line in the ions.⁷⁴ Using the distribution function, it can be seen that

for a Doppler broadened distribution function, that is, one where the ions have significant thermal spread, a narrow laser can be scanned across the ion velocity distribution function as shown in Figure I-1. This leads to the spontaneous decay from the upper state being a direct measure of the ion distribution function. Specifically, the intensity of the light from the spontaneous decay corresponds directly to the population of ions in the distribution function at that laser wavelength.

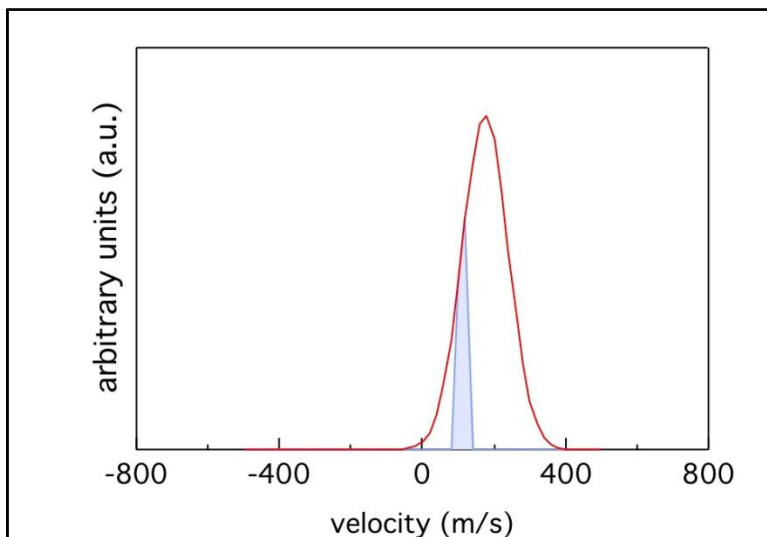


Figure 0-1: Artistic example indicating the relationship between the laser linewidth (blue) and the Doppler broadened ion velocity distribution function (red)

The LIF studies in ALEXIS are performed on singly ionized argon ions (Ar II), and use a “standard” transition scheme that has been used by numerous groups.^{78,79} In this LIF scheme, the $3d^2G_{9/2}$ line is optically pumped at 611.6616 nm to the meta-stable $4p^2F_{7/2}$ state. This state decays to $4s^2D_{5/2}$ state and emits a photon at 461.10 nm. This transition is illustrated in Figure I-2.

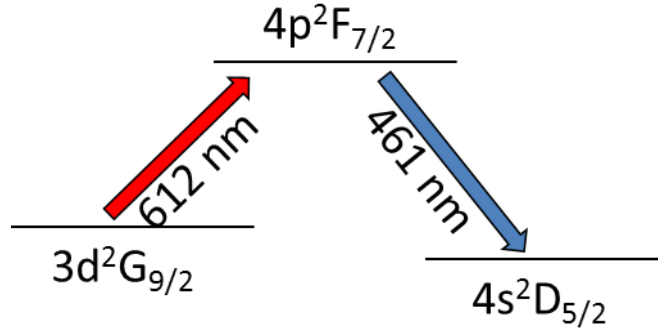


Figure 0-2: Pictorial representation of the transition scheme used in ALEXIS.

To find the flow velocity of the ions in the probed region of the plasma, a Gaussian is fit to the measured ion velocity distribution function. The wavelength of the maximum of the Gaussian is then converted to a velocity using the relativistic Doppler shift, which relates the observed wavelength, the rest wavelength, and the velocity by equation (I-4)⁷⁴

$$\frac{\lambda_o}{\lambda_r} = \sqrt{\frac{1 + \beta}{1 - \beta}}$$

(0-4)

Where λ_o is the observed, or measured, wavelength of the peak of the ion velocity distribution function, λ_r is the known value of the spectral line being excited by the laser, and β is the ratio of the ion velocity to the speed of light. While the speeds measured in ALEXIS are far from relativistic, solving the full relativistic Doppler equation instead of the low velocity limit (where $v \ll c$) contributes no significant increase in the computational requirements.

To determine the temperature, it is typically assumed that Doppler broadening is the dominant broadening mechanism.⁸⁰ Some of the other broadening mechanisms that affect the width of a velocity distribution function for ions in a plasma, including Zeeman splitting, Stark

broadening, and pressure broadening. Below is a brief description of each mechanism, and a discussion of their relevance to ALEXIS.

1. Line Broadening Mechanisms

To determine the temperature, it is typically assumed that Doppler broadening is the dominant broadening mechanism.⁸⁰ Some of the other broadening mechanisms that affect the width of a velocity distribution function for ions in a magnetized plasma are Stark broadening, Zeeman splitting, and instrumental broadening.^{81,82} Additionally, the natural line broadening, due to the uncertainty principle, should be considered. Below are brief descriptions of each mechanism, and a discussion of their relevance to ALEXIS.

a) Doppler Broadening

Random thermal motion of radiating or absorbing atoms introduces a broadening of a distribution function. If the thermal motion is parallel or anti-parallel to direction of observation, the resultant broadening will be detected in the measurement. The shift in frequency due to the Doppler Effect is given in equation (I-5).⁸⁰

$$\Delta\nu = \pm\nu_0 \frac{v}{c}$$

(0-5)

Where ν_0 is the rest, or unshifted, frequency, and v is the velocity. If the motion of the atoms is purely thermal, the distribution function for the emitters and absorbers is Maxwellian, where:

$$f(v) = \sqrt{\frac{m_i}{2\pi k_B T_i}} e^{-\frac{m_i(v-v_0)^2}{2k_B T_i}}$$

(0-6)

Here, T_i is the ion temperature (the relevant emitter for studies in ALEXIS), m_i is the ion mass, v_0 is the average ion velocity and k_B is Boltzmann's constant. The intensity of the light emitted at a particular frequency is proportional to the number of particles at that frequency. Then for a Maxwellian distribution of emitters or absorbers the line shape becomes Doppler broadened and the intensity of the line becomes: ⁸⁰

$$I(\nu) = I(\nu_0)e^{-\frac{m_i^2(\nu-\nu_0)^2 c^2}{2k_B T_i \nu_0^2}} \quad (0-7)$$

Where ν_0 is the un-shifted center frequency (unbroadened) of the ion distribution. To find the full width at half maximum (FWHM), the exponent in equation (I-7) is set equal to $\frac{1}{2}$ to give:⁸⁰

$$\Delta\nu_{1/2} = \frac{\nu_0}{c} \frac{2k_B T_i}{m_i} \sqrt{2 \ln 2} \quad (0-8)$$

In terms of wavelength, this is written as:

$$\Delta\lambda_{1/2} = \frac{\lambda_0}{c} \frac{2k_B T_i}{m_i} \sqrt{2 \ln 2} \quad (0-9)$$

Using typical parameters for ALEXIS, with argon ions at room temperature ($T_i = 0.03$ eV), equation (I-9) yields $\Delta\lambda_{1/2} \approx 1 \times 10^{-3}$ nm. Here a low value for the ion temperature has been used, resulting in the narrowest anticipated Doppler broadening.

b) Natural Linewidth

A natural linewidth for the transition between two energy levels arises from the Heisenberg uncertainty principle.⁸³ Let an excited state have energy E_i , and a lifetime of τ_i . Then, the uncertainty is written as:

$$\Delta E_i = \frac{\hbar}{\tau_i}$$

(0-10)

For the in the transition used in the LIF scheme for ALEXIS, the lower level state for the transition is not the ground state. It is another excited state with energy E_k and lifetime of τ_k . The total uncertainty, then, is the sum of the two uncertainties:

$$\Delta E = \Delta E_i + \Delta E_k$$

(0-11)

Using the angular frequency, and including all transitions from any allowable level to either level i or k , equation (I-11) can be rewritten as

$$\Delta\omega_{ik} = \sum_m A_{mi} + \sum_n A_{nk}$$

(0-12)

Where A_{mi} and A_{nk} are the Einstein coefficients for each transition.⁸² In the ALEXIS LIF scheme, the lower state (i) is the $3d^2G_{9/2}$ metastable state and the upper state (k) is the $4p^2F_{7/2}$ level. Transitions originating from the lower level metastable state have a very small spontaneous transition probability compared to transitions from the upper $4p^2F_{7/2}$ level. This lets

the total angular frequency uncertainty (equation (I-12)) in the atomic transition to be dominated by the metastable state and is approximately:

$$\Delta\omega_{ik} \approx \sum_m A_{mi} \tag{0-13}$$

Using the given values for the Einstein coefficient,⁸⁴ and the angular frequency uncertainty is:

$$\Delta\omega_{ik} \approx 1.2 \times 10^{-5} \text{nm} \tag{0-14}$$

Writing this in terms of wavelength gives the spreading of the absorption line due to the natural linewidth:

$$\Delta\lambda_{ik} \approx 2.3 \times 10^{-5} \text{nm} \tag{0-15}$$

c) Stark Broadening

Stark broadening results from collisions between charged particles.⁸⁵ A full derivation of Stark broadening is beyond the scope of this work, but the full width at half max is found to be:⁸⁰

$$\Delta\lambda_{1/2} \approx 2 \times 10^{-16} \omega n_e [1 + 1.75 \times 10^{-4} n_e^{1/4} \alpha (1 - 1.02 \times 10^{-3} n_e^{1/6} T_e^{-1/2})]$$

Where α is the ion broadening parameter, ω is the electron impact half width parameter, n_e is the electron density, and T_e is the electron temperature. Using previously calculated values

for ω and α , and assuming 3 eV electrons with an electron density of 10^{16} m^{-3} , the Stark broadening is given as approximately

$$\Delta\lambda_{1/2} \approx 2 \times 10^{-8} \text{ nm}$$

(0-16)

d) Zeeman Broadening

Zeeman broadening results from the interaction of the magnetic moment of an electron in an applied magnetic field.⁸¹ This interaction results in the spectral line becoming split into three components. If the line is split into four or more components the effect is called anomalous Zeeman splitting.⁸⁰

When a spectral line Zeeman splits, the component lines are polarized parallel to the magnetic field, or perpendicular to the magnetic field. The components polarized parallel to the magnetic field are π lines, and the perpendicularly polarized components are σ lines. The component lines are set symmetrically about the center frequency such that the three lines are located at $f - \Delta f$, f , and $f + \Delta f$. The energy difference between the component lines is given as:⁸¹

$$\Delta E = \mu_B B g_j M_j$$

(0-17)

Where μ_B is the Bohr magneton ($\mu_B = e h/4\pi m_e$), M_j is the magnetic orbital quantum number, B is the magnetic field strength (in Gauss), a g_j is the Lande factor. Rewriting equation

(I-17) in terms of wavelength for the two energy levels gives an expression for the broadening due to Zeeman splitting:⁸¹

$$\Delta\lambda = \mu_B B \frac{\lambda^2}{c h} (g_2 M_2 - g_1 M_1) \quad (0-18)$$

Using the largest value of magnetic fields used in ALEXIS gives the maximum value of broadening due to Zeeman splitting possible in ALEXIS. Thus, equation (I-18) yields,

$$\Delta\lambda \approx 2.6 \times 10^{-4} \text{ nm} \quad (0-19)$$

e) Instrumental Broadening

There are two sources of instrument broadening in the LIF scheme used for ALEXIS. One is the dispersion related to the collection optics and detection photomultiplier tube (PMT). The light collected from the plasma passes through a narrow passband filter before entering the PMT, centered on the emission light (460 ±1 nm). This filter eliminates dispersion from the collection system.

The second source of instrumental broadening is the linewidth of the laser itself. The laser bandwidth for the Coherent 899 Ring Dye Laser used for the LIF studies on ALEXIS is given by the manufacturer as less than 1 MHz.⁸⁰ For a central wavelength of 611.6 nm, this gives,

$$\Delta\lambda \approx 1.3 \times 10^{-6} \text{ nm}$$

(0-20)

f) Comparison of Line Broadening Mechanisms

Using LIF to determine the ion flow velocities is the main focus of this work. The above broadening mechanisms do not affect the determination of the flow velocity, because they do not affect the location of the maximum of the velocity distribution function. To accurately determine the temperature, however, it is essential that Doppler broadening be the dominant broadening mechanism. Table I-9 shows a summary of the values calculated in the previous sections.

Table I-0-1: Comparison of the emission line broadening effects calculated for ALEXIS

Broadening Mechanism	Broadening Width (FWHM) (nm)
Doppler	1×10^{-3}
Natural Linewidth	2.3×10^{-5}
Stark	2×10^{-8}
Zeeman	2.6×10^{-4}
Instrumental	1.3×10^{-6}

As can be seen, Doppler broadening is larger than any other effect by an order of magnitude. The closest broadening mechanism list in Table I-9 is Zeeman broadening. Recall, however, that it was the maximum possible magnetic field strength used to calculate this value.

All of the LIF data presented in this work is for magnetic fields of 300 Gauss or less, which would give a Zeeman splitting value of 7.8×10^{-5} nm.

B. LIF Hardware

The laser used in the research on ALEXIS is a ring dye laser. The simple premise is that an organic dye, with a large number of vibrational modes, is excited by a high power laser. The photons emitted from these vibrations are sent in a path around a resonant cavity that can be adjusted to “tune” the resonances to specific frequencies, and, therefore, specific wavelengths.

Specifically, the laser used for the ALEXIS studies is a Coherent 899 Ring Dye Laser that is optically pumped by a Coherent Innova 90 Argon Ion Laser. The Innova 90 is capable of up to 9 Watts of constant (CW) power; however, most of the studies in ALEXIS use only 8.5 W to conserve the lifetime of the laser system. The light from the Innova 90 enters the 899 dye laser where it strikes a stream of dye. The stream is composed of rhodamine 6G dye suspended in an ethylene glycol solution. The 899 is then tuned to near the desired wavelength of light that is to be used for the experiment. Once the 899 is stabilized and set to scan a 20 GHz frequency range, the light leaves the laser. The layout of the optical table is shown in Figure I-3.

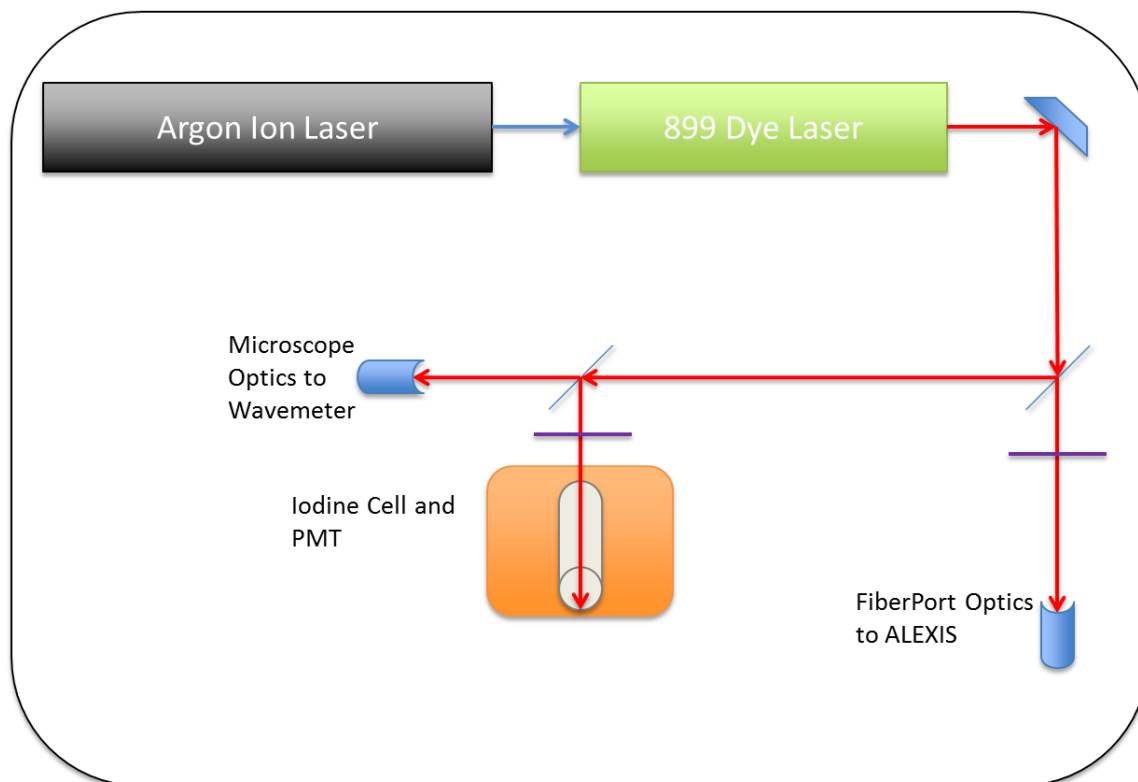


Figure 0-3: Layout of the lasers and optics used for LIF. The ArII laser (black) is injected into the dye laser (green). All optical elements (mirror and beam-splitters) are in blue, and the optical choppers are represented by purple lines. The Iodine cell used for absolute reference is shown with its PMT (orange).

The laser beam is reflected 90° by hitting an adjustable 45° front-surface mirror. From here, the beam hits a 10-90 beam splitter where 90% of the beam passes straight through the splitter, and 10% is reflected at 90° back down the optical table, parallel to the laser system. It should be noted that this configuration was designed because of physical constraints, not to optimize the system.

The beam that is reflected from the first beam splitter then hits a second beam splitter. The 50-50 splitter sends half of the light through an optical chopper and then into an Iodine vapor cell that is used as an absolute wavelength reference. The light that passes through the 50-50 splitter then enters a Newport MV-5x 0.10 microscope objective lens and is focused into a single-mode fiber optic which takes the light to a Bristol model 621-A VIS wavemeter, which

can measure the light to an accuracy of up to ± 0.2 parts per million at a measurement frequency at 4 Hz. The Bristol wavemeter connects to the laser lab PC via USB, where the measured wavelength and power are broadcast via the Data Socket Server.

The light that passed through the first beam-splitter, the 90-10, passes through an optical chopper and is focused with a ThorLabs 5 mm focal length SMA FiberPort into a SMA tipped AFS105/125Y, 0.22 NA multimode fiber optic cable. This cable transports the light from the laser lab to the ALEXIS lab, which are separated by a hallway.

Beneath the Iodine vapor cell is a Hamamatsu R292 photomultiplier tube that captures the light emitted from the atomic lines that are excited as the laser is swept through the 20 GHz frequency range. These lines have been extensively studied and are very well characterized, providing an absolute reference to compare the measured signal against. The signal from the PMT is sent (with the signal from the corresponding lock-in amplifier) to a Stanford Research Systems model SR830 lock-in amplifier. The lock-in amplifier is a power tool that is used to greatly reduce the noise in a measurement, and to isolate only the desired signal. The simple model of the operation of the complicated device is that two signals are sent into the digital logic of the lock-in; a reference signal and the data signal. The reference signal is from the optical chopper, which is usually set to approximately 600 Hz. The lock-in uses this reference signal to isolate from the data signal only the contribution that corresponds to the frequency of the reference signal. This powerful ability to isolate only the desired, meaningful signal is of great use to experimentalists who often work in electrically noisy environments.

After processing in the lock-in, the output signal is sent to a National Instruments model BNC-2090A, which is connected to a PC via a NI PCI-6225 PCI card. This PC runs software

from National Instruments, including LabVIEW and NI's Data Socket Server. The signals acquired by the PCI-6225 are captured and made available to the PC controlling the experiment over an internet connection utilizing the Data Socket Server protocol (dstp). This voltage signal is then recorded on the remote PC and is used in analysis as an absolute reference for the wavelength.

After the laser light to be used in the experiment enters the fiber, it is guided to the ALEXIS lab. On the experiment side, the light out of the fiber is collimated and focused with a ThorLabs 11 mm focal length FiberPort. The FiberPort is mounted on the Velmex Bi-Slides described in Chapter 3, and is used to focus the light down to a 3 mm diameter spot at the interrogation region inside the plasma. The light at this spot is collected with a set of optics, designated the "collection optics," that consist of a 300 mm lens in front of a ThorLabs F810SMA-635 fiber-optic coupler. The coupler focuses the collected light into a FT-1.0-UMT fiber optic cable. The cable transports the light to a Hamamatsu PMT. Between the fiber optics and the PMT is a 1 nm wide filter, centered at 460 nm. This filter cuts out much of the extraneous light before it reaches the PMT, improving the signal-to-noise ratio and helping to protect the PMT. The voltage output of the PMT is sent to a second SRS SR830 lock-in amplifier. The reference used by this lock-in is the optical chopper that sits between the 90-10 beam splitter and the 5 mm FiberPort in the laser lab. The outputs of the lock-in amplifier are then sent back to the laser lab via two RJ-45 BNC cables. These signals are also recorded by the PC in the laser lab. By utilizing a single PC for all of the laser related measurements, the measurements can be made almost simultaneously. This PC is also used to send the control voltage to the dye laser controller, which is used to sweep the dye laser through its wavelength range. The alignment of the optics is shown schematically in Figure I-4.

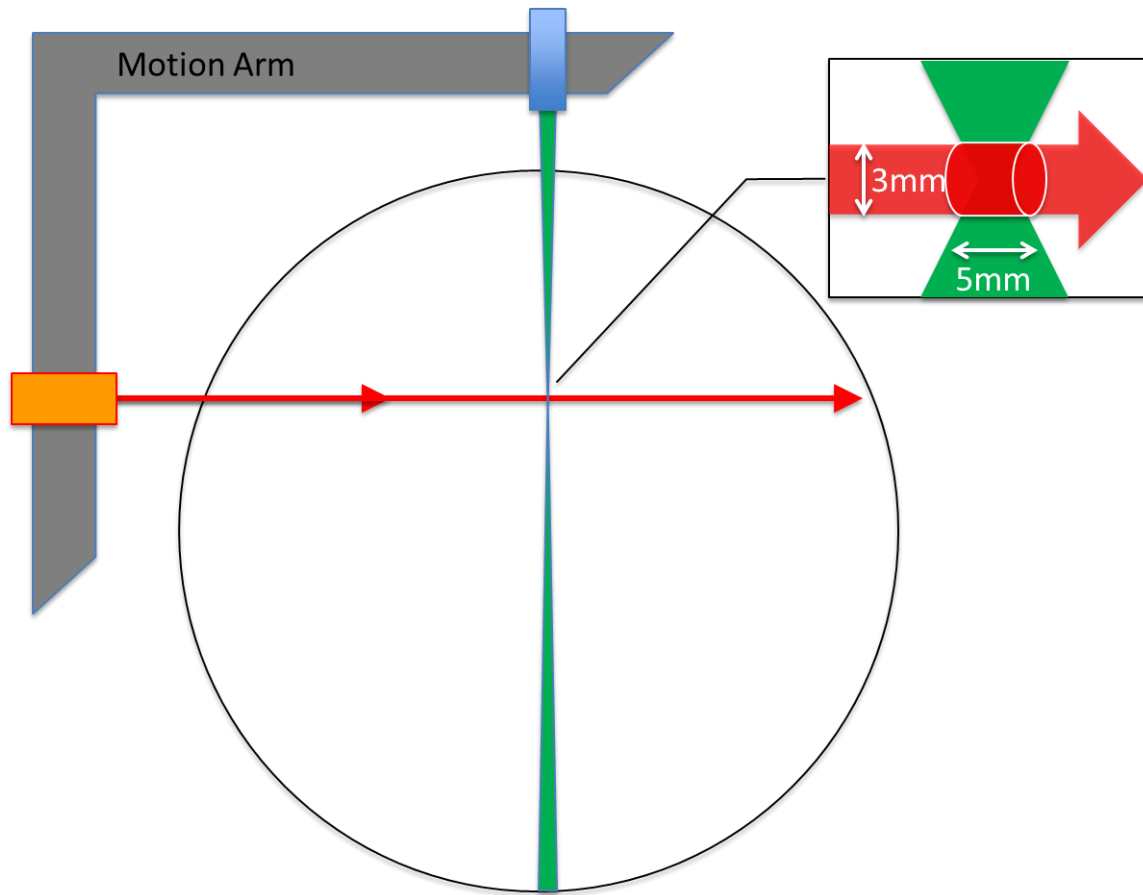


Figure 0-4: Schematic showing the motion arm (gray), the injection optics (orange), laser light (red), collection optics (blue), and collected light (green). The enlarged section shows the interrogation region, where the laser light intersects the path of light collected by the collection optics.

A typical experimental measurement consists of a wavelength scan centered on the rest line of argon, 611.661. While the maximum frequency width for the Coherent 899 is 30 GHz, a typical scan is usually only about 5 GHz wide. Figure I-5 shows the results of a typical laser scan. The vertical axis is the voltage output from the lock-in, and the data points correspond to the discrete measurements for the steps in the voltage, which has been transformed into velocity.

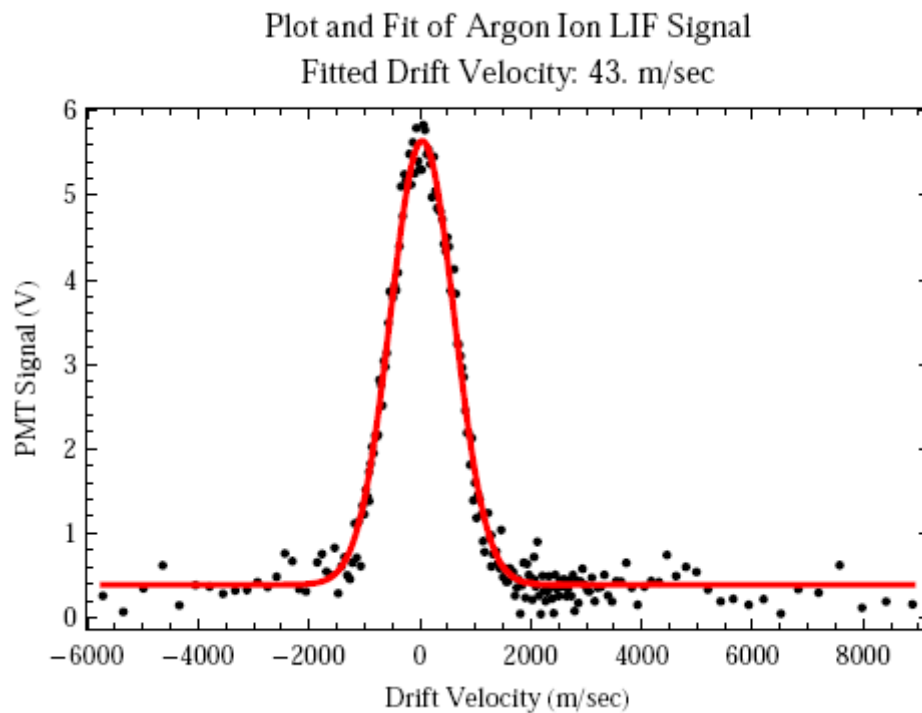


Figure 0-5: Example of LIF data from ALEXIS. The horizontal axis has been processed to be cast in velocity space. The vertical axis is the voltage output from the lock-in amplifier, and corresponds to the voltage from the PMT at the frequency of the optical chopper.

C. Measured Flow Velocities

Direct, non-invasive measurements of the ion flow velocity parallel and perpendicular to the axial magnetic field are performed using the LIF system. The geometry of the LIF measurements as compared to the probe measurements is illustrated in Figure 4-34. Here, a cross-section of the ALEXIS vacuum vessel is shown. The viewpoint from the plasma source toward the end of the chamber, so that the axial magnetic field points into the page. The radial locations of the combination Langmuir/emissive probe system (orange) is located at Port 6 ($z = 127$ cm, $\theta = 0$), the double probe (blue) is located at Port 5 ($z = 109$ cm, $\theta = \pi$) are shown. Both of these probe system can move radially. The LIF hardware on ALEXIS consists of injection optics (I.O.) and collection optics (C.O.) that are mounted on a two-dimensional translation stage that can be moved horizontally and vertically in a plane at $z = 150$ cm.

A radial scan of the LIF system will be performed by aligning the injection optics at $\theta = \pi/2$ and moving the collection optics vertically. This is illustrated in Figure 4-35. Because the LIF measurement gives the component of the velocity along the direction of the injected laser beam, this orientation will allow the component of the ion velocity perpendicular to the magnetic field to be determined.

For these measurements, the main objective was to make detailed measurements at the same radial positions where the largest variation in the plasma potential is measured. In this case, in the region from the center of the plasma column, at $r = 0$ cm outward to $r = 2.8$ cm in step sizes of 4 mm. The results of this measurement are shown in Figure I-8. Each data point

represents two separate velocity measurements at each point. Measurements for Case A (-50V bias on Ring 2) are shown as the red line with circle markers and measurements for Case B (+30V bias on Ring 2) are shown as the blue line with diamond markers.

A second measurement with lower spatial resolution, a separation of 1 cm, is shown in Figure I-9. This measurement is done to obtain a profile of the ion flow velocities over the entire plasma column. Both figures show that the perpendicular flow velocity is significantly modified by changing the bias on Ring 2. In Case A (the -50 V bias) shows the expected symmetry about the center, but with an offset velocity of ~ 50 m/s.

However, the surprising result is that the perpendicular flow velocity for Case B (+30 V bias) is actually peaked near the center of the plasma column. This result indicates that the positively biased case appears to “break” the azimuthal symmetry of the ALEXIS plasma column at the location of the LIF measurement. This is in contrast to the upstream measurements of which suggest that the cylindrical symmetry has been maintained.

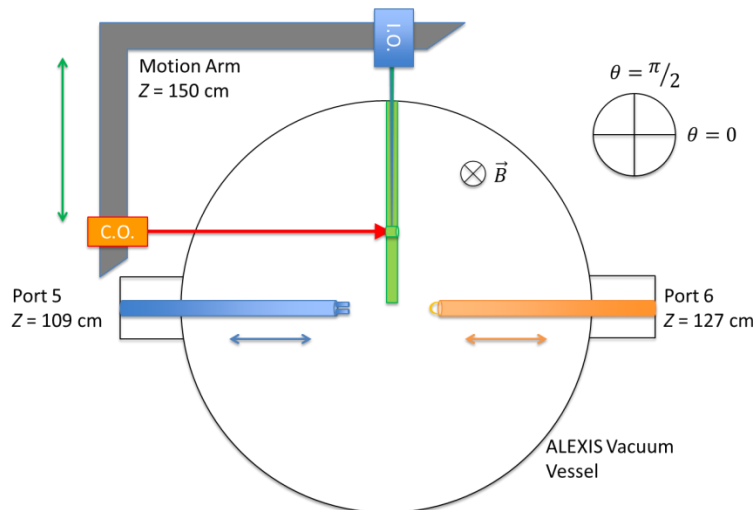


Figure 0-6: Representative drawing of the relative locations of the diagnostics used on ALEXIS. The combination Langmuir probe and emissive probe (orange) is located at Port 6 ($z = 127$ cm, $\theta = 0$), the double probe (blue) is located at Port 5 ($z = 109$ cm, $\theta = \pi$), and the LIF system is located at $z = 150$ cm, $\theta = \pi/2$. The arrows indicate the direction of motion of

the diagnostics to construct the radial profiles presented here. The green area shows the area scanned by the LIF system to measure the azimuthal (i.e. perpendicular) velocity.

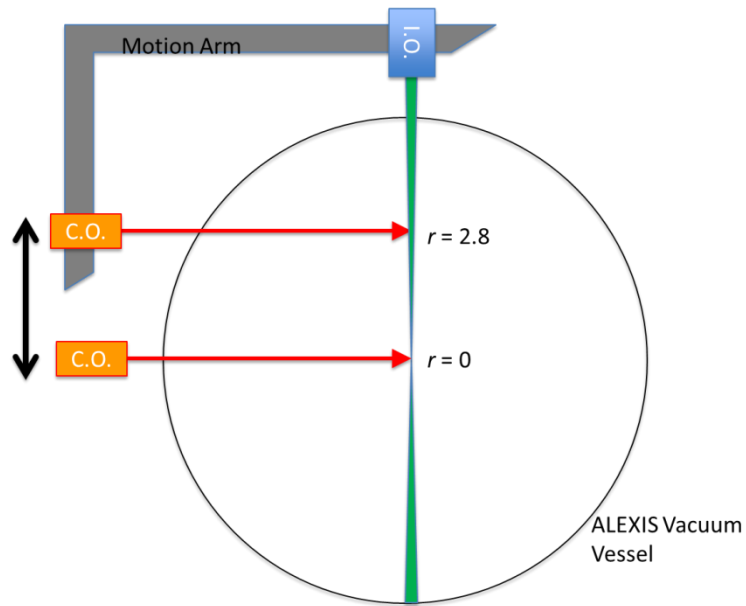


Figure 0-7: Schematic showing how the motion arm is moved (vertically) to make a radial scan of the perpendicular velocity. The relative placement of the injection and collection optics does not change, but the entire Motion Arm is moved vertically.

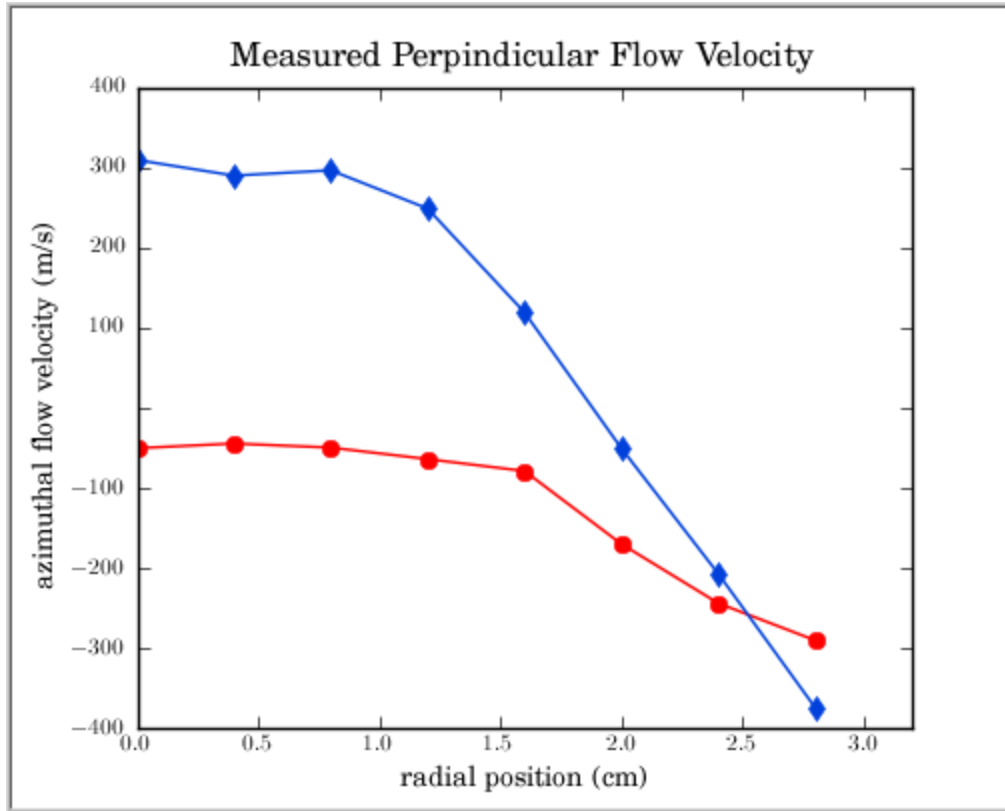


Figure 0-8: Perpendicular flow velocities measured using LIF. The scans were done with two measurements at each point, and each point is separated by 4mm. Case A (-50V bias on Ring 2) is shown as the red line with circle markers, and Case B (+30V bias on Ring 2) is shown as the blue line with diamond markers.

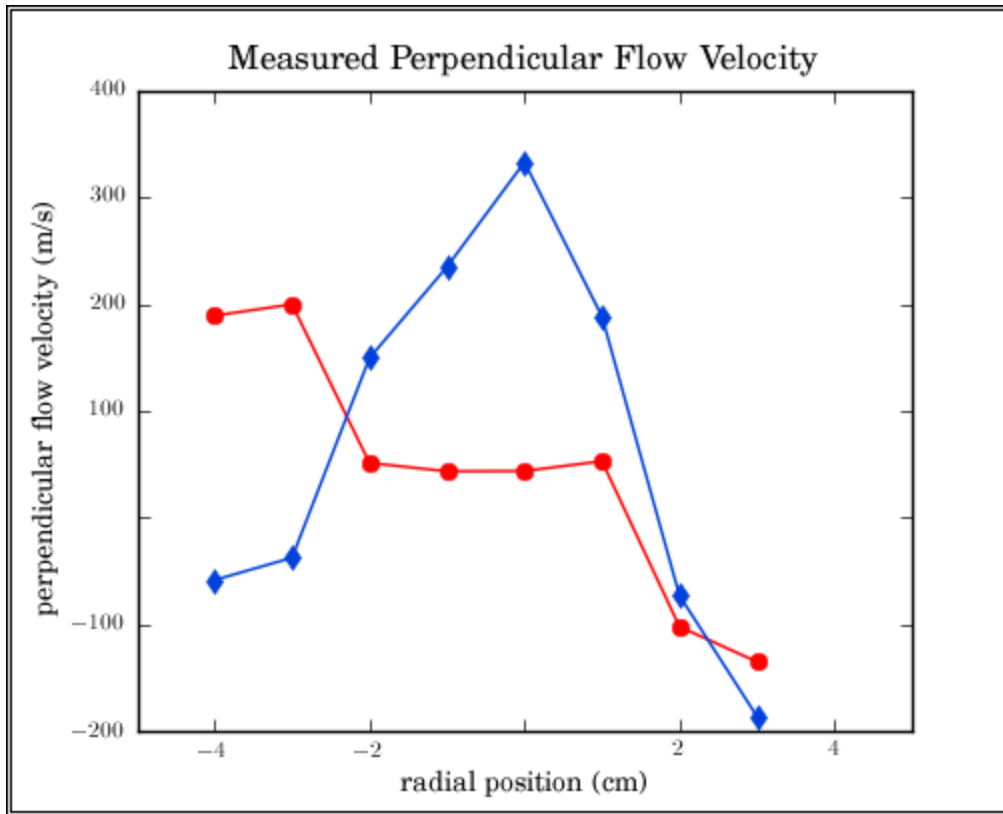


Figure 0-9: Flow velocities measured using LIF. The scans were done with one measurement at each point, and each point is separated by 1 cm. The red circles are Case A, and the blue diamonds are Case B.

To look more closely at the modification of the perpendicular flow velocity, an experiment was done with the optics fixed at a radial position of $r = 15$ mm and the bias on Ring 2 was increased from -50 V to + 50 V in 10 V increments. The results of this experiment are shown in Figure I-10.

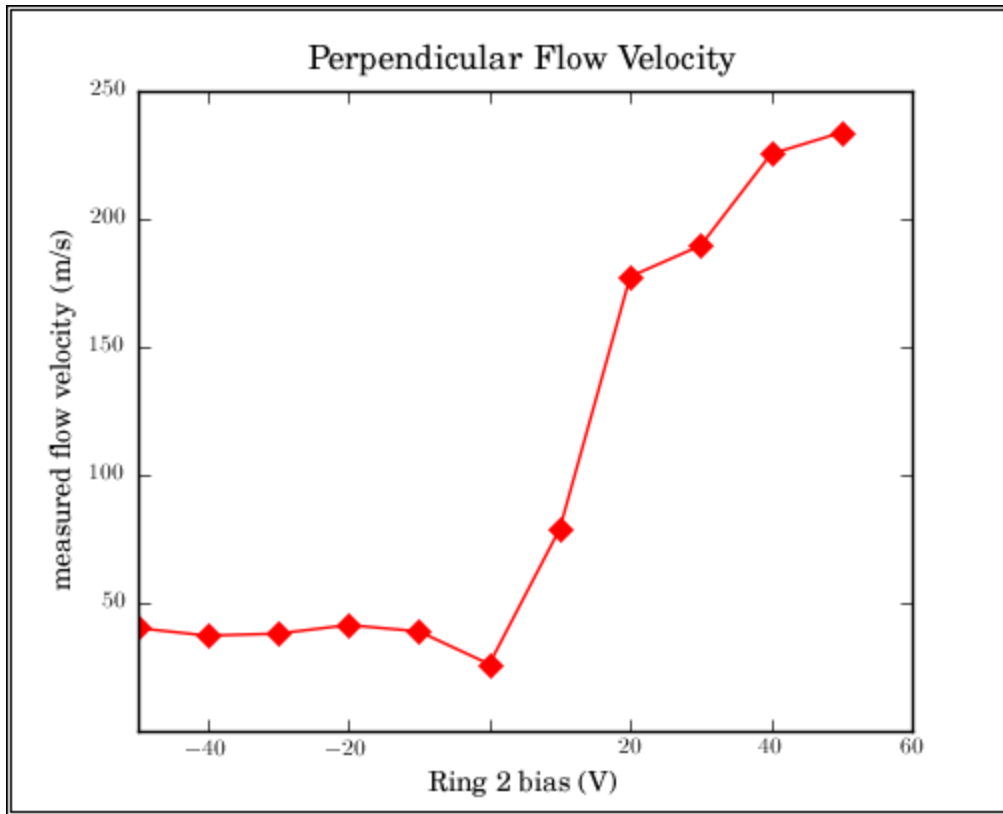


Figure 0-10: LIF measurements of the perpendicular component of the ion velocity measured at $r = 15$ mm as a function of bias applied to Ring 2.

Figure I-10 shows that the response to the bias voltage is not linear, that is, the measured perpendicular flow velocity does not increase incrementally with the bias applied to Ring 2. Instead, it appears that the perpendicular flow remains relatively unchanged for bias voltages less than, or equal to, zero. As the bias to Ring 2 becomes positive there is a rapid increase in the measured perpendicular velocity. It is noted that this behavior closely matches the increase in the parallel current collected by Ring 2. This observation motivated an attempt to measure the axial ion flow velocity in the plasma.

Ideally, to measure the axial flow, the laser would be injected parallel to the magnetic field. Currently, such a measurement is not possible with the current configuration of ALEXIS. It is, however, possible to inject the laser light at an angle α with respect to the background

magnetic field and then extract the components of the velocity. If the measured velocity is V , then components are:

$$v_z = V \cos \alpha$$

$$v_\theta = V \sin \alpha$$

An experiment is performed by orienting the injection optics so that an angle of approximately 65° to the magnetic field is made. The motion arm is scanned radially for the two cases, $V_2 = -50$ V and $V_2 = +30$ V. The measured values of V are presented in Figure I-11.

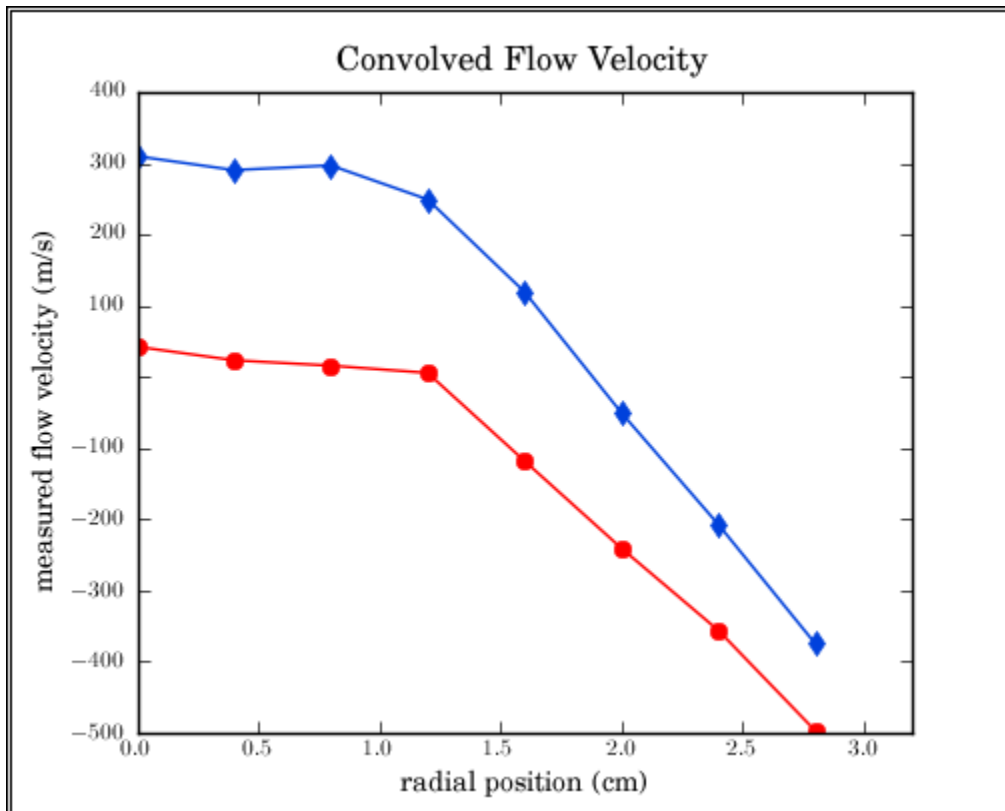


Figure 0-11: Measured velocity with laser injection at finite angle with respect to the magnetic field. The red circles are Case A, and the blue diamonds are Case B.

Using the equations from above, the parallel and perpendicular velocity components can be resolved. The parallel velocity component is plotted in Figure I-12, and the perpendicular velocity component is presented in Figure I-13.

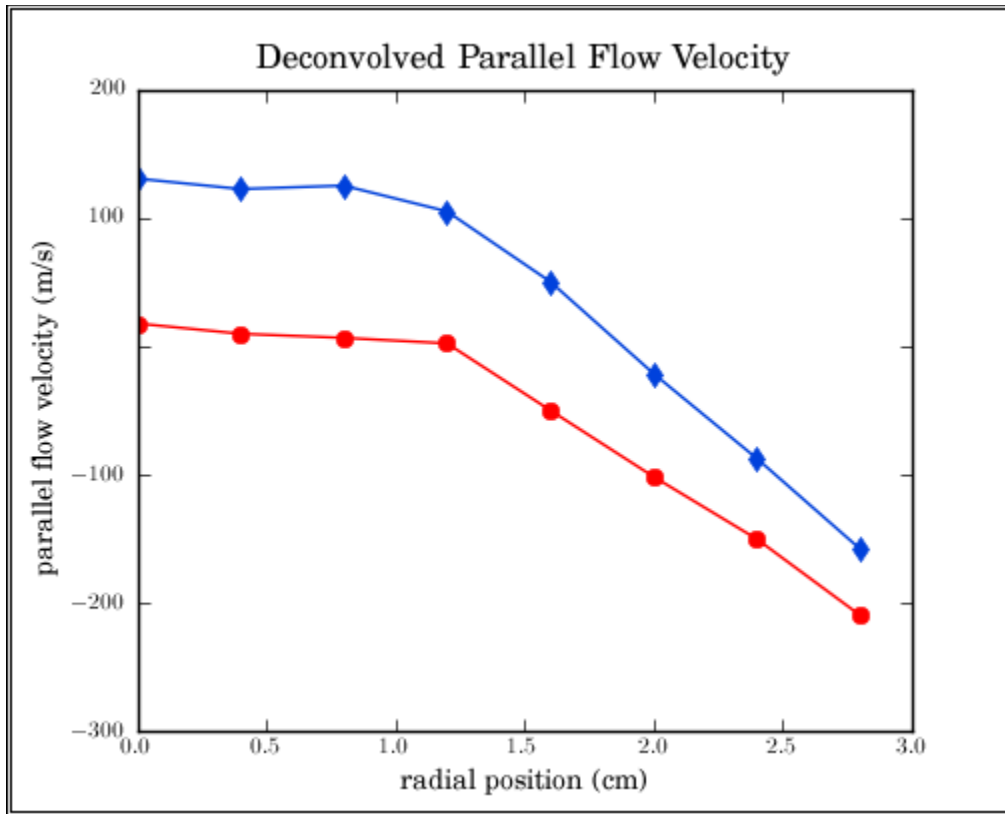


Figure 0-12: Parallel velocities as a function of position measured using LIF. The red circles are Case A ($V_2 = -50$ V), and the blue diamonds are Case B ($V_2 = +30$ V).

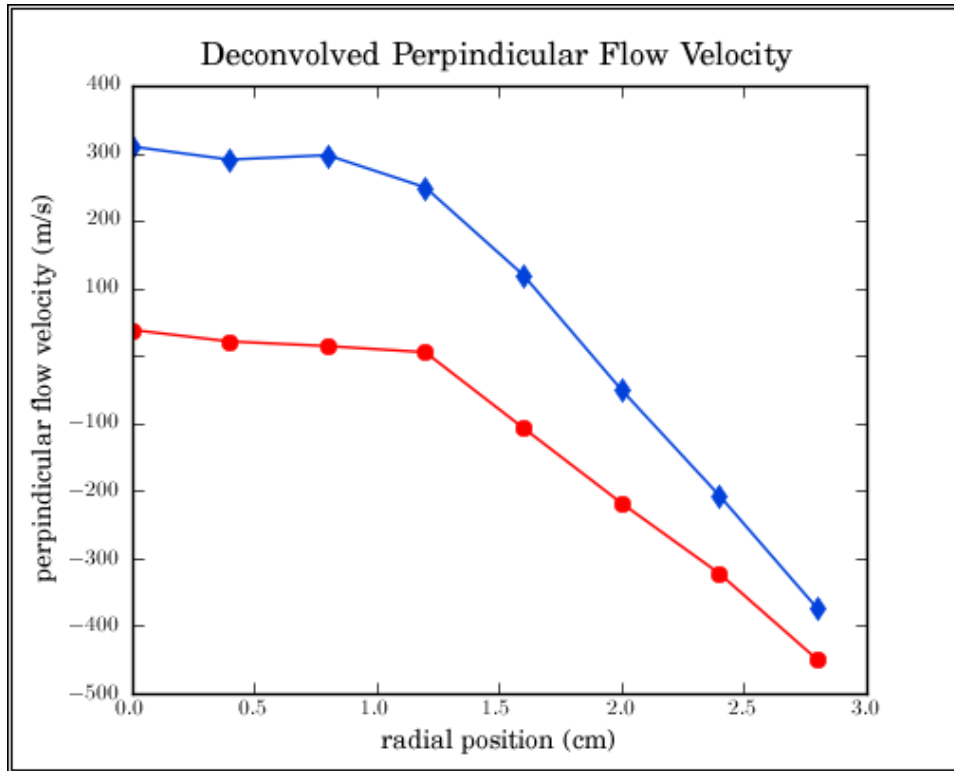


Figure 0-13: Perpendicular velocities calculated from the angled injection of the laser. The red circles are Case A ($V_2 = -50$ V), and the blue diamonds are Case B ($V_2 = +30$ V)

To validate this approach for determining the components of the ion flow velocity, a comparison is done between the directly measured and deconvolved perpendicular ion velocities. This is shown in Figure I-14. Here, the perpendicular velocity is shown for both Case A and Case B. The measurements show that for both experimental configurations, there is generally good agreement between the directly measured and deconvolved perpendicular velocities. This gives a degree of confidence in the reliability of this approach.

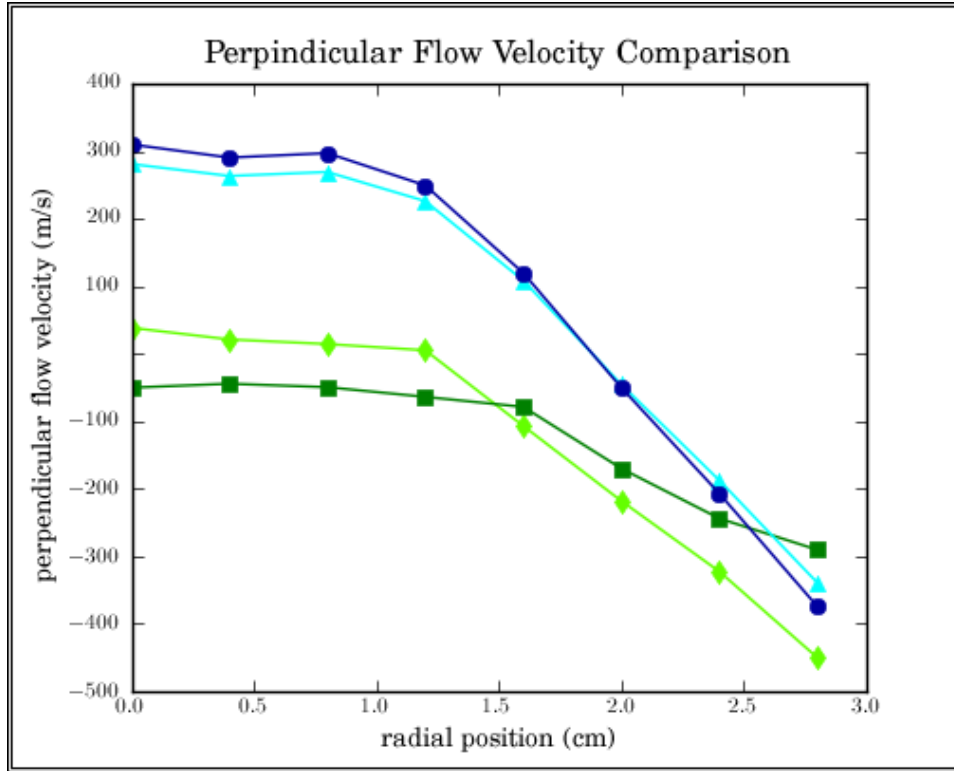


Figure 0-14: Comparison between the directly measured (DM) perpendicular velocity, and the velocity resolved from the angled laser injection (RV). Case A: DM (dark green squares), RV (light green diamonds). Case B: DM (dark blue), RV (light blue triangles).

While the measurements of the parallel velocity component cannot be directly verified with LIF in ALEXIS, it is possible to compare the measured velocities with the value predicted by the modeled axial electric field.

Using the calculated axial electric field, shown in Chapter 4, it is possible to make an estimate of the parallel drift of the ions. If τ is the time between collisions for an ion (defined as the inverse of the collision frequency) and assuming that the neutrals are at rest before being ionized, the velocity of a newly created ion due to the axial electric field can be determined from $v_{ion} = (q_i \tau E / m_i)$. The results of this calculation compared to measured parallel velocity are shown in Figure I-15.

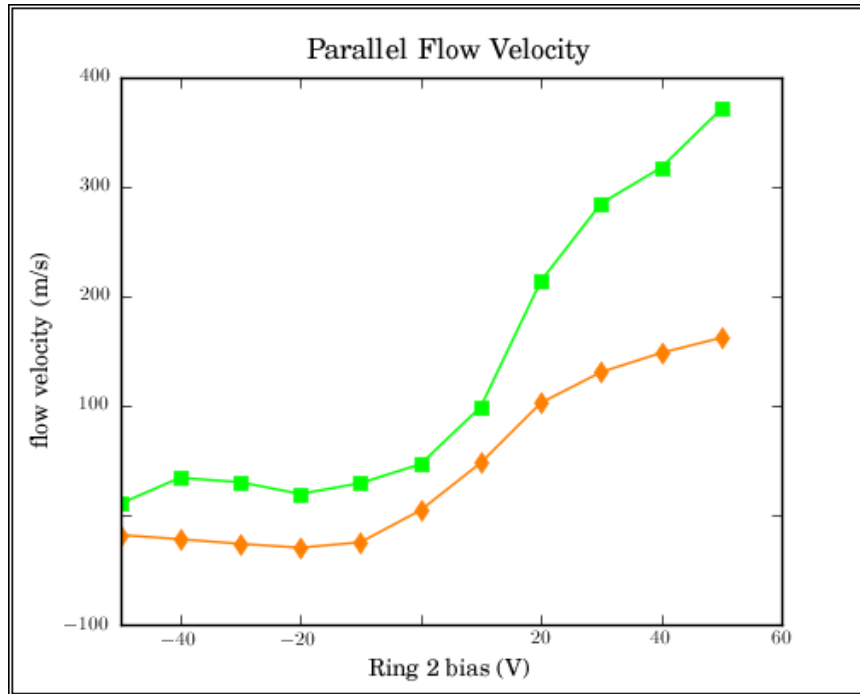


Figure 0-15: Comparison of the measured (green squares) and calculated (orange diamonds) axial velocities at a fixed radial position ($r = 1.5$ cm) as a function of the bias applied to Ring 2.

The calculated parallel velocity (the orange line in Figure I-15) shows reasonable agreement with the structure of the LIF measurements (green line). The magnitude of the calculated velocity is lower than the measured velocity, which is in contrast to the perpendicular velocities presented previously. The calculated value is found from the current collected by Ring 2, which would effectively integrate over the entire surface area of the ring. If the plasma conditions were not azimuthally symmetric, as the measurements of the perpendicular velocity suggest, this spatial variation would not be resolvable by the measurement of the current collected.

D. Discussion

The addition of LIF to ALEXIS was a significant undertaking, but the initial results show that the time and expense are well justified. The ability to non-invasively measure the ion flow velocity and temperature increase the range and detail of the experiments that can be performed in ALEXIS. These differences are illustrated in the figures below. From these figures, there are two outstanding issues that will be the focus of these discussions. First, the measured flow velocities using LIF are significantly below the values calculated using the cylindrically corrected $E \times B$ velocity. Second, the radial profiles of the perpendicular velocity (while similar) appear to show a difference in the flow profiles near the rings as compared to those further upstream. Each of these will be discussed below.

Sources of error in the ion velocity measurement:

Possible reasons for this discrepancy in the magnitude of the perpendicular velocity are: axial separation between the diagnostics, azimuthal separation of the diagnostics, and a large interrogation area for the collection optics. Each of these possible sources of error will be briefly discussed below.

The most difficult possible source of error to resolve, and perhaps the most important, is the axial separation of the three diagnostics used. Ideally, the measurements of the plasma potential and density could be made at the same location as the LIF measurements. In the current configuration, there are several challenges to implementing such alignment. If the LIF diagnostic was moved to the location of the emissive probe, i.e. into the main chamber, the optical access

would be severely compromised. While point measurements near the center of the column would be possible, scans of a radial chord would be limited to a maximum of $r = 1\text{cm}$. This is because the laser light and the collection optics would be entering the chamber through windows attached to QF-40 ports, with an inner diameter of approximately 4 cm.

An alternative scheme to collocate the emissive probe and LIF measurements would be to get an emissive probe to the custom vacuum box. Currently, no side of this box has a motion feed-through. If the side opposite the injection optics were to be replaced (the only “free” side), the task of getting the injected light out of the chamber could prove challenging. To accomplish this, a linear motion feed-through could be mounted on the polycarbonate window (Figure 0-16) such that the probe enters the chamber at an angle of roughly 45° . This would allow the probe to be retracted from the path of the laser light when not in use. The measurements would still be separated by roughly 135° , but the collocation of the measurements in z should help improve the correlation between calculated and measured perpendicular velocities.

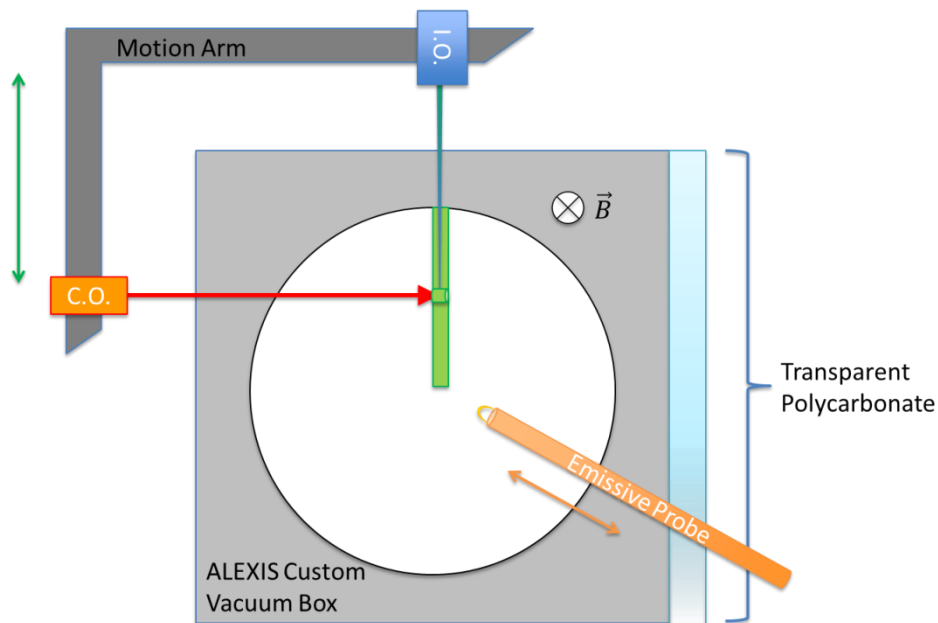


Figure 0-16: Rendering of a possible means of better collocating the emissive probe (orange) and LIF measurements (green). The emissive probe would need a linear motion feed-through mounted to the clear polycarbonate window (light blue).

To test for azimuthal symmetry, multiple emissive probes could be mounted at the same z location, *e.g.* Port 6. While a similar test has been performed with Langmuir probes, no such test has been performed to measure the plasma potential. This would also afford a good opportunity to attempt to measure any axial electric fields if an additional emissive probe were placed at a different z location. The motivation for performing both of these measurements at a similar time is the practical aspect of manufacturing multiple identical probes.

To reduce the volume of the interrogation volume of the collection optics there are a number of options available. First, changing the fiber optic cable used to one with a smaller numerical aperture (NA) would result in a smaller interrogation region. A more significant improvement could be made by decreasing the distance between the collection optics and the interrogation region. When the laser light stimulates a volume of plasma, the photons from the decaying state are emitted evenly in all directions. This means that the intensity of light falls off at a rate of $1/r^2$, where r is the distance between the stimulated plasma and the collection optics.

Two of the difficulties with reducing the volume are that the optical alignment becomes more challenging and there would be a reduction in signal (*i.e.*, fewer photons to enter the collection optics). Both of these could be overcome. To improve the alignment, a redesign of the motion arm to make it more rigid might be necessary. To overcome the reduction in signal, an increase in the PMT voltage may be sufficient. It is noted, however, that raising the PMT voltage generally increases the noise in the measurement. This will be mitigated somewhat by the

reduction in the overall collection volume of the collection optics, but the end result of the combination of these two factors is currently unknown.

The challenge of decreasing the distance is the physical limitations of the system. There are implementations of LIF that utilize a probe for injection of the laser light and collection of the signal, but the physical dimensions of such experiments are much larger. Implementing such a system on ALEXIS would likely prove difficult in that the perturbative effect of the probe would disturb the flows in the plasma.

Sources of error in the velocity profile:

Finally, even with these possible experimental modifications, these considerations do not explain the loss of azimuthal symmetry observed in the positively biased case presented in the previous section. The measurement of the perpendicular flow velocity provides evidence for a breaking of the cylindrical symmetry in the presence of the increased parallel flow. For example, based upon the data presented in the previous section, it is possible to construct a qualitative picture of the flow velocity profiles based upon the LIF measurements. These are shown in Figure 0-17.

For the Case A model, it is assumed that the central part of the plasma column has a drift velocity near 0 m/s. This is generally consistent with the experimental data which – for different measurement techniques, shows that the velocity is $\sim \pm 50$ m/s. This model gives a flow pattern that is generally azimuthally symmetric with the flow structure forming just to the outside of the ring electrodes. Here, there is little current drawn to the ring electrodes so there is not a significant source of electrons to modify the ion flow.

For the Case B model, however, there is good evidence that that plasma in this region no longer has an azimuthal flow. The measured flow pattern suggests that there is, in fact, a strong horizontal drift of the plasma with the central part of the plasma flowing in one direction and the outer part of the plasma drifting in the opposite direction. This loss of azimuthally symmetric flow does offer an explanation for the disappearance of the velocity shear driven ion cyclotron instability that was present in the original ALEXIS configuration.

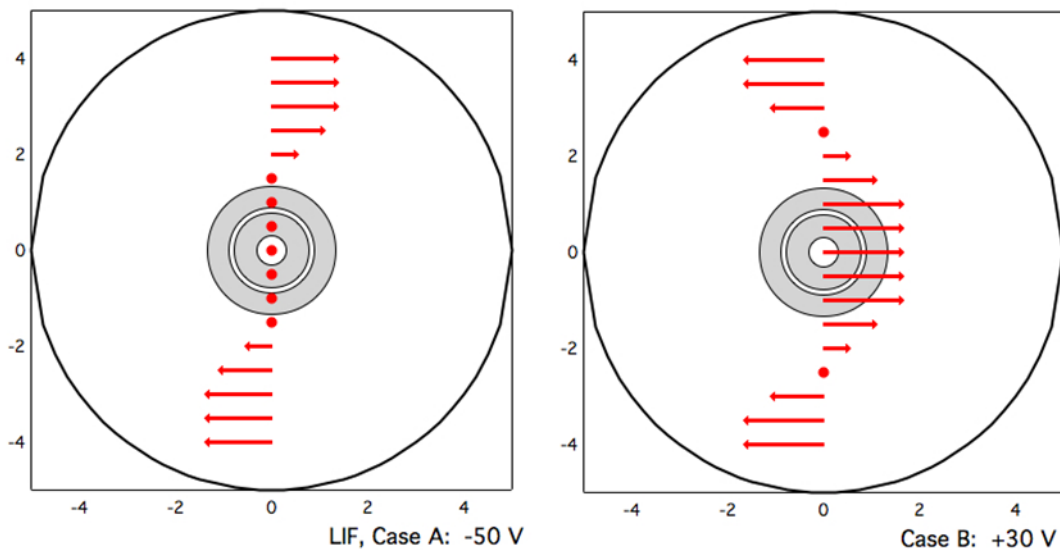


Figure 0-17: Models of the perpendicular velocity profiles based upon the LIF measurements for Case A and Case B. The plots show velocity vectors (shown as the red arrows) along a central chord of ALEXIS. The length of the arrow corresponds to magnitude of the velocity with a maximum length of 250 m/s for Case A and a maximum length of 300 m/s for Case B. The locations of the rings are shown as the gray circles in the background of each image.

These two plots are to be compared against a model of the cylindrically corrected velocity profile as computed from the electric field measurements. Case A is shown in Figure 0-18, and Case B is shown in Figure 0-19. First, it is noted that the electric field measurements are constructed from the plasma potential profiles one port upstream from where the LIF measurements are made, and on a port perpendicular to the plane of the LIF measurements.

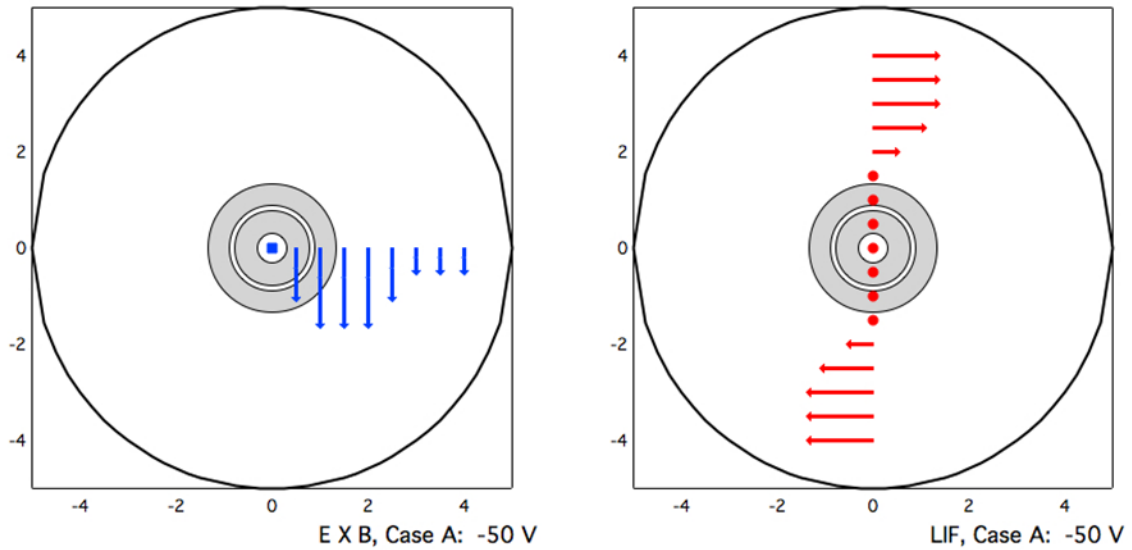


Figure 0-18: Models showing the different flow patterns for Case A ($V_2 = -50V$) from the measured electric field (blue, left), and the measured ion flows from the LIF measurement (red, right). The length of the arrow corresponds to magnitude of the velocity with a maximum length of 2000 m/s (blue) and 250 m/s (red). The locations of the rings are show as the gray circles in the background of each image.

For Case A (Figure 0-18), The two models show qualitatively similar results, with plasma flows being driven counter-clockwise around the column. The LIF system measures a velocity that increases with radius, while the $E \times B$ velocity predicts a maximum velocity between $r = 1\text{cm}$ and $r = 3\text{cm}$. This difference may be due to the different z locations of the measurements.

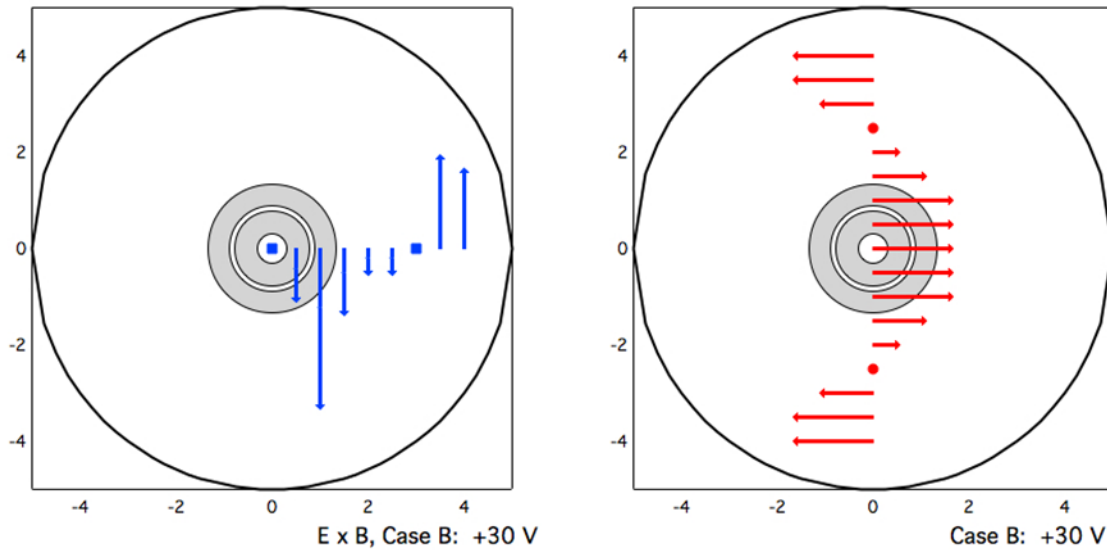


Figure 0-19: Models showing the different flow patterns for Case B ($V_2 = +30V$) from the measured electric field (blue, left), and the measured ion flows from the LIF measurement (red, right). The length of the arrow corresponds to magnitude of the velocity with a maximum length of 2000 m/s (blue) and 300 m/s (red). The locations of the rings are shown as the gray circles in the background of each image.

For the Case B measurements (Figure 0-19), there is a fairly significant difference between the flow velocity calculated from the cylindrical $E \times B$ velocity, and the measured flow from the LIF. The flow profile from the electric field predicts a higher velocity than Case A, with a very strongly sheared azimuthal flow. The LIF measurements show strong shear, but a loss of azimuthal symmetry. This breaking of azimuthal symmetry explains why the previously observed shear driven mode is not seen, despite the electric field measurements indicated an increase in shear.

An outstanding question is what is the role of the parallel current in giving rise to this somewhat unexpected flow structure. The data does show a growth of the parallel current (and a parallel electric field). In Chapter 3, it was shown that electric fields of this strength should not adversely impact the measured LIF signal, so there is still confidence in the velocity

measurements. However, if the flow of electrons towards the end of the plasma column is causing charge to be built up on the Macor insulator, that could adversely impact the ability to control the potential structure at the end of ALEXIS and lead to a modification of the flows.

One possible means to address this would be to construct a two-dimensional map of the perpendicular flow velocities. The major limitation to doing this now is the time required for each individual scan of the laser. The current approach uses the wavelength measured by the Bristol wavemeter as an integral component of the data analysis. The Bristol has a 4 Hz sample rate, and serves as the limit to the data acquisition rate. With a typical data run consisting of 600 data points, the result is that a successful measurement can require almost five minutes at each point in space. Also, the dye laser is prone to a loss of power (“de-tuning”) and transitions to different wavelength ranges (called “mode-hopping”) that can interrupt a data scan and require it to be repeated. These factors, combined with the finite lifetime of the Rhodamine dye, make such a detailed scan difficult.

Appendix II – Computer Codes Used

LabVIEW codes used in Data Acquisition

Langmuir Probe

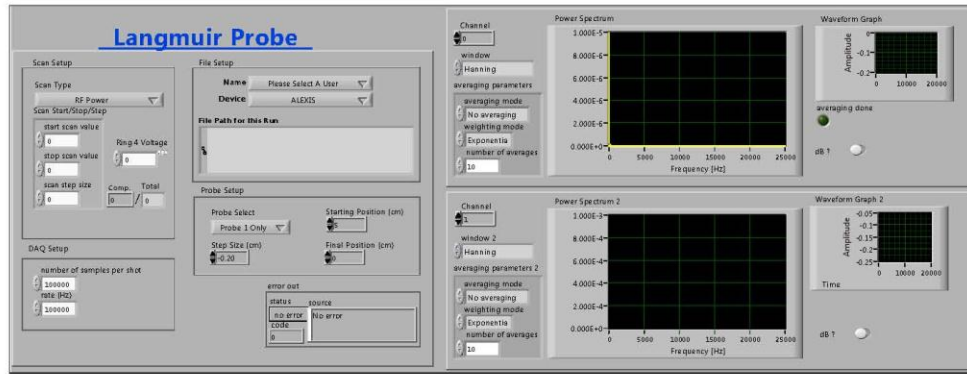
Connector Pane

LP frequency radial sweep GFITS Only.vi



Shows how to connect multiple input modules in a VI.

Front Panel



Controls and Indicators



[dB ?]

Allows to display the power spectrum in dB or not.



window

window is the time-domain window to be used.



averaging parameters



averaging mode



weighting mode



number of averages

number of averages specifies the number of averages that is used for RMS and Vector averaging. If weighting mode is Exponential, the averaging process is continuous. If weighting mode is Linear, the averaging process stops once the selected number of averages have been computed.



Channel

























[dB ?]

Allows to display the power spectrum in dB or not.



window 2

window is the time-domain window to be used.

-  **averaging parameters 2**
-  **averaging mode**
 -  **weighting mode**
 -  **number of averages**
 number of averages specifies the number of averages that is used for RMS and Vector averaging. If weighting mode is Exponential, the averaging process is continuous. If weighting mode is Linear, the averaging process stops once the selected number of averages have been computed.
-  **Channel**
-  **Starting Position (cm)**
 -  **Final Position (cm)**
 -  **Step Size (cm)**
 -  **[Probe Select]**
 -  **Scan Type**
 -  **Scan Start/Stop/Step**
 -  **start scan value**
 -  **stop scan value**
 -  **scan step size**
 -  **Ring 4 Voltage**
-  **VISA session 2**
 VISA session is a unique reference to an instrument I/O session. It identifies which device to communicate with and all configuration information to perform the I/O.
-  **number of samples per shot**
 -  **rate (Hz)**
 -  **Name**
 -  **Device**
-  **error out**
 error out is a cluster that describes the error status after this VI executes. If an error occurred before this VI was called, error out is the same as error in. Otherwise, error out shows the error, if any, that occurred in this VI. Use the error handler VIs to look up the error code and to display the corresponding error message. Using error in and error out clusters is a convenient way to check errors and to specify execution order by wiring the error output from one subVI to the error input of the next.
-  **status**
 status is TRUE if an error occurred, or FALSE if not. If status is TRUE, code is a non-zero error code. If status is FALSE, code can be zero or a warning code.



code

code is the number identifying an error or warning. If status is TRUE, code is a non-zero error code. If status is FALSE, code can be zero or a warning code. Use the error handler VIs to look up the meaning of this code and to display the corresponding error message.



source

source is a string that indicates the origin of the error, if any. Usually source is the name of the VI in which the error occurred.



Power Spectrum

Displays the power spectrum.



Waveform Graph



Power Spectrum 2

Displays the power spectrum.



Waveform Graph 2



averaging done

averaging done returns TRUE when averages completed is greater than or equal to the number of averages specified in averaging parameters. Otherwise, averaging done returns FALSE. averaging done is always TRUE if the selected averaging mode is No averaging.



File Path for this Run

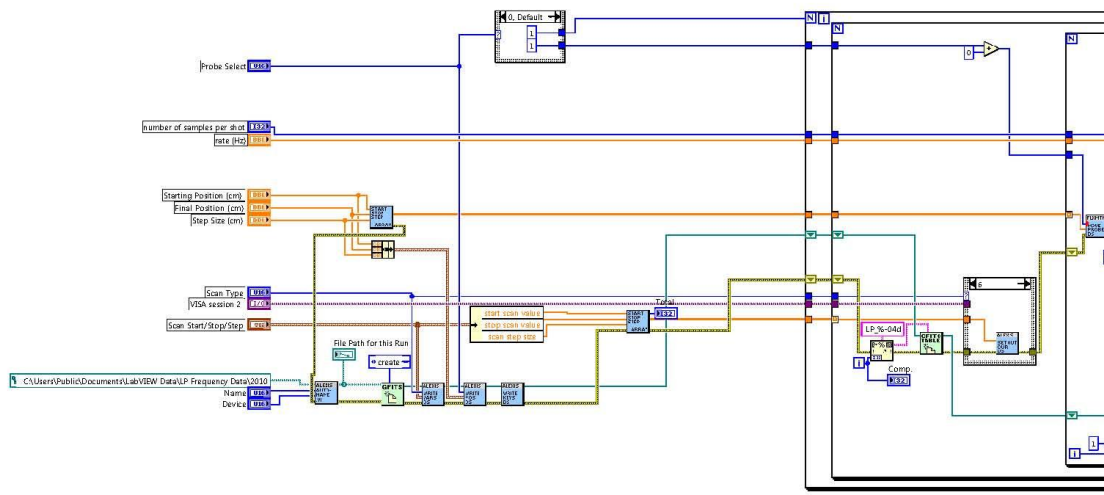


Total

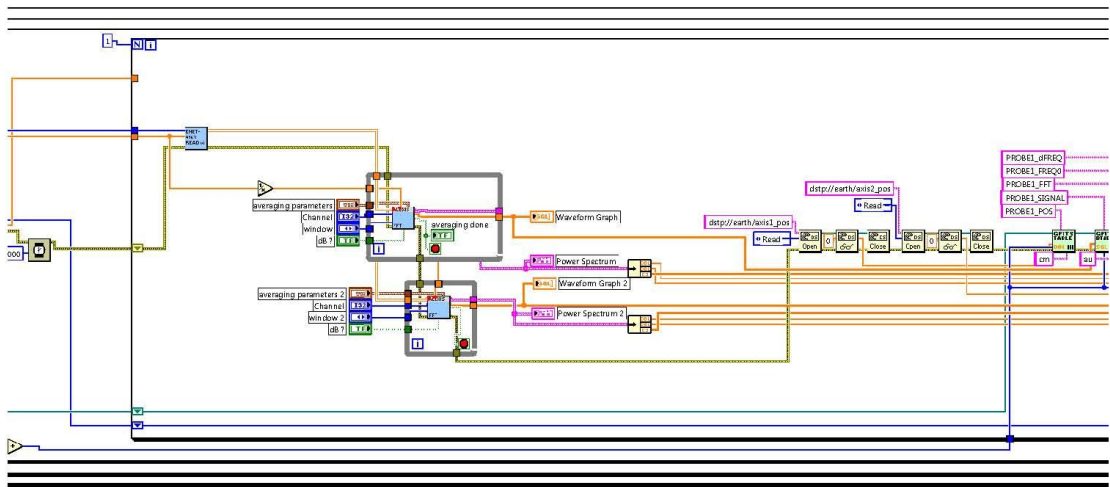


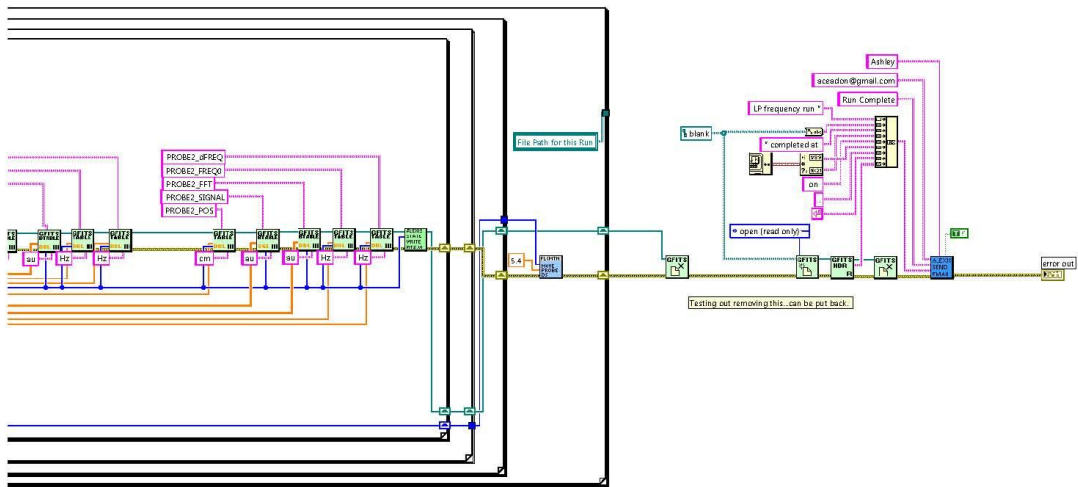
Comp.


Block Diagram



List of SubVIs and Express VIs





	fft_wrapper.vi C:\Users\Public\Documents\LabVIEW VI's\alexis_sub_vi's\fft_wrapper.vi
	ENET9163 read.vi C:\Users\Public\Documents\LabVIEW VI's\ENET9163 read.vi
	gfitsio-write-column-sgl-1d_new.vi C:\Program Files (x86)\National Instruments\LabVIEW 2009\user.lib\gfitsio\gfitsio-write-column-sgl-1d_new.vi
	gfitsio-write-column-dbl-1d_new.vi C:\Program Files (x86)\National Instruments\LabVIEW 2009\user.lib\gfitsio\gfitsio-write-column-dbl-1d_new.vi
	gfitsio-write-column-dbl-scalar_new.vi C:\Program Files (x86)\National Instruments\LabVIEW 2009\user.lib\gfitsio\gfitsio-write-column-dbl-scalar_new.vi
	gfitsio-write-column_new.vi C:\Program Files (x86)\National Instruments\LabVIEW 2009\user.lib\gfitsio\gfitsio-write-column_new.vi
	Machine_state_FITS.vi C:\Users\Public\Documents\LabVIEW VI's\alexis_sub_vi's\Machine_state_FITS.vi
	Wait with Error IO.vi C:\Program Files (x86)\National Instruments\LabVIEW 7.1\user.lib\NRL\Wait with Error IO.vi
	set_mfc_voltage_ds.vi C:\Users\Public\Documents\LabVIEW VI's\alexis_sub_vi's\set_mfc_voltage_ds.vi
	set_out_mag_cur_ds.vi C:\Users\Public\Documents\LabVIEW VI's\alexis_sub_vi's\set_out_mag_cur_ds.vi
	set_in_mag_cur_ds.vi C:\Users\Public\Documents\LabVIEW VI's\alexis_sub_vi's\set_in_mag_cur_ds.vi
	set_bipop_voltage.vi C:\Users\Public\Documents\LabVIEW VI's\alexis_sub_vi's\set_bipop_voltage.vi
	set_rf_power_ds.vi C:\Users\Public\Documents\LabVIEW VI's\alexis_sub_vi's\set_rf_power_ds.vi
	gfitsio-open-create-replace-table_new.vi C:\Program Files (x86)\National Instruments\LabVIEW 2009\user.lib\gfitsio\gfitsio-open-create-replace-table_new.vi
	gfitsio-read-header.vi C:\Program Files (x86)\National Instruments\LabVIEW 2009\user.lib\gfitsio\gfitsio-read-header.vi
	move_probe_ds.vi C:\Users\Public\Documents\LabVIEW VI's\alexis_sub_vi's\move_probe_ds.vi

**AutoGenerate_Filenames_v2.vi**

C:\Users\Eadon\Documents\My Dropbox\Lab Shared\ALEXIS Research\
AutoGenerate_Filenames_v2.vi

**gfitsio-open-create-replace-file_new.vi**

C:\Program Files (x86)\National Instruments\LabVIEW 2009\user.lib\gfitsio\gfitsio-open-
create-replace-file_new.vi

**gfitsio-close-file_new.vi**

C:\Program Files (x86)\National Instruments\LabVIEW 2009\user.lib\gfitsio\gfitsio-close-
file_new.vi

**write_var_keys_ds2.vi**

C:\Users\Public\Documents\LabVIEW VI's\alexis_sub_vi's\write_var_keys_ds2.vi

**write_probe_keys_ds.vi**

C:\Users\Public\Documents\LabVIEW VI's\alexis_sub_vi's\write_probe_keys_ds.vi

**write_fits_keys_ds.vi**

C:\Users\Public\Documents\LabVIEW VI's\alexis_sub_vi's\write_fits_keys_ds.vi

**Start Stop Step to Array.vi**

C:\Program Files (x86)\National Instruments\LabVIEW 2009\user.lib\NRL\Start Stop Step to
Array.vi

**gfitsio-open-create-replace-file.vi**

C:\Program Files (x86)\National Instruments\LabVIEW 2009\user.lib\gfitsio\gfitsio-open-
create-replace-file.vi

**gfitsio-close-file.vi**

C:\Program Files (x86)\National Instruments\LabVIEW 2009\user.lib\gfitsio\gfitsio-close-
file.vi

**Alexis_Gmail_No_Attachments.vi**

C:\Users\Public\Documents\LabVIEW VI's\alexis_sub_vi's\Alexis_Gmail_No_Attachments.vi

Double Probe

Connector Pane

DP_scan_FITS.vi



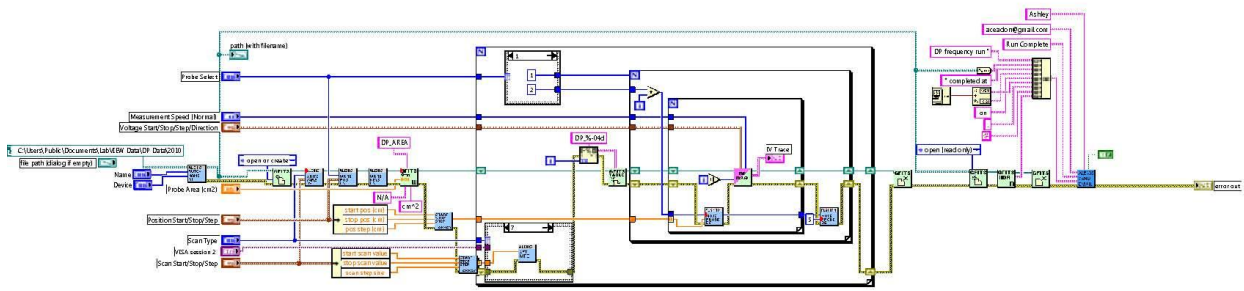
Front Panel

The front panel of the DP_scan_FITS.vi instrument is divided into several functional sections:

- Top Right:** User selection controls including a "Name" dropdown menu set to "Please Select A User" and a "Device" dropdown menu set to "ALEXIS". Below these is a "path (with filename)" field with a file selection icon.
- Left Column:** "Voltage Start/Stop/Step/Direction" controls with four knobs: High Voltage (V) at 0.00, Low Voltage (V) at 0.00, Voltage Step (V) at 0.00, and Sweep Direction set to "UP".
- Center Column:** "Probe Area (cm2)" knob at 0.75, "Measurement Speed (Normal)" dropdown set to "Normal", "Probe Select" dropdown set to "Probe 2 Only", and "Scan Type" dropdown set to "RF Power".
- Bottom Left:** "Position Start/Stop/Step" controls with three knobs: start pos (cm) at 5.4, stop pos (cm) at -0.4, and pos step (cm) at -0.2.
- Bottom Center:** "Scan Start/Stop/Step" controls with three knobs: start scan value at 0, stop scan value at 0, and scan step size at 0. A "Ring 4 Voltage" knob is also present at 0.
- Bottom Right:** "error out" status panel with "status" (green checkmark), "code" (00), and "source" (empty text box).
- Bottom:** An "IV Trace" plot showing Current (A) on the y-axis (ranging from -0.0005 to 0.0005) and Voltage (V) on the x-axis (ranging from -35 to 35). The plot is currently empty. A "DP I-V Trace" button with a waveform icon is located to the right of the plot.

Controls and Indicators

Block Diagram



List of SubVIs and Express VIs

	Alexis_Gmail_No_Attachments.vi C:\Users\Public\Documents\LabVIEW VI's\alexis_sub_vi's\Alexis_Gmail_No_Attachments.vi
	gfitsio-close-file.vi C:\Program Files (x86)\National Instruments\LabVIEW 2009\user.lib\gfitsio\gfitsio-close-file.vi
	gfitsio-read-header.vi C:\Program Files (x86)\National Instruments\LabVIEW 2009\user.lib\gfitsio\gfitsio-read-header.vi
	gfitsio-open-create-replace-file.vi C:\Program Files (x86)\National Instruments\LabVIEW 2009\user.lib\gfitsio\gfitsio-open-create-replace-file.vi
	Start Stop Step to Array.vi C:\Program Files (x86)\National Instruments\LabVIEW 2009\user.lib\NRL\Start Stop Step to Array.vi
	gfitsio-write-key.vi C:\Program Files (x86)\National Instruments\LabVIEW 2009\user.lib\gfitsio\gfitsio-write-key.vi
	gfitsio-write-key-double.vi C:\Program Files (x86)\National Instruments\LabVIEW 2009\user.lib\gfitsio\gfitsio-write-key-double.vi
	write_fits_keys_ds.vi C:\Users\Public\Documents\LabVIEW VI's\alexis_sub_vi's\write_fits_keys_ds.vi
	write_probe_keys_ds.vi C:\Users\Public\Documents\LabVIEW VI's\alexis_sub_vi's\write_probe_keys_ds.vi
	write_var_keys_ds2.vi C:\Users\Public\Documents\LabVIEW VI's\alexis_sub_vi's\write_var_keys_ds2.vi
	AutoGenerate_Filenames_v2.vi C:\Users\Eadon\Documents\My Dropbox\Lab Shared\ALEXIS Research\AutoGenerate_Filenames_v2.vi
	gfitsio-open-create-replace-table.vi C:\Program Files (x86)\National Instruments\LabVIEW 2009\user.lib\gfitsio\gfitsio-open-create-replace-table.vi
	set_rf_power_ds.vi C:\Users\Public\Documents\LabVIEW VI's\alexis_sub_vi's\set_rf_power_ds.vi
	set_bipop_voltage.vi C:\Users\Public\Documents\LabVIEW VI's\alexis_sub_vi's\set_bipop_voltage.vi
	set_in_mag_cur_ds.vi C:\Users\Public\Documents\LabVIEW VI's\alexis_sub_vi's\set_in_mag_cur_ds.vi



set_out_mag_cur_ds.vi

C:\Users\Public\Documents\LabVIEW VI's\alexis_sub_vi's\set_out_mag_cur_ds.vi



set_mfc_voltage_ds.vi

C:\Users\Public\Documents\LabVIEW VI's\alexis_sub_vi's\set_mfc_voltage_ds.vi



move_probe_ds.vi

C:\Users\Public\Documents\LabVIEW VI's\alexis_sub_vi's\move_probe_ds.vi



DP-GFITS-daq.vi

C:\Users\Public\Documents\LabVIEW VI's\alexis_sub_vi's\DP-GFITS-daq.vi

Emissive Probe

Connector Pane

EP_scan_FIT S.vi



Front Panel

Name Please Select A User **Device** ALEXIS

file path

Probe Probe 1 Only

Position Start/Stop/Step

start pos (cm) 5.4

stop pos (cm) -0.4

pos step (cm) -0.2

Scan RF Power

Scan Start/Stop/Step

start scan value 0 Samples (1) 10

stop scan value 0 Ring 4 Voltage

scan step size 0

Only reads Kiethly DMM with Address 26

Rings Enable Ring Measurements?

Ring Name 1 Address/Port (22) 20

Ring Name 2 Address/Port (22) 20

Ring Name 3 Address/Port (22) 22

Ring Name 4 Address/Port (22) 22

Statistics

0 max value

0 min value

0.00 mean

0.00 standard deviation

error out

status code 0

source

Current Sweep Completed Sweeps

Current Sweep Graph

Amplitude

Time

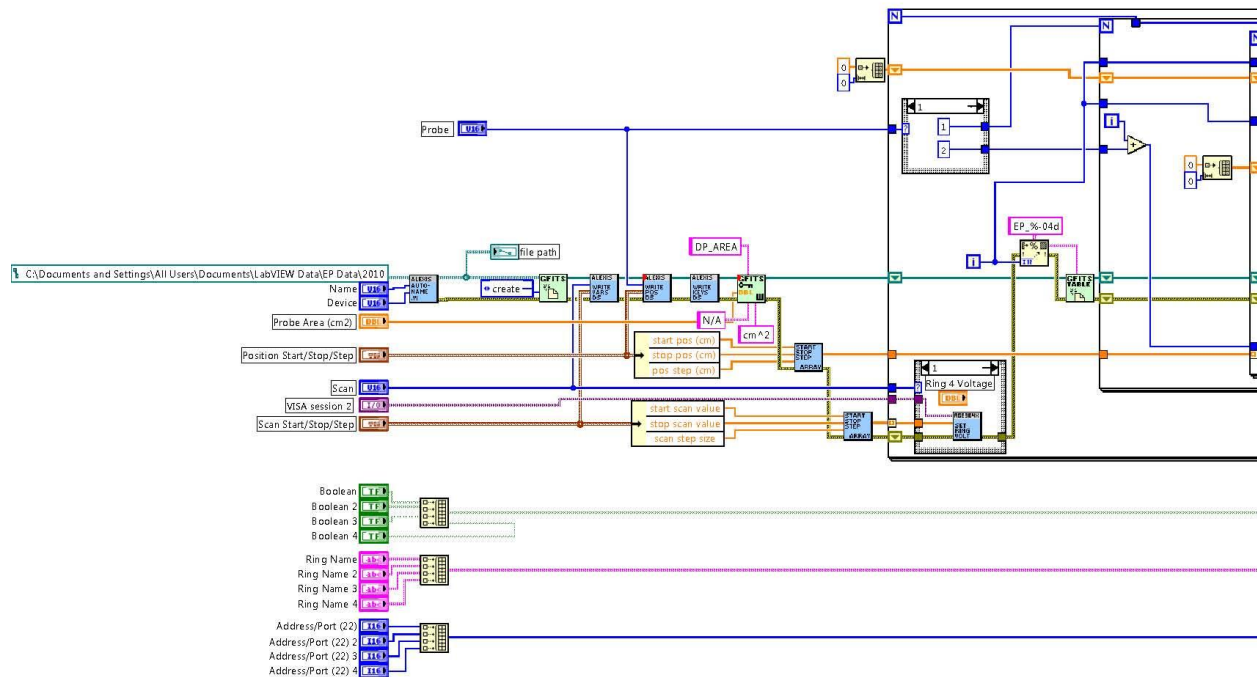
subarray

0 0

0 0

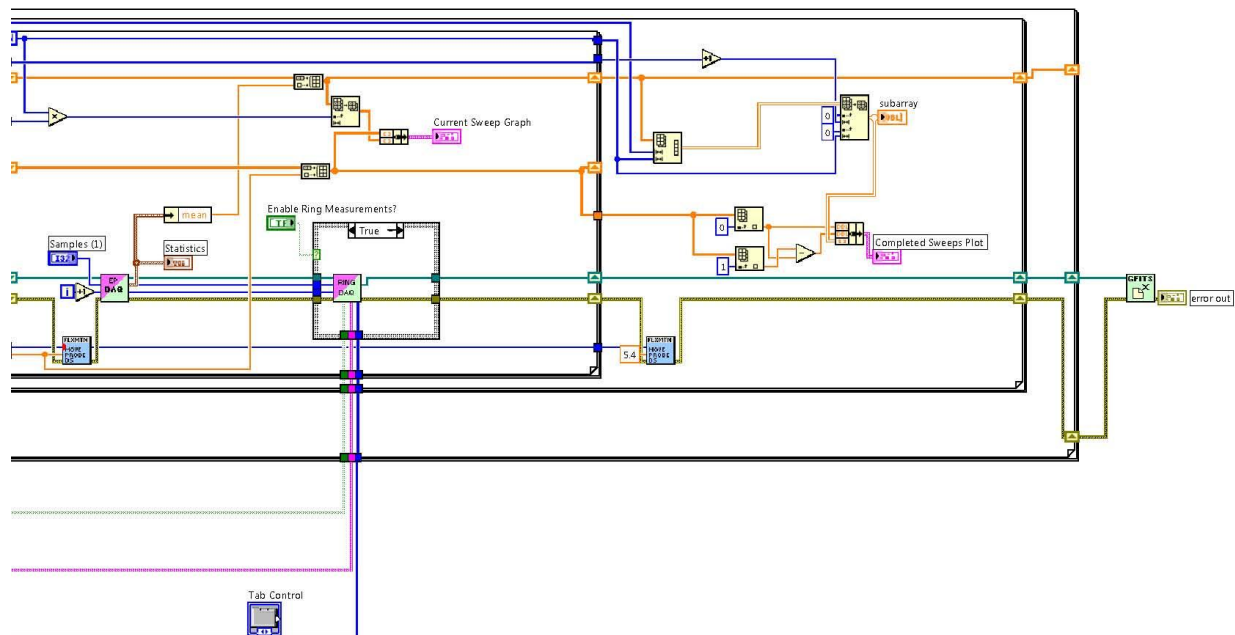
Controls and Indicators

Block Diagram



List of SubVIs and Express VIs

	gfitsio-close-file.vi C:\Program Files (x86)\National Instruments\LabVIEW 2009\user.lib\gfitsio\gfitsio-close-file.vi
	Start Stop Step to Array.vi C:\Program Files (x86)\National Instruments\LabVIEW 2009\user.lib\NRL\Start Stop Step to Array.vi
	write_fits_keys_ds.vi C:\Users\Public\Documents\LabVIEW VI's\alexis_sub_vi's\write_fits_keys_ds.vi
	write_probe_keys_ds.vi C:\Users\Public\Documents\LabVIEW VI's\alexis_sub_vi's\write_probe_keys_ds.vi
	gfitsio-open-create-replace-file.vi C:\Program Files (x86)\National Instruments\LabVIEW 2009\user.lib\gfitsio\gfitsio-open-create-replace-file.vi
	set_rf_power_ds.vi C:\Users\Public\Documents\LabVIEW VI's\alexis_sub_vi's\set_rf_power_ds.vi
	set_bipop_voltage.vi C:\Users\Public\Documents\LabVIEW VI's\alexis_sub_vi's\set_bipop_voltage.vi
	set_in_mag_cur_ds.vi C:\Users\Public\Documents\LabVIEW VI's\alexis_sub_vi's\set_in_mag_cur_ds.vi
	set_out_mag_cur_ds.vi C:\Users\Public\Documents\LabVIEW VI's\alexis_sub_vi's\set_out_mag_cur_ds.vi
	move_probe_ds.vi C:\Users\Public\Documents\LabVIEW VI's\alexis_sub_vi's\move_probe_ds.vi



	RING-VOLTAGE-CURRENT-GFITS-DAQ.vi C:\Users\Public\Documents\LabVIEW VI's\Control VI's\RING-VOLTAGE-CURRENT-GFITS-DAQ.vi
	gfitsio-write-key.vi C:\Program Files (x86)\National Instruments\LabVIEW 2009\user.lib\gfitsio\gfitsio-write-key.vi
	gfitsio-write-key-double.vi C:\Program Files (x86)\National Instruments\LabVIEW 2009\user.lib\gfitsio\gfitsio-write-key-double.vi
	EP-GFITS-DAQ.vi C:\Users\Eadon\Desktop\Misc. Desktop VI's\EP-GFITS-DAQ.vi
	gfitsio-open-create-replace-table.vi C:\Program Files (x86)\National Instruments\LabVIEW 2009\user.lib\gfitsio\gfitsio-open-create-replace-table.vi
	AutoGenerate_Filenames.vi C:\Users\Eadon\Documents\My Dropbox\Lab Shared\ALEXIS Research\AutoGenerate_Filenames.vi
	write_var_keys_ds.vi C:\Users\Public\Documents\LabVIEW VI's\alexis_sub_vi's\write_var_keys_ds.vi

LabVIEW codes used in Data Analysis

Langmuir Probe

Connector Pane

LP_analysis_auto.vi



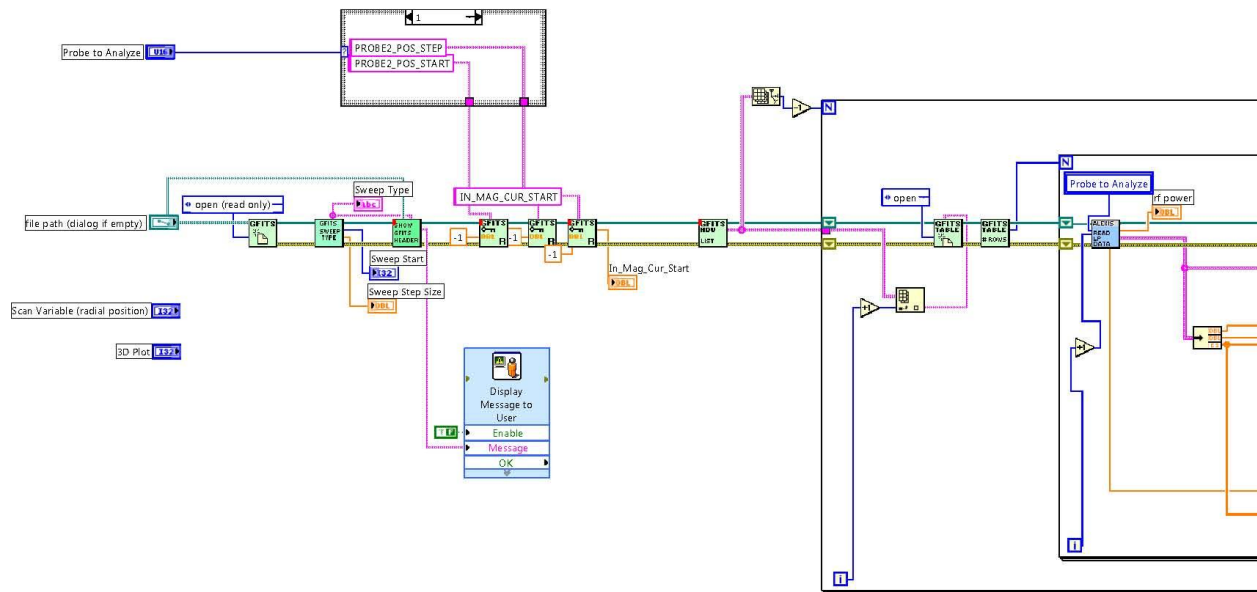
Front Panel

The screenshot displays the front panel of the LabVIEW program 'LP_analysis_auto.vi'. The interface is organized into several sections:




- File Path:** A text field labeled 'file path (dialog if empty)' with a browse button.
- Control Knobs:** 'rf power' (0), 'Sweep Type', 'Sweep Start' (0), 'Sweep Step Size' (0), 'Row (ring voltage)' (0), 'Sweep Value' (0), and 'Scan Variable (radial position)' (0).
- Waveform Graph:** A graph titled 'Waveform Graph' showing 'Amplitude' on the y-axis (ranging from 0 to 3E-5) and 'Time' on the x-axis (ranging from 0 to 25000). The plot area is currently empty.
- Probe and Gas Settings:** 'Probe to Analyze' is set to 'Probe 1', and 'Gas Species' is set to 'Argon'. There is an 'error out' section with 'status' (checked) and 'code' (40) fields, and a 'source' field.
- 3D Plot and Surface:** A '3D Plot' knob is set to 0, and the 'Plot Style' is 'cwSurface'. Below it is a '3D Surface' plot showing a heatmap of data points. The plot has axes labeled 0, 1, 2, 3, 4, 5.
- Projection and Scaling Controls:** A 'Transparency (%)' knob is set to 40. There are 'XY Projection', 'xz projection', and 'yz projection' buttons, along with a 'Show Projections Only' button. 'auto scale x (radius)', 'auto scale y (frequency)', and 'auto scale z' are all set to 'OFF'. Axis minimum and maximum values are set for X, Y, and Z axes.
- STOP Button:** A prominent red 'STOP' button is located in the center-right area.

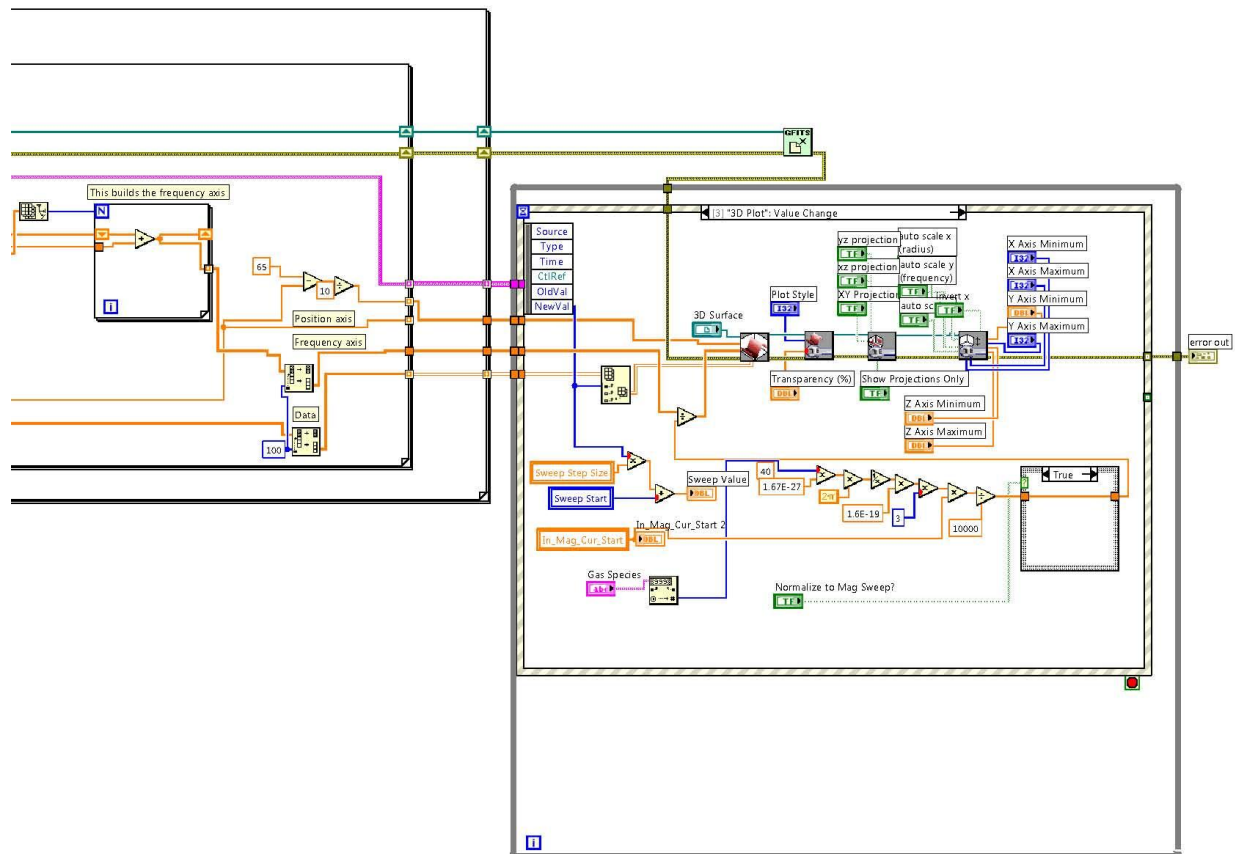
Controls and Indicators



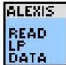








Block Diagram



List of SubVIs and Express VIs

- 
gfitsio-close-file_new.vi
 C:\Program Files (x86)\National Instruments\LabVIEW 2009\user.lib\gfitsio\gfitsio-close-file_new.vi
- 
gfitsio-open-create-replace-file_new.vi
 C:\Program Files (x86)\National Instruments\LabVIEW 2009\user.lib\gfitsio\gfitsio-open-create-replace-file_new.vi
- 
gfitsio-open-create-replace-table_new.vi
 C:\Program Files (x86)\National Instruments\LabVIEW 2009\user.lib\gfitsio\gfitsio-open-create-replace-table_new.vi
- 
NI_3dgraph.lvlib:3D Surface.vi
 C:\Program Files (x86)\National Instruments\LabVIEW 2009\vi.lib\Platform\3dgraph.llb\3D Surface.vi
- 
NI_3dgraph.lvlib:Basic Properties.vi
 C:\Program Files (x86)\National Instruments\LabVIEW 2009\vi.lib\Platform\3dgraph.llb\Basic Properties.vi



-  **NI_3dgraph.lvlib:Projection Properties.vi**
C:\Program Files (x86)\National Instruments\LabVIEW 2009\vi.lib\Platform\3dgraph.llb\Projection Properties.vi
-  **NI_3dgraph.lvlib:Axes Properties.vi**
C:\Program Files (x86)\National Instruments\LabVIEW 8.6\vi.lib\Platform\3dgraph.llb\Axes Properties.vi
-  **read_lp_data.vi**
C:\Users\Public\Documents\LabVIEW VI's\alexis_sub_vi's\read_lp_data.vi
-  **gfitsio-get-num-rows_new.vi**
C:\Program Files (x86)\National Instruments\LabVIEW 2009\user.lib\gfitsio\gfitsio-get-num-rows_new.vi
-  **FITS_Sweep_Selector.vi**
C:\Users\Eadon\Desktop\Misc. Desktop VI's\FITS_Sweep_Selector.vi
-  **show_gfits_header.vi**
C:\Users\Public\Documents\LabVIEW VI's\alexis_sub_vi's\show_gfits_header.vi
-  **Display Message to User**
Display Message to User
-  **gfitsio-read-key-double_new.vi**
C:\Program Files (x86)\National Instruments\LabVIEW 2009\user.lib\gfitsio\gfitsio-read-key-double_new.vi
-  **gfitsio-read-key_new.vi**
C:\Program Files (x86)\National Instruments\LabVIEW 2009\user.lib\gfitsio\gfitsio-read-key_new.vi
-  **gfitsio-read-key-double.vi**
C:\Program Files (x86)\National Instruments\LabVIEW 2009\user.lib\gfitsio\gfitsio-read-key-double.vi
-  **gfitsio-read-key.vi**
C:\Program Files (x86)\National Instruments\LabVIEW 2009\user.lib\gfitsio\gfitsio-read-key.vi
-  **gfitsio-get-hdu-list_new.vi**
C:\Program Files (x86)\National Instruments\LabVIEW 2009\user.lib\gfitsio\gfitsio-get-hdu-list_new.vi

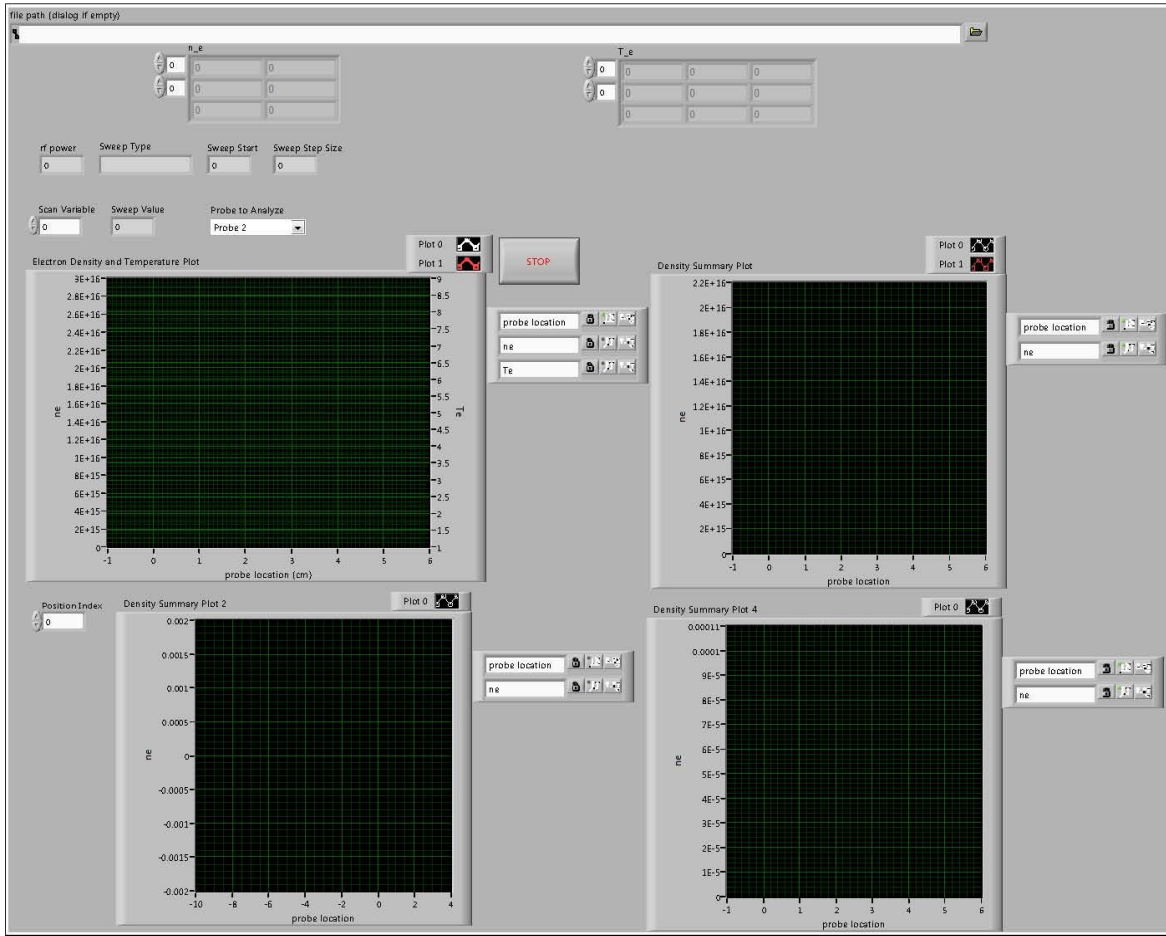
Double Probe

Connector Pane

DP_analysis_auto.vi

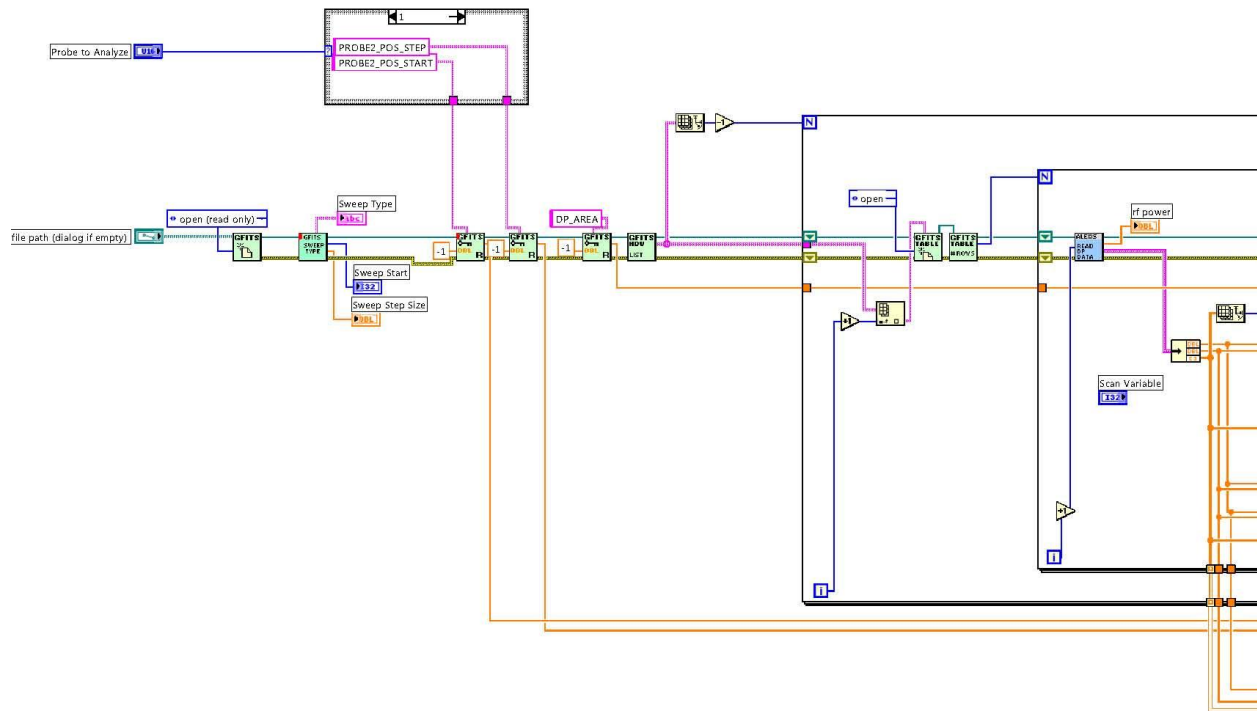


Front Panel



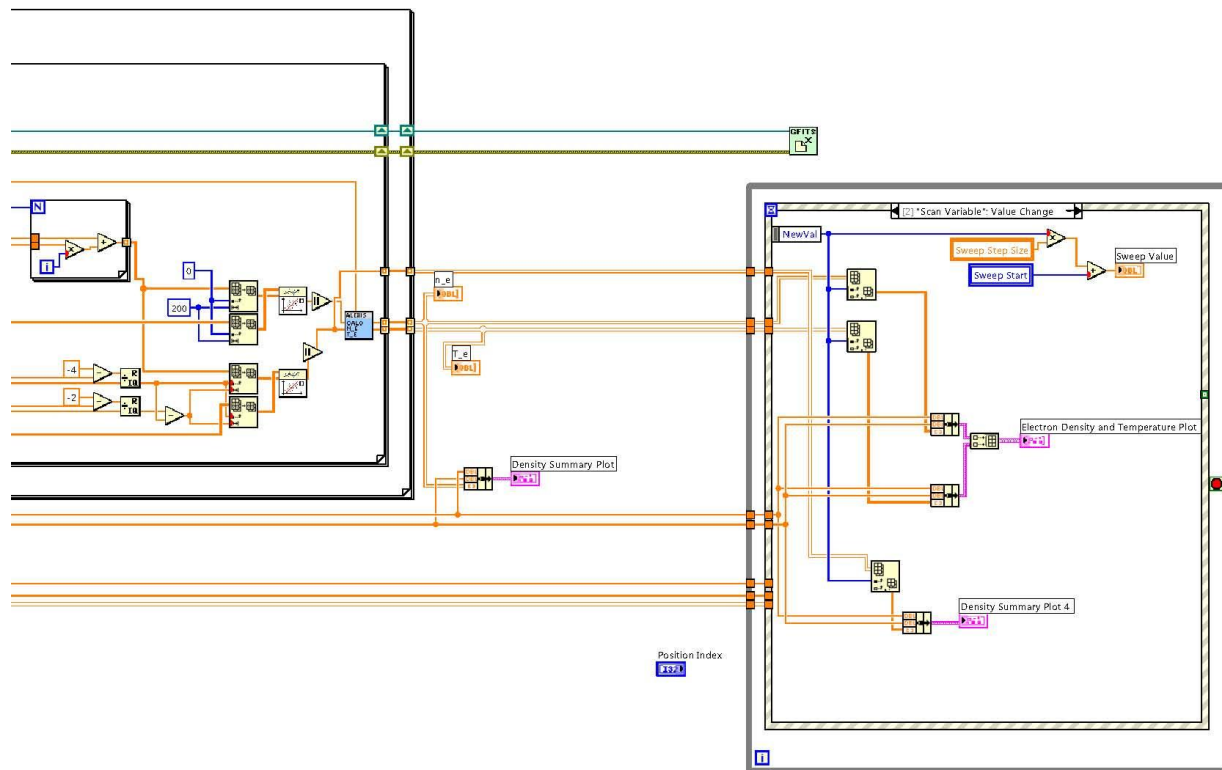
Controls and Indicators

Block Diagram



List of SubVIs and Express VIs

- 
gfitsio-close-file.vi
 C:\Program Files (x86)\National Instruments\LabVIEW 2009\user.lib\gfitsio\gfitsio-close-file.vi
- 
gfitsio-get-hdu-list.vi
 C:\Program Files (x86)\National Instruments\LabVIEW 2009\user.lib\gfitsio\gfitsio-get-hdu-list.vi
- 
gfitsio-read-key.vi
 C:\Program Files (x86)\National Instruments\LabVIEW 2009\user.lib\gfitsio\gfitsio-read-key.vi
- 
gfitsio-read-key-double.vi
 C:\Program Files (x86)\National Instruments\LabVIEW 2009\user.lib\gfitsio\gfitsio-read-key-double.vi
- 
FITS_Sweep_Selector.vi
 C:\Users\Eadon\Desktop\Misc. Desktop VI's\FITS_Sweep_Selector.vi
- 
gfitsio-open-create-replace-file.vi
 C:\Program Files (x86)\National Instruments\LabVIEW 2009\user.lib\gfitsio\gfitsio-open-create-replace-file.vi
- 
gfitsio-get-num-rows.vi
 C:\Program Files (x86)\National Instruments\LabVIEW 2009\user.lib\gfitsio\gfitsio-get-num-rows.vi





gfitsio-open-create-replace-table.vi

C:\Program Files (x86)\National Instruments\LabVIEW 2009\user.lib\gfitsio\gfitsio-open-create-replace-table.vi



read_dp_data.vi

C:\Users\All Users\Documents\LabVIEW VI's\alexis_sub_vi's\read_dp_data.vi



NI_AALPro.lvlib:Linear Fit.vi

C:\Program Files (x86)\National Instruments\LabVIEW 2009\vi.lib\Analysis\6fits.lib\Linear Fit.vi



DP_calculate_ne_Te.vi

C:\Users\All Users\Documents\LabVIEW VI's\alexis_sub_vi's\DP_calculate_ne_Te.vi

Emissive Probe

Connector Pane

EP_analysis.vi



Front Panel

file path (dialog if empty)

Probe Start: 0, Probe Stop: 0, Probe Step: 0
Sweep Type: [], Sweep Start: 0, Sweep Step Size: 0

Probe to Analyze: Probe 1

Output Text File? []

Instructions:
1.) Input path for FITS file containing the radial emissive probe scans, or run VI and select path from dialog box
2.) Select "Probe to Analyze". Selecting the wrong probe will result in an error
3.) Adjust "Radial Scan Number" to display the plasma potential and calculated electric fields
Note: Negative electric fields correspond to radially inward.

Potential Plot 0: Y-axis Potential (V) 0-55, X-axis Probe Position (mm) 0-5

Electric Field Plot 0: Y-axis Electric Field (V/cm) -10 to 10, X-axis Probe Position (mm) 0-5

Radial Scan Number: 0, Sweep Value: 0

STOP

Potential Summary Plot: Y-axis Potential (V) 0-55, X-axis probe location -1 to 5

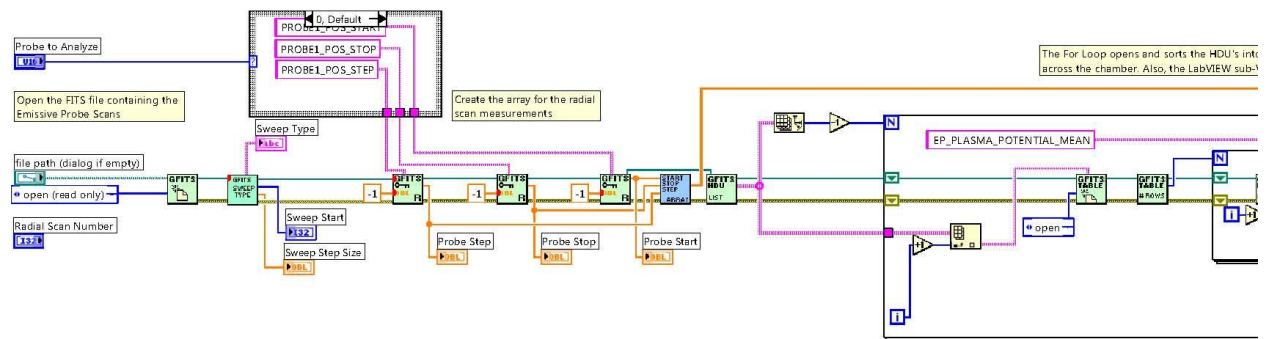
Electric Field Summary Plot: Y-axis Electric Field (V/cm) -6 to 0, X-axis probe location 0 to 4.5

probe location: Potential (V), Electric Field (V/cm)

Plot 0-8 selection buttons

Controls and Indicators

Block Diagram

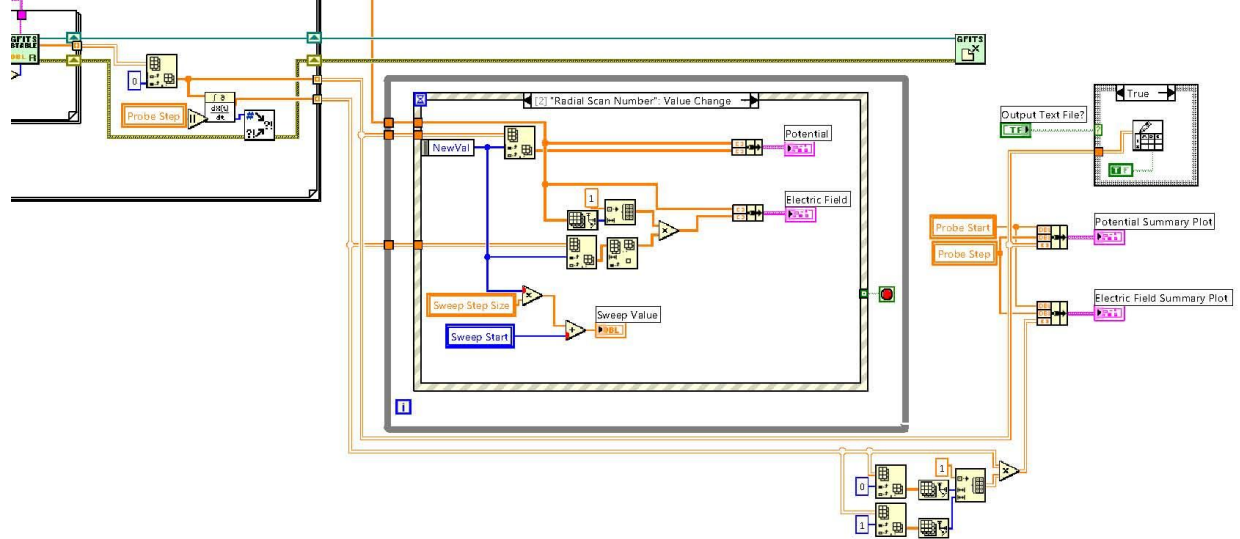


List of SubVIs and Express VIs

- 
gffitsio-close-file.vi
 C:\Program Files (x86)\National Instruments\LabVIEW 2009\user.lib\gffitsio\gffitsio-close-file.vi
- 
gffitsio-get-hdu-list.vi
 C:\Program Files (x86)\National Instruments\LabVIEW 2009\user.lib\gffitsio\gffitsio-get-hdu-list.vi
- 
Start Stop Step to Array.vi
 C:\Program Files (x86)\National Instruments\LabVIEW 2009\user.lib\NRL\Start Stop Step to Array.vi
- 
gffitsio-read-key.vi
 C:\Program Files (x86)\National Instruments\LabVIEW 2009\user.lib\gffitsio\gffitsio-read-key.vi
- 
gffitsio-read-key-double.vi
 C:\Program Files (x86)\National Instruments\LabVIEW 2009\user.lib\gffitsio\gffitsio-read-key-double.vi
- 
FITS_Sweep_Selector.vi
 C:\Users\Eadon\Desktop\Misc. Desktop VI's\FITS_Sweep_Selector.vi
- 
gffitsio-open-create-replace-file.vi
 C:\Program Files (x86)\National Instruments\LabVIEW 2009\user.lib\gffitsio\gffitsio-open-create-replace-file.vi
- 
Error Cluster From Error Code.vi
 C:\Program Files (x86)\National Instruments\LabVIEW 2009\vi.lib\Utility\error.lib\Error Cluster From Error Code.vi
- 
gffitsio-open-create-replace-table.vi
 C:\Program Files (x86)\National Instruments\LabVIEW 2009\user.lib\gffitsio\gffitsio-open-create-replace-table.vi

arrays, with one row for each potential scan
V1 calculates the derivative of the potential

This While Loop and Event structure work to display the radial Potential and Electric field measurements.
Also, the derivative of the potential is multiplied by a constant array of 10 to finish the calculation of the
electric field and convert from V/mm to V/cm.





Write To Spreadsheet File (DBL).vi

C:\Program Files (x86)\National Instruments\LabVIEW 2009\vi.lib\Utility\file.llb\Write To Spreadsheet File (DBL).vi



Write To Spreadsheet File.vi

C:\Program Files (x86)\National Instruments\LabVIEW 2009\vi.lib\Utility\file.llb\Write To Spreadsheet File.vi



gfitsio-read-column-dbl-1d.vi

C:\Program Files (x86)\National Instruments\LabVIEW 2009\user.lib\gfitsio\gfitsio-read-column-dbl-1d.vi



gfitsio-get-num-rows.vi

C:\Program Files (x86)\National Instruments\LabVIEW 2009\user.lib\gfitsio\gfitsio-get-num-rows.vi



gfitsio-read-column.vi

C:\Program Files (x86)\National Instruments\LabVIEW 2009\user.lib\gfitsio\gfitsio-read-column.vi



NI_AALPro.lvlib:Derivative x(t).vi

C:\Program Files (x86)\National Instruments\LabVIEW 2009\vi.lib\Analysis\2dsp.llb\Derivative x(t).vi